Landing Gear Design for Forest Firefighting Drone and Introduction of Novel Extinguishing Method

João Filipe Vieira Festas

Mater's Thesis

Advisor: António Torres Marques
Co-Advisor: José Miguel Silva

Master's Degree in Mechanical Engineering

2022-09-26

Resumo

Design de um Trem de Aterragem para um Drone de Combate a Incêndios Florestais e Introdução de um Novo Método de Extinção de Fogos

O desafio foi proposto inicialmente pelo Prof. Dr. António Torres Marques.

Começando como uma proposta para o desenvolvimento de um drone de combate a incêndios florestais, os objetivos foram alterados quando se tornou evidente que as considerações iniciais estavam a convergir com um drone previamente projetado.

Assim, o objetivo principal passou a ser criar um trem de aterragem em compósitos para o drone e introduzir um método de extinção de incêndios florestais melhorado.

Foi realizado um estudo de técnicas de extinção convencionais e inovadoras, a fim de obter uma amostra de grande tamanho a partir da qual se pudesse selecionar o método mais apropriado. Além disso, foram estudados e implementados os modelos teóricos necessários para o desenvolvimento de componentes críticos ao processo.

Considerando que já estão disponíveis trens de aterragem em materiais compósitos, a viabilidade desta opção será investigada.

Inicialmente, foi realizada uma investigação sobre o estado da arte destas estruturas e sobre os regulamentos e legislação de design.

O passo seguinte envolveu a escolha da configuração básica do trem de aterragem e do material a ser utilizado.

Para prever o comportamento das estruturas, foi realizado um estudo sobre os modelos teóricos para vigas curvas, o teorema de Castigliano, e as teorias de camadas equivalentes para materiais laminados.

A seleção da sequência de empilhamento do laminado e a definição iterativa das propriedades geométricas das pernas do trem de aterragem constituíram a concepção inicial dos componentes. Para proporcionar capacidades computacionais mais rápidas, foram criados códigos em MATLAB.

Finalmente, a análise FEM foi utilizada para validar os resultados obtidos e os códigos criados. Além disso, a fixação ao drone foi concebida em pormenor e o modelo foi ainda optimizado.

Palavras Chave : Trem de Aterragem Frontal, Trem de Aterragem Principal, Drone, Canhão de Neve a CO_2, Método de Elementos Finitos, Sistemas Compósitos

Abstract

Prof. Dr. António Torres Marques was the first to propose the challenge.

Beginning as a proposal for the development of a forest firefighting drone, the main objectives shifted when it became apparent that the initial considerations were converging with a drone already projected.

Hence, the primary objective has been to create a composite landing gear for the drone and enhance the extinguishing method.

A study of conventional and innovative extinguishing techniques was conducted in order to obtain a large sample size from which to select the most appropriate method. In addition, the necessary theoretical models for the development of process-critical components were studied and implemented.

Considering that composite materials are already available for UAV landing gear, the feasibility of this option will be investigated.

Initially, research was conducted on the state of the art of these structures and the applicable design regulations.

The next step involved choosing the landing gear's basic configuration and the material to be used.

To predict the behavior of leaf struts, a study was conducted on the theoretical models for curved beams, Castigliano's theorem, and the equivalent layer theories for laminate materials.

Selecting the laminate stacking sequence and iteratively defining the geometric properties of the landing gear legs comprised the initial design of the components. To provide faster computing capabilities, MATLAB coding was developed.

Finally, FEM analysis was used to validate the results obtained and the codes created. In addition, the attachment to the drone was designed in detail and the model was optimized further.

Key Words: Nose Landing Gear, Main Landing Gear, UAV, CO_2 Snow Cannon, Finite Element Method, Leaf Strut, Composite Systems

Acknowledgements

I would like to thank my advisor Prof. Dr. António Torres Marques for his availability, support during this entire process and ability to recommend the best way I could get information on any given area;

To my coadvisor Eng. José Miguel Silva for always helping with anything I needed and for his eagerness to assist me on getting the best final product possible;

To Eng. Joaquim Matos for his assistance on certain areas of this project, for letting me in his work and for true sympathy and dedication to a project he could have just dismissed;

To Profs. Albertino Arteiro, Marco Parente, Abílio de Jesus, Pedro Leal Ribeiro and José Esteves for insightful advice on specific situations;

To my family, who have always been there for me, put me through university and who I owe the most;

To my girlfriend, who had to put up with some bad mood days and with my not easy stressed-out self. But who kept me sane during these months and with whom I could not have done this without;

To my friends, for some amazing memories and things to come.

"Look, if you had one shot, or one opportunity. To seize everything you ever wanted in one moment. Would you capture it or just let it slip?"

Marshall Mathers

Contents

Acronyms and Symbols

List of Acronyms

UAV	Unmnanned Aerial Vehicle
NLG	Nose Landing Gear
MLG	Main Landing Gear
SF	Safety Factor
FEM	Finite Element Method
CAD	Computer Assisted Design
PSE	Primary Structure Elements
CG	Center of Gravity
MAC	Mean Aerodynamic Cord
HS	High Strength
ESL	Equivalent Laminate
NATO	North Atlantic Treaty Organization
STANAG	Standardization Agreement
CS-VLA	Certification Specialization for Very Light Aeroplanes
CFR	Council on Foreign Relations
WWI	World War 1
VTOL	Vertical Takeoff and Landing
FLIR	Teledyne FLIR LLC, subsidiary of Teledyne Technologies

List of Symbols

$[A]$	Extensional stiffness matrix
$[D]$	Bending stiffness matrix
T	Wheel Track
B	Wheel Base
B_M	Distance between CG and MLG
B_N	Distance between CG and NLG
a'	Distance between CG and NLG projected with 14^o angle
b'	Distance between CG and MLG projected with 14^o angle
d'	Wheel Base projected with 14^o angle
X^T	Tensile strength on main direction
X^C	Compressive strength on main direction
X^T	Tensile strength on transverse direction
X^T	Compressive strength on transverse direction
E^T	Young's Module
E^C	Compressive Modulus
E_1	Young's Module on the 1 direction for orthotropic materials
E_2	Young's Module on the 2 direction for orthotropic materials
E_x	Young's Module on the x direction for orthotropic materials
E_y	Young's Module on the y direction for orthotropic materials
v_{12}	Poisson's ratio referent to direction 2 when loading is in direction 1
v_{21}	Poisson's ratio referent to direction 1 when loading is in direction 2
v_{xy}	Poisson's ratio referent to direction y when loading is in direction x
G_{12}	Shear Modulus for the plane perpendicular to direction 3
G_{xy}	Shear Modulus for the plane perpendicular to direction z
a_s	Cross section dimension for laminate thickness
b_s	Cross section dimension perpendicular to laminate thickness
h_{LG}	Landing gear height
T	Temperature (when not regarding Landing Gear)
p	Pressure
ρ	Density

List of Figures

List of Tables

Chapter 1

Introduction

Every year, Portugal is confronted with significant forest fire problems and their repercussions. The causes of these fires include direct fire origins, accidental and structural causes. arson origins, natural phenomenons, and unknown origins have all been linked to fires.

Moreover, changes in global climate conditions have a direct effect on wildfires. Conditions that are hotter and drier are dehydrating ecosystems and increasing their risk. Large quantities of carbon dioxide, carbon monoxide, and fine particulate matter are released into the atmosphere by wildfires, affecting the weather and climate simultaneously. Air pollution can also result in a variety of health issues, including respiratory and cardiovascular concerns. Wildfires have a significant impact on mental health and psychosocial well-being.

1.1 Motivation

In the past, a VTOL drone project was developed in an effort to introduce a mechanism to control forest areas and guarantee initial firefighting.

This drone, lightweight, is made of carbon fiber reinforced polymers, has a wingspan of 3.5 m, 12.7 kg maximum takeoff weight and a proposed endurance of 1.5 h at a cruise speed of 100 km/h [1].

In analyzing this project, we determined that the approach taken was extremely preliminary and that additional structural and aerodynamic analyses were necessary to ensure that the vehicle could be maneuverable.

In order for this drone to land on a runway, it will need landing gear, which was not designed during this earlier work [1].

As a result, the purpose of the current work is to design and investigate a landing gear that can be integrated into the drone, as well as to investigate the project as a whole in order to make some modifications and improvements.

1.2 Objectives

The primary objectives of this project involve the landing gear. It is anticipated that, in the end, a detailed design will be developed that will allow the VTOL drone to land using the combustion engine, on a runway.

A VTOL aircraft is one that can take off and land vertically while flying horizontally..

As with the rest of the drone, this component should be made primarily of composites to be lightweight, be able to withstand the loads associated with different landing conditions, not incur excessive costs in comparison to the rest of the design, minimize added drag as much as possible, and enable simple production. It is also expected that a proper attachment to the fuselage is defined.

1.3 Layout

This master thesis is organized in seven chapters, as followed:

- **Chapter 1** - Introduction and justifications for the proposed project. Initial objectives that will be analyzed and confirmed at the conclusion of the thesis.

- **Chapter 2** - Presentation of the state of the art, research on alternative possibilities or paths forward, and technologies addressing the same issue. Problem formulation presented. Analysis of the previously developed drone and potential areas for modification. Definition of the regulations that must be followed to design the landing gear correctly.

- **Chapter 3** - Clarification of the primary landing gear requirements. Initial design approach for determining the fundamental configuration and geometry. Definition of functional and geometric requirements and presentation of models to be followed in order to obtain the dimensions needed for the conceptual design. Theoretical models that will allow for preliminary calculations to predict the behaviour of the landing gear. Selection of the material and considerations to be taken into account when choosing the exact configuration and orientation based on the selection made. Criteria to be used to verify the system's reliability.

- **Chapter 4** - Methodology and procedures used designing purposes. Various mathematical models are defined. Software employed.

- **Chapter 5** - Selecting a new method of fire suppression to be implemented in the drone. Complementary calculations and adjustments to the drone's characteristics. Obtaining the design's initial dimensions using the methods described in Chapter 3. Determining the stacking sequence in the composite material. Analytical calculation to predict the landing gear's behavior. Conceptual design.

- **Chapter 6** - Validation of the functions used in the preceding Chapter 5 using FEM. Design and verification of the materials' behaviour and consequent safety factors. Possible minor geometrical modifications to improve the response to several loading conditions. FEM analysis of the structure's most demanding landing conditions.
- **Chapter 7** - Brief analysis of the work performed and its results. Verification of the objectives proposed. Suggestions for future work and areas for additional analysis outside the scope of this project.

Chapter 2

State of the Art and Project Scope

2.1 Fires and Firefighting

2.1.1 Fire behaviour and development

Fire consists of a chemical reaction, called combustion, accompanied by the release of heat, giving it the designation of an exothermic reaction [2].

This reaction happens between combustible and oxidizer. Combustible being the substance that will react and oxidizer the gas area or atmosphere that surrounds the combustible and reacts with it.

However, mixing combustible and oxidizer does not create combustion by itself. A source of energy is needed to provide the required amount for activation of the process. These 3 factors are on the source of a combustion reaction and they make up the triangle of fire, figure 2.1 [2].

After initiating, the combustion still needs to be maintained in order to have a fire. The fourth element is the chain reaction, responsible for expanding the phenomenon. With this element, the tetrahedron of fire is formed, figure 2.1 [2].

A forest fire consists of an uncontrolled, in space and time, combustion of forest areas. Its behaviour is mainly influenced by the characteristics of the combustibles (distribution, quantity, humidity, combustibility), the characteristics of the forest area (shape, inclination) and the meteorological conditions (temperature, humidity of the air, wind speed) [3].

2.1.1.1 Combustible

Combustibles can be in any of the 3 states of matter making the establishment of general rules very difficult [2].

For forest fires, the combustibles range from every vegetable materials, therefore driving of plants. These can be split into two main groups: living and dead.

On the living ones, the quantity of humidity is high when compared to low amounts on the dead combustibles, being examples dry grass, dead leaves, branches of trees or pine needles [3].

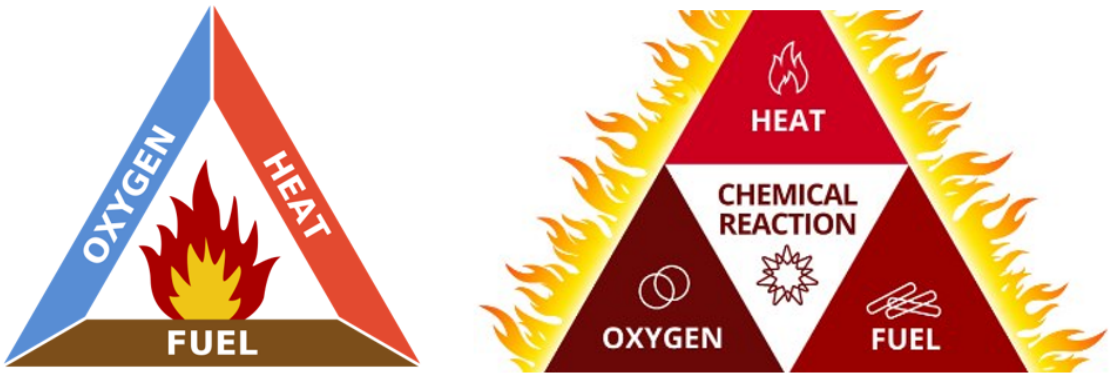

Figure 2.1: Triangle and tetrahedron of fire [3]

Being the water a retardant of the fire, the amount of humidity on the combustibles on a certain forest is of great importance. The higher the humidity, the more difficult the ignition and consequent development of a forest fire [3]. That explains why a proper cleaning of the forests leads to a much smaller risk of forest fires.

Besides eliminating all the dead vegetation, the cleaning of the forest also includes the creation of horizontal discontinuities of forest combustible. If there are no interruption of vegetation on the soil level, the conditions for the propagation of the fire are improved [3].

With the vegetation being horizontally distributed on non continuous spots and the creation of tracks to interrupt this vegetation, the propagation of fires may be controlled and interrupted.

2.1.1.2 Influence of the terrain

On a certain terrain, different types of situation may be present. They can be divided into elevation, depressions and plateaus [3].

An important concept for firefighters is the inclination. This value is usually given in percentage and represents the relation between the difference in height of two points and their horizontal distance.

For forest actuation, different inclinations are associated with different *modus operandi*. On inclinations of up to 10% people and normal vehicles can reach it and of 10% to 20% it is advisable that only walking intervention is made since normal vehicles start to present some difficulties to reach these spots. On higher inclinations, the difficulties of fighting a possible fire start to be shown. For more than 20%, only all-terrain vehicles are used and when it is higher than 50% only special vehicles can be used. Therefore, high inclination implies remarkable limitations in firefighting [3].

High inclinations also entail a different concern since with its increase, there is also an increase in the effect of convection currents that heat up the vegetation above the fire and increase the speed of propagation on the uphill direction.

2.1.1.3 Meteorological conditions

Forest fires are highly influenced by meteorological conditions. More specifically they are affected by the temperature and humidity of the air and the direction and speed of the wind.

Temperature affects the humidity of the combustibles. When it increases, the vegetation becomes drier and the conditions for ignition are favored.

Atmospheric humidity is the amount of water vapor existing on the atmosphere. It is directly related to the temperature, since, when it is warmer, the air has a higher amount of water that can be absorbed without condensation. During the day, the hotter, drier air absorbs humidity from the vegetation, while at night the phenomenon is reversed [3].

The behaviour of the wind will affect the propagation of a fire. Wind is, essentially, the movement of air in a certain direction.

Besides the main atmospheric wind, several local types of wind are created in a natural environment. Examples of these winds are mountain or ocean breezes. For the analysis of propagation of the fire these two types must be taken into consideration since both will affect its the direction [3].

2.1.1.4 Convection currents

With the action of a forest fire, a different type of air movement is created. Since the hot air is less dense than the cold one, the air surrounding a fire, when getting hotter, will move upwards while the denser cold air will move in the opposite way, creating convection currents.

These, as it was already mentioned, are responsible for the propagation of a fire on the uphill direction. Moreover, since the hot air moves to the area on top of the fire, the temperatures reached above it are of considerable magnitude. A schematic example of a convection current is shown in figure 2.2.

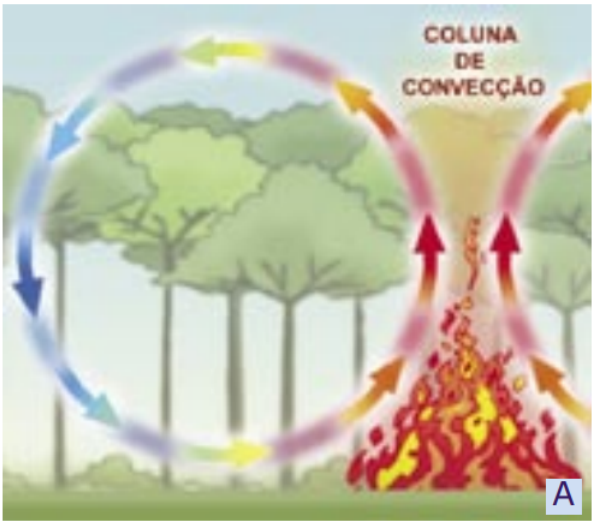

Figure 2.2: Forest fire creating a convection current [3]

This is of great importance when analysing the firefighting on a position above the occurrence, since the ascending hot air currents can affect any kind of vehicle being used.

2.1.2 Fire fighting in Portugal

While working on extinguishing a forest fire, the goal is to, at least, eliminate one of the sides of the triangle of fire or stop the chain reaction, represented on the tetrahedral of fire, figure 2.1. However, for this to be achieved, firefighters need to take advantage of the normal means of firefighting but also, due to the specific circumstances and environmental conditions of forest fires, some dedicated ones that are used in this type of operations.

2.1.2.1 Extinguishing Agent

Water is the extinguishing agent most commonly associated with firefighting. This agent is the most well-known due to its low price and wide availability.

On the other hand, water can present challenges in certain circumstances. As it can be difficult to collect for some fires due to a lack of water sources, and its transportation can be impacted by the characteristics of the area affected by a fire. Another factor that contributes is the scarcity of water in some areas; this needs to be monitored and its use should be controlled to prevent excessive water use.

This indicates that the available water may be limited, so it should be used with caution. Foam-forming liquids and spraying solutions are two additional extinguishing agents that can be used as additives to increase efficiency [3].

The foam forming liquid is made of different phosphates and it is added to the water in order to reduce its evaporation and run-off (aiming for a better fixation of the water), improving the efficiency. The recommended mix is 1 l of foam forming to 100 l of water. During the summer, this mix can last for 30 minutes until the water completely evaporates [3].

The retardants of long duration are the spraying solutions. This additive is composed of ammonium sulphate and phosphate that decompose with the heat of the fire and that slow down the emission of gases that are responsible for the ignition. In this situation, the water is not crucial in firefighting since the retardant depends on its own components and its effect lasts longer, even after the water evaporates. Gum Arabic can be added to increase viscosity, which leads to a better adherence to forest fuels. Spraying solutions are applied with the help of aerial vehicles of direct combat or can be used to create chemical containing areas [3].

2.1.2.2 Ground Vehicles

Relating to forest fires, the most used vehicles are the forest vehicle for firefighting type. They can operate in search and rescue or, as expected, firefighting. As a complement, there also exists tank vehicles responsible for the water supply and restocking, and tactic commanding vehicles.

It is important and recommended that all these vehicles are off-road but the minimum required is that they all offer all-wheel drive.

Besides the vehicles that belong to the fire department, others can be used for specific functions. In order to create clean and open ways in the middle of the forest (to contain the dissemination of the fire by eliminating its fuel) tractors with ploughs or disc harrows or even crawler bulldozers, as the ones seen in figure 2.3 may be used, even though they are more connected to other industries.

Figure 2.3: Examples of a tractor with disc harrows, on the left, and a crawler bulldozer, on the right [3]

2.1.2.3 Aerial Vehicles

This type of vehicles are essential in the extinguishing of forest fires and as support for the ground teams. The several fire departments can have access to helicopters and planes.

The helicopters are very versatile in the different functions they might perform during an operation. From the transportation of firefighters to search, evacuation and rescue of possible victims that get stuck due to the uncertain behavior of a fire, they can also help in extinguishing the fire by projecting water, foam forming liquid or spraying solutions. To achieve this, they can either possess a suspending bucket or an attached tank [3]. On figure 2.4, examples of helicopters used in Portugal for forest firefighting are shown.

The benefits achieved by using extinguishing agents released from helicopters is, however, somewhat limited in effectiveness since much of the fluid used is lost and dispersed through the air, until it reaches the ground. Thus, it is understood that the action on or right next to the ground is essential and the best way to ensure the full extinction of the fire.

Typically, helicopters have 2 rotors, the main one, placed above the cockpit, that is responsible for creating thrust and lift and allowing the aircraft to move; the secondary one, placed vertically on the tail, is responsible to counteract the rotational force created by the main propeller that would make the helicopter spin [3].

Figure 2.4: Example of helicopters used in forest firefighting. On the left, an helicopter with a bucket and, on the right, one with a water tank [3]

2.1.3 Other Extinguishing Agents

2.1.3.1 Fire Extinguishing Ball

This extinguishing agent provides continual protection since it self-activates in the presence of a flame without the need for human involvement. After contact with fire, the ball releases its extinguishing chemicals in 3-10 seconds [4].

An outside layer of polystyrene that will be consumed by the fire composes it and on the inside, there is a non-toxic gas, suppressor of fire and eco-friendly, ammonium phosphate [5].

It is said by the company that created this gadget (ELIDEFIRE) that it can act on an area of 8-10 m^2 and it does not need any maintenance, during the guaranteed 5 year life span, and it does not require any prior training because it is easy to use [5].

The price range for the gadget is between 100 € and 170 €. An example of a fire extinguishing ball is shown in figure 2.5.

2.1.3.2 Soundwave Fire Extinguisher

A project created by two engineering students of the George Mason University, in Florida, proposed a portable subwoofer gun that is able to manipulate soundwaves in order to extinguish a fire [6].

By eliminating the use of chemicals or fluids that can harm buildings and the environment or even bring health risks to the community, this option presents itself as being the cleanest and least destructive way to put out flames.

Figure 2.5: Fire extinguishing ball by ElideFire [5]

It works by directing soundwaves in a specific direction. The sound is a pressure wave that fluctuates between high and low pressure levels. This oscillation allows the air molecules to separate from the fire, effectively extinguishing it. It has been shown in research that high frequencies are useless for this operation and the most effective ones lay in between 30 and 60 Hz [6].

Despite being a promising and innovative idea, it is still restricted to small-scale fires. The research is evolving, and its effectiveness is expected to improve. Some researchers have also been working with this soundwave approach in order to create an artificial, acoustic sound barrier by directing the waves in the right direction [7].

2.1.3.3 CO_2 Snow cannon

This is a novel approach to firefighting being developed by Engineer Joaquim Matos. A mechanical engineer, specialized in project and design who has experience in several areas and also works in agriculture.

The hypothesis relies on tackling the 3 main factors that contribute to maintaining a forest fire: high temperature, lack of humidity and the existence of combustible, in this case being O_2 and cellulose.

With these factors in mind, the proposed solution was a cannon that will extinguish a fire using H_2O pressurized with CO_2. This mixture can be called a pseudogas. It is able to reduce the temperature on the fire and increase the humidity on its surroundings due to the action of the water. CO_2 is used for the pressurization and it will not serve as combustible for the fire.

Nevertheless, this method is still in an early stage of development.

For project purposes, the integration of this technology requires designing the pressure vessels that will contain both the gas and the water and design or selection of a nozzle that will be responsible for mixing the two components and discharge it into the fire.

2.1.4 Other Aerial Vehicles and Long Range Approach

2.1.4.1 Sikorsky Firehawk Aircraft

The Sikorsky Firehawk aircraft, which evolved from a BLACK HAWK® helicopter, relies on its established military configuration to withstand the physical stresses of aerial firefighting and related missions. This aircraft is shown in figure 2.6.

Figure 2.6: A Sikorsky Firehawk Aircraft [8]

The new generation of this type of aircraft brings enhanced capability and flight safety but also full maneuverability while fully loaded at 4g. This abilities combined with the possibility of overcoming high winds and bad vision states due to smoke or night skies proves its motto “we fly when and where others can’t” [8].

It has a fixed landing gear extension that provides excellent ground clearance [8].

It can be described as a multi-mission aircraft and has the ability to reconfigure itself mid flight. The missions it is able to accomplish have many different ranges [8]:

- firefighters transportation (up to 11 firefighters and their gear can be dropped straight on the fire line);
- precision water drop, able to carry 3785 l of water and release it with higher precision than other planes since it can fly on a lower altitude;
- search and rescue, with the ability to access remote and difficult areas it can use baskets, rescue strops or its cargo hook to extract victims;
- humanitarian assistance, able to carry up to 4000 kg of supplies;
- emergency medical transport.

Actually, Portugal has recently acquired 6 Sikorsky firefighters that aim to be included on the nation's means to fight rural fires. The first two are scheduled to be delivered in the beginning of next year [9].

2.1.4.2 Canadair

Canadair is a firefighting aircraft purpose built to tackle the fire with the highest precision of water drops. With its high lift wing, that increases elevation, and turbo-prop engines it is possible for this aircraft to be safely handled at lower altitudes and speeds then others that need to drop water at higher altitudes due to safety concerns. The higher precision is directly related with this better conditions of the drop [10].

Being able to fly for approximately 3 hours, this aircraft also offers great productivity since it can carry close to 6000 l of water and is able to perform 6 rotations per hour (rotation is fly to get water and then drop it over the fire) [10].

Right now, in Portugal, there are 2 Canadair aircraft available for firefighting although several instances of them being inoperable for a certain period of time have been reported [11]. Two more are scheduled to be delivered in 2024 [12]. These aircraft are represented in figure 2.7.

Figure 2.7: A Canadair aircraft on firefighting operations [12]

2.1.4.3 Autonomous Firefighting Drone – Ehang

This aerial firefighting autonomous flying vehicle developed by EHang was built with the intent to tackle fires in high buildings with its ability to reach heights up to 600 m [13]. It is seen in action on figure 2.8.

It has the ability to be auto-piloted or remote controlled. The company promises that the response time can be way shorter than the usual firefighting departments since it can arrive earlier

Figure 2.8: EHang's firefighting drone in action tackling a fire on a tall building [13]

to the affected area. Mainly on higher population density cities where emergency services can be delayed due to traffic [13].

To perform its function the vehicle is able to carry 180 l of firefighting foam and 6 fire extinguishing balls. Aside from these features, it also has a built-in camera to assist in locating the fire and laser aiming technology to be used in order to locate potential obstacles, such as windows in a building, which would be broken using a projectile [13].

2.1.4.4 Aerones

A Latvian company, Aerones, had been developing a drone to put out fires. With the ability to fly up to 275 m and the added bonus of being able to carry 200 kg of extinguishing agents (or this capacity could be used for rescue missions) [14].

This electric vehicle uses its 16 batteries to power 28 engines allowing it to take flight. Several fire extinguishing tests had been carried out with positive results [14].

While still in development the drone was only able to fly for 30 minutes after a 90 minutes battery charge. An extended period of inactivity compared to the allowable working time, showing that it is not yet ready for situations that may arise in the real world scenarios. [14].

2.2 Drone Developments

A drone is essentially a remotely-controlled or autonomously flying robot equipped with software-controlled flight plans, sensors, and a GPS. There are numerous varieties and sizes of drones that

serve several purposes [15].

Drones have played a pivotal role in providing new capabilities for European defense and have demonstrated significant growth as a product for consumer leisure [16].

2.2.1 Types of Drones

Drones classification is relatively a novel topic and adjustments are continuously being made as new innovations arise and different kinds of UAV are introduced into the market. These can be divided into different categories according to several criteria and characteristics. They can, for example, be sorted due to their maximum take-off weight and airspeed as according to the classification proposed by the United States department of defense, that splits the type of drones into 5 different categories [17].

However, as of mid 2021, the European Commission as introduced its own legislation. This new distinction encloses 7 different categories, each with a series of criteria regarding integrated systems that must be followed so that a UAV is apart of a certain category. These seven classes range from C0 to C6 and its criteria follow briefly described [18]:

- Class C0
  - Takeoff weight < 250 g
  - Max cruise speed of 19 m/s
  - Max height from takeoff point 120m
  - All-electrical
- Class C1
  - Takeoff weight < 900 g and impact energy < 80 J
  - Max cruise speed of 19 m/s
  - Max height from takeoff point 120 m
  - All-electrical
  - Geo-awareness
- Class C2
  - Takeoff weight < 4 kg
  - Low speed mode available
  - Max height from takeoff point 120 m
  - All-electrical
  - Geo-awareness
  - Protected against non authorized access to remote control

- Class C3
  - Takeoff weight < 25 kg and wing length < 3 m
  - Max height from takeoff point 120 m
  - All-electrical
  - Geo-awareness
  - Protected against non authorized access to remote control
- Class C4
  - Takeoff weight < 25 kg
  - No automatic control except for flight stabilization or in case of lost connection
- Class C5
  - Takeoff weight < 25 kg
  - Low speed mode available
  - All-electrical
  - Geo-awareness
  - Protected against non authorized access to remote control
- Class C6
  - Similar to Class C5
  - System that allows for flight control to be recovered or to be safely terminated in case of lost connection

Besides this classification, drones can more easily be separated according to their main way of functioning into 4 major types: Single-rotor, Multi-rotor, Fixed Wing and Fixed Wing Hybrid.

Single rotor are compact and durable drones. Their configuration is similar to helicopters with only one rotor on top to give lift and a smaller one on the tail to provide stability and control the direction [19].

Multi rotors are usually the cheapest and simplest option. They offer great stability and control over positioning. Having multi rotors, they exist in different configurations of 3, 4, 6 or 8 rotors. The most popular one is the quadcopter (4 rotors) [15].

Fixed wing have a configuration much similar to an airplane. Here, lift is provided by a fixed wing and not by rotors so energy is only required to move forward and not actually to maintain the drone in the air [15].

Fixed wing hybrid is a version of the former one. It joins the advantages of rotor drones to the fixed wing ones. It has rotors that provide vertical and horizontal takeoff, as well as possibility of hovering. The other motion is provided in horizontal movement. Mostly still in development but a technology that is becoming increasingly popular [15].

These 4 types of drones can be seen in figure 2.9.

Figure 2.9: From left to right and top to bottom: Single rotor; Multi rotor; Fixed wing; Fixed wing hybrid.

2.2.2 Innovative Drones

2.2.2.1 X57 Maxwell

The X57 project, developed by NASA, presents an all electric aerial vehicle, with a configuration similar to a common plane. The goal behind this project is to achieve developments in the electric propulsion technology, bringing improvements to its efficiency, reducing emissions and noise pollution. The intent is to develop certification standards to aerial vehicles and keep bringing air mobility closer to an everyday reality [20].

The new configuration of this aircraft uses the latest composite technology and has completed load bearing tests. It is shown on figure, 2.10.

Figure 2.10: NASA's X57 Maxwell [20]

NASA tested different configurations in this development. It was understood that to reduce drag and increase efficiency different options were successful. Examples of which are increasing the aspect ratio of the wing, reducing the total area of the wing even while flying at a greater weight or locating the electric propulsion motors at the tip of the wings [20].

Besides the objectives of developing certification standards, there are also other goals such as reducing 30% of the power utilized on the same (not electric) aircraft while maintaining the same cruise speed. With all this NASA is also trying to demonstrate that a vehicle can be optimized when electric propulsion is introduced [20].

2.2.2.2 Elixir Aircraft Company

This company, based in France, developed a new small aircraft since they figured out that the market for this type of aerial vehicles had been a long time without any innovations. With ambitious goals from dominating 30% of the European, Pacific and Latin American market to selling close to 80 aircrafts per year, the company relies on innovative technology to create somewhat of a disruption in the market.

Regarding this new technologies, this novel aircraft offers simple maintenance, an airframe parachute system to ensure the safe landing of the aircraft and an explosion proof fuel tank [21].

Above all these, the most exciting feature is the one-shot production. With this style of manufacture, the entire structural part, made out of carbon fiber composites, is produced all at once in a single piece eliminating the need of following assemblies. This factor increases the aircraft safety by reducing the deficits of strength on the joint areas like standard bonded or riveted structures [21].

2.2.2.3 AirTaxi

As the name suggests, this innovation features an aerial taxi that aims to revolutionize the way passenger transportation is thought- After a successful proof of concept this project can proceed to more advanced steps on the way to proper commercialization.

This aerial vehicle presents a different way of flying since it proposes a vertical takeoff and horizontal movement. The vertical takeoff is allowed by 8 rotors that are able to lift this aircraft weight (about 1500 kg) and to carry 4 passengers. At 150 m and air speed of 160-180 km/h the transition occurs [22].

While the lift is promoted by a fixed wing part, propellers that are positioned on the back provide the horizontal movement, while the rotors stop and stay stuck in their position. Different power on left or right propellers allow the aircraft to turn. This horizontal flight has proven to be more efficient [22].

Although the aircraft keeps on passing development stages, some questions remain. The energetic efficiency of the device stills need to improve for this way of transportation to be competitive. Lot of similar projects of this type have already failed, which rises doubt on the new ones and the cost of operation remain high so it would not be an affordable option for everyone.

2.3 Drone projected in previous thesis

This thesis will primarily focus on the optimization and continuation of the development of a firefighting drone begun by Engineer Lucia Moura in previous work, its technical drawings are shown in figure 2.11. A drone was chosen because it is capable of fighting a fire without endangering human lives and allows for an approach that does not require the use of many assets or a great cost [1].

The unmanned aerial vehicle (UAV) developed for this study was intended to patrol a forest area to prevent the spread of fires by identifying them in the early stages and to assist firefighters in checking the burnt area, after a fire has been extinguished, for hotspots that can reignite and must also be controlled. In addition, it is responsible for monitoring the behavior and spread of active fires to provide vital information to firefighting crews.

During this work, the UAV's fundamental behavior was defined so that it could function as a VTOL. The thesis states that in the event that the electric motors lose power or vertical landing and takeoff are not possible, the aircraft must be able to land and take off like a normal aircraft (on a runway) using a combustion engine that also provides horizontal motion during flight.

In addition to the requirement that all proposed firefighting goals be met, the basic requirements for this VTOL included the creation of a lightweight aircraft (with a total mass of less than 15 kilograms) capable of flying at a cruise speed of 100 km/h for at least 1.5 hours. Also, a simple, basic structure that could let the plane land and take off on a variety of surfaces and terrains.

All the electrical components responsible for vertical movement were selected, including batteries and electric motors, as well as the combustion engine for the horizontal movement, and the propellers responsible for both the possible flight situations, as well as the servomotors that will help with all the motions required in different situations of the aircraft's maneuver. Just about all of the components necessary for the movement of the UAV. Additionally, the aircraft's structure was studied.

The proper configuration for the fixed wing and tail was chosen so that it could provide the necessary lift for the aircraft's horizontal flight while also accommodating the possibility of a runway takeoff. Lastly, the fuselage constituting the exterior portion of the VTOL was defined.

Noting that the landing gear was not designed in this thesis so a detailed design of a landing gear for this UAV will be projected. This will be the primary focus of the subsequent sections.

Some of the choices taken for the proposed UAV will also be analyzed and alternatives with higher efficiency and greater impact will be presented.

2.3.1 Extinguishing method

For the development of this drone, the selected method for firefighting was including two of the extinguishing balls, mentioned in section 2.1.3.1. These would be positioned in the lower part of the fuselage with the same longitudinal coordinate as the CG of the UAV at maximum weight, so that when they are released, the CG does not suffer major changes.

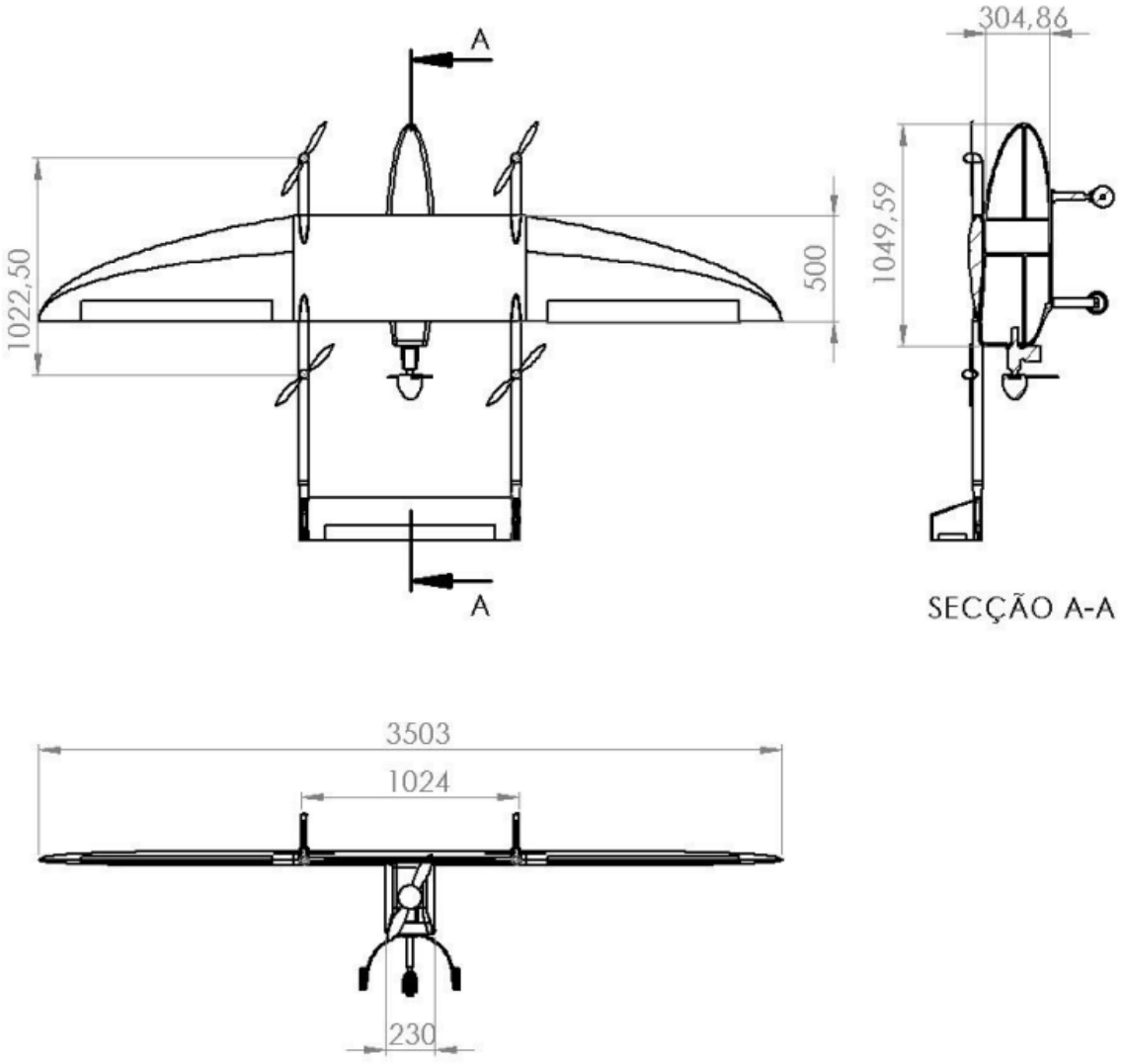

Figure 2.11: Technical drawings for the drone projected in prior developments [1]

A rough estimate of their weight is 2.8 kg. The action of the balls on the fire would require for the drone to be positioned directly on top of the fire before releasing the extinguisher.

The method, however, raises some concerns regarding the specific applicability on forest fires.

First of all, it would require the attack on the fire to be made at a maximum height of 2.5 m since if it is done on a greater altitude the balls will lose efficiency. However, on forest fires, the flames may rise to way greater heights than that (on normal fires or if a tree is on fire), making it impossible for this method to work.

Being made of chemicals, some may not be proper to be used on a forest, There is the possibility of affecting the natural environment. It is advisable that the use of chemical compounds is reduced to a minimum on forest actuation.

Moreover, this system is mainly applied on closed locations such as computer rooms or garages. There are doubts regarding its use on open environments and it may not be effective

on putting out a forest fire.

It would also have close to no impact on aftermath operations of putting out underground fires. The chemicals that suppress the fire would not be able to infiltrate on the ground and still have the capacity to act on the fire.

Therefore, a different method should be applied to this UAV from the ones mentioned before or using a new approach. This selection will be made before the calculations for the landing gear. These will be approached for an UAV with the different technology for extinguishing a fire already integrated.

2.3.2 Fire detection

With the selection of any kind of available extinguisher for this application, the actuation on the fire must be made in a rapid and early manner since the amount of extinguishing agent allowed to be transported will be limited, due to the low takeoff weight permitted.

Therefore, an efficient fire detection system is required.

For the designed UAV, Moura selected a Vue Pro radiometric thermal camera provided by FLIR. This camera differs from other thermal camera options since it does not limit itself to detect the heat, it also measures the temperature with an error of less than 5% [1].

This is an optimal solution since it also offers other benefits such as allowing for the recording and saving of images and videos, remote control, making temperature measurements without contact and it is optimized for thermal radiometric while already used in search and rescue operations.

However, the distance from the fire to where the drone is flying may be a problem due to the signal that can be lost from crossing natural barriers and due to the fuselage material's nature. On the other hand, the lost of signal in rain or snow is not a big problem since in this situations the risk of a fire is greatly reduced.

Nonetheless, the possibility of incorporating different mechanisms for fire detection should be analysed.

2.3.3 Landing Gear

Briefly mentioned in section 2.3, the project and analysis of a landing gear for this UAV will be the primary focus of the present work.

On the analysis of the designed drone, the fuselage must be, carefully, considered since it will be the point of attachment with the landing gear. The material chosen for its development was a composite of carbon fiber and epoxy matrix, its properties will be taken into consideration during the material selection phase due to incompatibility. Moreover, the bottom part of the fuselage was designed in a flat, straight, manner, as it can be seen in figure 2.11 which offers more design flexibility for the landing gear connection.

Some requirements that must be retrieved from the analysis of this prior thesis are related to the maximum takeoff weight. For the design, it was set at 12.7 kg.

On the other hand, it is of extreme importance to properly consider the possible positions of the CG during different operations. This value was obtained in a descriptively manner however, some discrepancies were found and a correction for these calculations will be presented.

Moreover, by changing the extinguishing method, it is expected that the maximum weight can be slightly reduced and the positions of the CGs altered.

The landing gear must allow for the aircraft to takeoff and land on a runway as for regular fixed wing aircraft.

Lastly, for the possibility that no proper runways exist near the area where the UAV is performing any kind of operation, it is preferable that the landing gear is adapted for rough terrain and unimproved runways.

2.4 Landing Gears for Fixed-wing Aircraft

A wide range of landing gear configurations are available for fixed-wing and rotor aircraft. The use of wheels and, in some cases, skids to allow the aircraft to operate on the ground is necessary because fixed-wing aircraft requires a runway for takeoff and landing. Landing gear is typically available in two basic wheel configurations: conventional and tricycle. Tandem or bicycle landing gear is also available in some cases [23]. All the possible options can be seen in Figure 2.12.

A conventional, tail dragger, or tailwheel-type landing gear is an aircraft undercarriage that consists of two wheels in front of the vehicle, ahead of the center of gravity, and a smaller wheel or a skid to support the tail. The word "conventional" has been in use since the early days when most airplanes used this design, despite the fact that most aircraft currently use other configurations. The term "taildragger" is uncommon and may be considered jargon. Some experts suggest it should be used only when the aircraft has a tailskid rather than a tailwheel [24] [25].

Tandem landing gear is distinguished by the placement of the main and secondary tail gears on the same longitudinal axis of the aircraft. It enables the use of flexible wings. It can present some different designs, for example, the secondary wheel can be replaced by a skid, as in the conventional configuration, that is placed under the tail, and some aircrafts also have auxiliary wheels under the wings for added support. Tandem landing gear is also known as single main landing gear. This is mostly found in military planes and sailplanes [23].

Tricycle landing gear is the most common in the present era, having replaced the conventional one as the primary configuration. This configuration is nearly the precise opposite of the conventional in that the two main wheels are placed behind the center of gravity, usually under the wings, and support the majority of the structure's weight. The smaller secondary wheel is placed in front of the aircraft (called nose wheel) and also offers proper steering control [23] [26].

The differences between conventional and tricycle configurations, highlighted in figure 2.13, create advantages and disadvantages when choosing one over the other, some of which are related to the different orientation of the aircraft on the ground caused by their opposite approaches. Because of its smaller size, a tailwheel creates less drag than a nosewheel, allowing an aircraft equipped with the first to cruise at a given speed while using less power. Due to the general

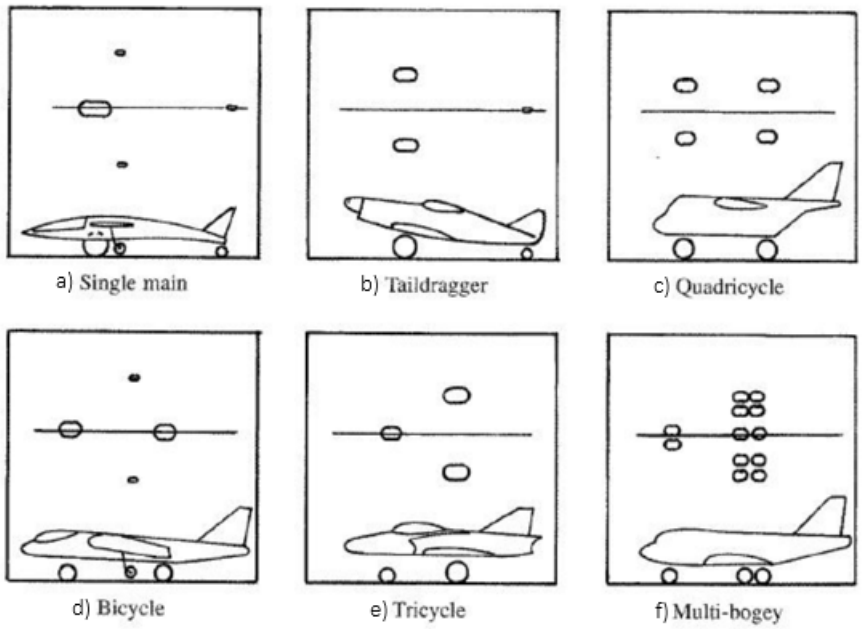

Figure 2.12: The different types of Landing Gear Configuration [27]

increased propeller clearance, this configuration results in less stone chip damage when operating on particularly rough or gravel airstrips [24] [28].

However, because the plane's center of gravity is positioned behind the two main gears,this design is extremely unstable. When landing, if one wheel reaches the ground first, the aircraft tends to deviate off in the direction of that wheel. This might lead the aircraft to spiral in an increasingly tighter "ground loop", which can culminate in a wingtip contacting the ground, collapsing the gear, or drifting off the runway [28].

Ground loop consists on the phenomenon that happens when a fixed-wing aircraft performs a rapid turn whilst on the ground. Here, aerodynamic and centrifugal forces are generated and may cause one wing to rise, resulting on, possibly, the contact of the other wing with the ground [29].

Furthermore, the tricycle landing gear has some more significant advantages. It provides a substantially improved view over the nose as well as cargo handling on a flat cabin floor. Another advantage is that the aircraft has a lower angle of attack, which means that the engine thrust is more parallel to the direction of motion, allowing for faster acceleration during takeoff. Additionally, the nosewheel prevents the plane from tipping over on its nose while landing, which can happen on taildraggers. Its main disadvantage is the increased weight and drag caused by the huge nosewheel, whereas most aircraft with conventional landing gear can use non-retracting gear with little influence on performance. This aspect implies the employment of a retraction system for the landing gear in nosewheel aircraft in order to minimize drag [28].

Some unusual types of landing gear can also be found in various aircraft.

As previously stated, tandem landing gear, also known as bicycle landing gear, uses two wheels on the center line of the aircraft and two on the wings to prevent it from tilting. This provides an

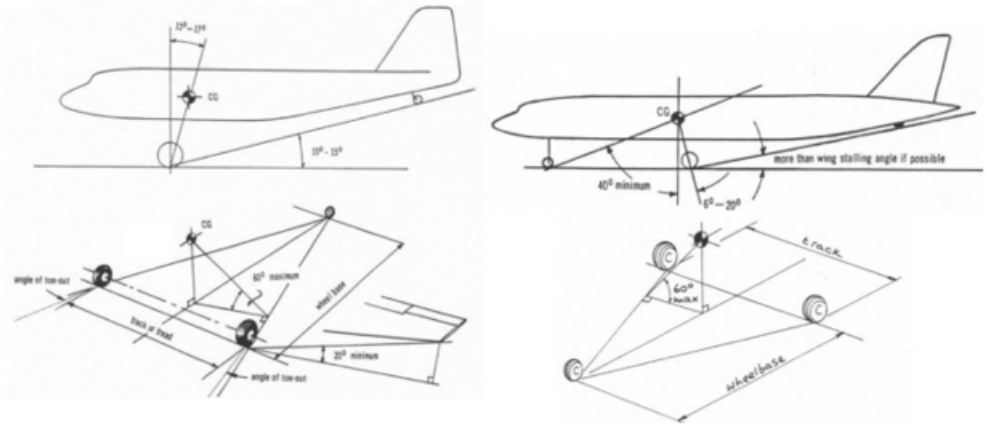

Figure 2.13: Differences between Conventional and Tricycle Landing Gear Configurations [28]

advantage in terms of weight and drag reduction when compared to the two previous compared models. However, it complicates the pilot's job because he or she must maneuver the aircraft to compensate for unbalanced landings on the supporting outrigger gears. The single main gear is a bicycle configuration with a much smaller wheel on the tail. This design allows for greater simplicity and a lower overall weight [28].

There is also the need to mention additional options.

The quadricycle landing gear consists of two wheels on the front and two on the tail of the aircraft, similar to the previous configuration with double the wheels. As a result, the weight and drag are significantly increased [28].

The final variant is known as the multi-boogey gear, and it is mostly used on tricycles when using multiple wheels per point of contact with the ground. It also results in a heavier aircraft, so it only makes sense to do so in heavier aircraft [28].

2.4.1 Fixed vs. Retractable Landing Gear

Years ago, as pilots gained experience, they were allowed to fly faster and more powerful planes, eventually earning the right to sit on the rare models with retractable landing gear. Retrieving the wheels into a compartment was considered to be a key solution to reduce parasite drag and increase an aircraft's speed and performance [30].

The landing gear of an aircraft can be classified into two types: fixed and retractable. Several small single-engine lightweight aircraft, as well as a few light twins, have fixed landing gear. This implies that the gear is connected to the airframe and is exposed to the slipstream while the aircraft flies. Mechanisms for retracting and stowing the landing gear to reduce parasitic drag add weight to the aircraft, even the simpler ones as the one schematically represented in figure 2.14. Because the lack of performance of this extra weight is not offset by a decrease in drag, on slow aircraft, fixed gear is preferred [31].

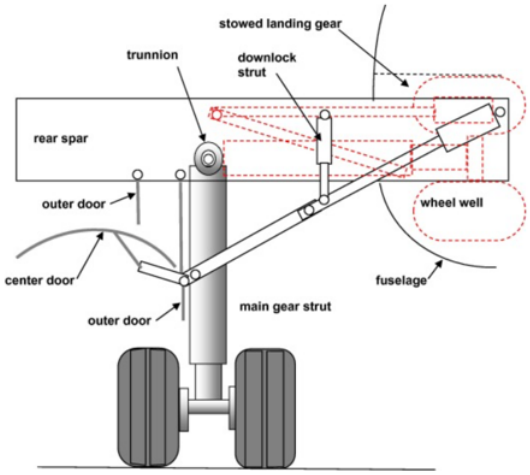

Figure 2.14: Example of a Retraction Mechanism for Landing Gear [32]

Furthermore, much of the parasite drag created by small aircraft landing gear may be decreased by designing the equipment as aerodynamically as feasible and adding fairings or wheel paints to streamline the airflow past the exposed components. Much in the same way as motorcycles are produced, fairings are also used in this industry, as seen in figure 2.15, in order to reduce the drag created while on movement and improve the total efficiency of the vehicle. A narrow, smooth profile toward the approaching wind decreases landing gear parasite drag significantly when compared to the exposure of the landing gear strut to this same wind [31], a comparison between both approaches can be seen in figure 2.16.

However, since the drag generated increases with a growing aircraft's speed, there is usually a need to employ a mechanism (figure 2.14) to retract the gear in order to reduce parasite drag, despite the weight of the equipment implanted [31].

While in flight, retractable landing gear is stored in the fuselage or wing sections. When gear is in these wheel reservoirs, it is out of the slipstream and does not produce drag. When the retractable gear is fully retracted, it is covered by a close-fitting covering that is level with the aircraft skin, blending with it. Other planes have individual entryways that open to enable the gear

Figure 2.15: A 2017 Suzuki GSX-R1000 without and with fairing components [33]

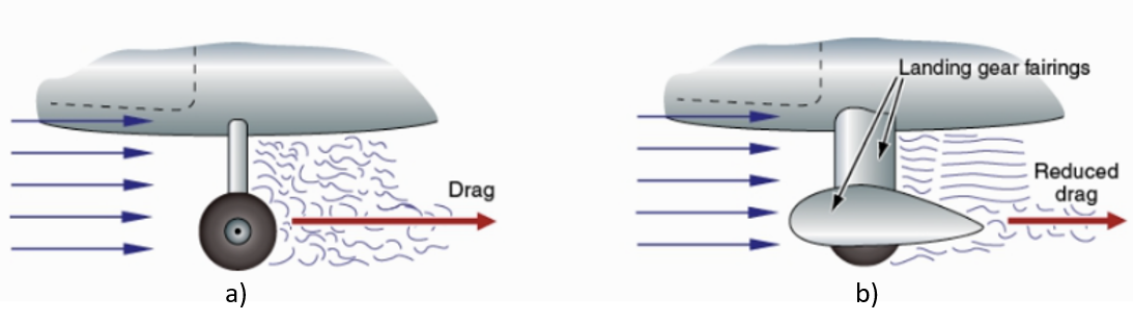

Figure 2.16: The effect of a fairing component on the drag produced by Landing Gear [34]

to enter or exit, then lock immediately [31].

The most obvious issue that may arise when selecting retractable landing gear is the possibility of making a gear-up landing. This would severely damage the aircraft and keep it out of service for an extended period of time, while also requiring a high cost for damage assessment and repair. Nevertheless, it is not a common phenomenon [30].

Aside from the costs already mentioned in relation to the mechanism's implementation, there are a few others that must be considered. The cost of maintaining and inspecting a retractable landing gear is significantly higher than that of a fixed landing gear. Besides that, the constant up and down movement of the wheels can lead to increased wear on the bushings and actuators, which may eventually lead to their replacement. Furthermore, the need for additional space in the fuselage for the gear to retract will reduce the useful space inside for other components such as fuel tanks, batteries, or motors [30].

However, even given all these drawbacks, retractable landing gears are widely used and considered for many aircraft. This is due to the demonstrable improvement in cruise performance by removing the drag created by the entire structure. When comparing different aircraft that share the same airframe with only fixed vs. retractable gears as a difference, the '78 Skylane RG (retractable gear) delivered 14 knots more speed than its counterpart, 78' Cessna Skylane. However, as previously stated, this applies primarily to larger aircraft, and there are some other ways to increase efficiency and flight speed that do not rely on this mechanism [30].

2.4.2 Types of Landing Gear Legs

Apart from assisting the aircraft during ground operations, the landing gear must also withstand the forces generated during landing, absorbing the loads created on impact. This can be accomplished via shock absorption, in which the energy is converted to heat, or by altering and transferring the energy through the airframe at a rate other than an instantaneous pulse [35] [31].

A strut is a piece of equipment that absorbs the force applied to the aircraft during landing. They are constructed in such a way that an improper landing will not result in vehicle damage [15].

Prior to the invention of curved spring steel landing struts, this equipment was rigid in its original configuration. German biplanes used during WW1, had rigid landing gears, as seen in

Figure 2.17: World War 1 German Aircraft [36] and a regular Helicopter [37] - Rigid Landing Gear

figure 2.17, on the left. The intention was to weld the wheels directly to the airframe. When the landing was not perfect, this configuration was useless, as the strong shock was transmitted directly to the entire airframe and its passengers. Engineers began using inflatable tires to soften the reaction, but it was an imperfect solution. This type of structure is still used in some vehicles that land vertically, such as helicopters (figure 2.17, right) or VTOLs, in the form of metal skids, because these vehicles land at lower speeds, creating a reduced impact that these rigid struts can completely absorb [31] [15].

However, nowadays, the most common way to accomplish the absorption of the impact ranges from the use of simpler landing gear types of legs like leaf-springs, rubber doughnuts or rubber bungees to coiled steel springs or different types of oleo-pneumatic shock absorbers [38].

The first three, presented schematically in figure 2.18 where d is the deflection of the gear that is directly related to its efficiency, bring several advantages due to their simplicity and relative light weight when compared to other solutions. On the other hand, they offer a lower shock absorption efficiency.

Numerous aircraft now incorporate a variety of flexible materials to aid in landing impact outcomes. These are leaf-spring landing gears. Their purpose is to absorb the impact of landing and return it to the airframe at a safe rate. The gear, relatively flat but a stiff cantilever beam, reacts to the landing loads by bending initially, and forces are transmitted continuously throughout the

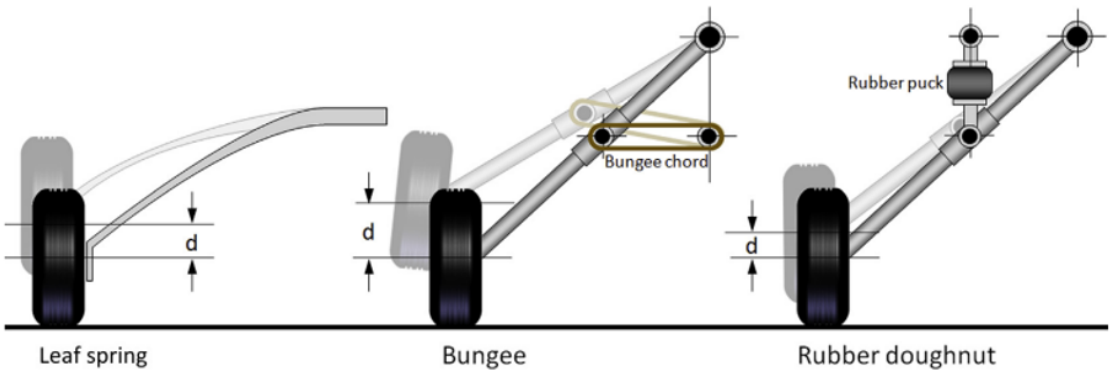

Figure 2.18: Schematic representation of leaf-spring, bungee and rubber doughnuts Landing Gear configurations [38]

structure. This configuration is extremely popular due to its simplicity, light weight, low cost and low maintenance requirements. Steel, aluminum, and composites are among the materials used, as the latter are the lightest and most flexible, with the added benefit of being corrosion-resistant [31] [15].

Leaf-spring configurations represents the simplest form of the landing gear. Its shape is not particularly applicable to a retractable form. Nonetheless, by having a low thickness-to-chord ratio, it presents a low drag external structure. This forces can substantially be generated by the other parts such as wheels, tires and braking calipers that must be covered using a wheel faring in order to reduce this effects. The leaf-spring landing gear is generally used as the main landing gear [38].

This option presents also some drawbacks, the primary one being the high reaction loads it creates on the airframe due to the large moment arm that the spring beam usually has. Besides this it has limited structural damping and poor efficiency of absorption of shock but these problems are somewhat diminished by the scrubbing motion of the tires [38].

Bungee chords are frequently used to increase the effectiveness of non-shock absorbing struts, such as the one described above. Between the airframe and the flexible gear system, these are a series of elastic cords. They contribute to a reduction in the rate at which the landing shock is transmitted to the airframe, thereby increasing its safety [31] [15].

On landings, the actual stress absorption occurs only after the landing impact is converted to thermal energy. When shock strut landing gear is used, this takes place. This pneumatic/hydraulic arrangement frequently utilizes compressed air or nitrogen in conjunction with hydraulic fluid to absorb and dissipate loads. Different types of approach can be seen in figure 2.19, on the right side

The shock strut is composed of two sealed telescopic cylinders on the outside that can be seen on figure 2.19, on the left side. The upper cylinder is attached to the fuselage, while the lower cylinder, dubbed the piston, is capable of sliding while also being connected to the wheels that will make contact with the airway's surface upon arrival. They are separated by a variable-area orifice. When the bottom cylinder suffers the impact of a landing, the hydraulic fluid is forced against air or nitrogen through the aperture and into the upper cylinder. This phenomenon allows the shock to be reacted to, initially, with a short deflection, followed by a bigger one once the oil goes back into its original chamber. This steps generates heat, which in this case is the impact loads converted into dissipative energy. This heat can then be expelled to the atmosphere throughout the strut's structure [39] [38] [15].

Following the initial reaction, the strut frequently stretches abruptly during the compression rebound. This can result in a large impact at the movement's conclusion and costly strut damage. Shock struts are typically equipped with a dampening or snubbing device to prevent this. During cylinder extension, a recoil valve on the piston restricts fluid flow, thereby slowing the motion and avoiding destructive impact loads. Most shock struts incorporate an axle into the bottom cylinder to facilitate the installation of aircraft wheels [39] [15].

A popular option within this type of landing gear legs is the oleo-pneumatic trailing-link landing gear since it offers a better response on uneven ground. This happens because the mechanism

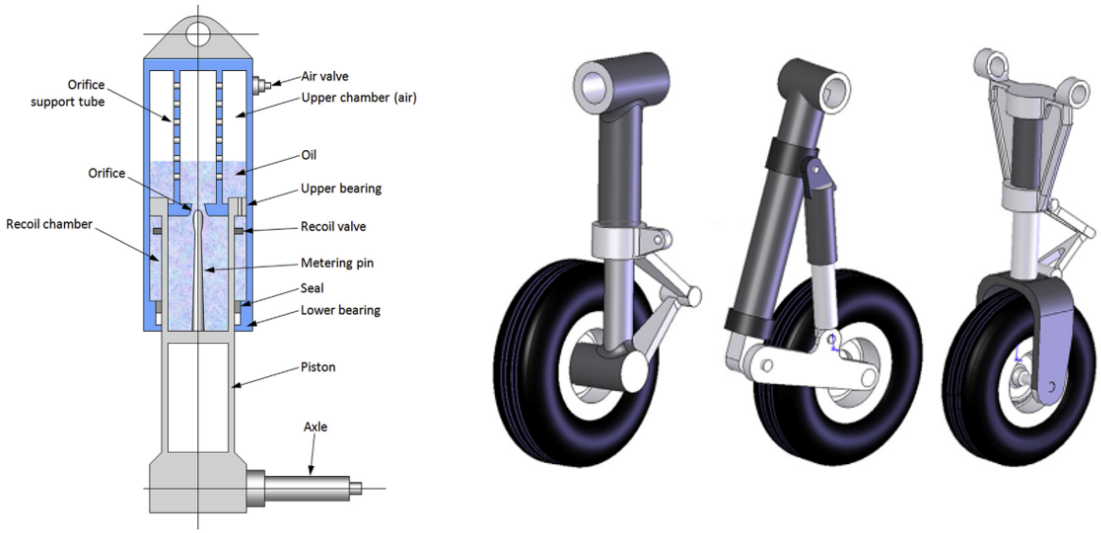

Figure 2.19: Schematically representation of an oleo-pneumatic strut - left; Different configurations of oleo-pneumatic strut (oleo-strut retractable main gear, oleo-strut retractable trailing-link main gear and steerable oleo-strut nose gear - right [38]

allows for larger deflection of the wheel and tire. The drawbacks related to this option are a great increase in weight and cost, while also requiring a large internal volume of the cylinders [38].

2.5 Materials used for Landing Gears

The structural parts of the landing gear withstand the enormous impact stresses and prevent the landing gear from buckling under the aircraft weight. The materials must be able to withstand the heavy takeoff weight of an airplane with its maximum load and fully fueled as well as the significant impact stresses on arrival. Materials for landing gear must have high static strength, a high elastic modulus, excellent fracture toughness, and fatigue resistance under repeated impact loads. High-strength steel and titanium alloy are the most typical materials utilized [40].

Because of its durability, high-strength steel used to be the most frequently utilized material in landing gear construction. Recently, the landing gears of some aircraft, notably the Boeing 787 and the Airbus A400m, have been constructed using ultra-high-strength steel with exceptional corrosion resistance. In order to replace the bulk of an aircraft's steel components, there is a continuing effort to discover alternative materials that are inexpensive, lightweight and durable. This is being done to boost the aircraft's efficiency. As was just said, titanium alloys are one substitute possibility. The Boeing B777 landing gear makes the most use of it, although it is also used on the landing gear of the Airbus A340 and the Boeing 787.

The need for high performance and lightweight aircrafts has also shifted the focus from the use of conventional advanced metallic materials such as aluminum alloys and sophisticated steel grades to composites [41].

The paradigm was altered as new production processes made this lightweight, durable, and reliable materials more widely available. Historically, these materials were not considered due to their high price, but that has decreased with advancements in manufacturing technology [42].

The doors of the landing gear retraction compartments are normally composed of composite materials, similar to the doors of several Airbus and Boeing aircraft versions. In the case of the B787, however, it has been proved that they may also be used for the landing gear's structural components [42].

Numerous firms have introduced and developed novel composite material varieties. At the 2019 Paris Air Show, several exhibits were devoted to this business. M. Torres demonstrated a potential new form of composite, a rib-stiffened dry carbon fiber skin structure made by resin infusion. GKN Aerospace also demonstrated this technology as a spar material for aircraft wings, while their ribs were revealed to be composed of thermoplastic composites and aluminum. Toray Advanced Composites presented their research on thermosets that, unlike thermoplastics, retain their stiffness in high-temperature environments. Many other companies have introduced all-composite aircraft, including Boom Aerospace, which debuted at the Air Paris Show but did not disclose the specific materials used; Volocopter, which developed a multicopter weighing less than 450 kg and a heavy-lift drone capable of carrying payloads of up to 200 kg, both made mostly from carbon fiber; and Toray, an experienced supplier of carbon fiber polymers, which developed the Lilium Jet, an all-electric, emissions-free VTOL with all its primary structures being made of carbon fiber composites [43].

In conclusion, there are several forms of composite materials, each with distinct properties and advantages. Carbon fiber reinforced polymers, which are extensively used and have a variety of applications, can be created in a multitude of ways depending on the placement of the fibers and the structure of the grid, which affects the final material's qualities. Properties that will be mentioned in manufacture, section 2.6, and on the selection of materials , section 3.4.

Also frequently contrasted are thermosets and thermoplastics; thermoplastics are lighter and more easily recyclable than thermosets. On the other hand, thermoplastics used to be significantly more expensive than thermosets, but as previously stated, new production processes have enabled prices to decrease [44]. However, there are still many concerns about the thermoplastics' behaviour when in high temperature situations, while the thermosets can have a good response to these environments, as before mentioned.

Lastly, wheels are typically composed of aluminum alloy, however magnesium alloy is also used. Wheels are fitted with tires. They are built more rigid to bear large impact loads during landing and to allow the aircraft to move at high speeds during taxiing without bursting or detaching from the rim [41]. Aircraft tires are often tubeless or tube type. Aircraft tire tubes are constructed with the natural rubber compound. Polyamide layered with rubber made heavy-duty tubes in order to impart strength. Modern tire materials are synthetic or chemical compound of rubber, fabric and wire [45].

2.5.1 Analysis of material properties

Z. Ceylan, while doing a design of a landing gear for Hurkus, studied the MLX17 Steel alloy, which is one of the most used materials for this application [45].

G.Vasanth et al. studied the mechanical behaviour of different alloys that usually compose landing gears. The materials analysed were Aluminium 6-4 (Al 6Al 4V), the most used material in the industry; also a novel form of steel alloys that has a better behaviour than the ones formally used in aviation, AerMet 100; and, finally, two different Titanium alloys, Ti 10-2-3 (Ti 10V 2Fe 3Al) and Ti 5-5-5-3 (Ti 5Va 5Mo 5Al 3Cr), the authors also mention that this latter ones have been changing the gear materials, particularly on new age wide-body airplanes. The conclusions obtained from this investigation allowed to understand that different segments of the landing gear require different materials since their solicitation is different. Moreover, it was possible to understand that the structural components should be made of Titanium alloys (out of the materials analysed here) since they offer the better safety coefficient [46].

H. Tran modeled and studied a landing gear impact response. The materials used were different for each section of the landing gear and it ranged from steel alloys, aluminium alloys and stainless steel, but also nickel and chrome alloys for parts of the fork assembly and the nose wheel assembly, respectively [47].

All this situations showed that this conventional materials don't show any kind of problems (apart for some concentration of tensions due to the geometry itself) and can be used for production of landing gears. However, composite materials can bring many advantages in mechanical properties but mostly in a reduction of weight and better efficiency.

J. Pauliny, studied the design of a landing gear for a four-seat aircraft. For the strut component, which will have to balance strength to carry the loads and elasticity to be able to allow for the required deflection, the author chose unidirectional glass-fiber reinforced plastic. This allows for an easy manufacture process since there is no need to lay angled plies of e-glass fiber and the material will behave as a simple orthotropic material. As for the other different components of the landing gear, different types of aluminium alloys were used and also some steel alloys but its use was meant to be shortened due to its greater weight [48].

A. Rashidi et al. [41] developed a model of an all-composite landing gear for finite element analysis. Here, the main landing gear was approximated to a thin curved shell and the part was composed by layers of carbon fiber reinforced polymer (CFRP) and glass fiber reinforced polymer (GFRP). The results obtained were very satisfactory since the landing gear was able to sustain all the loads applied to it in the simulations while maintaining a high safety factor. Walden, studied the application of composite materials in commercial airplanes and his findings suggest that this materials are very promising for design of landing gears due to their orthotropic nature, if placed on the right direction, since the principal stress components in landing gears is mainly normal stress along the length of the gear [49]. Goyal, replaced an aluminum landing gear for one made of composite materials. After analysing both structures under maximum load situations, both were able to sustain this stresses but the results suggested that the weight ratio of composite materials

was allowing for a greater efficiency than the one obtained for the aluminum landing gear [50].

With all the research that as already been developed regarding different materials to manufacture landing gears many options emerge as suitable. Depending on the specific requirements of the project, different ones may be selected since all of them offer advantages and disadvantages. These options may differ from conventional materials such as different forms of steel like the most novel ones that are high strength and offer corrosion resistance, to different kinds of titanium and aluminum alloys. The offer also extends to several different composite materials like carbon and glass fiber reinforced polymers, using as a resin either thermosets or thermoplastics. The properties of each one must be properly analysed and studied in relation to the requirements in order to select the most adequate material for the landing gear. Further, in section 3.4, these characteristics will be compared and the a selection of the material will be made.

2.6 Manufacture

In order to properly produce the landing gear, a manufacturing process must also be selected. This selection is usually made taking into consideration two major factors: the cost of production and production rate for a part. However, for a prototype production, production rate does not have a great importance.

2.6.1 Composite parts

For manufacturing of composite parts of thermoset matrix one major step is the curing of the resin which involves elevated temperatures. Such high temperatures are required to transform via chemical reactions the uncured material into a fully cured solid composite. This process (curing of the resin) is called the polymerization reaction, transforming the liquid prepolymers to a solid polymer. The fibers are combined prior, with the precured liquid state [51].

The first mode of manufacturing was the hand-layup technique however, as the name implies, this process is very time consuming leading to low production rates and relies on intensive labor by the operator. Due to advances in the composite industry, several new techniques have emerged that can offer high production rates and can, mostly, be automated. Compression moulding and filament winding represent two of the most used methods, for example in automotive industry, mainly because of their high production rates at low costs. Resin transfer moulding and wet compression moulding, two forms of liquid injection moulding procedures, also provide relatively high rates and allow for the ability to create complex shapes [51].

Nonetheless, for the creation of prototypes, the primarily used technique is the vacuum bag moulding.

2.6.1.1 Vacuum bag moulding

This procedure has limited use in the industry due to being of very intensive labor and requiring a long time cycle to complete the manufacturing of components. Nonetheless, it is very common

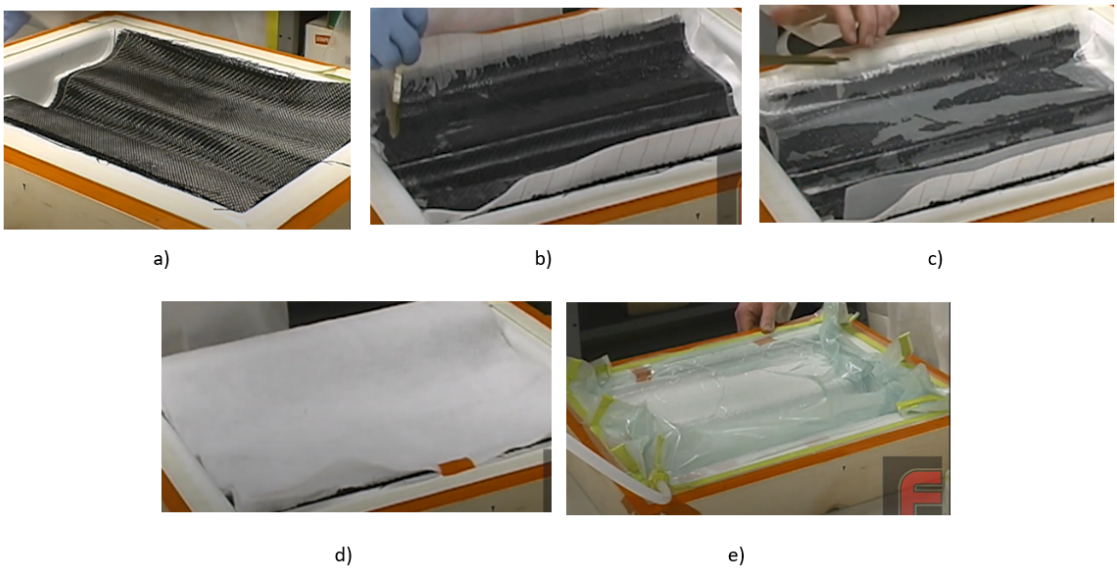

Figure 2.20: Different stages of the stacking a) Reinforcement material b) Peel ply c) Perforated film d) Bleeder material e) Vacuum bag [53]

for making laminated structures in the aerospace industry and also used for prototyping [51].

The starting raw material for this method is a prepreg containing unidirectional continuous fibers or bidirectional fabric impregnated in partially cured resin, usually of a thermosetting type and, therefore, after the placement of the material the process evolves straight away to the curing of the resin [51]. On other cases, if the material is not yet impregnated, the raw material is just the reinforcement and the resin will be injected.

The first stage is related to the design requirements. A mould must be created following the geometric criteria defined for the final piece. On this mould, a release wax must be applied, before the continuation of this process, to allow for the proper dismounting when everything is concluded [52].

With the mould in place follows the stacking of several layers of material. Plies of desired shape and size are cut from the reinforcement roll and disposed over the mould according to the desired fiber orientation on the stacking sequence. This can be done by hand or via automated tape-lying machine [51]. Over the material, a single layer of peel ply is applied to prevent the vacuum spots and the resin line from sticking to the composite. Above this one, a layer of perforated film to avoid the contact between the next layer and the peel ply [52], also regulates resin flow and assures for an even distribution of resin by allowing it to drain evenly throughout the part [53]. Next, two layers of breather or bleeder material to facilitate the flow of resin. These layers will absorb and retain the excess resin. Finally, the last layer consists of the vacuum bag which must be cut oversized [52] [53]. On figure 2.20, the different stages of the stacking of these layers can be seen.

For the injection of resin, the line of injection and vacuum points must be created. To make the process of resin infusion more rapid and effective, the selection of the points must be optimized.

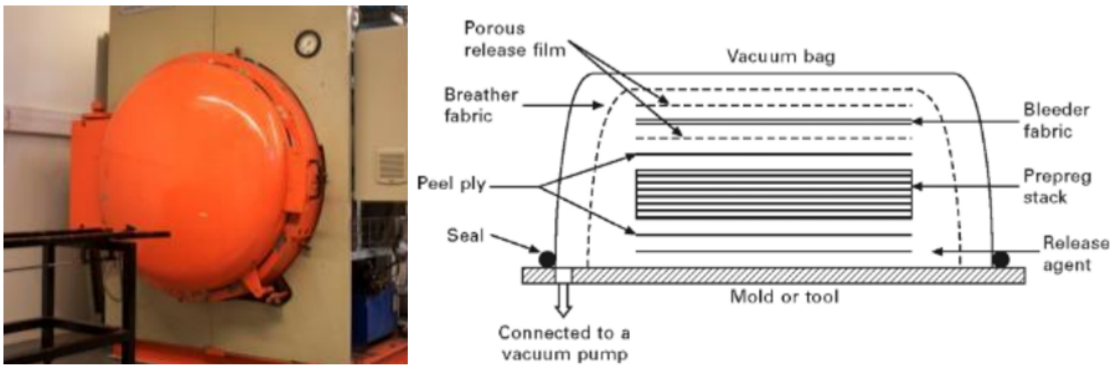

Figure 2.21: On the left, an autoclave [52]; on the right, a schematic example of a vacuum bag set-up [51]

The focus should be on minimize the distance covered by the resin from injection to the vacuum points however, due to surface requirements, this is not always possible. On the spots near the injection and vacuum locations, finishing operations will be required. This correct positioning is always important to avoid zones where the resin doesn't reach and the creation of porosity [52].

When everything is in place, the injection tubes and vacuum spots are created and the vacuum bag is ready to be sealed. the bag is secured and the vacuum system is tested to analyse for possible leaks [52].

For the infusion process the vacuum pump is turned on and it remain on until the ending of the curing process, continuously removing the air from the vacuum bag [53]. The resin canals are opened for the resin to move from the injection points to the vacuum spots. When the component is filled with resin, the injection points can be closed but the vacuum line remains connected [52].

To cure the resin, the assembly can be placed inside an autoclave, as the one seen in figure 2.21 or on an air-circulating oven depending on the requirements for the final piece. Using the first one, a positive pressure is applied to consolidate the separated plies so it doesn't just rely on high temperature. Therefore, while oven curing may take from 30 minutes to several hours, autoclave works faster and produces better consolidation and generally lower void content on the final cured laminate. However, autoclaves are highly expensive and entail large operating costs. A new generation of prepregs may serve as a solution since they allow for the production of components with autoclave-like final properties while using a normal air circulating oven. These are called vacuum bag only (VBO) prepregs. [51]

After the curing process is completed, the material is hardened and ready for dismounting. The tubes and vacuum points are removed as well as vacuum bags and all the other layers of the assembly. The peel ply may remain on the component until finishing operations are required since it can work as a protection layer for its surface [52].

2.6.2 Prepreg Fiber

Prepreg refers to pre-impregnated reinforced fibers. This material is ready for the implementation on a mould without the need for adding any extra resin. The resin system present on this layers already includes a proper curing agent and comes in partially cured stage, to allow for a better handling of the material. For the curing, the process mentioned before can be used since it requires heat and pressure [54] [55].

The main advantages resulting from this form of composite raw material compared to traditional one are [54]:

- Easy to use and process;
- Optimal resin proportion, reducing the possible errors of resin-reinforcement mixture;
- Reduced amount of excess resin;
- Higher strength;
- Uniform thickness, repeatability - reduced human related errors;
- Less waste during the vacuum bag process;
- Shorter curing cycle;
- Usually allow for a smooth surface.

However, a few concerns are also associated with prepregs. Its cost is relatively high when compared to other techniques and it must be stored in a refrigerated environment since its shelf life at ambient temperature is quite short [55].

For its fabrication, fibers are mixed uniformly in a resin bath allowing them to be impregnated by the resin. The product can then be cut to be placed and oriented in compliance with the desired stacking sequence. On figure 2.22, a schematic of this procedures is shown.

There are numerous types of prepreg fiber-resin on the market and it is a configuration compatible with carbon or glass fibers embedded in epoxy resin.

2.7 Legislation for UAVs

NATO has developed a set of standard requirements on the technical integrity for fixed-wing UAVs regarding design and manufacturing. This set of requirements aim to certify the airworthiness of UAVs with a maximum take-off weight not greater than 150 kg and an impact energy greater than 66 J [57].

This document was created since NATO understood that a pure traditional perspective set of airworthiness codes (CS or FARs) could not fulfil the objectives proposed for this new systems.

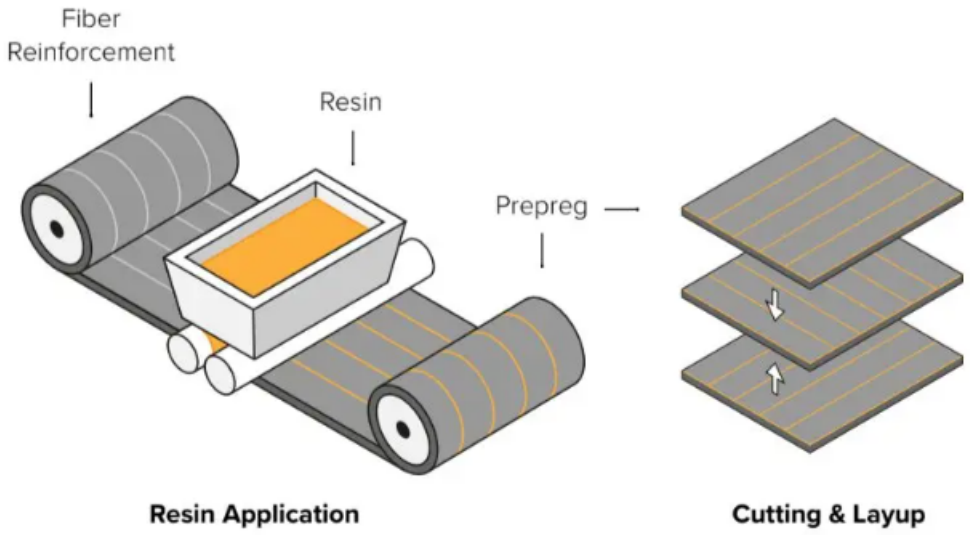

Figure 2.22: Schematic of reinforcement impregnation with resin, cutting and layup of plies [56]

The scope of this document is create a minimum amount of certification evidence needed for an acceptable level of airworthiness, mention and control all design attributes which may be considered a danger for safety and allow for flexible design solution [57].

By having this new regulated standards for NATO countries, UAVs should enjoy easier access from one country to other's airspace since the airworthiness certification should be accepted within all NATO countries [58].

However, it is important to consider, that NATO does not certify aircrafts. It is only the institution that created the legislation to guarantee airworthiness. The certification procedure is performed by national entities. As for the Portuguese case, the institution responsible for this is ANAC. Since there is no active legislation in Portugal, the National Certifying Authority shall certify UAVs according to this NATO STANAG.

2.7.1 STANAG 4703

The legislation identifies PSE for which there are some certifications required regarding the applied loads. The landing gear is considered to be a PSE, since it is considered a part which failure could reduce the structural integrity. According to the norms, all operational loads that the landing gear must withstand on the ground must be obtained. In order to evaluate the compliance with the legislation, all applied loads must be obtained for extreme conditions, so maximum design weight [57].

As for the landing moment, the worst combination of loads must be used, corresponding to the worst possible scenario in the moment of landing. All scenarios must be determined, but according to the Annex B, different situations of landing create the worst loads for either the nose gear and the main gear. These different load situation will be discussed in chapter 3.2.3

Taking into consideration the cyclic use of the landing gear, the dynamic behaviour must also be guaranteed to obtain airworthiness. According to the legislation, effects of cyclic loading, degradation and damage must not reduce the structural integrity. Specifically with fatigue, during the design phase, as far as practicable, any points of stress concentration where variable stress above the fatigue limit might occur must be eliminated. Moreover, for composite materials, the use of strain levels compatible with the no-growth criterion for the Damage Tolerance may be taken as sufficient evidence, in conjunction with good design precautions to avoid the local development of out-of-plane stresses (corners, ply drop-off or stringer run-outs are of primary importance).

Besides this, for production, the manufacturing processes and materials must result in known structural properties. The material allowables used for structure design must be identified so that no structural part is under great stress due to material variations interface or load concentrations. The materials also need to be classified in order to perform design calculations. This calculations will be thoroughly approached on section 5.3 and chapter 6. Moreover, if temperature and moisture have significant impact on the mechanical properties of materials, the worst possible scenario must be the on used for operational conditions on calculations [57].

Finally, all necessary instructions to comply with a continued airworthiness. A method to identify technical problems or safety issues must exist so does a preventive program and a set of corrective actions, if necessary [57].

2.7.2 FAR 23

Legislation FAR 23 is very similar to STANAG 4703. Some features must be considered in this application.

FAR 23 mentions that if limit drop tests are performed, they must be done in the full airplane or equivalent assemblies consisting of wheel, tire and shock absorber, using a proper relation. Free drop height is limited by the norm. The limit inertia load factor must be determined using a determined formula, in a rational or conservative manner, during the drop test, with the landing gear unit attitude and drag loads representing the landing conditions.

2.7.3 CS-VLA

This certification specifications for very light aeroplanes also present many similarities with the norms defined by STANAG 4703. However, it defines some extra requirements for the landing gear that must be complied.

Limits and a formula for descent velocity are given in this legislation. And it also mentions that the inertia load factors used for design cannot have values below 2.67 at design maximum weight, unless lower values will nor be exceeded in taxiing at speeds up to take-off speed in terrain as rough as can be expected in service.

As in the FAR 23 legislation, it refers compliance with the criteria for free drop tests.

Chapter 3

Landing Gear Conceptual Design and Theoretical Principles

All of the information gathered from the landing gears market study is used to rationally and methodically design one that applies to the UAV proposed in the thesis mentioned in section 2.3.3 As with any other design process, it will require various stages, including the definition of the application's specific requirements, preliminary design, advanced design, testing, and possibly the development of a prototype. Nonetheless, it is essential to recognize that this is an iterative process. Throughout the various phases of development, various tests will be conducted, and if failure or defects are discovered, a step back is taken so that they can be fixed. Section 2.7, mentions the different legislation and standards that must be followed during the design process.

During the various phases of requirements specification and design, various mathematical models and calculations derived from the literature will be required. All employed models will be explained in detail.

3.1 First Design Approach

3.1.1 Landing Gear Requirements

A list of essential requirements for this project of a landing gear is provided below, summarizing and elaborating on crucial considerations. The requirements are not defined, as they should, in a measurable way but refer to the preferred option when comparing different solutions.

- Low weight
- Cheaper price: manufacturing and materials
- Easier to design and manufacture
- Respect the positioning characteristics
- Able to withstand the ground loads calculated for different situations

- Reduced drag
- Able to absorb the necessary energy on landing
- Resist water damage
- Resistance to fire and high temperatures

Some requirements such as geometrical definitions and the resistance to several types of loads applied will be discussed further in this topic. Several criteria must be analysed and complied to in order for the landing gear to function properly and for the UAV to safely land, take-off and perform any kind of ground operations.

3.1.2 Selection of Landing Gear Configuration

The preliminary landing gear design process for this firefighting UAV must begin with the selection of the optimal configuration. Several criteria will be considered when comparing and separating the landing gear configurations presented in section 2.4 in order to properly select one. This consists of the configuration's total cost; its weight, which relates to the aircraft's performance; its stability on the ground for landings; its ground control while taxiing; its behavior during take-off runs; and its manufacturability and durability. This comparison will be made on table 3.1, according to a scale from 1 to 5. with 1 being the worst and 5 being the best relating behaviour to the referred requirement.

Only the usual options of tricycle, tail-wheel and bicycle landing gears will be considered for this selection. Quadricycle and multi-boogey landing gears consist of options of very high weight and cost that are usually employed in way larger aircraft than the one being studied in this project, for that reason they will not be considered.

Table 3.1: Decision Matrix for Type of Landing Gear Configuration

Requirement	Conventional	Tandem	Tricycle
Cost	3	4	2
Weight	3	4	3
Manufacture	2	3	4
Performance (Drag)	2	4	3
Ground Control	1	3	5
Stability on Landing	3	2	5
Take-Off Run	3	2	5
Average rating	2.43	2.14	2.86

The selected configuration was the tricycle landing gear. It can be seen on table 3.1 that this solution offers the most benefits when compared with the other two. Easily available manufacturing since it is the most prominent type of landing gear. The tricycle configuration allows for an optimal control for ground operations either for taxiing or take-off/landing since it is the one that creates the highest stability on the aircraft.

3.1.3 Retractable vs Fixed Landing Gear

The main criteria that will mostly affect the selection between retractable or fixed landing gear are the cost of the structure and the performance of the UAV. The characteristics of both options were approached in detail in section 2.4.1 and it is understandable that retractable landing gear allows for better performance of the aircraft but leads to a higher cost of production and extra weight. A comparison between them is made in table 3.2.

For this selection, the comparison will only infer which option presents itself as the most appropriate for each of the criteria involved in the decision.

Table 3.2: Decision Matrix for Fixed vs Retractable Landing Gear

Requirement	Fixed	Retractable
Cost	Cheaper	More expensive
Weight	Lighter	Heavier
Complexity of Design	Easier to Design	More complex (extra parts)
Manufacture	Easier to manufacture	More challenging
Maintenance	Easier to maintain	Harder to maintain (extra systems)
Performance (Drag)	More drag	It is stored - no drag
Need for Storing Compartment	Does not require	Requires storing compartment
Need for Retraction System	Does not require	Requires a retraction system
Available Aircraft Space	More space available	Less space available

As it is seen on the table, the most advantageous option is the fixed landing gear, so it won't require any retraction mechanism or a storage bay for the landing gear. However, it is noticeable that this selection can lead to a reduction in aircraft performance due to the drag forces created while in flight. For this reason, the aerodynamics of the structure should be optimized and measures must be taken to reduce these forces.

3.1.4 Type of Leg for Landing Gear

After selecting the tricycle configuration as the optimal one for this project and its position as fixed, there is the need to select the type of leg for the landing gear from the options mentioned in section 2.4.2.

The type of material is also selected in this section, however it will be specified in the following topics. Right now, the type of material must be selected since different types are more suitable to some of the configurations.

Recapitulating the options, the decision comes down to 3 configurations: oleo-pneumatic cylinder, leaf-spring or a rigid strut.

For the oleo-pneumatic solution usually metal is the type of material employed. This solution allows for the best response to the landing impact and allows for an easy design since its characteristics can be obtained via tabulated formulas and the material properties are isotropic. However, by relying on oil as the fluid inside the cylinders, it creates the need for oil inspection and the possibility of oil leaks that need to be solved in a rapid way. Besides all this, the different components

on this advanced form of strut allied to the use of metal as the main material make this option way heavier than other solutions.

The leaf spring gives a cheap, simple and light weighted option for the legs of the landing gear. However, offering lower efficiency for shock absorption. Here, either metal or composite materials could be selected but the latter offer better fatigue resistance and other mechanical properties in general with lighter weight, even though it lacks on impact load allowed. Galvanic corrosion may can occur between composite materials and some metals.

Finally, the rigid strut could be an option if the UAV only had vertical landing and take-off but its little to none shock absorption gets exposed for different landing conditions that must be available for this aircraft.

For this application, it is expected that the stresses applied on this landing gear will not be of such great dimension that an oleo-pneumatic strut would be needed, due to the light weight of the entire aircraft. So, using the requirements of low-cost and light weight for this selection, the type of landing gear leg used will be the leaf-spring strut with composite materials.

Knowing that this strut is usually applied to main landing gear, here it will also be used for the nose landing gear. It is referred that it presents a problem for retractable configurations but it has been decided that this aircraft will have a fixed landing gear.

As for the geometry of the struts, some different designs can be adopted. Nonetheless, points of stress concentration must be avoided, so both the sections of the landing gear will have a geometry similar to a curved beam with some straight sections. Therefore, for the analysis of the structure, curved beam theoretical models can be employed and they are introduced in section 3.3.

3.1.5 Selection of Landing Gear Geometry

3.1.5.1 Main Gear

For the geometry of the main gear, according to all the references analysed, all the options on a leaf spring structure offer an elliptical like approach, symmetrical when comparing left and right main gears.

The main gear can be done in one component or two separate ones that will be attached to the fuselage on different points.

For sake of simplicity, a one part main landing gear will be selected, with the leg part (outside the attachment with fuselage) approximate to an elliptical form.

The main gear will have two mounting brackets.

On the top, attachment to the fuselage. With the lower fuselage's flat configuration, section 2.3.3, the center of the main gear leaf strut will also have a straight geometry. The mounting bracket must support the stresses on this area and counter the maximum bending moments created by the strut.

The lower mounting bracket is the connection to the wheel and the tire assembly. Here stresses must also be supported and it allows for the forces to be transmitted from the assembly to the strut.

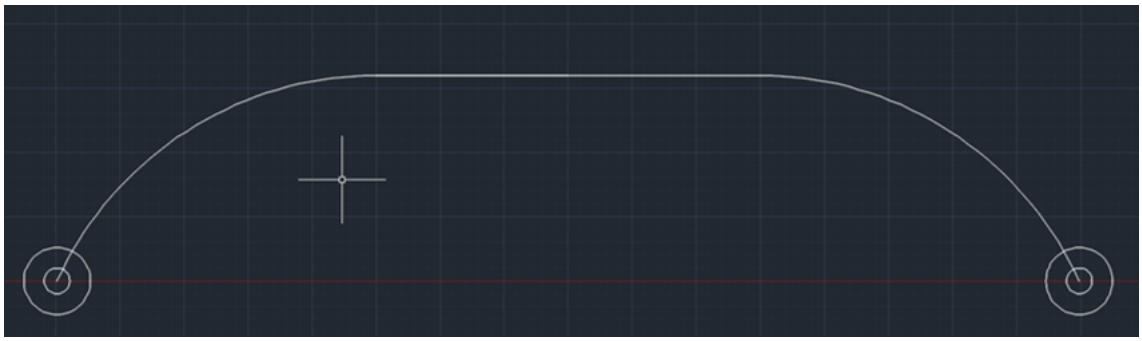

Figure 3.1: Front view for preliminary design for the Main Landing Gear

On the geometry of the main gear stress concentration points must be avoided. The focus must be on the transition from flat geometry to the elliptical parts. Then, a first design for the main landing gear follow on figure 3.1

3.1.5.2 Nose Gear

For the geometry of the nose gear, the same criteria of avoiding stress concentration points must be satisfied.

Since it consists of a single gear attached to the fuselage, the simplest option emerges as a simply vertical leg from the fuselage to the ground.

However, this option lacks on absorbing any kind of force differing from its directional axis, so a configuration that allows for absorption of other stresses is required.

Sforza, in his book, presents an option that introducing an angle θ, permits the gear to absorb not only the vertical efforts but also the horizontal ones [32], figure 3.2.

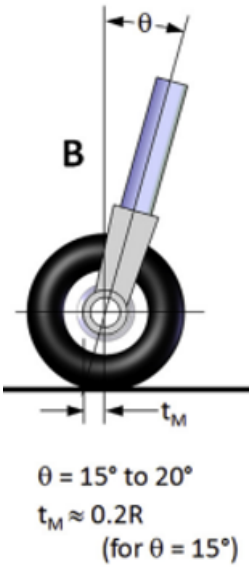

Figure 3.2: Nose gear configuration on the connection with the tire wheel assembly [32]

For the rest of the leg, with the avoidance of stress concentration in mind, a first design of the nose landing gear follows in figure 3.3,

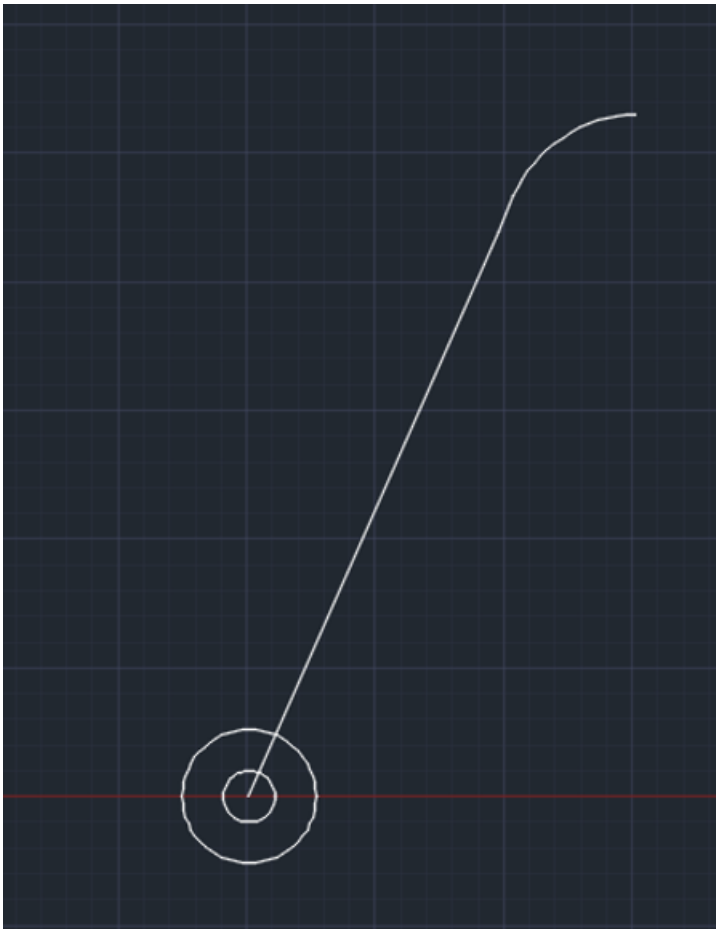

Figure 3.3: Side view for preliminary design for the Nose Landing Gear

Several subsystems are also required on the nose gear that will be projected on the detailed design. For the attachment to the fuselage the configuration is similar to the one explained for the main gear. The attachment to the tire-wheel assembly relies on the use of a metal component, the fork, that connects the end of the leg strut to both sides of the wheel's axis.

Moreover, since it is expected that the UAV might need to land on rough runways, the need for steering might be present. Therefore, a steering system must be implemented on the nose gear. The other option would be differential braking on the main gear but this system is not used in aircraft of small dimensions.

3.1.5.3 Cross Section

The selection of the geometry of the cross section will follow a similar path for both main and nose landing gear.

In section 3.1.3, it was decided that the landing gear would have a fixed configuration, therefore drag reduction is of great importance.

Consequently, the cross section should have a shape similar to a symmetrical airfoil, similar to the ones found in wings, as the one seen in figure 3.4

Figure 3.4: Example of a symmetrical airfoil configuration

However, this configuration would generate difficulties in the manufacturing department and complications for mathematical calculations.

A simpler method that can maintain these drag reduction advantages is having a rectangular section on the landing gear and placing around it fairings with no structural function. Similar to the motorcycle example also referenced in section 2.4.1, exemplified in figure 3.5.

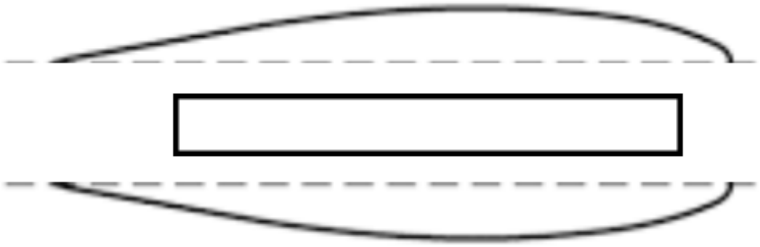

Figure 3.5: Rectangular section and possible two halves of a fairing that must be applied

For the rectangular section, the most important aspect is reducing the dimension that might enhance the drag created by the drone while in air. Therefore, the aim should be on reducing the dimension perpendicular to the movement.

3.1.6 Wheel and Tire Selection

Tires must be able to withstand the stresses related to landing and takeoff operations. Its selection involves tyre sizing, selection of tyre type and wheel [38].

The wheel refers to the circular metal or plastic object around which the tire is mounted. The most used materials for tires are synthetic or natural rubber, fabric and wire, along with other chemical compounds [59] [38].

FAA regulations define several criteria for the proper selection of the tires. For the main wheels, the loads on each tire on the most critical situation multiplied by 1.07 may not exceed the maximum load of the selected tire [32].

For nose tires, the applicable constraints, according to FAA 25.733 [32] are:

- The static load on the nose wheel for the worst combination of CG and total weight may not exceed the load rating of the tire;
- With combined forces of 1g downward and 0.33 g forward acting on the CG, for the worst combination of CG and total weight, the load on the nose tire may not exceed 1.5 times the load rating, with a drag reaction equal to 0.31 the vertical load on the wheel;

Generally speaking, for a tricycle configuration, nose tires may be assumed to be about 50 -100% the size of the main tires [59].

The selection of wheel and tire will be made in section 5.3.2.

3.2 Functional and Geometric Requirements

As previously stated, in the initial stages of landing gear design, it is crucial to define the part's precise performance requirements in order to prevent catastrophic UAV failures. At this stage, in compliance with the laws that must be followed, the structural requirements for stresses and strains must assume the worst-case scenario for optimal performance in any circumstance.

Initial requirements of the landing gear design also include longitudinal and lateral positioning components that are affected by the aircraft's center of gravity limits, energy absorption requirements, and geometric constraints. To reduce the risk of ground looping, overturning, crosswind canting, and tail angle, and to allow the airplane to be maneuvered as necessary during the take-off and landing ground run, the correct positioning of the main and nose gears in relation to the center of gravity must be fullfilled [38]. The CG limits that affect this positioning are the forward-aft CGs and also its vertical range. Concerning the energy absorption requirements, it is necessary to comprehend the required landing gear deflections in order to ensure the limit ground reaction load factor; the inertia load factor cannot be exceeded during the worst-case landing scenario [48]. Furthermore, the geometric constraints include the tip over and ground clearance criteria. The tip over criteria is based on maintaining the longitudinal position of the aircraft's center of gravity (CG) and the range of CG travel, as fuel is consumed and payload (in this case the firefighting component) is loaded/unloaded, between the nose and the main landing gear, while the aircraft's center of gravity (CG) remains centered laterally [60]. Being divided into longitudinal and lateral components, the first prevents the UAV from tail-tipping during ground operations, while the second prevents the wing from side-tipping during taxi operations. The criteria for ground clearance can also be divided into longitudinal and lateral categories [48]. A proper landing gear design provides clearance between all parts of the vehicle and the ground in any combination of flat tires and worst case scenarios [38]. Longitudinal ground clearance guarantees a suitable distance between the ground and the rear part of the fuselage during a tail-down landing, as well as between the ground and any propeller for all ground operations (since the propeller is placed in the aft part of the fuselage, ground clearance for propeller should consider tail-down landing as should ground clearance for the tail). The lateral component ensures ground-to-wingtip clearance during possible crosswind takeoffs and landings [48].

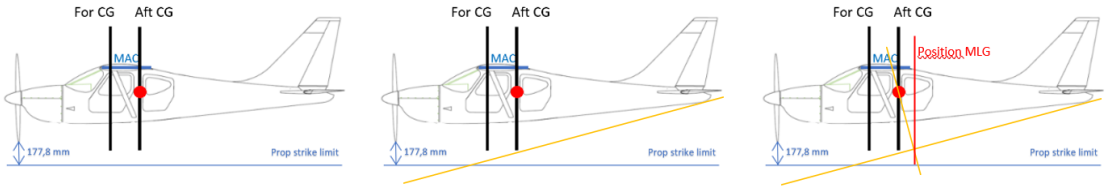

Figure 3.6: Different steps to graphically obtain the longitudinal position of the Main Landing Gear

Likewise, a number of factors impact the necessary geometrical characteristics of the structure. At this stage, which is already associated with the preliminary design, the basic geometry for the nose and main wheels must be selected. Furthermore, in order to determine the mechanical properties of the part, it is also necessary to select the material for the landing gear.

3.2.1 Positioning of the Landing Gear

There are steps that can be taken to ensure that the landing gear is properly located. For precisely defining the longitudinal position of the main gear, there are graphical methods available.

Initially, a cruise-attitude side view of the design is required. Here, the MAC (mean distance between aft and forward most points of the wing), as well as the aft and forward CG limits, are drawn. The highest vertical CG location is then determined at its rearmost position and plotted on the diagram. The prop-strike limit (the closest the propeller should get to the ground in the worst-case scenario) is then drawn parallel to the ground. Per the legislation 14 CFR 23.925(a) the limit stands at 7 inches which is equal to 177.8 mm [38].

To guarantee ground clearance during a tail-down landing, the tail-strike line is drawn at the recommended 15-degree angle (in this case, not only the tail needs to be considered but also the propeller, explained in 3.1) since it represents the maximum pitch angle during tail-down landings [38].

Another line is drawn perpendicular to this last one, crossing the CG drawn earlier. At the intersection of these two lines, a final vertical line is created. If possible, this vertical line represents the position of the main landing gear leg [38].

One can comprehend the multiple steps for this graphical positioning of the main gear on the longitudinal axis with the aid of an illustration, figure 3.6. The different stages follow the various preceding paragraphs, from left to right.

According to N.Currey, this position should be at around 50-55% of the MAC [61].

When the CG is at its forward limit, the nose landing gear should be positioned so that it carries less than 20 percent of the aircraft's design weight, and more than 6 percent when the CG is at its aft limit, as stated in equations 3.1 and 3.2.

$$for\ CG \rightarrow F_{NLG} \leq 0.2W \tag{3.1}$$

$$aft\ CG \rightarrow F_{NLG} \geq 0.06W \tag{3.2}$$

Where F_{NLG} is the reaction force acting on the nose landing gear.

Too much weight on the nose wheel makes it difficult to rotate the UAV for takeoff, while too little weight makes steering more difficult due to reduced friction and can also cause "porpoising".

To conclude the correct alignment of the landing gear, the overturn angle must be taken into account [61].

When an UAV spins, centrifugal forces are generated due to the CG's distance from the ground. These forces can result in an overturning moment that can cause the wing to roll beyond the aircraft's trajectory. The closer the center of gravity is to the ground, the greater the lateral stability [38]. This can also be determined with a graphical way and will be explained in section 3.2.1.3.

However, several criteria will be used to determine the height and the wheel track of the main landing gear and the problems regarding the forces created on overturning will be approached. If a problem is encountered, it must be known that, in order to increase the lateral stability, measures must be taken, such as [38]:

- Increase the space between main wheels (wheel track)
- Reduce the height of the landing gear
- Increase the space between nose and main gears (wheel base)

This method usually provides reasonable results that can be followed for the design of a landing gear. However, it will only work as a preliminary step to obtain the first coordinates. These will be tested according several criteria that define the landing gear height and the distance of the base. Finally, wheel track of the main component must also be calculated as before mentioned.

3.2.1.1 Landing Gear Height

Landing gear height is defined by the distance between the ground and the point of connection between the main gear strut and the aircraft. In this case, since the gear will be attached to the bottom of the fuselage the distance will be measured from the ground till the lowest point of this component. For a proper definition this value is obtained for a ground situation with a level attitude [59].

According to M. Sadraey [59], there are several main design requirements where the landing gear height play an important role, being:

- Provide ground clearance on taxiing
- Rear clearance during take-off rotation

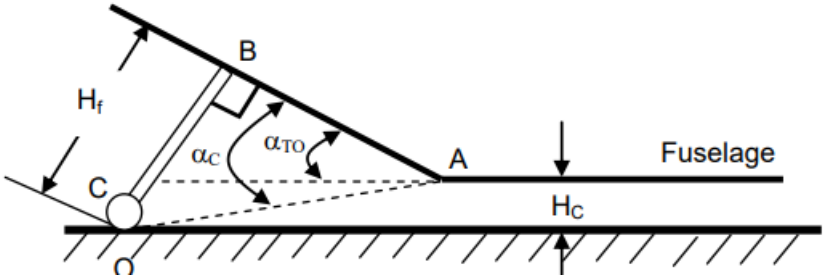

Figure 3.7: Representation of Clearance Angle and Rotation Angle on a take-off rotation [59]

- Tip-back prevention
- Overturn prevention
- Satisfy loading and unloading requirements

The first criteria is already taken into account via the graphic calculation of the main gear positioning. However, some references defend that for a land aircraft the minimum distance from the propeller (in this case the lowest point is the prop tip) to the ground is 0.2 m [59].

As far as overturn and the satisfaction of loading requirements, they will be approached for the calculation of the required wheel track (much more important for overturn prevention) and on the proper analysis of the landing gear.

The most important criteria to obtain landing gear height, besides ground clearance, is related to clearance during take-off rotation, which is directly related to tip-back prevention.

Take-off Rotation Ground Clearance Requirement

During take-off operation, an aircraft or, in this case, the UAV will rotate on the main landing gear in order to increase lift. A similar case also happens during tail-down landings, where the rotation happens for gaining of angle of attack. However, the most critical situation is take-off since, even after the UAV has lifted from the ground, some more rotation may occur which can lead to contact of the rear part with the ground [59].

It is mentioned by J. Pauliny that a first measure to diminish the possibility of rear parts to hit the ground is setting a minimum of a 12º angle with the horizontal of any line crossing a possible rear point of contact and the point of the main landing gear on the ground, with the vehicle in a level attitude [48]. This is already assured by the graphical method.

The possibility of rear parts hitting the ground on take-off must be eliminated. To do so, the clearance angle must be bigger than the rotation angle [59].

$$\alpha_C \geq \alpha_{TO} \tag{3.3}$$

The representation of these angles can be seen in figure 3.7. For this aircraft, it is the fuselage that is the most critical point. In the case of the rear propeller, the reasoning is the same.

Clearance angle can be obtained by the following formula [59];

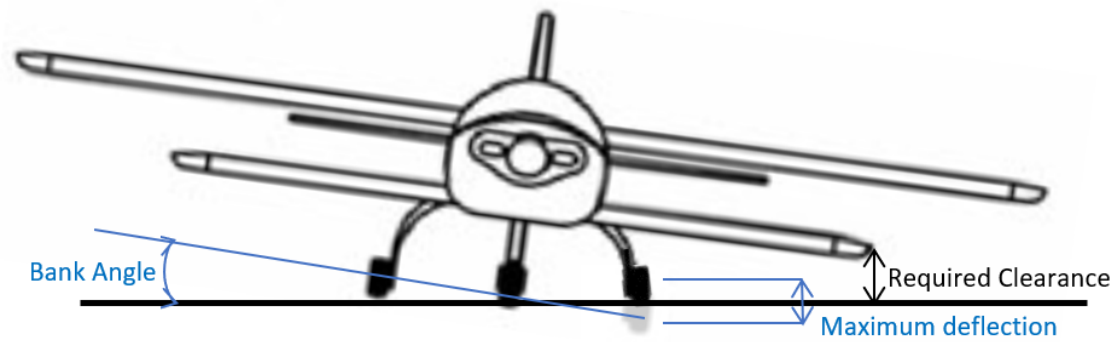

Figure 3.8: Illustration of a main landing gear on maximum bank angle [62]

$$\alpha_C = tan^{-1}\left(\frac{H_f}{AB}\right) \tag{3.4}$$

Where H_f is the fuselage height which, in this application's case, will be the distance of prop clearance and AB is the longitudinal distance from the main gear to the propeller. With an increase in landing gear height, the clearance angle also increases.

The angle of attack on take-off is not specified on the design of the UAV where the landing gear will be applied however, a referenced typical rotation angle is 12º [48].

Moreover, the clearance angle must also take into consideration the extra rotation the aircraft suffers even after the main gear has lifted from the floor. Therefore, multiplication factor for the landing gear height or an extra 3 or 4 degrees for the rotation angle should be considered [32].

Sidetipping Clearance Requirement

This is an extra consideration to include in the landing gear height calculation. On landings with environment conditions of considerable crosswind there is the possibility of side-tipping occurrence. Therefore, bank angle must be determined. The maximum bank angle is obtained for maximum deflection of one side of the main gear and no deflection on the other [38]. For this extreme situation, clearance from the tip of the wing to the ground must be maintained. This situation follows illustrated on figure 3.8.

3.2.1.2 Wheel Base

The wheel base (B) comprehends the longitudinal distance between the nose landing gear and the main one. This characteristic is important, specially, for load distribution but also on ground controllability and stability, even tough these two are mostly affected by the wheel track.

The criteria for load distribution have already been discussed in section 3.2.1. The main gear always carries about 80-95% of the entire weight of the UAV. Furthermore, this explains why nose wheels can be smaller than main wheels, The minimum weight that must be supported by the nose gear is related to the necessary ground controllability.

The approached situations were on the static domain. However they must be maintained for any combination of CG position and total weight of the aircraft.

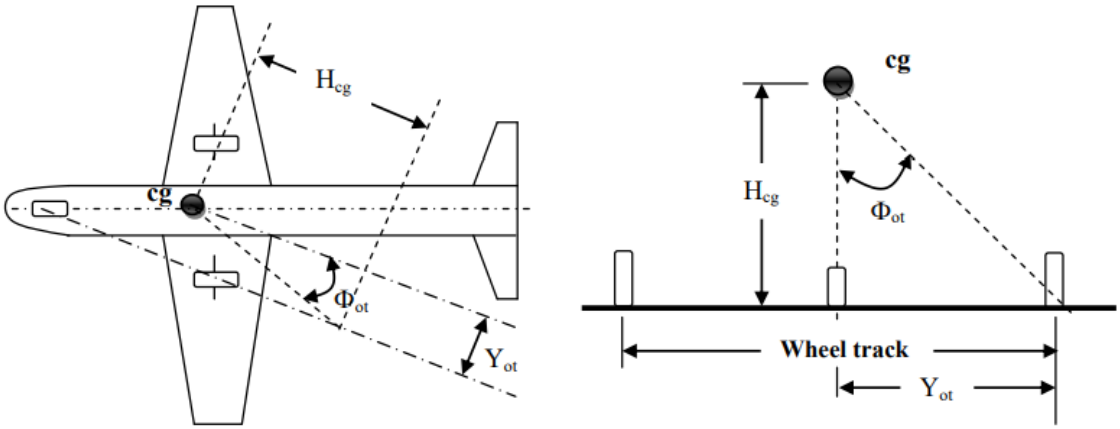

Figure 3.9: The two different overturn angles and their graphic determination [59]

3.2.1.3 Wheel Track

This characteristic is defined by the distance between the most left and right gears, in this case between the wheels of the main gear, and it is measured on the ground.

It is on the definition of wheel track (T) that the prevention of overturning is a criteria and, therefore, overturn angle is introduced.

There are two overturn angles (ϕ_{OT}) that can be obtained graphically. As a rule for an approximated determination, overturn angle must be at a minimum of 25º. The two forms of graphically determination follow presented on figure 3.9, on the left using a top-view and on the tight a front-view of a regular aircraft.

Using trigonometrical relations, these conditions result in,

$$\begin{gathered} \phi_{ot} \geq 25^\circ \\ tan^{-1}\left[\frac{tan\left(\pi-\left(tan^{-1}\left(\frac{T}{2B}\right)+tan^{-1}\left(\frac{2B_M}{T}\right)\right)\right) * cos\left(\pi-tan^{-1}\left(\frac{2B_M}{T}\right)\right) * 2}{TH_{CG}}\right] \geq 25^\circ \\ tan^{-1}\left(\frac{T}{2H_{CG}}\right) \geq 25^\circ \end{gathered} \tag{3.5}$$

A more accurate determination can be done and for that 3 design requirements should be analysed. For minimum allowable wheel track, ground lateral control and stability, and for the maximum value, structural integrity [59].

Ground Lateral Control

Typically two disturbing moments may be responsible for overturning an aircraft. The first one is the centrifugal force generated on a ground turn [59]. This force can be calculated via the following equation:

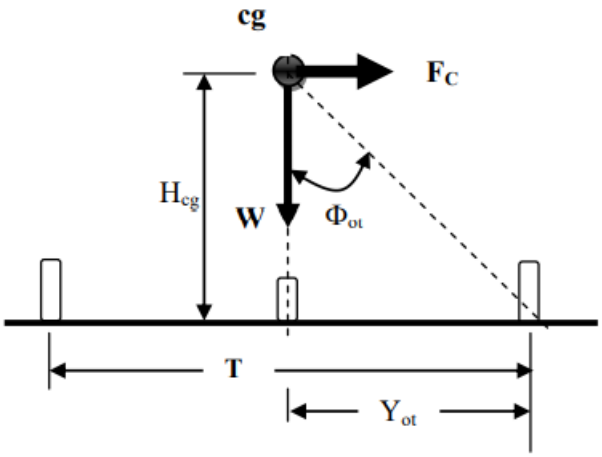

Figure 3.10: Representation of the forces acting on the CG when a turn is performed [59]

$$F_C = m\frac{V^2}{R} \tag{3.6}$$

Where m represents the maximum takeoff mass, V the aircraft ground speed and R the radius of a given turn. The force that works contrarily and prevents the overturning is the weight of the entire structure. So, the critical situation happens for the minimum possible weight [59].

A schematic representation of the forces is given in figure 3.10. Here the height represented by H_{cg} is the distance from the ground to the CG. The restoring moment created by the weight is a function of the wheel track [59]:

$$W \cdot \frac{T}{2} + F_c \cdot H_{CG} = 0 \tag{3.7}$$

Solving to obtain the minimum value for wheel track:

$$T > 2\frac{F_C \cdot H_{CG}}{m \cdot g} \tag{3.8}$$

Solving for the overturning angle on equation 3.8:

$$\phi_{OT} > tan^{-1}\left(\frac{F_C}{mg}\right) \tag{3.9}$$

An increase in landing gear height also affects the wheel track since it will increase the minimum allowable value.

This conditions should be calculated for the maximum centrifugal force that can be created on a turn. For that the worst scenario for a possible turn should be analyzed, therefore maximum velocity and minimum radius.

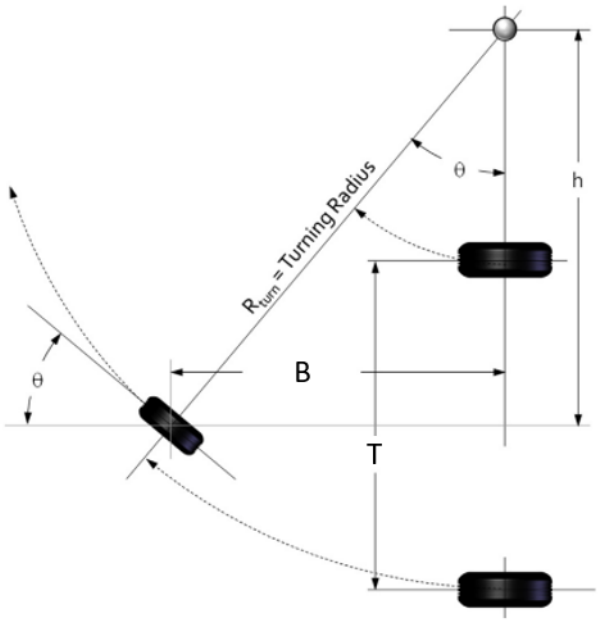

Figure 3.11: Schematic representation of a turn by an aircraft with tricycle landing gear [38]

The values of movement on the ground for this UAV are not give on its project. Since this UAV must have the ability to land in not so favourable runways, that can be shorter or not as straight as would be preferable, an important feature to have is being capable to turn on a dime [38].

On that scenario the **turning radius** should be analysed. On figure 3.11, the important geometric definitions to calculate it are represented. So, the value for turning radius is given by:

$$R_{turn} = \sqrt{B^2 + h^2} \tag{3.10}$$

Or,

$$R_{turn} = B\sqrt{1 + \frac{1}{tan\,\theta^2}} \tag{3.11}$$

Where, h is the distance to the center of the turn and θ is the rotation of the nose wheel. The requirement of turning on a dime requires that the nose gear is able to rotate a minimum of [38]:

$$tan\,\theta = \frac{2B}{T} \quad OR \quad h = \frac{T}{2} \tag{3.12}$$

Ground Lateral Stability

Ground stability is mostly affected by winds. Specifically, the most challenging type for the aircraft is the crosswind, acting perpendicularly to the drone. This force generates a moment that can be responsible for overturning the aircraft.

The crosswind force (F_W) can be modeled as a drag force, calculated via:

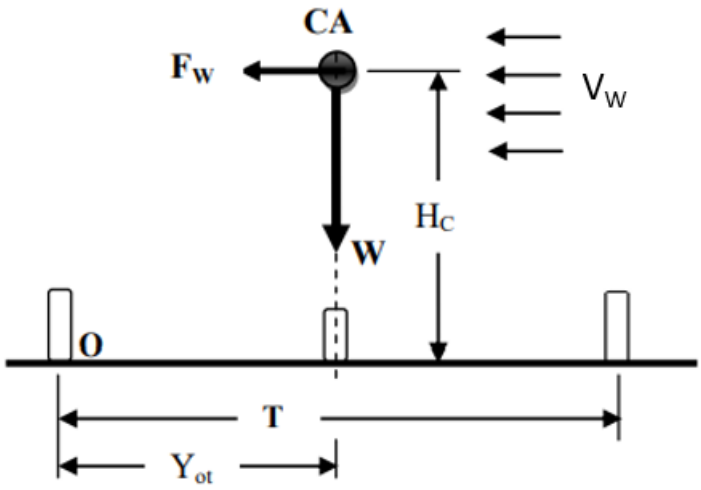

Figure 3.12: Representation of the forces acting on the Centroid when crosswinds act [59]

$$F_W = \frac{1}{2}\rho V_W^2 A_S C_{D_S} \tag{3.13}$$

Where V_W is the wind speed, A_S the side area of the aircraft, C_{D_S} the side drag coefficient with a value that varies from 0.3 to 0.8.

This situation is actually very similar to the centrifugal force one except instead of analysing on the CG, the analysis will be made on the centroid, with H_c being the distance from the ground to this point. The situation is represented in figure 3.12.

Here, the equilibrium of moments gives that:

$$W \cdot \frac{T}{2} + F_W \cdot H_C = 0 \tag{3.14}$$

Solving to obtain the minimum allowable T,

$$T > 2\frac{F_W \cdot H_C}{W} \tag{3.15}$$

The critical situation is obtained for the minimum weight possible of the aircraft and for a situation at sea level. However, some of the required components of F_W may not be obtainable in certain conditions. It must be said that in almost every case, if the ground controllability aspect is respected so will be the ground stability.

Structural Integrity

After the minimum value for T is obtained, structural integrity is the criteria that defines the maximum allowable value. Here, the aircraft is viewed as a straight beam composed by the wing with two simple supports on the main landing gear [59].

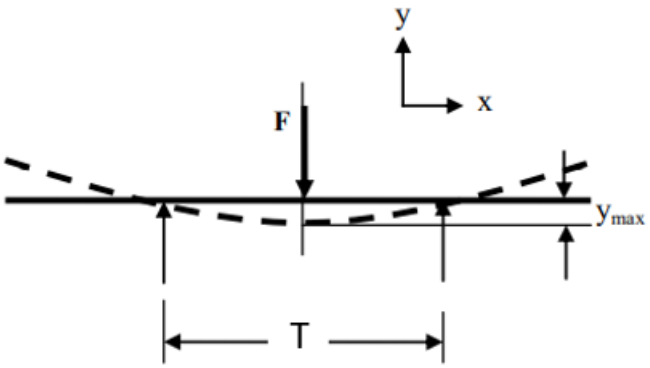

Figure 3.13: Deflection on a beam with two supports

This beam, according to basic theory of structures, will deflect with its maximum happening at the middle of the beam. With an increase in T, the maximum deflection increases. This situation also leads to [59]:

- An increase in wing dihedral -> degradation of lateral stability and decreased roll control;
- Bigger deflection, worst case scenario the fuselage touches the ground;
- Degradation of structural and aerodynamic integrity, structure may break.

The situation of straight beam with two supports is presented in figure 3.13.
The maximum deflection in a beam subjected to a force F is given by:

$$\gamma_{max} = -\frac{FT^3}{48EI} \tag{3.16}$$

With E the modulus of elasticity and I the second moment of area of the beam. Applied to the aircraft, the force is the maximum load on the main landing gear.

Therefore, the equation to obtain the maximum value for the wheel track can be obtained from equation 3.16 and the relations mentioned prior.

$$T \leqslant \left(\frac{48EIB\gamma_{max}}{WB_{n_{max}}}\right)^{\frac{1}{3}} \tag{3.17}$$

The critical situation is given for the maximum allowable take-off weight. This technique can be applied by testing the chosen wheel track and checking the maximum deflection (if it is viable) or by defining the maximum allowable deflection, depending on the situation and calculating the maximum value for wheel track

3.2.2 Energy absorption requirements

Landing gear must be able to absorb energy during impact with the ground without transmitting it to the rest of the UAV, or at least transmitting a residual amount.

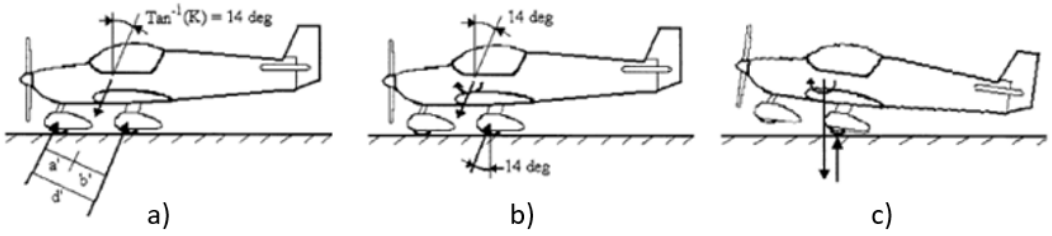

Figure 3.14: Types of landing: a) landing with inclined reactions; b) a level landing with the nose wheel just off the ground; c) a tail down landing

According to the NATO UAV legislation, STANAG 4703, there are three distinct landing types that must be accounted for when calculating the forces acting on the nose and main gears and the energy involved during landing. They consist of a level landing with inclined reactions, a level landing with the nose wheel just off the ground, and a tail-down landing in stall attitude.

Figure 3.14 schematically represents all these three types of landing and several geometrical references that will be used for load calculations.

In addition, for one-wheel loading conditions, it is assumed that the UAV has a level attitude and only one wheel contacts the ground. Here, the same ground reactions must be obtained as for that side under level landing conditions (inclined reactions) [57].

Since the most demanding situation must be considered for each component, the situations for either nose or main gears will differ for calculations of deflection, energy involved on impact and forces on the landing gear.

3.2.2.1 Main landing gear

The most challenging landing configuration for main landing gears is the tail-down configuration (figure 3.14 c)), as these touch the ground first.

Acknowledging that a portion of the energy is nullified by the lift created by the wings. Respecting the law of conservation of energy,

$$\frac{1}{2}mV_y^2 + mgd = Lmgd + E_{strut} \tag{3.18}$$

Where,

- m - design landing mass (maximum landing mass possible = max design mass; worst conditions possible for this calculations) [kg]
- V_y - descent Velocity [ms^{-1}]
- g - standard gravitational acceleration [ms^{-2}]
- d - landing gear deflection [m] = dtire + dshock (or d of the landing gear strut)

- L - lift ratio [1]
- E_{strut} - the energy the strut is able to absorb on impact

The kinetic energy that will be absorbed on landing depends on both the design landing weight and the descent velocity of the aircraft. The designing landing weight needs to be the maximum design weight since it would result in the worst case scenario.

The descent velocity that should be used for design purposes is also defined in the norms and its value can be calculated, with the expression given and explained in section 3.2.4. The horizontal speed stays approximately constant on touchdown and its variation is mostly due to drag so there is no variation of kinetic energy important for the landing gear.

The gravitational potential energy also depends on the design landing weight but also on standard gravitational acceleration and the landing gear deflection.

For the value of the energy absorbed by the lift, it is similar to a potential energy with a constant applied. This constant represents the wing lift to weight of the aircraft ratio which for descent flights is always lower than 1 [63]. According to the UL.GL.1 criteria of the STANAG 4703 legislation, this value is assumed to be two-thirds [57].

For the energy stored on the landing gear, its material can be defined as an elastic object. Than, the behaviour can be modeled identically to one of a regular spring. The force of a spring is calculated according to the Hooke's law,

$$F = k\,x \tag{3.19}$$

Where k is the constant of spring and x represents the deflection on the spring. Energy is given by,

$$E = \int F\,dx = \frac{kx^2}{2} \tag{3.20}$$

For the application on the landing gear, x will represent the required deflection. The spring constant requires further calculation and will depend on the tire and the leg.

The spring constant of the tire (k_{wheel}) may be given or obtained by applying a certain load to the tire and measuring the respective deflection.

For the leg of the landing gear, some approximations will be required. The leg will be approached as a regular beam with a rectangular cross section.

The shape will also be slightly altered for this approximation, explained in figure 3.15, to allow for cantilever beam equations to be applied.

Figure 3.15: First approximation of beam shape for cantilever beam equations

Since the strictly vertical portion of the beam can be disregarded for the analysis of a vertical force being applied to the beam's tip, the analysis can be further simplified. Finally, the beam is represented by the figure 3.16.

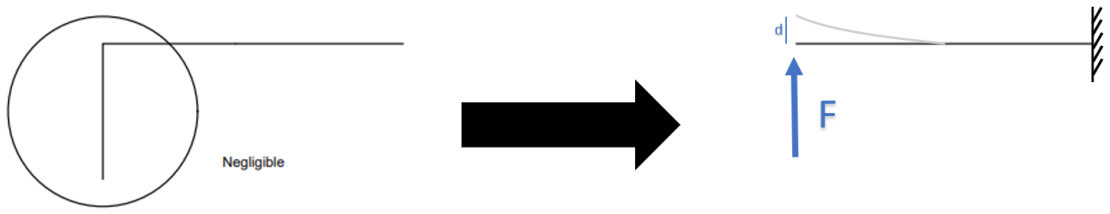

Figure 3.16: Schematic representation of the cantilever beam approximation

For the given beam, max deflection is obtained by,

$$d_{Max} = \frac{FL^3}{3EI} \tag{3.21}$$

Where L is the length of the beam, here the longitudinal distance from the attachment point of the landing gear with the fuselage and the contact point of the wheel with the ground; E is the elasticity modulus of the material; I is the moment of inertia.

For a rectangular section, I is,

$$I = \frac{a^3 b}{12} \tag{3.22}$$

From equation 3.21, the spring constant is given by,

$$k_{leg} = \frac{F}{d_{Max}} = \frac{3EI}{L} \tag{3.23}$$

The main gear's spring configuration can be explained schematically in figure 3.17 with the springs arranged in series. Than, the spring constant on the main gear is,

$$k_{MLG} = 2\left(\frac{k_{wheel}k_{leg}}{k_{wheel}+k_{leg}}\right) \tag{3.24}$$

And equation 3.18 can be written as,

$$\frac{mV^2}{2} + mg(1-L)d = \frac{k_{MLG}d^2}{2} \tag{3.25}$$

3.2.2.2 Nose landing gear

For the nose landing gear, the most demanding touchdown situation is the level landing with inclined reactions (3.14 a)). In this case, it is a 3 point landing so it becomes less challenging for the main gear.

Regarding the equation of energy conservation to obtain the deflection required for this nose landing gear, it is very similar to the one in section 3.2.2.1. However, since the weight of the

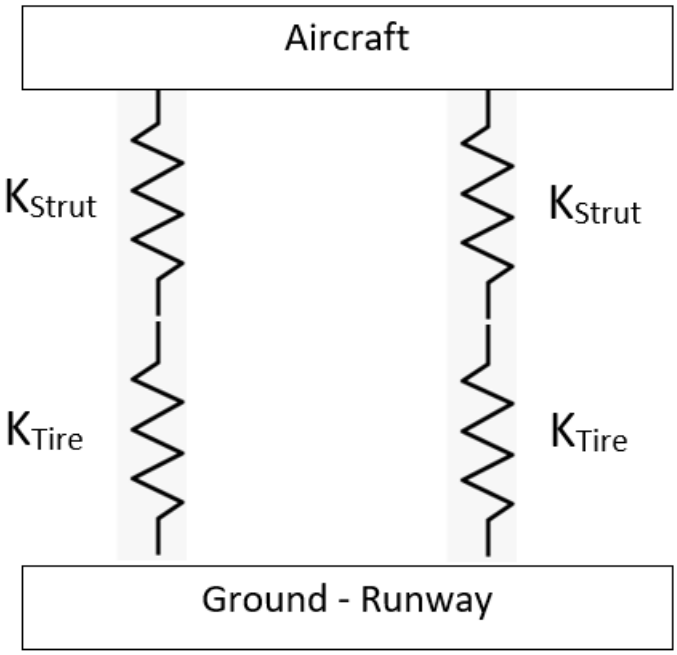

Figure 3.17: Schematic representation of the springs representing each side of strut and tire

aircraft is now distributed along the entire landing gear, only the percentage of weight acting on the nose gear is considered.

Besides this, since the nose gear is composed of only one beam instead of two symmetrical ones, the spring constant is now,

$$k_{NLG} = \frac{k_{wheel} k_{leg}}{k_{wheel} + k_{leg}} \tag{3.26}$$

Note: This relation implies that the landing gear only has vertical deflection. In reality, horizontal deflection is also present. Since STANAG legislation accounts for total deflection on force calculation, further iteration will be made before selecting wheel factor and correspondent reaction force on landing configurations.

3.2.3 Ground Loads on the Landing Gear

The landing gear force matrix consists of three components: a vertical force, drag force, and side force. For the calculation of the magnitude of these loads two methods can be used: regulatory or rational analysis. The regulatory loads comprise a standard style calculation, based on legislation and norms, that is designed to be very conservative. It saves a lot of analysis time required to accurately perform a rational approach.

As mentioned in section 2.7.1, all the operational loads must be obtained at the worst possible situation, so the maximum design weight is always the weight considered for the aircraft even though we are considering a landing situation. This makes sense because this primary structure must be able to sustain the UAV at any and every condition without creating any safety issues. This includes the remote possibility of a UAV having to land right after takeoff so, approximately, at maximum weight.

The standard tabulates the loads involved for the different landing gear sections and possible landing situations [57].

3.2.3.1 Main gear

As it was mentioned in chapter 3.2.2.1, the most challenging situation for the main landing gear is the tail-down landing.

For the tail-down landing condition, the aircraft is assumed to be in a tail down attitude with the main landing gear contacting the surface before the nose landing gear. Here, the ground reaction only has a vertical component. This is because it is assumed that the main landing gear wheels are up to speed before the vertical load reaches its maximum value. Therefore, a moment imbalance is created which is cancelled by introducing an inertial moment with the opposite direction of said imbalance [48].

Considering that the sum of all the vertical forces involved at the landing impact equal to zero, the reaction force on the main landing gear will be equal to the total load on the Center of Gravity of the UAV.

$$F_a = V_m = n_j * W \tag{3.27}$$

So that n_j is the load factor on wheels, W is the design landing weight and F_a the total load on the CG because of the weight (in this condition only vertical component).

According to annex B of the NATO legislation n_j equals to:

$$n_j = n - L \tag{3.28}$$

Where n is the actual load factor.

Substituting equation 3.28 in 3.27, the main wheel loads are given by:

$$V_m = (n - L) * W \tag{3.29}$$

Where V_m is the vertical component (and only component in this case) of the reaction created on the main landing gear. If the wanted value is referent to only one wheel this expression should be divided by 2.

Actually, for a level landing condition with the main gear having a first contact with the runway while the nose gear is just clear of the ground, the value for the vertical component of the reaction in the main landing gear maintains the same. In this case, the main gear also has to support the

entire weight of the aircraft initially. The same imbalance moment is created due to the way the aircraft lands but it is also canceled with the introduction of an inertial moment with opposite direction.

However, for this latter situation a drag component for the landing gear force matrix is introduced. The magnitude of this drag component is given by the norms [57] and can be obtained with this equation:

$$D_m = K * n_j * W \tag{3.30}$$

Where K is the assumed drag coefficient between the wheel and the ground. For this calculations it is defined that this value should be equal to 0.25 [57].

Besides the different landing conditions that can induce stress on the main landing gear, other supplementary conditions must be mentioned in order to calculate the reactions in every possible scenario.

For the side load condition, the aircraft is assumed to be in a level attitude with only the main landing gear touching the runway. The shock absorbers and tires are considered to be in a static position [64].

Here, FAR 23 norms define the established vertical load factor is 1.34, which is divided by two when obtaining the ground reaction load for each of the main landing gear wheels, since the loads should be equal [64]. So, the limit vertical ground reaction acting on one wheel is:

$$V_m = 1.34 * \frac{W}{2} \tag{3.31}$$

The limit side load inertia factor is defined as 0.83, with the side ground reaction divided by the main wheels so that the inertia factor is 0.5 when acting inboard on one side of the main landing gear and 0.33 when acting outboard on the other side. So, the limit side ground reactions on the wheels are obtained by:

$$F_m^y = 0.5W(inboard) \tag{3.32}$$

$$F_m^y = 0.33W(outboard) \tag{3.33}$$

(If the vertical reaction is defined on the z axis and the reaction due to drag forces on the x axis, the side ground reactions must be applied on the y axis)

The side loads prescribed for this condition are assumed to be applied at the ground contact point and the drag loads can be assumed equal to zero.

Lastly, the landing gear must be designed in a way that it withstands a constant and steady application of brakes during taxiing operations [65]. This condition is called the braked roll condition.

Considering that the UAV is at a level attitude and that the shock absorbers and tires are in a static position, the loads acting on the main wheels are also given by legislation STANAG 4703.

The established vertical load factor will be the same as for the side load condition and equal to 0.67 for each wheel of the main section. On the other hand, for rearward forces, the load factor defined is 0.54 [57]. To obtain the forces that will affect the landing gear in each component, the safety factors must be multiplied by the total design weight of the aircraft.

3.2.3.2 Nose gear

For the nose landing gear a level landing with inclined reactions, as it was mentioned in section 3.2.2.2, the worst landing configuration is level landing with inclined reactions, figure 3.14 a). Resulting in the total weight being distributed through both the nose and main landing gears.

According to the norm, the forces in the nose landing gear are:

With this landing condition, the aircraft is assumed to be at a level attitude with both the nose and the main landing gear making contact with the runway at the same time [48].

Here the vertical reactions for both sections of the landing gear need to cancel the total weight of the aircraft:

$$V_n + V_m = V_a \tag{3.34}$$

With V_n being the vertical reaction of the nose landing gear, V_m the vertical reaction on the main landing gear and finally V_a the vertical load at the CG which, as it happens on the last chapter, is obtained by:

$$V_a = n_j * W \tag{3.35}$$

So that n_j is the load factor on wheels and W is the design landing weight.

Considering the sum of the moments at the nose landing gear equal to zero, it is possible to obtain the vertical reaction at the main landing gear:

$$V_m * d' = V_a * a' \tag{3.36}$$

$$V_m = F_a * \frac{a'}{d'} \tag{3.37}$$

In a same way, but, this time, having the sum of the moments on the main landing gear equal to zero, the vertical reaction at the nose landing gear can be obtained:

$$V_n * d' = F_a * b' \tag{3.38}$$

$$V_n = V_a * \frac{b'}{d'} \tag{3.39}$$

As in the previous example, the drag forces at the wheel (horizontal component of the force matrix on the landing gear) are obtained by multiplying the drag factor K for the vertical component, so:

$$D_m = K * F_a * \frac{a'}{d'} \tag{3.40}$$

$$D_n = K * F_a * \frac{b'}{d'} \tag{3.41}$$

With the same K being defined by the norm/legislation and equal to 0.25.

These results can be verified by:

$$F_m = \sqrt{V_m^2 + D_m^2} \tag{3.42}$$

$$F_n = \sqrt{V_n^2 + D_n^2} \tag{3.43}$$

$$F_m = \sqrt{\left(F_a * \frac{a'}{d'}\right)^2 + \left(K * F_a * \frac{a'}{d'}\right)^2} \tag{3.44}$$

$$F_n = \sqrt{\left(F_a * \frac{b'}{d'}\right)^2 + \left(K * F_a * \frac{b'}{d'}\right)^2} \tag{3.45}$$

Considering the relation between the total load on the Center of Gravity and the weight of the aircraft of equation 3.35:

$$F_m = \sqrt{\left(n_j * W * \frac{a'}{d'}\right)^2 + \left(K * n_j * W * \frac{a'}{d'}\right)^2} \tag{3.46}$$

$$F_n = \sqrt{\left(n_j * W * \frac{b'}{d'}\right)^2 + \left(K * n_j * W * \frac{b'}{d'}\right)^2} \tag{3.47}$$

So, utilizing equations 3.46 and 3.47 and considering that:

$$F_a = F_m + F_n \tag{3.48}$$

It can be defined that:

$$F_a = \sqrt{\left(n_j * W * \frac{a'}{d'}\right)^2 + \left(K * n_j * W * \frac{a'}{d'}\right)^2} + \sqrt{\left(n_j * W * \frac{b'}{d'}\right)^2 + \left(K * n_j * W * \frac{b'}{d'}\right)^2} \tag{3.49}$$

On another hand, it can be said that,

$$F_a = \sqrt{V_a^2 + D_a^2} \tag{3.50}$$

Assuming the constant K for drag force components and equation 3.35,

$$F_a = \sqrt{(n_j * W)^2 + (K n_j * W)^2} = \sqrt{(K^2+1)(n_j * W)^2} \tag{3.51}$$

Replacing in equation 3.49

$$\sqrt{(K^2+1)(n_j * W)^2} = \sqrt{\left(n_j * W * \frac{a'}{d'}\right)^2 (K^2+1)} + \sqrt{\left(n_j * W * \frac{b'}{d'}\right)^2 (K^2+1)} \tag{3.52}$$

$$n_j * W \sqrt{(K^2+1)} = n_j * W * \frac{a'}{d'} \sqrt{(K^2+1)} + n_j * W * \frac{b'}{d'} \sqrt{(K^2+1)} \tag{3.53}$$

$$nj * W = \frac{n_j * W * \frac{a'}{d'} \sqrt{K^2+1} * + n_j * W * \frac{b'}{d'} \sqrt{(K^2+1)}}{\sqrt{K^2+1}} \tag{3.54}$$

$$n_j * W = n_j * W * \frac{a'}{d'} + n_j * W * \frac{b'}{d'} \tag{3.55}$$

$$n_j * W = n_j * W * \left(\frac{a'}{d'} + \frac{b'}{d'}\right) \tag{3.56}$$

Noting that,

$$b' + a' = d' \tag{3.57}$$

$$\frac{b'}{d'} + \frac{a'}{d'} = 1 \tag{3.58}$$

Proving that, using equation 3.56,

$$n_j * W = n_j * W \tag{3.59}$$

So, it can be concluded that, for a level landing with inclined reactions, the vertical loading on the nose landing gear due to inertia forces can be represented by:

$$V_n = (n - L) * W * \frac{b'}{d'} \tag{3.60}$$

A drag component also needs to be considered in this level landing condition, so the magnitude of this component can be obtained by using the drag coefficient between wheels and the ground assumed prior. So, the drag component can be obtained by:

$$D_n = K * n_j * W * \frac{b'}{d'} \tag{3.61}$$

The load factor on the wheels is given in NATO legislation by,

$$n_j = \frac{h + \frac{d}{3}}{ef * d} \tag{3.62}$$

Where h is the drop height in inches (minimum of 9 inches), ef the efficiency of the landing gear, for leaf spring equal to 0.5 and d the deflection of the landing gear.

The table from NATO for forces involved in basic landing condition is presented in figure 3.18

Condition	Tail Wheel Type		Nose Wheel Type		
	Level Landing	Tail-down Landing	Level Landing with Inclined Reactions	Level Landing with Nose Wheel Just Clear of Ground	Tail-Down Landing
Vertical component at CG	nW	nW	nW	nW	nW
Fore and aft component at CG	KnW	0	KnW	KnW	0
Lateral component in either direction at CG	0	0	0	0	0
Shock absorber deflection (rubber or spring shock absorber), %	100 %	100 %	100 %	100 %	100 %
Tire deflection	Static	Static	Static	Static	Static
Main wheel loads (V_r)	(n-L)W	(n-L)Wb/d	(n–L)Wa'/d'	(n-L)W	(n-L)W
(both wheels) (D_r)	KnW	0	KnWa'/d'	KnW	0
Tail (nose) wheels (V_r)	0	(n-L)Wa/d	(n-L)W'/d'	0	0
Loads (D_r)	0	0	KnWb'/d'	0	0

Figure 3.18: Forces involved on basic landing conditions [58]

For level landing conditions, according to CS legislation, normative AMC VLA 479(b), spin-up and spring back conditions must also be analysed.

For spin-up condition the reaction on the z axis must be limited by 0.6 the maximum reaction in this axis and for the x axis limited to 0.5 the same force in the direction towards aft of the aircraft.

In spring back conditions the reaction on the z axis is limited by 0.8 the maximum reaction force, while towards forward of the aircraft, the limit for this reaction is 0.5 the max on the z axis.

Supplementary conditions for the nose wheel are also mentioned in UL.GL.6 of the STANAG 4703 NATO legislation. This can be divided in aft, side and forward loads. For all this situations, the static load must be considered for the combination of weight and CG that result in worst case scenario for the nose landing gear. The different situations are presented in figure 3.19.

Aft loads are all the loads acting on the aircraft that push it towards its tail direction. For this loads, the vertical force component on the nose landing gear must be lower than 2.25 times the static load on the wheel and the drag component as a maximum at 1.8 times the same static load.

Side loads are the same as considered for the side load condition for the main landing gear. These can happen, for example during a cross wind landing. With this situation, the vertical force component at the nose wheel cannot also be higher than 2.25 times the static load on the wheel and the side component has its maximum at 1.57 times the same static load.

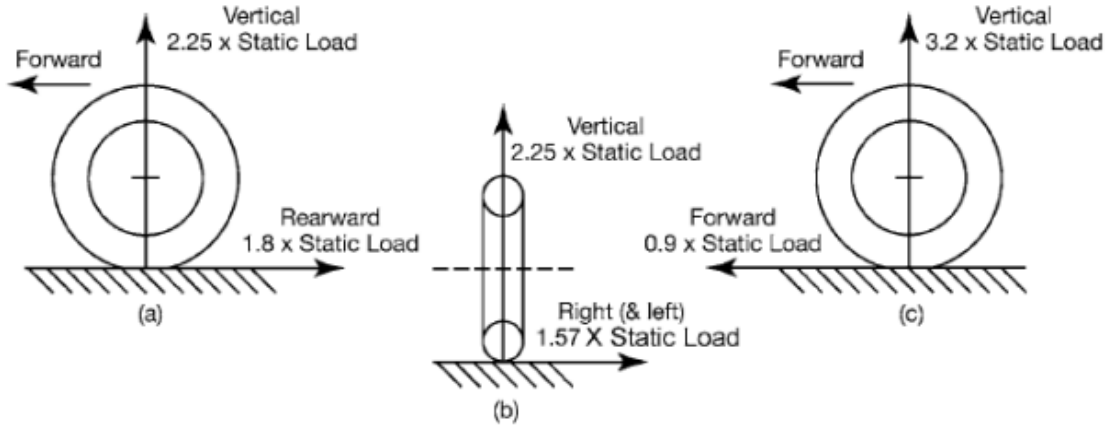

Figure 3.19: Supplementary conditions for nose wheel: a) aft load; b) side load; c)forward load [57]

Forward loads refer to any load that "pushes" the UAV towards its nose. With this type of forces, the vertical component at the nose landing gear has a limit of 3.2 times the static load on the wheel and the forward component sets it at 0.9 times the same static load.

3.2.3.3 Safety Factors

After determining the maximum operational loads, which in the case of the landing gear are presented for the aforementioned landing situations, the safety factor must also be considered.

The ultimate loads, loads at which the structure must not collapse, must be determined by multiplying the calculated values by a safety factor that is given by the UAV legislation, STANAG 4703, used in several topics so far.

As previously mentioned, the landing gear is considered a PSE because its failure can cause severe damage to the aircraft. For this category of structures, the safety factor specified in UL2.3 must be at least 1.5.

Moreover, it also specifies that this safety factor must be multiplied by a further special one, for several different cases. Besides most that are not relevant for this situation, the norm defines that if the structure is composed by composite materials, this special situation is triggered.

According to the legislation, in composite structure, if A or B material allowables are not statistically justified for hot and wet conditions, the following special factors should be used: a minimum of 1.2 for moisture conditioned specimen tested at maximum service temperature, assuming that a well-established manufacturing and proper quality control procedure is used; 1.5 or higher for specimen tested with no specific allowance for moisture and temperature.

A and B material allowables are also explained. "A" values are those that at least 99 percent of the total population of values are predicted to exceed with a 95 percent degree of confidence. Using the same level of confidence, "B" values are those for which at least 90 percent of the entire population will fall above.

This means that for "A" values only 1% of the material strength values are expected to be below the values presented, while for "B" values this criteria is expanded as it increases to 10%.

For the selection between each type of material allowable there is also a defined criteria according to UL9.2.

If the applied loads are ultimately distributed through a single component and its failure would result in the loss of structural integrity, the assured minimum design mechanical properties should be met by the "A" values. If the structures are redundant, the loads can be safely distributed to other components if a single element fails, they can be designed with only meeting "B" values for mechanical properties.

For the landing gear, "A" values should be used.

3.2.4 Rate of Descent

The rate of descent can also be called sink speed or touchdown rate. It represents the vertical speed of the aircraft before it touches the ground on landing. Derived from the CS legislation, specifically the normative CS-VLA 473, the value for this characteristic can be obtained by:

$$V_d = 0.51 * \left(\frac{W}{S}\right)^{\frac{1}{4}} \tag{3.63}$$

With W representing the total design weight of the aircraft and S the surface area of the wing in landing conditions. To be noticed that, according to CS-VLA legislation, this velocity must be comprehended in an interval between 2.13 m/s and 3.05 m/s [66].

3.2.5 Limit Drop Tests

As it was mentioned in section 2.7.2 drops tests must be made on the complete aircraft. If it is done on elements consisting of wheel, tyre and shock absorber, a proper relation must be used. The minimum free drop height is given by normative CS-VLA 725 and can be calculated by the formula:

$$h = 0.0132 * \left(m * \frac{g}{S}\right)^{\frac{1}{2}} \tag{3.64}$$

This value, however, cannot be less than 0.235 m and should not surpass the limit of 0.475 m according to this legislation. Via the STANAG norms, the minimum value for h is 0.229 m.

If wing lift is provided for in drop tests, the effective weight to be used when dropping the landing gear needs to be adjusted and is dependent on the specified free drop height, the deflection of the tyre on impact, wing-lift ratio and the total design mass.

3.3 Theoretical models for Curved Beams

Choosing leaf spring struts as the leg type for the landing gears enables the approximation to structures comprised of straight and curved beams. In order to perform calculations regarding

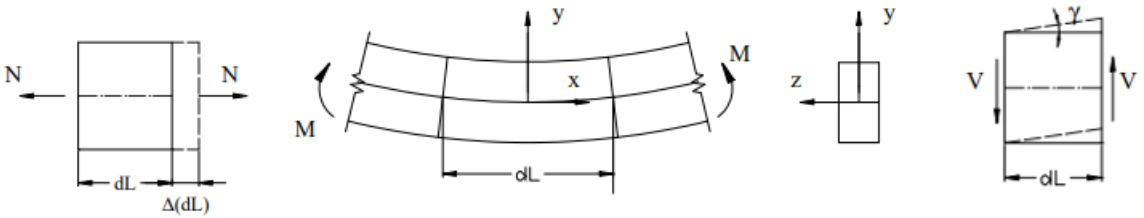

Figure 3.20: The 3 components of solicitation: on the left, traction; at the middle, flexure; on the right, shear [67]

displacements and stresses on the landing gears, these structures are viewed as linear element associations with rigid connections that permit the transmission of moments. Typically, these structures are referred to as reticulated structures. Consequently, it is possible to apply theoretical models for curved and straight beams.

The Castigliano theorem simplifies the analysis and approach for calculating the vertical and horizontal displacements of the beams. This procedure requires the determination of the internal variation of energy, or strain energy. For these structures, the internal stresses can be used to calculate strain energy.

3.3.1 Vertical and Horizontal displacements

3.3.1.1 Strain Energy

The loads that will be applied to the landing gear will generate internal axial and transverse forces and bending moments. Therefore, there will be three distinct strain energy components.

Strain energy can typically be calculated for a continuous structure using the stress tensor and strain tensor. For a linear strategy, we have:

$$U = \int w_0 \, dv \tag{3.65}$$

Where

$$w_0 = \frac{1}{2}\left(\sigma_x\varepsilon_x + \sigma_y\varepsilon_y + \sigma_z\varepsilon_z + \tau_{xy}\gamma_{xy} + \tau_{xz}\gamma_{xz} + \tau_{yz}\gamma_{yz}\right) \tag{3.66}$$

The 3 components that create strain energy in this situation are represented in figure 3.20 for a beam with a rectangular section. These are axial and transverse forces and bending moment.

For a section with length dL, an area A and subjected to an axial nominal force N, such as in figure 3.20, left, the normal stress and axial strain will be, respectively

$$\sigma_x = \frac{N}{A} \; ; \; \varepsilon_x = \frac{N}{EA}$$

Substituting in (3.65) (having dV = dA*dL)

$$U = \frac{1}{2}\int_L \int_A \frac{N^2}{EA^2} \cdot dAdL \tag{3.67}$$

Since the area is constant along the beam

$$U = \frac{1}{2}\int_L \frac{N^2}{EA} \cdot dL \tag{3.68}$$

The internal energy stored in an element dL is

$$dU = \frac{1}{2}\frac{N^2 \cdot dL}{EA} \tag{3.69}$$

For the same section subjected to a bending moment M, represented in figure 3.20, middle, at a certain point with vertical coordinate y, the normal stress and axial strain will be, respectively [67],

$$\sigma_x = \frac{M \cdot y}{I_z} \; ; \; \varepsilon_x = \frac{M \cdot y}{EI_z}$$

Substituting on the same equation (3.65), the strain energy on a certain segment dL

$$U = \frac{1}{2}\int_L \int_A \frac{M^2 y^2}{EI_z^2} \cdot dAdL \tag{3.70}$$

Knowing that I_z can be given by $I_z = \int_A y^2$ dA, the latter equation comes

$$U = \frac{1}{2}\int_L \frac{M^2}{EI_z} \cdot dL \tag{3.71}$$

The internal energy stored in an element dL is

$$dU = \frac{1}{2}\frac{M^2 \cdot dL}{EI_z} \tag{3.72}$$

For the transverse force, situation seen on figure 3.20, right, a shear stress (τ_{xy}) and strain (γ_{xy}) will be created on the section, given by τ and $\frac{\tau}{G}$, respectively. Substituting in (3.65), the strain energy is

$$U = \frac{1}{2}\int_L \int_A \frac{\tau^2}{G} \cdot dAdL \tag{3.73}$$

Where τ is the shear stress and G is the shear modulus. The shear stress is not constant along the section. For a rectangular section, with $dA = b \cdot dy$ and d being the dimension of the section on the yy axis

$$\tau = \frac{V}{2I_z}\left(\frac{d^2}{4} - y^2\right) \tag{3.74}$$

With V being the transversal force. Substituting in (3.73)

$$U = \frac{1}{2}\int_L \frac{V^2}{4GI_z}\cdot\left[\int_{-\frac{d}{2}}^{\frac{d}{2}}\left(\frac{d^2}{4}-y^2\right)b\cdot dy\right]dL \tag{3.75}$$

$$U = \frac{1}{2}\int_L \frac{CV^2}{GA}\cdot dL \tag{3.76}$$

Considering a correction form factor C for the total area of the section. This value considers the relation between the shear area and the total real area of the section. Shear area is defined as the area of the section that effectively resists shear deformation [68].

According to different references the value for the form factor can differentiate but it can be used that, for a rectangular section, A_r = A/1.2. So, using the shear area represented by A_r on equation (3.76)

$$U = \frac{1}{2}\int_L \frac{V^2}{GA_r}\cdot dL \tag{3.77}$$

The internal energy stored in an element dL is

$$dU = \frac{1}{2}\frac{V^2 dL}{GA_r} \tag{3.78}$$

Therefore, the total strain energy in obtained combining equations (3.68), (3.71) and (3.77)

$$U = \frac{1}{2}\left(\int_L \frac{N^2}{EA}\cdot dL + \int_L \frac{M^2}{EI_z}\cdot dL + \int_L \frac{V^2}{GA_r}\cdot dL\right) \tag{3.79}$$

This equation represents the total strain energy for a straight beam with a total length L.

For a curved beam with the centerline being half of a circle, as in figure 3.21,

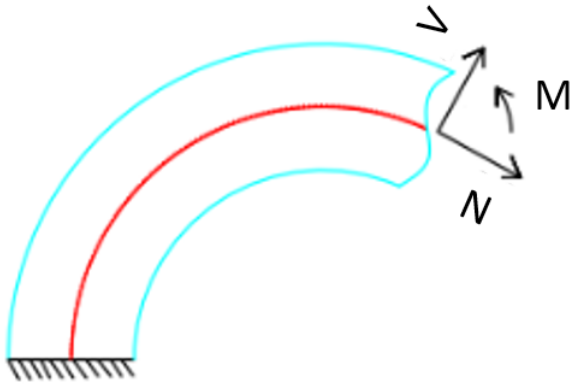

Figure 3.21: Curved beam with a circle as its centerline

$$dL = Rd\theta \tag{3.80}$$

With R representing the radius of the circle and $d\theta$ the variation of angle that any point along the curved beam does with the horizontal axis.

Replacing on equation (3.79), the total strain for a curved beam with half of a circle as its centerline is given by

$$U = \frac{1}{2}\left(\int_\theta \frac{N^2R}{EA}\cdot d\theta + \int_\theta \frac{M^2R}{EI_z}\cdot d\theta + \int_\theta \frac{V^2R}{GA_r}\cdot d\theta\right) \tag{3.81}$$

If the situation represents a curved beam with the centerline being half an ellipse, like the situation on figure 3.22.

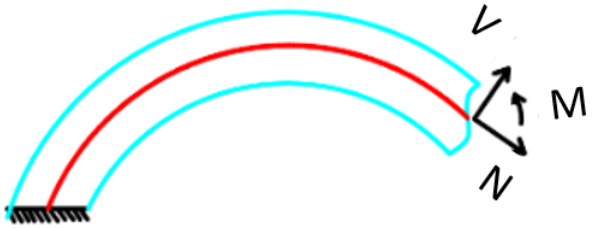

Figure 3.22: Curved beam with an ellipse as centerline

The governing equation of an ellipse is [69]

$$\frac{x^2}{a^2} + \frac{y^2}{b^2} = 1 \tag{3.82}$$

Converting to a parametric form

$$x = acos(\theta)\ ;\ y = bsin(\theta) \tag{3.83}$$

The surface integral is given by [69]

$$S = \int_\theta \sqrt{\left[\frac{\partial x}{\partial \theta}\right]^2 + \left[\frac{\partial y}{\partial \theta}\right]^2}\, d\theta \tag{3.84}$$

Using the parametric equations from (3.83) ,the infinitesimal arc length on the ellipse, dS is then given by

$$ds = \sqrt{a^2sin^2(\theta) + b^2cos^2(\theta)}d\theta \tag{3.85}$$

$$ds = a\sqrt{1 - cos^2(\theta) + \frac{b^2}{a^2}cos^2(\theta)}d\theta = a\sqrt{1 - cos^2(\theta)\left(1 - \frac{b2}{a^2}\right)}d\theta \tag{3.86}$$

With the infinitesimal part now as a function of θ, one can replace dL on equation 3.79 for dS in a same way that was performed for the curved beam with half a circle as its centerline.

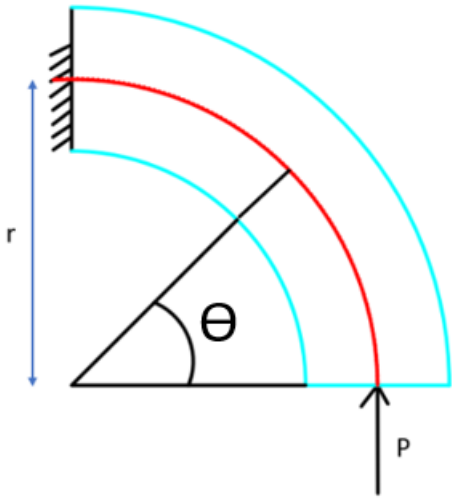

Figure 3.23: Vertical Force acting on a curved beam with a quarter of a circle as its centerline

Therefore, the strain energy for a curved beam with half an ellipse as its centerline is given by

$$U = \frac{1}{2}\left(\int_L \frac{N^2 K}{EA}\cdot d\theta + \int_L \frac{M^2 K}{EI_z}\cdot d\theta + \int_L \frac{V^2 K}{GA_r}\cdot d\theta\right) \tag{3.87}$$

With K = dS

3.3.1.2 Castigliano´s Theorem

In order to calculate both the vertical and horizontal displacements on the beams, the Castigliano's theorem may be used.

This theorem says that: "in a structure with an elastic linear behaviour, the derivative of the strain energy in order to a certain load P_i, is equal to the displacement on the point of application of that same load, on its direction and orientation."

$$\frac{\partial U}{\partial P_i} = d_i \tag{3.88}$$

Taking as an example a curved beam with its centerline being half of a circle of radius R with a load P acting vertically and up on one end of the beam, while the other one is recessed.

To calculate the **vertical displacement** of the point of application of this load, the derivative of the strain energy in order to the load P must be obtained.

The internal loads for this situation, taking figure 3.23 as the representation of the problem, are given by:

$$N = -P\cdot cos(\theta)$$

$$V = P\cdot cos(\pi-\theta) = -P\cdot sin(\theta)$$

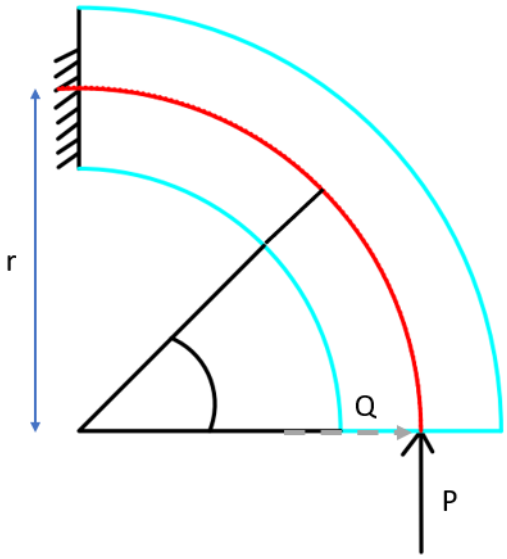

Figure 3.24: Vertical Force and Fictional Horizontal Force acting on a curved beam with a quarter of a circle as its centerline

$$M = P \cdot R(1 - cos(\theta))$$

So, using equation 3.81, of the strain energy for this curved beam when P is applied, and calculating via the Castigliano´s theorem

$$\delta_v = \frac{\delta U}{\delta P} = \frac{1}{2}\left(\frac{R}{EA}\int_0^{\pi}\frac{\delta P^2 cos^2(\theta)}{\delta P}\cdot d\theta + \frac{R}{EI_z}\int_0^{\pi}\frac{\delta P^2 R^2(1-cos(\theta))^2}{\delta P}\cdot d\theta + \frac{R}{GA_r}\int_0^{\pi}\frac{\delta P^2 sin^2(\theta)}{\delta P}\cdot d\theta\right) \tag{3.89}$$

$$\delta_v = \frac{RP}{EA}\int_0^{\pi} cos^2(\theta)\cdot d\theta + \frac{R^3P}{EI_z}\int_0^{\pi} P(1-cos(\theta))^2\cdot d\theta + \frac{RP}{GA_r}\int_0^{\pi} sin^2(\theta)\cdot d\theta \tag{3.90}$$

Solving the integrals,

$$\delta_v = \frac{RP\pi}{2EA} + \frac{3R^3P\pi}{2EI_z} + \frac{RP\pi}{2GA_r} \tag{3.91}$$

If it can be considered that R/h, h being the height of the rectangular section, is very high, two terms can be dismissed and the vertical displacement is given by

$$\delta_v = \frac{3R^3P\pi}{2EI_z} \tag{3.92}$$

For the **horizontal displacement** originated from the same load P, a new fictional load Q must be created with an horizontal orientation. The situation is represented in figure 3.24.

Taking into consideration only the term of energy strain performed by the bending moment, M is now given by

$$M = P \cdot R(1 - cos(\theta)) + QR \cdot sin(\theta)$$

Returning to the Castigliano's theorem 3.88, the horizontal displacement for the node where the loads are applied is given by

$$\delta_h = \frac{\partial U}{\partial Q} \tag{3.93}$$

Using the equation for strain energy 3.81, again dismissing the terms given by the axial and shear stresses, the latter one referring the bending moment comes

$$\delta_h = \frac{R}{2EI_z} \int_0^\pi \frac{\partial M^2}{\partial Q} d\theta \tag{3.94}$$

Note:

$$\frac{\partial M^2}{\partial Q} = \frac{\partial (MM)}{\partial Q} = \frac{M \partial M}{\partial Q} + \frac{\partial MM}{\partial Q} = \frac{2M \partial M}{\partial Q}$$

Substituting on equation (3.94)

$$\delta_h = \frac{R}{EI_z} \int_0^\pi \frac{M \partial M}{\partial Q} d\theta \tag{3.95}$$

Using the relation obtained for the bending moment

$$\delta_h = \frac{R}{EI_z} \int_0^\pi (PR(1 - cos(\theta)) + QR \cdot sin(\theta)) Rsin(\theta) d\theta \tag{3.96}$$

$$\delta_h = \frac{R^3}{EI_z} \int_0^\pi (P(1 - cos(\theta)) + Q \cdot sin(\theta)) sin(\theta) d\theta \tag{3.97}$$

Since Q is a fictional load that was only added so that the Castigliano's theorem could be used, it can now be equalled to 0, so

$$\delta_h = \frac{PR^3}{EI_z} \int_0^\pi (1 - cos(\theta)) sin(\theta) d\theta \tag{3.98}$$

$$\delta_h = 2\frac{PR^3}{EI_z} \tag{3.99}$$

Curved Beam - Centerline quarter ellipse

For a closer example to the landing gear the displacements must be calculated on a curved beam with centerline a quarter of an ellipse. For the configuration on figure 3.25 , the horizontal dimension of the ellipse is smaller than the vertical one. The new parametric equations are,

$$x = bcos\theta \; ; \; y = asen\theta \tag{3.100}$$

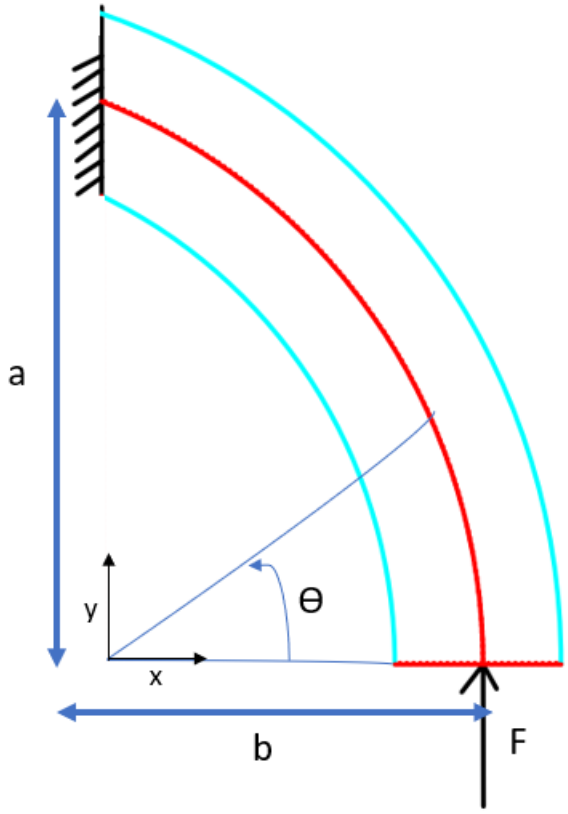

Figure 3.25: Vertical Force acting on a curved beam with a quarter of an ellipse as its centerline

The infinitesimal arc length is given by,

$$ds = \sqrt{a^2cos^2\theta + b^2sen^2\theta}ds = a\sqrt{(1 - sen^2\theta \left(1 - \frac{b^2}{a^2}\right)} \tag{3.101}$$

Where the eccentricity e is,

$$e = \sqrt{1 - \left(\frac{b}{a}\right)^2} \tag{3.102}$$

Remembering equation 3.71 and replacing $dx = ds$,

$$dU_3 = \frac{M^2 \, a \, \sqrt{1 - e^2sin^2(\theta)}}{2E \, I_z} \, d\theta \tag{3.103}$$

For the vertical displacement, equation 3.89,

$$\delta_v = \frac{a}{2EI_z}\int_0^{\pi/2} \frac{\delta M^2 \sqrt{1-e^2 sin^2(\theta)}}{\delta P}\, d\theta \tag{3.104}$$

From the note in section 3.3.1.2, $\frac{\delta M^2}{\delta P} = \frac{2M\delta M}{\delta P}$

$$\delta_v = \frac{a}{2EI_z}\int_0^{\pi/2} \frac{2M\delta M}{\delta P}\sqrt{1-e^2 sin^2(\theta)}\, d\theta \tag{3.105}$$

And for this configuration the moment generated by a vertical force P is,

$$M = P(b - bcos\theta) \tag{3.106}$$

So replacing in 3.105,

$$\delta_v = \frac{Pab^2}{EI_z}\int_0^{\pi/2} (1-cos\theta)^2 \sqrt{1-e^2 sin^2(\theta)}\, d\theta \tag{3.107}$$

For the horizontal displacement, the virtual force Q is introduced on the horizontal axis. With this, the moment is now given by,

$$M = P(b - bcos(\theta)) + Q\, asin(\theta) \tag{3.108}$$

The horizontal displacement,

$$\delta_h = \frac{a}{2EI_z}\int_0^{\pi/2} \frac{2M\delta M \sqrt{1-e^2 sin^2(\theta)}}{\delta Q}\, d\theta \tag{3.109}$$

$$\delta_h = \frac{a}{EI_z}\int_0^{\pi/2} [P(b - bcos(\theta)) + Q\, asin(\theta)] * asin(\theta) \sqrt{1-e^2 sin^2(\theta)}\, d\theta \tag{3.110}$$

And knowing that $Q = 0$,

$$\delta_h = \frac{Pba^2}{EI_z}\int_0^{\pi/2} sin(\theta) * (1-cos(\theta)) \sqrt{1-e^2 sin^2(\theta)}\, d\theta \tag{3.111}$$

3.3.2 Bending stresses along the beams

For a straight beam loaded only in bending, pure bending, tensile stresses can easily be calculated for any point of a section by

$$\sigma = \frac{My}{I} \tag{3.112}$$

With M being the bending moment acting on the beam, y the distance from the neutral axis to the point where the stress is being calculated and I the moment of inertia of the cross section with respect to the neutral axis.

This equation can be applied with certain limitations:

- The beam must be initially straight and loaded on a plain of symmetry;
- Material must be homogeneous and the elastic range cannot be surpassed;
- The section where the distribution of stress is being calculated cannot be located too close to significant stress raisers, zones of stress concentration, or to regions where external loads are applied

For this straight beams, if the neutral bending axis and the centroidal axis of the section are on the center of the beam, the maximum compressing and traction stresses are the same. However, if the CG of the section is not located in the middle of the beam, the maximum values will differ.

However, for curved beams, the usual equations for straight beams only work as approximations and are not reliable to calculate the distribution of stress in any section. Along the length of a curved beam, there is the shortest path, on the inside surface. Considering relative stiffness, it suggests that the stresses along this inside surface are greater than the values obtained by the straight beam equations.

Therefore, there is the need to approach this problem in a different way for curved beams. In order to obtain a new equation, some considerations are needed to be taken:

- The centerline of the beam is a plane curve;
- There must be at least an axis of symmetry of the cross section;
- The forces acting on the beam must be in the plane of symmetry;
- Bending also takes place in the plane of symmetry;
- The cross sections originally plane and normal to the centerline shall remain the same way after bending

For a part of a curved beam represented in figure 3.26 With M being the bending moment applied on the beam, dφ is the angle between to sections of the beam ab and cd, δdφ is the rotation caused by moment M on section cd. As for as coordinates, y is the distance between the fibers where the stress is being calculated and the axis that crosses the CG of the section, e the distance between the neutral axis and the CG and r the curvature radius on the centers of gravity.

Here, the strain is given by

$$\varepsilon = \frac{(y-e)\Delta d\varphi}{(r-y)d\varphi} \tag{3.113}$$

Since $\sigma = E\varepsilon$

$$\sigma = \frac{E(y-e)\Delta d\varphi}{(r-y)d\varphi} \tag{3.114}$$

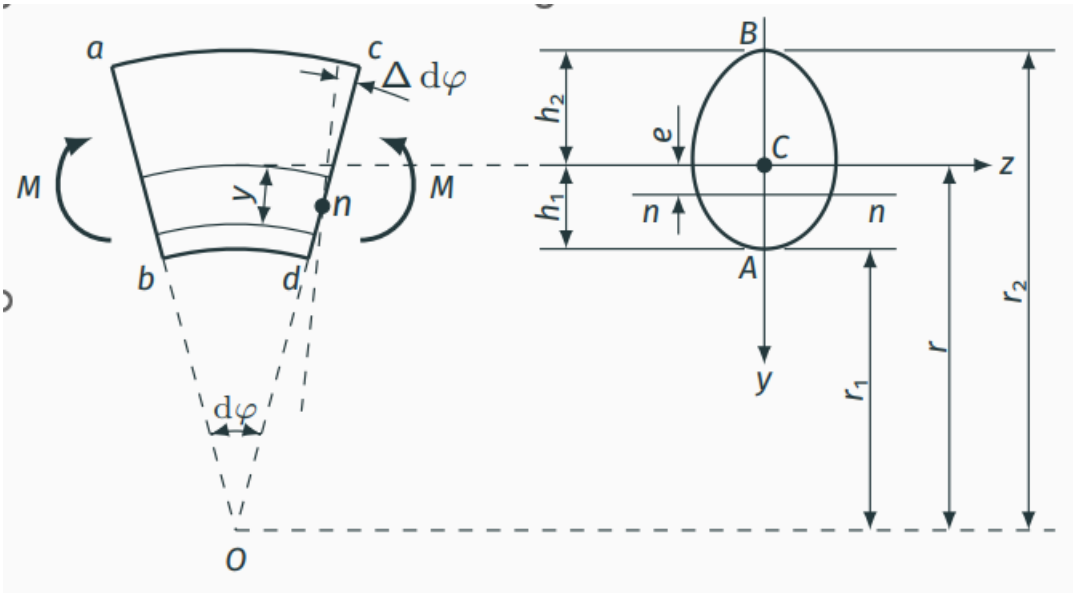

Figure 3.26: Curved beam and cross section on pure bending [70]

With the equation containing two unknown variables e and $\delta \mathrm{d}\varphi$. In order to calculate their value, static equations are used: normal forces distributed in the section equal to zero and the moment created by these forces equal to the applied bending moment

$$\int_A \sigma dA = \int_A \frac{E(y-e)\Delta d\varphi}{(r-y)d\varphi} dA = 0 \tag{3.115}$$

$$\int_A \sigma y dA = \int_A \frac{E(y-e)y\Delta d\varphi}{(r-y)d\varphi} dA = M \tag{3.116}$$

From equation (3.115)

$$\int_A \frac{(y-e)dA}{(r-y)} = 0 \equiv \int_A \frac{ydA}{(r-y)} - e\int_A \frac{dA}{(r-y)} = 0 \tag{3.117}$$

Where, the first term, can be simplified to an area mA with m being a value that relates to each particular shape of the section.

$$\int_A \frac{ydA}{(r-y)} = mA \tag{3.118}$$

The second term can also be manipulated using this relation

$$e\int_A \frac{dA}{(r-y)} \equiv e\int_A \frac{r}{r(r-y)} dA \equiv e\int_A \frac{y+r-y}{r(r-y)} dA = e\left(\frac{mA}{r} + \frac{A}{r}\right) = e\left((m+1)\frac{A}{r}\right) \tag{3.119}$$

Replacing on equation (3.117)

$$mA - e\left((m+1)\frac{A}{r}\right) = 0 \tag{3.120}$$

So, the relation between m and e can be obtained

$$e = \frac{mr}{m+1} \tag{3.121}$$

Now using the relation obtained in (3.118) on equation (3.116)

$$\int_A \frac{y^2}{r-y}dA = -\int_A \left(y - \frac{ry}{r-y}\right)dA = -\int_A ydA + r\int_A \frac{ydA}{(r-y)} = +mrA \tag{3.122}$$

$$\int_A \frac{ey}{r-y}dA = e\int_A \frac{y}{r-y}dA = emA \tag{3.123}$$

Replacing on the equation

$$\frac{E\Delta d\varphi}{d\varphi}(mrA - emA) = M \tag{3.124}$$

$$\frac{E\Delta d\varphi}{d\varphi} = \frac{M}{mA(r-e)} = \frac{M}{Ae} \quad ; \quad \textit{via relation } (3.118) \tag{3.125}$$

Finally, going back to equation (3.114)

$$\sigma = \frac{M(y-e)}{Ae(r-y)} \tag{3.126}$$

For the maximum values of stress, the value of y can be equal to the distance from the CG of the section to the maximum outer radius in both directions. With the example from figure 3.23, the outside part of the beam will be in compression while the concave side will suffer traction. So the maximum values are

$$\sigma_a = \frac{M(h_1-e)}{Aer_1} \; ; \; \sigma_b = -\frac{M(h_2+e)}{Aer_2} \tag{3.127}$$

The distances used for y and r can also be related to the neutral axis, instead of the axis that intercepts the CG. That way, with y' being the distance from the neutral axis to the point where the stress is being calculated and r' the radius of the neutral axis on the section

$$\sigma = \frac{My'}{Ae(r'-y')} \tag{3.128}$$

For the particular case of a curved beam with a rectangular section, the value e can be obtained. Considering the section in figure 3.27 and recapitulating the modified area relation given on (3.118, the analytical solution will be given by

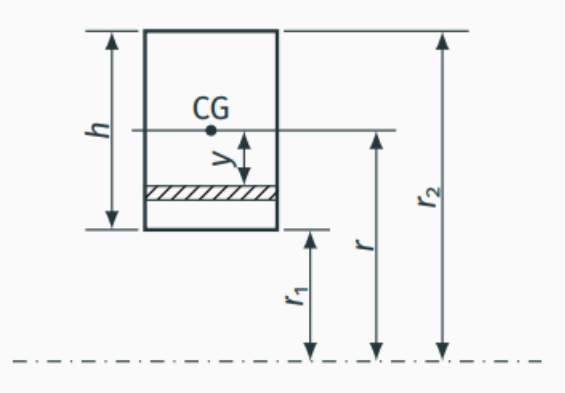

Figure 3.27: Rectangular section of a curved beam [70]

$$mA = \int_{-\frac{h}{2}}^{\frac{h}{2}} \frac{by}{(r-y)} dA = br \ln \frac{r_2}{r_1} - bh \tag{3.129}$$

Given the relation for e from (3.121),

$$e = r - \frac{h}{\ln \frac{r_2}{r_1}} \tag{3.130}$$

Another simpler way to obtain the bending stresses on curve beams is by multiplying the equation used for a straight beam by a certain factor K, different for different sections, that takes into consideration the geometry and works as a concentration of stress factor. This expression would be

$$\sigma = K_t \frac{My}{I} \tag{3.131}$$

With the factor obtained via tables or graphics such as the one on figure 3.28

3.4 Selection of the Composite Material

3.4.1 Main criteria for material selection

For the selection of the final material of the landing gear, several options must be analyzed and compared regarding criteria that must be considered for the proper functioning of a landing gear and regarding the unique application of the drone where it will be applied. A compromise must be met because there is no perfect material that will fulfill every requirement in an optimal manner.

The main criterion is the mechanical properties. The landing gear is supposed to have high strength, impact and fatigue resistance. However, as it is explained on the functional requirements, some deflection of the landing gear is required in order to absorb the energy on impact. Besides these, several other criteria must also be met:

- Fire resistance;

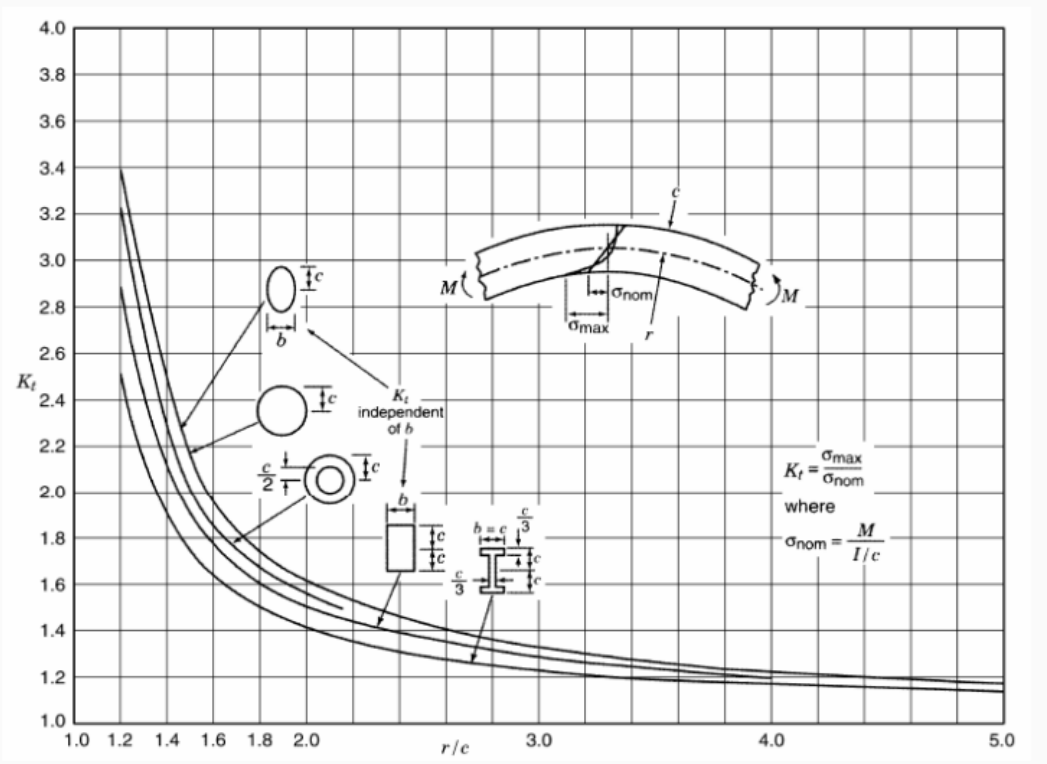

Figure 3.28: Stress concentration factors for a curved beam in bending for different sections [71]

- Humidity resistance;
- Low price;
- Low weight;
- Resistant to corrosion;
- Easy to manufacture;
- Some design flexibility.

3.4.2 Composites vs Metals

As it was already introduced in section 2.5, in aircraft manufacturing, more specifically, in the development of a landing gear, many diverse types of materials can be used varying from metals to composites.

First, it must be decided if the main material for the landing is a composite or a metal. For that decision, the advantages and disadvantages regarding each one must be analyzed.

According to Gay and F. Smith, composite materials have several remarkable characteristics [72]:

- Extremely low density;

- Mostly optimal mechanical properties;
- Do not yield, so their elastic limits correspond to the rupture limit of the material;
- Relative high fatigue resistance;
- Not sensible to common chemicals used in engines, such as grease, oils, etc;
- Excellent fire resistance but the smokes emitted from certain matrices can be toxic so they must be considered;
- Not corrosive, although in the case of contact between aluminum with carbon fibers a galvanic phenomenon creates rapid corrosion.

However, they also offer some less desired traits such as [72]:

- Medium to low level impact resistance, compared with metals;
- Aging subject to humidity and heat;
- Some paint cleaners attack epoxy matrices;
- Lack of experience.

Following these aspects and taking into account the main criteria regarding the selection of the material, this research will proceed focusing on a composite based landing gear. Nonetheless, the mentioned disadvantages cannot be overlooked, and measures will be taken to mitigate these negative effects.

The impact resistance must be increased so, for the final material, the selection of the reinforcement shall be targeting fibers that above the average for composite materials regarding this characteristic. In order to slow down the aging of the material due to humidity and heat, an ablative outside layer will also be composing the final landing gear [72]. Finally, if an epoxy matrix is selected, the paint cleaners that can attack this material shall not be used. The possible problem with corrosion aluminum-carbon fiber is not considered, since the entire drone is made of carbon fiber composite.

The most used composite materials in landing gear construction are Carbon Fiber or Glass Fiber with an Epoxy Resin [73].

3.4.3 General Characteristics and Properties of Composites

Composite material has been introduced in almost every area of engineering in some way and its use has only been recently increasing. This term refers to a material having strong fibers, which can be continuous or non-continuous, impregnated in a weaker matrix material. This second phase of the composite is responsible to achieve proper distribution of the fibers and it transmits loads between the different layers [73].

In aircrafts, the paradigm is the same since a large variety of composites has been implemented in several parts of this industry, as it was briefly mentioned in chapter 2.3. To assure the integrity of the structure these components are, not only, used in PSE components, whose integrity, as it was already explained, is vital for the aircraft to function properly, as is the case of landing gear, but also on control components such as the ailerons, for exterior components like the fairings and for several interior components [72].

The bonding between fibers and matrix is created during the manufacturing process and this stage is of great importance since it will have direct impact on the final mechanical properties.

3.4.3.1 Matrix

The matrix can be polymeric. either a thermoplastics or a thermoset; ceramic, since silicon carbide and carbon can be used as the matrix of a composite material; or metallic when mentioning aluminum or titanium alloys.

The most used types of matrices for composites applied to aircrafts are of polymeric nature [72].

In table 3.3, there is an approach to the characteristics of the two main types of polymeric matrix, therefore comparing thermoplastic resins characteristics with thermoset ones.

Table 3.3: Characteristics and differences between Thermoplastic and Thermoset resins [74] [75] [76]

Thermoplastics	**Thermosets**
Some have good adherence to metals	Easier to combine with fibers – low viscosity
Corrosion resistant	Corrosion resistant
Offer several unique production options	Allow for flexible product designs
No need for chemical bonding	Able to be applied to different tolerances
Good electrical insulation	Excellent electrical insulation
Resistant to chemicals and detergents	Dimensional stability
Excellent improved toughness	High strength to weight ratio
High impact resistance	Typically cheap
Resists chipping	Water resistant
Can create both rubbery and hardened crystalline surfaces	Far cheaper tooling and setup
Softening when heated. Is not suitable for high temperature applications	**Superb heat resistance to high temperatures**
Can be recycled with little to no impact to material properties	Cannot be recycled, reshaped or remolded
	Longer processing time

As it is known, for this application, the drone will have to sustain elevated temperatures, at least during the attack on a given forest fire. Therefore, the lack of suitability of thermoplastic matrices on high temperature environments clearly lead to a selection of a composite material with a thermoset matrix.

The most important thermoset resins are epoxy, polyester and polyimide resins [73]. Their main characteristics are presented on table 3.4.

Table 3.4: Properties of different thermoset resins [74]

Epoxy (EP)	**Polyester (PE)**	**Polyimide (PI)**
Pros		
Best mechanical properties	Very low cost	Good mechanical properties
Chemical resistant	UV resistant	Fire resistant
Adhesion to glass fiber	Subzero temperatures	Can be used with
Heat resistant	High toughness compared	several metals
Resistant to cracking	to other lowcost thermosets	Low smoke emission
No shrinkage	Low shrinkage	
Easy to process	Easy to proccess	
Cons		
Bad UV resistance	Inferior heat resistance	Low impact strength
Expensive	Bad mechanical properties	Very high cost
Requires precise formulation	Low shelf life	Difficult to process
Need for high pressure molding	Affected by high humidity	

3.4.3.2 Fibers

Fibers consist of filaments mixed. Fibers should be as thin as possible (lower diameter), since its rupture strength decrease with an increasing diameter, also, small fibers allow for effective radius of curvature of the fibers during bending to be in the order of half a millimeter (except for boron fibers) [72].

Before the production of the materials, the layers of fibers must be subjected to a surface treatment to decrease the abrasion action when inside the forming machines and to improve its adhesion to the matrix material [72].

The main type of fibers used are glass, aramid, carbon, boron and silicon carbide [73]. However, on the following analysis, table 3.5, of different fibers' characteristics the focus will rely on glass fibers (E and S type, high strength), carbon fibers (high modulus and high strength), Kevlar 49 (aramid fibers) and Boron fibers.

Table 3.5: Properties of different fibers [74] [72]

	E glass	S glass	Carbon (HM)	Carbon (HS)	Kevlar 49	Boron
Density (kg/m3)	2550	2490	1800	1800	1440	2600
Stiffness (MN.m/kg)	27.9	34.5	203	124	86.5	153.8
Strength (kN.m/kg)	737	1510	1310	2060	1560	1308
Price (€/kg)	1.39	16.7	44.7	21.4	59.8	500

3.4.4 Selection of the Materials

In order to properly organize the selection of the different components, matrix and fiber, of the main composite material, decision matrices will be presented comparing the behavior of the different formerly presented options regarding several criteria that must complied.

3.4.4.1 Matrix - Decision Matrix

For the matrix of the material, it has already been explained that a thermosetic material is required, so the main options will fall between epoxy and polyester. Polyimide will fall directly out of consideration due to its extremely high cost [74]. The decision matrix is presented below, table 3.6. Criteria where none of the options are clearly advantageous are presented with no X:

Table 3.6: Decision matrix for fiber selection [74]

	Epoxy (EP)	Polyester (UP)
Weight saving	X	
Strength	X	
Creep	X	
Corrosion resistance		X
Impact Strength		
Mechanical Properties	X	
Fire resistance	X	
Water resistance	X	
Design flexibility		X
Bonding to fibers	X	
Manufacturability	X	
Machinability		X
Price		X
Global Rating	**8**	4

According to the decision matrix, the approach should follow a material with an epoxy matrix. This decision could be made by giving the criteria different importance (by balancing their weight on the final rating) but, even then, most of the more important characteristics would fall under the epoxy option. The bigger problems would rely on the lack of corrosion resistance for the fuselage-landing gear connection. However, it is not a problem since the fuselage is made of carbon-epoxy material. The price remains as an issue to consider, anyway the savings that could be achieved using polyester don't eclipse its negative characteristics.

3.4.4.2 Fibers - Decision Matrix

After selecting the proper matrix, logically, the next step is identify which fiber will serve as the reinforcement for the final material. The options approached are the ones in section 3.4.3.2. However, only carbon and glass fibers will be included in the decision matrix since the prices associated with Kevlar and Boron are impracticable in this application [74]. High modulus is

also not applicable for the landing gear due to its high specific stiffness. The matrix presented below, table 3.7, evaluates from 1 to 5 the behavior of the three fiber options based on a variety of material selection criteria. The properties analysed are referent to prepreg laminae of fiber with epoxy matrix:

Table 3.7: Decision matrix for fiber selection [74]

	E-Glass	S-Glass	HS Carbon
Impact Resistance	1	3	4
Specific strength	1	3	5
Fatigue resistance	1	4	3
Specific stiffness	1	2	5
Weight saving	4	2	5
Fire resistance	3	1	4
Water resistance	5	5	5
Price	4	5	2
Global Rating	2.5	3.25	**4.13**

With this decision matrix, it can be understood that the most advantageous fiber to be used as reinforcement on the composite material is the high strength carbon fiber. Once again, as it was observed for the selection of the matrix, a weighted analysis of the different criteria could be made but the most important ones, weight saving and most mechanical properties favor this fiber, with its price not being way off the other ones.

Carbon fiber presents many qualities such as low density and high strength but its brittle fracture and high cost may become a limitation. In theory, by mixing two or more types of fiber in a certain resin, the advantages of each type can be combined while mitigating the less desired qualities [77]. In addition, it should be possible to control the final properties to respect certain requirements.

In many engineering situations, a high modulus material with high stress resistance is required but its brittle failure and low elongation can present an unacceptable problem. In the specific situation of a landing gear strut, the perfect material would have a high initial modulus to react to the stresses involved, allied to limited yielding to allow energy absorption and a small to no reduction of the load carrying capacity with yielding.

To combine the advantages of the individual components carbon and glass fiber, A. R. Bunsell and B. Harris proposed and studied a novel hybrid composite material. Consisting of laminated layers of carbon fiber and glass fiber disposed in an alternative manner and using epoxy as the resin [77].

There are two ways to create this mixed fiber composites: intimately mingling the fibers in a composite matrix or laminating alternate layers of each type of main composite. For this study, the latter possibility was followed. Two distinct types of this material were made, one relying on unbonded alternate layers and the other having them bonded [77].

After fracture, as expected, well bonded specimens had a behavior quite different than the one given by the unbonded ones. With the good bond, occurs a phenomenon of load transfer between

the plates [77].

This study, concluded that, with a good bond between different materials and different layers of composite material, novel composites can be obtained with controlled load bearing and strain behaviors. The load and elongation curves obtained with this hybrid specimens were similar to the ones proposed as being desirable for a regular strut which can be approximated to the situation of a landing gear. The comparison can be observed below on figure 3.29. The study also considers possible the design of three or even four phased composites but does not develop this research.

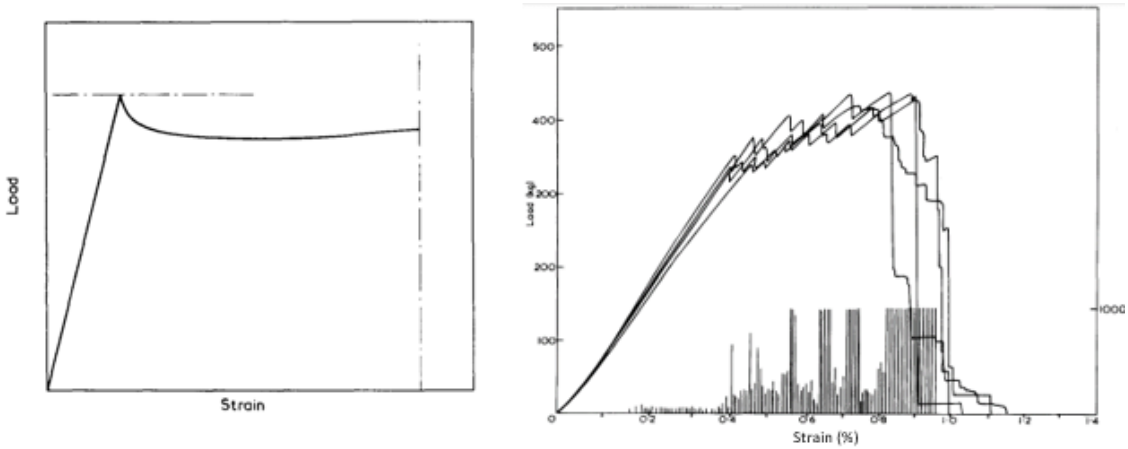

Figure 3.29: On the left, the ideal situation for a landing gear strut; on the right, the values obtained with the tested material [77]

Ciobanu et al. went a step further developing and studying a landing gear made of this combined composite material. Using a not mentioned relation between glass and carbon fibers but relying on the balance between flexibility given by the glass and stiffness given by the carbon fibers, the matrix used was epoxy on a 55/45 fiber to resin ratio. With their research, they were able to conclude that this is a reliable material for the construction of a landing gear while observing positive results. This serves as a proof of concept [78].

Therefore, and relying on the results from the decision matrix on table 3.7, the material selected for this landing gear is a composite made of epoxy resin, carbon fiber (HS) and S-glass fiber.

3.4.4.3 Composite for thermal protection

Even though the selected material for the landing gear would present an adequate fire and heat resistance, the temperatures that it would have to withstand are really high. Since the drone would have to operate on top of the fire in order to expel the extinguishing agent on it and properly fight it, the temperatures faced by the vehicle are of a greater order than just the temperature that would be felt at a same distance from the fire. As seen in section 2.1.1.4.

Therefore, a certain type of thermal protection is required on the landing gear and also suggested for the rest of the UAV.

Taking for example the measures used in aerospace applications, several types of thermal protection can be observed in different zones of equipment [72]:

- Heat sinks that provide insulation which are made of a composite boron/aluminum. It allows for the maintaining of great mechanical properties on an environment of the same temperatures registered over the fire;
- Introduction of a reflective thermal barrier serving as liner on the material. This can reflect the heat flux received and therefore protect the component;
- Ablative facing, which relies on the transformation of the surface according to several processes that absorbs the heat and on vaporized gases that cool the remaining layer;
- Insulation with ablative materials.

The use of Boron composites has already been approached and its price is completely impracticable for this application. On the other hand, surface treatments also emerge as a rather expensive option. Remaining the reflective barrier and the insulation with ablative materials options.

Ablatives are traditional materials although have been considered the best system for thermal protection [79]. Advances in simulation methods and computational engineering have allowed for developments on novel materials and ablation processes. Its use is approached in more detail in the following section.

Ablative Materials

The ablative material is usually placed on the surface of a given material using natural adhesives. It has a main function of maintaining the temperature at the surface of the prime material within a certain interval by increasing the heat flow [80].

For mechanical project and, specifically, this application, the objective is to reduce the conduction heat transmitted to the landing gear while having the minimum thickness of the layer. The energy balance is affected by the imposed heat by the fire and rest of environment (as in radiation and convection) and the response of the material [79]. A schematic representation of the energy balance on the layer is shown in figure 3.30.

To achieve its purpose, the material performs different mechanisms for energy dissipation such as converting energy by endothermic reactions via matrix thermal decay, reduction of heat flux via radiation and convection (via emission of pyrolysis gases and carbon particles, respectively) and energy conversion due to sublimation of an outside, carbonized, layer.

The design of the layer is beyond the scope of this project because it requires active measurements of heat and temperature, which are not currently available. However, the material selection must be made.

The ideal ablative should satisfy some fundamental requirements [82]:

- Optimal isolation characteristics;
- Low thermal conductivity;

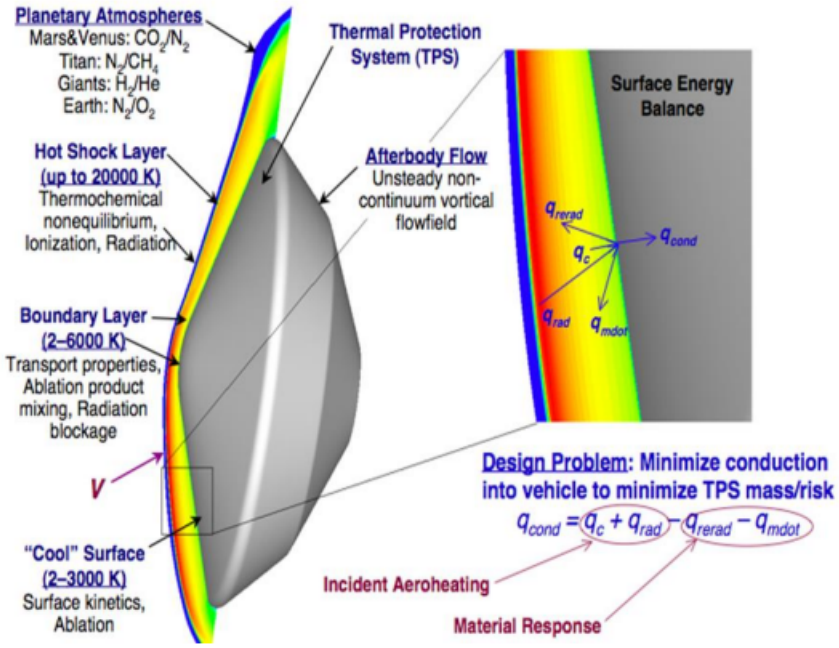

Figure 3.30: Energy balance on ablative material [81]

- Low density, for mass reduction;
- High thermal capacity;
- Elevated endothermic heat;
- High melting point and presence of fire retardants;
- Low thermal diffusivity;
- Flexibility at lower temperatures to allow for easier manufacture;
- Low cost.

After analysing several suppliers and comparing material characteristics, the decision converged for the composite solution provided by Amorim Cork Composites.

The offer includes several types of cork based composite materials that provide different benefits on thermal insulation, density, acoustic insulation and fire performance. Focusing on the first two, the selection would be ACM 30 however, this material is designed for fairings on metallic substrates. Therefore, the best option is ACM 40.

This material offers the main benefits of usual ablatives but also provides damping by dissipating structural vibrations. It is also non brittle and of sustainable characteristics. It has a density of 200-250 kg/m^3 and a thermal resistivity of 21.7 mK/W. Its thermal insulation properties are the best out of multilayer panel materials from this supplier, the comparison between the several options is shown in figure 3.31.

Key benefits*	ACM15	ACM16	ACM17	ACM18	ACM40
Lightweight	●●●○○	●●●○○	●●○○○	●●○○○	●●●●○
Accoustic performance	●●●●○	●●●●○	●●●●●	●●●●●	●●○○○
Thermal insulation	●●●○○	●●●○○	●●○○○	●●○○○	●●●●●

Figure 3.31: Comparison of Cork Composites' ablative material properties [83]

3.4.5 Ply arrangement and orientation

The component architecture must also be properly defined. As in the arrangement of the several plies (semi-product matrix + reinforcement) that will compose the material. The weaker properties of the fibers on the direction perpendicular to their orientation must be considered. Therefore, for this application, the proper configuration will be a mutltidirection laminate, as the name indicates, a laminate composed by several laminae with different orientations

The number, orientation and sequence of this stacking is variable according to the application. During this design, some characteristics must be considered such as [72]:

- Fiber orientation enables the optimization of mechanical properties along a certain direction;
- The composite material is elastic up to rupture, does not have plastic deformation;
- Fatigue resistance is good.

And when projecting the ply configuration, criteria should be [72]:

- Minimize the weight of material;
- Support the loading required;
- Limit the deformation (however not applicable for landing gear since deflection is required on landing).

For the representation of the several orientations, the description begins by the lowest ply on z<0 and proceeding till the upmost ply at z>0, with the middle plane situated at z=0. Some conditions are suggested for the orientations [72]:

- Each ply is noted by its orientation (usually 0º, 90º or +/- 45º);
- The grouping of too many plies of the same orientation has to be avoided in order to reduce the introduction of interlaminar stresses. A reference is to not surpass a limit of 4 consecutive plies;
- Midplane symmetry (symmetric on both sides of the midplane), this imposes symmetry of stresses during cooling of the material on manufacturing processes therefore prevents deformations (Figure 3.32);

- Technological minimum is usually a practice, consists of using a minimum of 10% of plies on each of the main orientations;
- For a dominant stress along the 0º direction, 90º plies placed on the surface, then 45º and -45º plies.

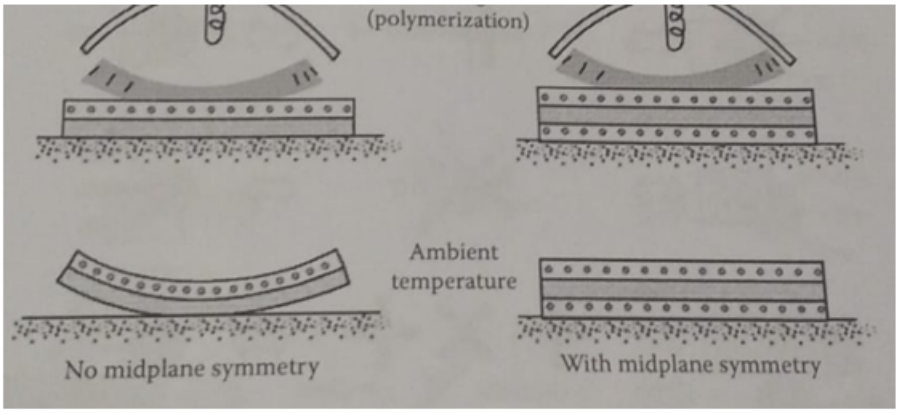

Figure 3.32: Effects of heating and cooling on composites with and without midplane symmetry

3.4.6 Laminated plates theory

Knowing the variation of stress and strain along the laminate is essential for the definition of the stiffness of the structure [84].

Since the several layers will have different orientations and materials, the elastic properties of the final element along the different axis must be determined. The conditions of these orthotropic materials must also be considered.

For the calculation, equivalent single-layer theories can be used. They derive from 3D elasticity theory by making assumptions regarding the behaviour of the material along its thickness. By construction, composite laminates have planar dimensions much larger than their thickness, allowing the problem to treat them as plate elements [85]. Transforming a 3D problem in a simpler 2D one.

3.4.6.1 Equivalent Single Layer Theories

First of all, according to J. N. Reddy, this theories are developed starting from an assumption that the displacement and stress fields are given as a linear combination of unknown functions along the thickness of the laminate [85]:

$$\varphi_i(x,y,z,t) = \sum_{j=0}^{N} (z)^j \varphi_i^j(x.y.t) \tag{3.132}$$

Where:

- φ_i is the component of displacement or stress on the i direction;

- (x,y) are the planar coordinates;
- t is the time;
- z is the thickness;
- φ_i^j are the unknown functions.

When the equations are related to displacements, the unknown equations are determined by the principle of virtual displacements:

$$0 = \int_0^T (\partial U + \partial V - \partial K)dt \tag{3.133}$$

Where the energy components are, respectively, the virtual strain energy, virtual work done by external forces and virtual kinetic energy.

For plate structures, the integration over the domain of the plate is equal to the (tensor) product of integration over the plane of the plate and its thickness [85]:

$$\int_{Vol.} (\cdot)dV = \int_{-\frac{h}{2}}^{\frac{h}{2}} \int_{\Omega_0} (\cdot)d\Omega dt \tag{3.134}$$

Where:

- h is the total thickness of the plate;
- Ω_0 is the midplane without any deformation;

With all the functions explicit in the thickness coordinate (independent variable), the problem can now be reduced to a 2D one. Then, the equations from 3.133 involve the dependent variables x,y and t and the thickness-averaged stress resultants $R_{ij}^{(m)}$ [85]:

$$R_{ij}^{(m)} = \int_{-\frac{h}{2}}^{\frac{h}{2}} (z)^m \sigma_{ij} dz \tag{3.135}$$

The resultants can also be written in terms of the unknown equations from 3.132 using stress-strain and strain-displacement relations [85].

The simplest ESL laminated plate theory, and the one that will be developed is the classical laminated plate theory, an extension of Kirchhoff plate theory to laminated composite plates. This classical theory requires the displacements to be given by [85]:

$$u(x,y,z,t) = u_0(x,y,t) - z\frac{\partial w_0}{\partial x} v(x,y,z,t) = v_0(x,y,t) - z\frac{\partial w_0}{\partial y} w(x,y,z,t) = w_0(x,y,t) \tag{3.136}$$

3.4.6.2 Classical Laminated Plate Theory

Being that this theory directly derives from Kirchhoff hypothesis, several assumptions are being made for the development of the mathematical model.

- Straight lines normal to the surface remain straight after deformation;
- Transverse normals are considered inextensible;
- Transverse normals, on deformation, rotate so that they continue perpendicular to the mid-plane.

Besides these points related to the classical laminate view, another assumption must be made to formulate the theory. The laminate is presumed to consist of perfectly bonded laminae. This is not an idealization since it can be realized in a practical situation. Nearly perfect bonded is required in order for the laminae to work together as a unit and there are tests to determine if layers are well bonded with each other. Laminates that are not correctly formed are rejected in usual manufacturing processes [84].

Assuming the midplane of the laminate on the *xy*-plane an example of the coordinate system used for the following formulation is presented on figure 3.33.

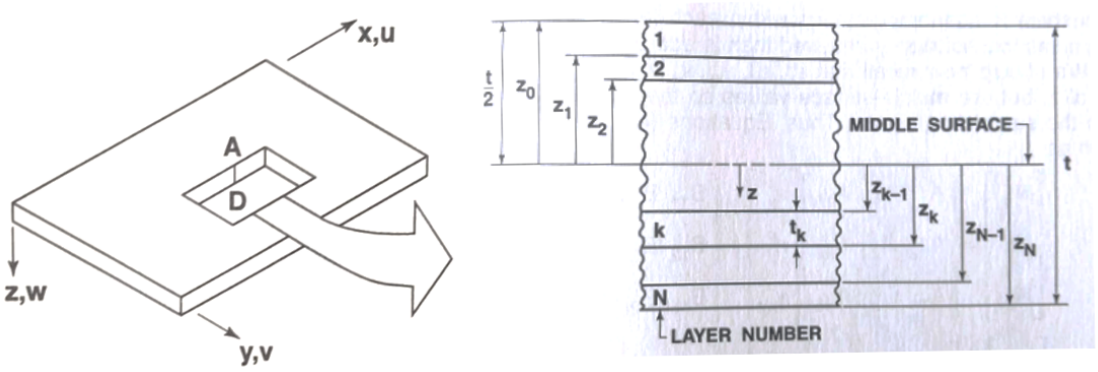

Figure 3.33: Coordinate system of the laminated plate

The 4 mentioned assumptions will have impact on certain properties. The first requirement is equivalent to deducing that the shear strains in perpendicular planes to the midplane are zero, γ_{xz}=0 γ_{yz}=0. In addition, the second assumption implies that the normals to the midplane have constant length, so the strain on this direction is null, ε_{zz}=0.

The method also encloses a few restrictions [85]:

- The material is linearly elastic and has 3 planes of material symmetry;
- Uniform thickness on each layer;
- Small strains and displacements;
- Transverse shear stress on top and bottom are zero.

Displacements and Strains

Remembering the assumptions created by the Kirchhoff theory, the laminate strains have been reduced to ε_{xx}, ε_{yy} and γ_{xy}. For small strains, linear strain-displacements may be used:

$$\varepsilon_{xx} = \frac{\partial u}{\partial x}$$

$$\varepsilon_{yy} = \frac{\partial v}{\partial y} \tag{3.137}$$

$$\gamma_{xy} = \frac{\partial u}{\partial y} + \frac{\partial v}{\partial x}$$

Using the Kirchhoff equations 3.136, becomes,

$$\varepsilon_{xx} = \frac{\partial u_0}{\partial x} - z\frac{\partial^2 w_0}{\partial x^2}$$

$$\varepsilon_{yy} = \frac{\partial v_0}{\partial y} - z\frac{\partial^2 w_0}{\partial y^2} \tag{3.138}$$

$$\gamma_{xy} = \frac{\partial u_0}{\partial y} + \frac{\partial v_0}{\partial x} - 2z\frac{\partial^2 w_O}{\partial x \partial y}$$

Noting that the strain equations have the form $\varepsilon = \varepsilon^0 + z\varepsilon^1$. Where ε^0 represents the membrane strains and ε^1 the bending strains, or curvatures.

If on equation 3.137, instead of linear strain-displacement equations, one were to use the non-linear equations and considering the rotations $\partial w_O/\partial x$ and $\partial w_O/\partial y$ to have moderate values the related terms of second order would not be negligible. Therefore, ε^0 would be given by,

$$\varepsilon^0_{xx} = \frac{\partial u_0}{\partial x} + \frac{1}{2}\left(\frac{\partial w_0}{\partial x}\right)^2$$

$$\varepsilon^0_{yy} = \frac{\partial v_0}{\partial y} + \frac{1}{2}\left(\frac{\partial w_0}{\partial y}\right)^2 \tag{3.139}$$

$$\gamma^0_{xy} = \left(\frac{\partial u_0}{\partial y} + \frac{\partial v_0}{\partial x} + \frac{\partial w_0}{\partial x}\frac{\partial w_0}{\partial y}\right)$$

With equations 3.138, if the displacements of the midplane are known, strain at any point can be calculated. From the same equations it is also implied that all strain components vary through the thickness of the laminate.

Lamina Stress Strain Behaviour

As of the classical laminated plate theory, ε_{zz}, γ_{xz} and γ_{yz} are equal to zero, as mentioned before. Therefore, for an orthotopic layer oriented arbitrarly in the xy-plane the transverse shear stresses are also zero (σ_{xz} and σ_{yz}). With the normal strain on the z axis null, the normal stress, although not equal to zero, does not appear on the equation of motion, and will be neglected [85].

Then, considering a lamina of orthotropic material under plane stress [84]:

$$\begin{bmatrix}\sigma_1\\ \sigma_2\\ \tau_{12}\end{bmatrix} = \begin{bmatrix}Q_{11} & Q_{12} & 0\\ Q_{12} & Q_{22} & 0\\ 0 & 0 & Q_{66}\end{bmatrix}\begin{bmatrix}\varepsilon_1\\ \varepsilon_2\\ \gamma_{12}\end{bmatrix} \tag{3.140}$$

Not considering thermal expansion nor piezoelectric effects.

The coefficients Q_{ij}, reduced stiffness, are defined in terms of engineering constants:

$$Q_{11} = \frac{E_1}{1-v_{12}v_{21}} \qquad Q_{22} = \frac{E_2}{1-v_{12}v_{21}} \qquad Q_{12} = \frac{v_{12}E_2}{1-v_{12}v_{21}} \qquad Q_{66} = G_{12} \quad with,\ \frac{v_{12}}{E_1} = \frac{v_{21}}{E_2}$$

To get this values dependent on the coordinates of the system, a transformation matrix must be applied to the coefficients of reduced stiffness so that $\sigma_k = [\bar{Q}]_k \varepsilon_k$ for any layer k of a laminate,

$$[\bar{Q}] = [T]^{-1}[Q][T]^{-T} \tag{3.141}$$

So that,

$$[T] = \begin{bmatrix} cos^2\theta & sin^2\theta & 2sin\theta cos\theta \\ sin^2\theta & cos^2\theta & -2sin\theta cos\theta \\ -sin\theta cos\theta & sin\theta cos\theta & cos^2\theta - sin^2\theta \end{bmatrix}$$

Finally, using the transformation matrix and substituting on equation 3.140, the values for stress on the xy-plane are given by:

$$\begin{bmatrix}\sigma_x\\ \sigma_y\\ \tau_{xy}\end{bmatrix} = \begin{bmatrix}\bar{Q}_{11} & \bar{Q}_{12} & \bar{Q}_{16}\\ \bar{Q}_{12} & \bar{Q}_{22} & \bar{Q}_{26}\\ \bar{Q}_{16} & \bar{Q}_{26} & \bar{Q}_{66}\end{bmatrix}\begin{bmatrix}\varepsilon_x\\ \varepsilon_y\\ \gamma_{xy}\end{bmatrix} \tag{3.142}$$

Or, using the relations from 3.139, the stresses in any layer k can be expressed in terms of the laminate middle-surface [84],

$$\begin{bmatrix}\sigma_x\\ \sigma_y\\ \tau_{xy}\end{bmatrix}_k = \begin{bmatrix}\bar{Q}_{11} & \bar{Q}_{12} & \bar{Q}_{16}\\ \bar{Q}_{12} & \bar{Q}_{22} & \bar{Q}_{26}\\ \bar{Q}_{16} & \bar{Q}_{26} & \bar{Q}_{66}\end{bmatrix}_k \left(\begin{bmatrix}\varepsilon_x^0\\ \varepsilon_y^0\\ \gamma_{xy}^0\end{bmatrix} + z\begin{bmatrix}\varepsilon_x^1\\ \varepsilon_y^1\\ \gamma_{xy}^1\end{bmatrix} \right) \tag{3.143}$$

From this final equation, it is interpreted that the values for transformed reduced stiffness can be different for each layer of the laminate, resulting on a non linear variation of stress on the laminate even though the strain variation is considered linear, via the assumptions made.

Laminate Resultant Forces and Moments

The resultant forces and moments on a given laminate are obtained by integrating the stresses in each lamina through the laminate thickness, for example,

$$N_x = \int_{-t/2}^{t/2} \sigma_X \, dz \qquad M_x = \int_{-t/2}^{t/2} \sigma_X z \, dz$$

Noting that the the stresses vary not only along the laminate but also within each layer, as it is shown in figure 3.34, the integration may not be trivial [84].

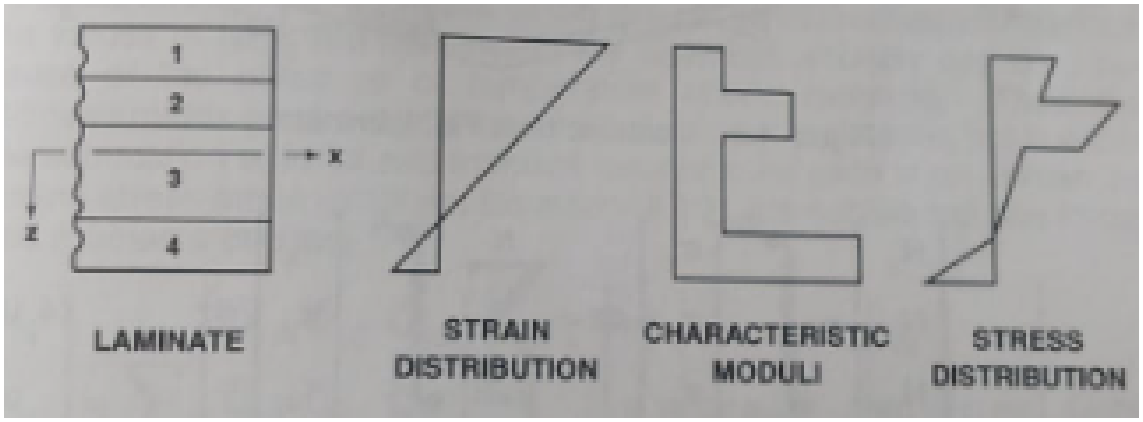

Figure 3.34: Hypothetical Variation of Strain and Stress on several laminae through the Laminate Thickness

Anyway, the resultants for forces and moments on a laminate with N layers is defined as,

$$\begin{bmatrix} N_x \\ N_y \\ N_{xy} \end{bmatrix} = \int_{-t/2}^{t/2} \begin{bmatrix} \sigma_x \\ \sigma_y \\ \tau_{xy} \end{bmatrix} dz = \sum_{k=1}^{N} \int_{z_{k-1}}^{z_k} \begin{bmatrix} \sigma_x \\ \sigma_y \\ \tau_{xy} \end{bmatrix}_k dz \tag{3.144}$$

And,

$$\begin{bmatrix} M_x \\ M_y \\ M_{xy} \end{bmatrix} = \int_{-t/2}^{t/2} \begin{bmatrix} \sigma_x \\ \sigma_y \\ \tau_{xy} \end{bmatrix} dz = \sum_{k=1}^{N} \int_{z_{k-1}}^{z_k} \begin{bmatrix} \sigma_x \\ \sigma_y \\ \tau_{xy} \end{bmatrix}_k z\, dz \tag{3.145}$$

Where $k-1$ and k are defined in figure 3.33. Axis z is according to the convention that it is positive downward.

Equations 3.144 and 3.145 can be arranged in a different way using the stiffness matrix for each lamina. This matrix will be constant unless a temperature gradient or moisture gradient exist in a lamina which properties may be dependent on these. Assuming that this is not the case, the matrix can be outside the integration over each layer. Rewriting the equations,

$$\begin{bmatrix} N_x \\ N_y \\ N_{xy} \end{bmatrix} = \sum_{k=1}^{N} \begin{bmatrix} \bar{Q}_{11} & \bar{Q}_{12} & \bar{Q}_{16} \\ \bar{Q}_{12} & \bar{Q}_{22} & \bar{Q}_{26} \\ \bar{Q}_{16} & \bar{Q}_{26} & \bar{Q}_{66} \end{bmatrix}_k \left[\int_{z_{k-1}}^{z_k} \begin{bmatrix} \varepsilon_x^0 \\ \varepsilon_y^0 \\ \gamma_{xy}^0 \end{bmatrix} dz + \int_{z_{k-1}}^{z_k} \begin{bmatrix} \varepsilon_x^1 \\ \varepsilon_y^1 \\ \gamma_{xy}^1 \end{bmatrix} z\, dz \right] \tag{3.146}$$

$$\begin{bmatrix} M_x \\ M_y \\ M_{xy} \end{bmatrix} = \sum_{k=1}^{N} \begin{bmatrix} \bar{Q}_{11} & \bar{Q}_{12} & \bar{Q}_{16} \\ \bar{Q}_{12} & \bar{Q}_{22} & \bar{Q}_{26} \\ \bar{Q}_{16} & \bar{Q}_{26} & \bar{Q}_{66} \end{bmatrix}_k \left[\int_{z_{k-1}}^{z_k} \begin{bmatrix} \varepsilon_x^0 \\ \varepsilon_y^0 \\ \gamma_{xy}^0 \end{bmatrix} z\, dz + \int_{z_{k-1}}^{z_k} \begin{bmatrix} \varepsilon_x^1 \\ \varepsilon_y^1 \\ \gamma_{xy}^1 \end{bmatrix} z^2\, dz \right] \tag{3.147}$$

In case the stiffness matrix is not constant, and the conditions prior discussed are, in fact, present, these values will be a function of z and must also be integrated. Therefore, the laminate is non homogeneous within each layer, so the solution is significantly more complicated. The equations for force and moment will be written in a compact way, dependent on matrices $[A]$, $[B]$ and $[D]$,

$$\begin{Bmatrix} \{N\} \\ \{M\} \end{Bmatrix} = \begin{bmatrix} [A][B] \\ [B][D] \end{bmatrix} \begin{Bmatrix} \{\varepsilon^0\} \\ \{\varepsilon^1\} \end{Bmatrix} \tag{3.148}$$

Where $[A]$ is the extensional stiffness matrix, $[B]$ the bending-extension coupling stiffness matrix and $[D]$ the bending stiffness matrix [85]. These matrices are also defined by the transformed matrix of laminate stiffness via,

$$\begin{aligned} A_{ij} &= \sum_{k=1}^{N} (\bar{Q}_{ij})_k \, (z_k - z_{k-1}) \\ B_{ij} &= \frac{1}{2} \sum_{k=1}^{N} (\bar{Q}_{ij})_k \, (z_k^2 - z_{k-1}^2) \\ D_{ij} &= \frac{1}{3} \sum_{k=1}^{N} (\bar{Q}_{ij})_k \, (z_k^3 - z_{k-1}^3) \end{aligned} \tag{3.149}$$

Equivalent Membrane Properties

The main objective of introducing the Classical Laminated Plate Theory is to obtain the equivalent properties of the composite laminate E_1, E_2, v_{12}, v_{21} and G_{22}. With these, the laminate constituted by several laminae can be considered a single layer of orthotropic material.

Recalling the relations between reduced stiffness and the mentioned properties:

$$Q_{22} = \frac{E_2}{1 - v_{12} v_{21}} \qquad Q_{12} = \frac{v_{12} E_2}{1 - v_{12} v_{21}}$$

Solving the equations in E_2 and equalling them,

$$E_2 = Q_{22} \ * \ (1 - v_{12} v_{21}) = \frac{Q_{12} \ * \ (1 - v_{12} v_{21})}{v_{12}} \tag{3.150}$$

From equations 3.149, the several components can be calculated for a single layer orthotropic material with a thickness t,

$$A_{ij} \ = \ Q_{ij}\, t$$

To note that, in a symmetric laminate (both for material properties and laminae orientation), bending-extension coupling stiffness is null, $B_{ij} = 0$ [84].

Substituting in equation 3.150,

$$\frac{A_{22}}{t} * (1 - v_{12}v_{21}) = \frac{A_{12} * (1 - v_{12}v_{21})}{v_{12} * t} \tag{3.151}$$

Simplifying,

$$A_{22} = \frac{A_{12}}{v_{12}} \quad \Rightarrow \quad v_{12} = \frac{A_{12}}{A_{22}} \tag{3.152}$$

Using the same reasoning but for E_1, the procedure becomes exactly the same only now for direction 1. Noting that $A_{12} = A_{21}$,

$$A_{11} = \frac{A_{12}}{v_{12}} \quad \Rightarrow \quad v_{21} = \frac{A_{12}}{A_{11}} \tag{3.153}$$

Recalling that,

$$Q_{11} = \frac{E_1}{1 - v_{12}v_{21}}$$

E_1 can be written so that it only depends of extensional stiffness components ($[A]$) using equations 3.152 and 3.153,

$$\frac{A_{11}}{t}\left(1 - \frac{A_{12}}{A_{22}}\frac{A_{12}}{A_{11}}\right) = E_1 \tag{3.154}$$

$$\frac{A_{11}}{t} - \frac{A_{12}^2}{A_{22}\,t} = E_1 \tag{3.155}$$

Concluding that E_1 is given by,

$$E_1 = \frac{A_{11}A_{22} - A_{12}^2}{A_{22}t} \tag{3.156}$$

E_2 can be obtained in a similar way so that,

$$E_2 = \frac{A_{11}A_{22} - A_{12}^2}{A_{11}t} \tag{3.157}$$

Finally, since $G_{12} = Q_{66}$

$$G_{12} = \frac{A_{66}}{t} \tag{3.158}$$

All the membrane properties are now defined dependent on the extensional stiffness and the thickness of the laminate:

$$E_1 = \frac{A_{11}A_{22} - A_{12}^2}{A_{22}t} \qquad E_2 = \frac{A_{11}A_{22} - A_{12}^2}{A_{11}t} \qquad v_{12} = \frac{A_{12}}{A_{22}} \qquad v_{21} = \frac{A_{12}}{A_{11}} \qquad G_{12} = \frac{A_{66}}{t}$$

Equivalent Bending Properties

Bending properties are related to flexure and bending of the material.

Here the same logic will be used but this time focusing on the bending stiffness. The values for D_{ij} are given by,

$$D_{ij} = \frac{Q_{ij}\, t^3}{12}$$

Going back to equation 3.150 and substituting now with the bending stiffness,

$$12\frac{D_{22}}{t^3} * (1 - v_{12}v_{21}) = 12\frac{D_{12} * (1 - v_{12}v_{21})}{v_{12} * t^3} \tag{3.159}$$

So, is a similar as for the membrane properties,

$$v_{12} = \frac{D_{12}}{D_{22}} \tag{3.160}$$

And, logically,

$$v_{21} = \frac{D_{12}}{D_{11}} \tag{3.161}$$

To obtain E_1 the methodology is the same as in equation 3.154,

$$12\frac{D_{11}}{t^3}\left(1 - \frac{D_{12}}{D_{22}}\frac{D_{12}}{D_{11}}\right) = E_1 \tag{3.162}$$

Simplifying the equation,

$$E_1 = 12\frac{D_{11}D_{22} - D_{12}^2}{D_{22}\, t^3} \tag{3.163}$$

In a similar way,

$$E_2 = 12\frac{D_{11}D_{22} - D_{12}^2}{D_{11}\, t^3} \tag{3.164}$$

For G_12, the calculation derives from

$$G_{12} = Q_{66}$$

so,

$$G_{12} = 12\frac{D_{66}}{t^3} \tag{3.165}$$

All the flexure properties are now defined dependent on the bending stiffness and the thickness of the laminate:

$$E_1 = 12\frac{D_{11}D_{22} - D_{12}^2}{D_{22}t^3} \quad E_2 = 12\frac{D_{11}D_{22} - D_{12}^2}{D_{11}t^3} \quad v_{12} = \frac{D_{12}}{D_{22}} \quad v_{21} = \frac{D_{12}}{D_{11}} \quad G_{12} = 12\frac{D_{66}}{t^3}$$

3.4.6.3 Failure criteria

Composite materials have several criteria that can be used in order to understand the possibility of failure. These are focused on biaxial loading.

The simpler and most used biaxial strength criteria are maximum failure stress criterion, maximum failure criterion, Tsai-Hill failure criterion, Hoffman failure criterion and Tsai-Wu failure criterion. In all these, the material is treated as orthotropic, although also regarded as homogeneous [84].

Maximum failure stress criteria consists of analysing each one of the stresses in principal material coordinates and verify if these are below the respective strengths. Otherwise fracture would occur [84]. For tensile stresses,

$$\sigma_1 < X_t \qquad \sigma_2 < Y_t$$

and for compressive,

$$\sigma_1 > X_c \qquad \sigma_2 > Y_c$$

For shear stress,

$$|\tau_{12} < S$$

Where X_t corresponds to fiber fracture, X_c fiber failure in compression, Y_t matrix fracture, Y_c matrix failure in compression and S is the shear strength.

When any of the inequations are not respected, the assumption is made that the material has failed by the failure mechanisms associated with the the respective strength.

Maximum failure strain criterion is very similar however, the strains are the ones being limited, not the stresses, by

$$\varepsilon_1 < X_{\varepsilon_t} \qquad \varepsilon_2 < Y_{\varepsilon_t} \qquad |\gamma_{12}| < S_\varepsilon$$

For materials with different strengths in tension and compression,

$$\varepsilon_1 > X_{\varepsilon_c} \qquad \varepsilon_2 > Y_{\varepsilon_c}$$

Where X_ε is the maximum normal strain in direction 1 (either tension, t, or compression, c), Y_ε the maximum normal strain in direction 2 and S_ε the maximum shear strain.

Nonetheless, these two criteria present one major problem since there are no interaction between failure modes.

Tsai-Hill Failure Criterion

Hill proposed a yield criterion for orthotropic materials. This criteria represents limits for linear elastic behaviour which on composite materials is both strength and failure criterion.

It is an extension of the von Mises criterion for metals related to the amount of energy an isotropic body uses to be distorted.

The criterion uses strength parameters F, G, H, L, M and N that will be related to the failure strengths by Tsai [84]. The yield criterion reads,

$$(G + H)\sigma_1^2 + (F + H)\sigma_2^2 + (F + G)\sigma_3^2 - 2H\sigma_1\sigma_2 - 2G\sigma_1\sigma_3 - 2F\sigma_2\sigma_3 + 2L\tau_{23}^2 + 2M\tau_{13}^2 + 2N\tau_{12}^2 = 1 \quad (3.166)$$

If only τ_{12} acts on the body, because its maximum value is S

$$2N = \frac{1}{S^2} \quad (3.167)$$

If only σ_1 is acting, then

$$G + H = \frac{1}{X^2} \quad (3.168)$$

And if only σ_2

$$F + H = \frac{1}{Y^2} \quad (3.169)$$

If the strength in direction 3 is given by Z, them, with only σ_3 acting on the laminate

$$F + G = \frac{1}{Z^2} \quad (3.170)$$

With the 3 prior equations, relations between F, G and H and the failure strengths will be

$$2F = \frac{1}{Y^2} + \frac{1}{Z^2} - \frac{1}{X^2} \quad 2G = \frac{1}{X^2} + \frac{1}{Z^2} - \frac{1}{Y^2} \quad 2H = \frac{1}{X^2} + \frac{1}{Y^2} - \frac{1}{Z^2} \quad (3.171)$$

Finally for the plane stress configuration, with fibers oriented on the 1-direction, Hill's equations can be rewritten as

$$\frac{\sigma_1^2}{X^2} - \frac{\sigma_1\sigma_2}{X^2} + \frac{\sigma_2^2}{Y^2} + \frac{\tau_{12}^2}{S^2} = 1 \quad (3.172)$$

The appropriate values of X and Y for tension or compression must be selected depending on the signs of σ_1 and σ_2.

If the value obtained on the left side of equation is less than 1, the criterion is validated.

The agreement between Tsai-Hill failure criterion and experimental results is quite good [84]. It is also much more applicable since via the equation, it assures dependency between failure modes.

Unit Circle Failure Criteria

This criteria is created as a simplification of the omni strain failure envelope. This is defined as a material property that is independent of the laminate layup configuration [86].

With this criteria an envelope is created by representing the strain space. These remain the same shape independently of the presence of other plies. The inner envelope defines first-ply failure and last-ply failure for all ply orientations of a material [86].

To simplify the laminate failure analysis, unit circle was created in the normalised principal space. A representation of this circle is shown in figure 3.35. This is a conservative approximation using only strain measurements [86].

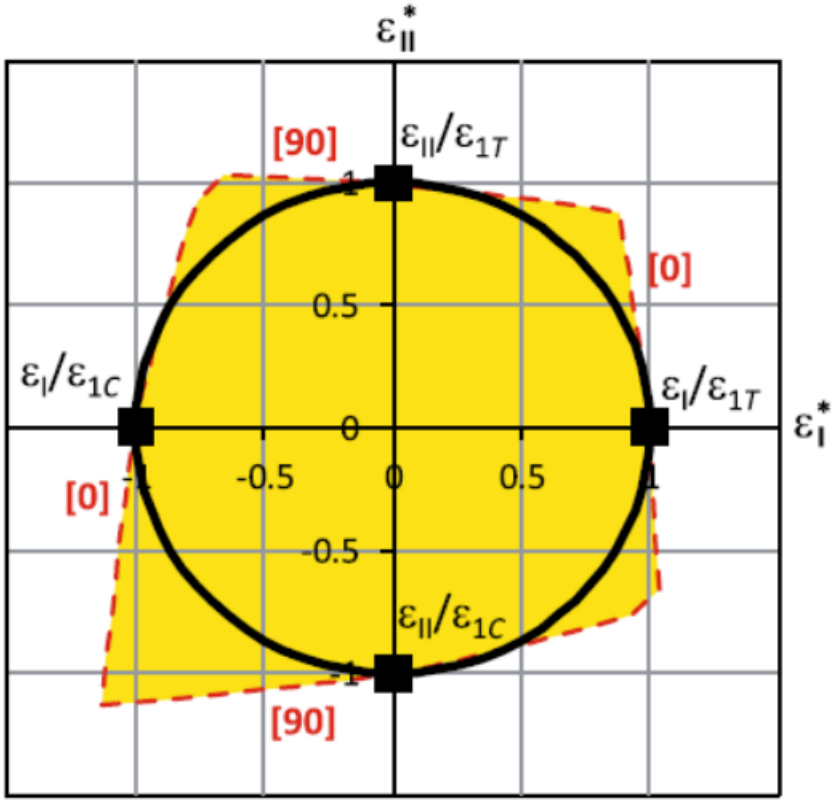

Figure 3.35: Representation of the unit circle failure criteria [86]

Here the failure index is given by:

$$k = \sqrt{k_1^2 + k_2^2} \tag{3.173}$$

Where

$$k_1 = \varepsilon_I/e_X \text{ and } k_2 = \varepsilon_{II}/e_X, \text{if } \varepsilon_I, \varepsilon_{II} \geq 0$$

$$k_1 = \varepsilon_I/e'_X \text{ and } k_2 = \varepsilon_{II}/e'_X, \text{if } \varepsilon_I, \varepsilon_{II} < 0$$

And,

$$e_X = X_T/E_X \qquad e'_X = X_C/E_X$$

So, for this criteria, only two strength properties are requires: X_T and X_C, the maximum allowable tensile stress and the maximum allowable compressive stress, respectively. Where E_X is the Young's Module and e_X the maximum allowable strain, both adjusted for either tensile or compressive solicitation.

3.4.7 Typical Failure of Laminates

3.4.7.1 Damages

Even when using a composite of optimal mechanical properties failures can occur when the loads exerted on the material exceed its limits. On figure 3.36, the main failure modes are represented.

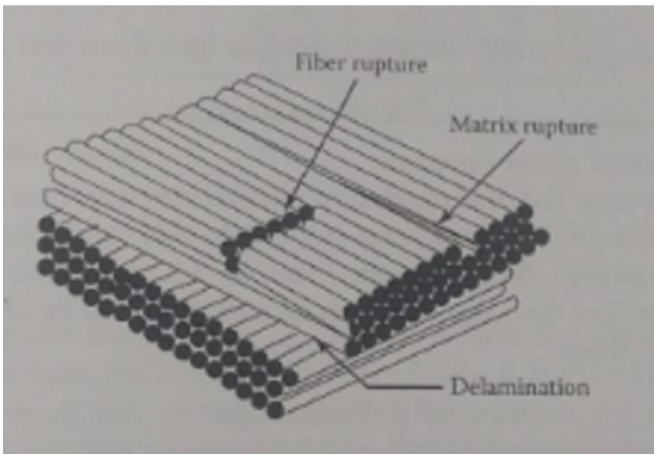

Figure 3.36: Different modes of failure [72]

The different modes of failure may also be associated with different kinds of damage to the structure. More specifically, 3 types of stresses being tension, compression or shear.

Fiber failure

This situation usually occurs due to tension on the longitudinal axis of the composite, along the direction of the fibers. Here, since the former usually has a smaller strain on rupture than the matrix it breaks first [87].

Not all fibers fail at the same time since the fibers' resistance varies from point to point and from fiber to fiber. Several small ruptures occur on the less resistant spots leading to a not uniform state of stress [87].

The failure in fibers can also occur via the development of microbuckling or kinking.

If the volumetric concentration of fibers is very high, shear failure can occur [72].

Matrix failure

On the contrary, this situation is mostly associated with stresses on the transversal direction, perpendicular to the fibers [87].

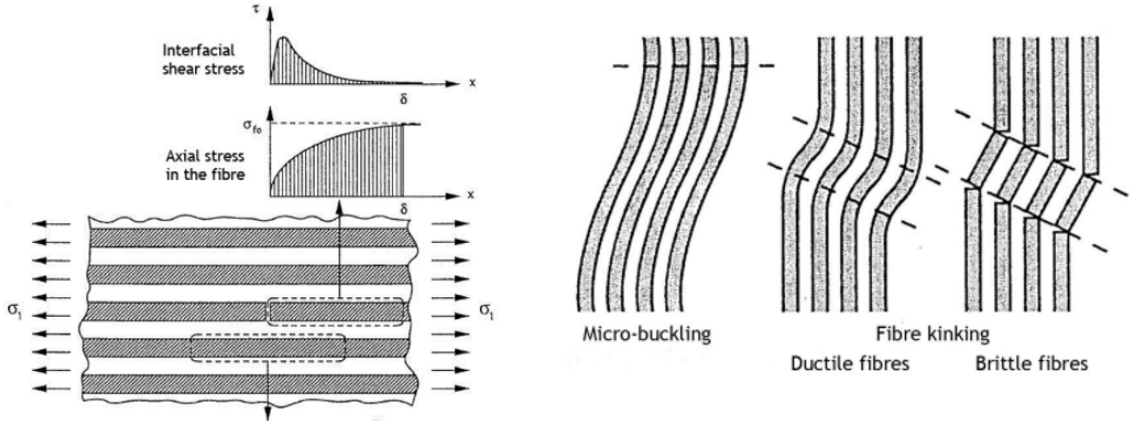

Figure 3.37: On the left, action of longitudinal tension and , on the right, compression stresses on the fibers [86]

Most specifically on traction, this forces create large concentrations of stress and deformation both on the matrix and the interface between matrix and reinforcement. With this circumstances, the rupture occurs on the matrix due to the increasing formation of micro cracks [87].

This situation may also occur due to shear stresses along the material that develop tension on the interface between fibre and matrix.

Delamination

The latter situation presented for matrix failure, most often, lead to the separation on the interface, delamination.

The phenomenon can also occur due to compression forces on the direction perpendicular to the fibers. Here, high shear stress develops on the interface leading to the decohesion between the components [87].

3.4.7.2 Joining and Bolting Failures

Besides designing the laminate and the material to properly support the loads, there is the need to also design the attachment of the landing gear to the fuselage. This can be done via bolted connections or adhesive bonding [72].

Assuming the use of bolted connections, holes will have to be created on the composite landing gear (molded-in or made by drilling) which will introduce stress concentrations. These are even higher on composite materials than metals. The regions affected can be weakened by a factor of 40-60% in tension and 15% in compression [72].

Hole degradation can occur due to different factors:

Stress concentration factors

Figure 3.38 shows the increase in stress in the region around the hole in the case of a laminate composite material. The maximum value can be given by:

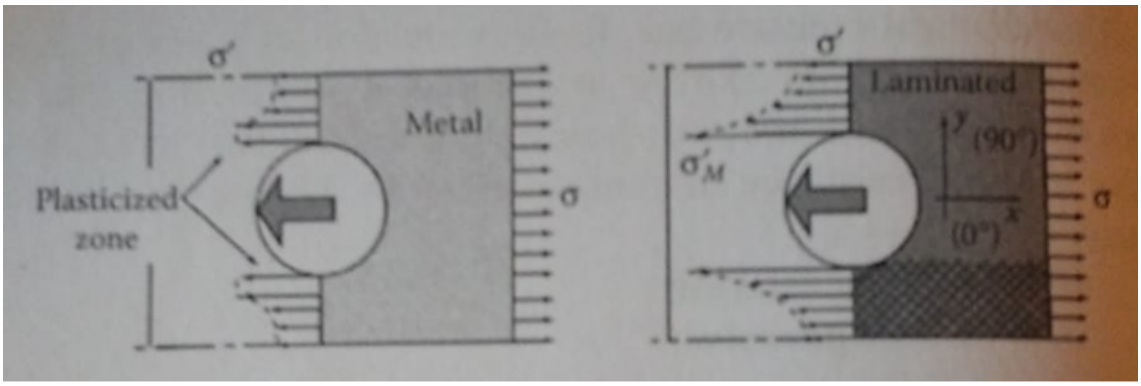

Figure 3.38: Concentrations of stress around a hole on a metal or a laminate segment [72]

$$\sigma'_M = \sigma' \left[1 + \sqrt{2 \left(\sqrt{\frac{E_x}{E_y}} - v_{xy} \right) + \frac{E_x}{G_{xy}}} \right] \tag{3.174}$$

Bearing due to lateral pressure

Regarding the pressure exerted by the bolt when inside the hole laterally on its wall. If this pressure is excessive it can lead to delamination. The resistance of the hole is weaker when occupied than that of an empty one [72].

Fracture of fibers

If the hole is created via drilling, fibers can be fractured or misaligned (if made before polymerization). Creating even weaker zones that will be over stressed [72].

The principal modes of failure and possible causes are represented in figure 3.39.

In order to mitigate the probability of these consequences, recommended values for pitch, edge distance and thickness of holes should be followed such as the proposed orientations of plies near them [72].

In figure 3.40, normal and shear loads acting on an assembly with a hole are represented. Here one must consider bearing pressure, which is responsible for possibly crushing the wall of the hole. This pressure must remain smaller than an admissible maximum dependant on the material, given by:

$$\frac{F}{\phi e} \leqslant \sigma_{admissible\ bearing\ pressure} \tag{3.175}$$

Where, for reference [72],

carbon $\sigma_{admissible\ bearing\ pressure} = 500$ MPa

glass $\sigma_{admissible\ bearing\ pressure} = 300$ MPa.

And with the other terms represented as in figure 3.40.

Finally, on this regions the admissible stress also needs to be evaluated regarding magnification coefficients, obtained empirically, that take into account the presence of the hole and the pressure

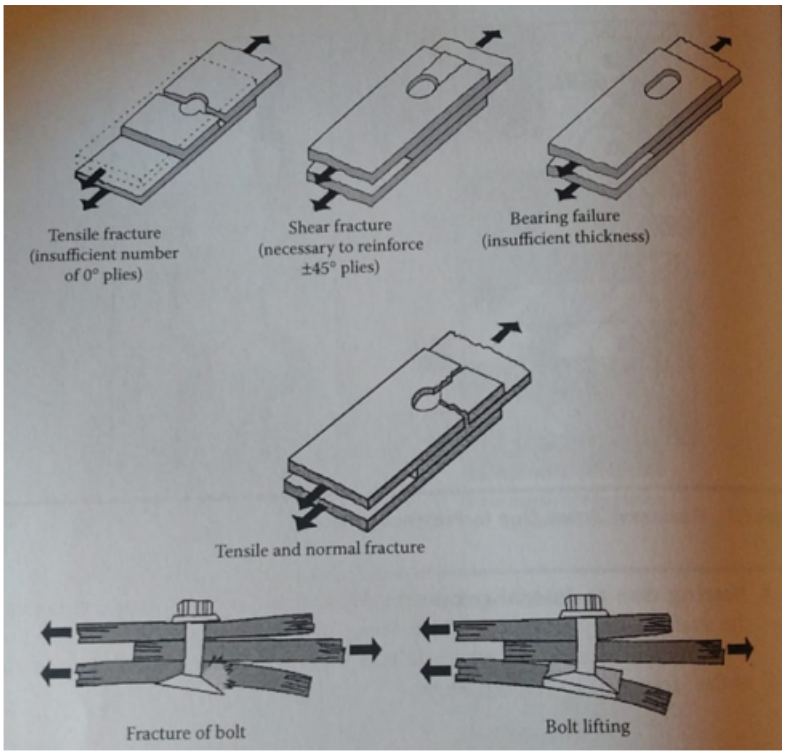

Figure 3.39: Principal modes of failure for composite segments with bolting [72]

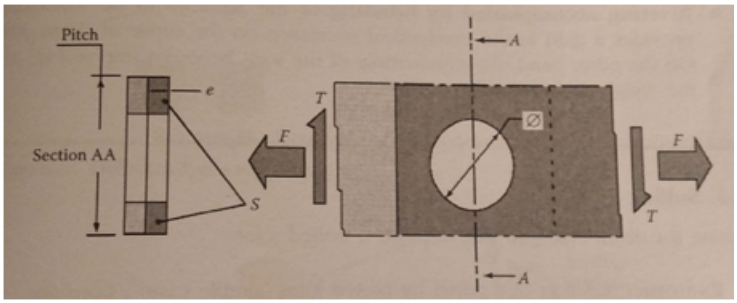

Figure 3.40: Normal and shear stress acting on the assembly with hole [72]

of contact or bearing on the wall [72]. The following equations give the values for magnified shear and tensile stresses [72].

$$\sigma_{magnified} = \frac{1}{\alpha}\left(\frac{F}{S} + 0.2\frac{F}{\phi e}\right) \tag{3.176}$$

tension : $\alpha = 0.6$
compression : $\alpha = 0.8$

$$\tau_{magnified} = \frac{1}{0.7}\frac{T}{S} \tag{3.177}$$

Where T and S are as represented in figure 3.40.

Chapter 4

Methodology

A proper methodology must be defined and adhered for the design process to run efficiently and in an organized manner.

Before beginning the calculation for the design of the landing gear, the modifications to the initial drone development outlined in section 2.3, will be defined. Selecting the extinguishing method that will replace the firefighting balls is the initial step. This will impact the design of the landing gear because it will have a direct effect on the total weight of the drone and shift the center of gravity.

After obtaining the drone's configuration, the multiple criteria for obtaining the landing gear's geometric characteristics are followed. Positioning and a few geometric constraints are interdependent in this case, necessitating a small iterative process. In addition, the conditions for the wheel track will be condensed into a MATLAB code in order to determine the optimal value.

After defining the initial characteristics, the cross section dimensions and material properties must be determined. Several laminae stacking sequences are computed in MATLAB in an effort to improve the material's properties in multiple directions without sacrificing total weight and thickness. With the selection of the laminate sequence, one of the dimensions of each landing gear's cross section is also specified.

The final dimensions can now be iterated (using MATLAB functions). The emphasis of this iteration will be on achieving a good relation deflection-stress.

At the same time, minimum deflection for energy absorption is calculated via the approximation deducted in section 3.2.2 for the same cross section. The values are compared to verify the validity of said comparison and to obtain the deflection used to calculate the NATO STANAG wheel factor and, consequently, the forces involved in various landing configurations.

Finally, the initial design approach for the landing gear is obtained, and numerical methods must be employed to provide more accurate approximations of the component's behavior and validate the preceding steps.

A schematic representation of the methodology is presented in figure 4.1.

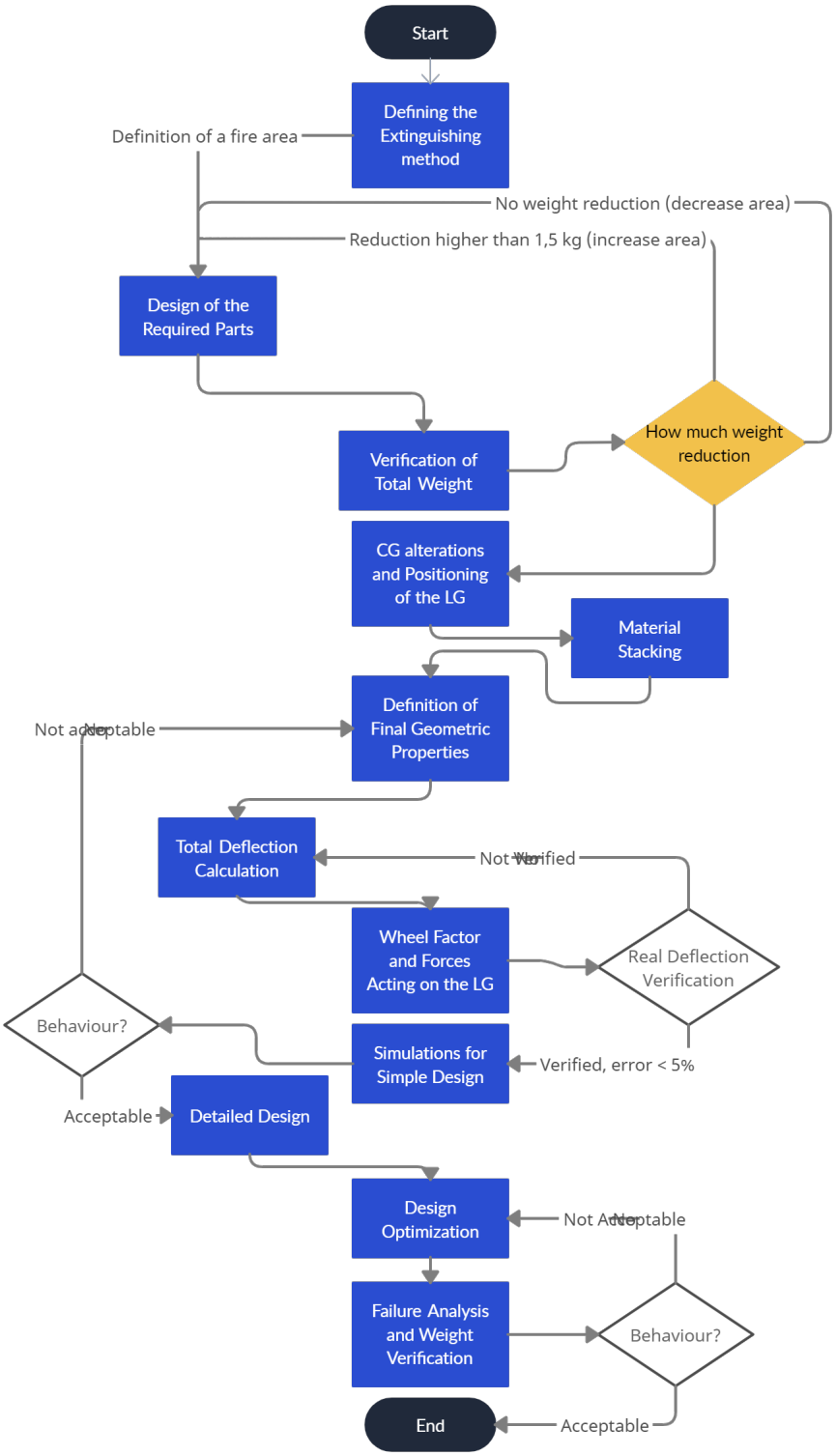

Figure 4.1: Schematic representation of methodology to be followed

4.1 Extinguishing Method Calculations

As previously explained, the fire suppression method chosen during the development of the drone may not be the most reliable. For this, a new method must be chosen, preferably from the conventional methods or the novel methods listed in section 2.1.3.

For this application, the CO_2 snow cannon was selected.

This method includes the design or selection of the fluid-expelling nozzle and the pressure vessels to be installed on the drone.

The design of the nozzle takes into account the pressures of admission for the two fluids mentioned by Engineer Joaquim Matos, as well as the fluid mechanics analysis of the behavior inside the nozzle.

Taking into account the required internal pressure, the vessels are designed to accommodate sufficient fluid to act on a specific area of operation.

4.2 MATLAB Operations

MATLAB codes will be used for complex operations that involve several iterations to obtain the optimal final result, the one that results in a better performance-cost relation, or rely on analysis of many options from which the most advantageous must be selected.

Firstly, a function was computed in order to obtain the value for **wheel track**. Several criteria were analysed however, due to lack of some data not all of the mentioned in section 3. were included in code. This is better explained in section 5.2.4. The code is given in Annex 1 (first code).

The inputs on this function are:

- H - the height of the landing gear to the CG;
- xMLG - longitudinal positioning of MLG;
- xNLG - longitudinal positioning of NLG;
- m - aircraft design lowest weight;
- V - maximum velocity on runway operations;
- CG - longitudinal position of the for CG;
- T - first value for the wheel track to start iteration.

The program will calculate other necessary properties such as the turning radius and wheel base.

Via an iteration cycle, the value for wheel tracks is computed regarding the criteria until the error is lower than 0.02 m. This value was defined arbitrarily as a value for which the difference to the optimal value is minimal.

The following is applicable to possible laminate sequences and computes the **equivalent properties of the laminate**. This code allows for rapid analysis of several stacking sequences. A task

that would take enormous amounts of time if performed via step by step calculations. The code is presented in Annex 1 as the second code.

For this function, the input values are:

- PropC - Vector with mechanical properties of prepreg UD carbon fiber;
- PropG - Vector with mechanical properties of prepreg S-glass fiber;
- k - Laminate stacking sequence, characterized by the orientation of the fibers in degrees;
- tC and tG - thickness of carbon and S-glass fibers, respectively.

Each output vector of mechanical properties, membrane and bending, includes the following,

- E1 - Young Modulus in fiber's direction;
- E2 - Young Modulus perpendicular to fiber's direction;
- v12 - Poisson ration in direction 1;
- v21 - Poisson ration in direction 2;
- G12 - Shear modulus;

This software expects the laminates to be symmetrical, both in orientation and selected material. Moreover, the disposition follows the method proposed by Bunsell of having the carbon fibers on the inside of the material and S-glass layers on the outside [77].

It works by computing the specific stiffness matrix for each lamina and than transforming to the global referential. With these, coefficients A_{ij} and D_{ij} are obtained, creating matrices A and D. B is not computed since for symmetrical laminates it is equal to 0.

As outputs the same mechanical properties are obtained in two vectors, so that outputs are,

- M - Vector with mechanical properties of equivalent laminate for membrane;
- B - Vector with mechanical properties of equivalent laminate for bending;
- T - Total thickness of the laminate and also one dimension for cross section;
- PGC - Percentage of carbon prepreg present on the laminate in volume

With the properties for the laminate calculated, a final function will allow for the use of curved beam theoretical models to compute stress and strain. Third function in Annex 1.

As mentioned before the inputs will be,

- EB1 - Young Modulus for bending;
- H - Height of LG;
- as - Known dimension for cross section (Thickness of laminate)
- b - Longitudinal distance from point of application of force to attachment with fuselage (or end of elliptical shape);
- F - Vertical force applied on a given solicitation

Several values for the dimensions will be studied and their resultant stress and strain analysed in order to choose the optimal combination. The output of this code is a matrix D with the values for width of the cross section and the equivalent total, vertical and horizontal deflection, and stress on critical zone.

4.3 Numerical Analysis: FEM

Analyzing simple mechanical components can sometimes be accomplished relying on basic mechanics methods that provide close-form solutions. For the majority of actual components, however, the analysis is not as straightforward, and the designer must rely on less effective approximations of closed-form solutions, experimentation, or numerical methods. There are numerous numerical techniques used in engineering for which digital computing is extremely useful. In mechanical design, computer-aided design software is prevalent, and finite element analysis is a numerical method that integrates well with it [88].

FEM provides a variety of applications, including static and dynamic stress and deflection analysis, free and forced vibrations, heat transfer, fluid dynamics, and buckling, among others. This work will concentrate primarily on mechanical analysis. The method is of great value to mechanical design and industry because it enables analyses and tests without requiring the physical piece, thereby accelerating product development and saving significant time and money.

A mechanical component is an elastic structure. With this analysis FEM discretizes the component in a finite number of small, well-defined, elastic elements [88]. Loads can be applied on either the elements or its nodes. The latter are the fundamental entities of the element as they are the connections between elements and define elastic properties, boundary conditions and applied forces. Figure 4.2 shows a FEM for a given structure.

A node has degrees of freedom, at most three transitional and three rotational degrees. Each element is defined locally and then all of them are assembled in a global matrix. With loads and boundary conditions, displacement on the degrees of freedom may be obtained using matrix operations. From there, strains and stress are easily obtained with equations of elasticity.

The displacements are obtained with,

$$[K]d = F \tag{4.1}$$

Where,

- K - Stiffness matrix;
- d - Displacements vector
- F - Applied forces vector

By discretizing the domain of a continuous structure, this method presents some errors that are inevitable. Firstly due to computational errors, related to round-off errors from the floating point calculations and formulation of the numerical integration employed however, most commercial

codes focus on reducing these errors. On the other hand, discretization errors may also occur. Using a finite number of elements to model a continuous structure introduces errors in matching geometry and the displacement distribution [88].

In figure 4.2, two problems can be seen. The large curvature is poorly modeled and the constant strain element will provide an average value for each element even though the displacements may differ a lot inside a given element.

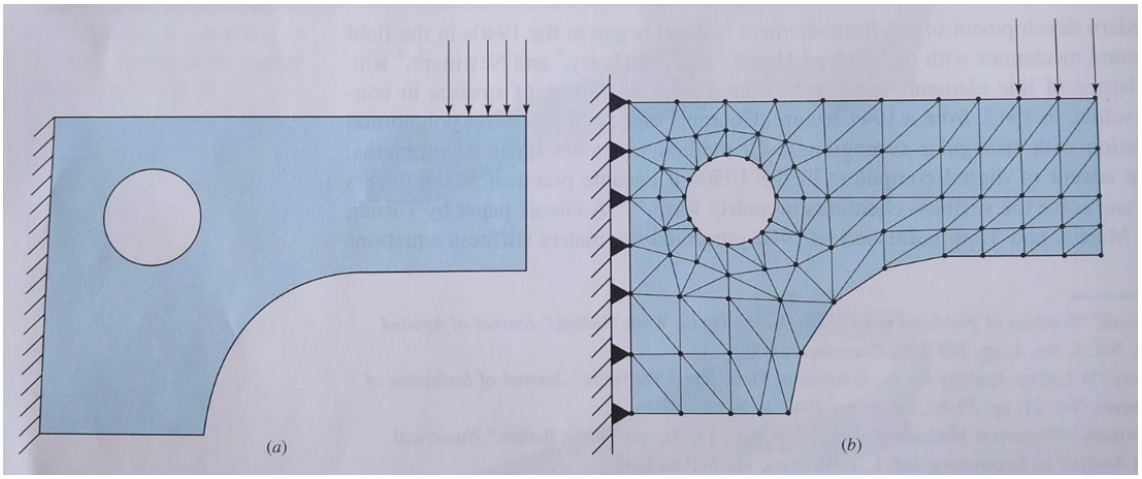

Figure 4.2: On the left, the idealized model; on the right, finite element model [88]

These problems can be solved by using smaller elements or using an element more suited to the application.

Convergence and error estimate is an important aspect of FEM calculations. The approximate solution should converge to an exact value when the number of elements increases to infinite. That is the solution of the model.

4.3.1 Software used

Two software were used for the development of FEM models:

SolidWorks

This software was used to model the first curved beams used as an approximation to the landing gear and finally the finished design itself.

It is a CAD 3D software based on parametric computation, creating 3D elements from elementar geometric operations.

Allows for files to be saved in several formats, some of which can later be imported on Abaqus.

It is provided by Dassault Systems.

Abaqus Unified FEA - Simulia

With a shorter name Abaqus, this is a commercial finite element software. It can be used in static, dynamic, linear or non-linear domains and offers an optimal approach to basic or sophisticated engineering problems.

It is also provided by Dassault Systems.

4.3.2 Elements

In finite element analysis, various geometric element shapes are used. The element library in the software's source code is comprised of these various types.

When creating the mesh for the component using the software, the preprocessor automatically generates the required nodes and elements.

Each element type has a distinct number of degrees of freedom that influence its application in various situations.

2D Line Elements

These elements are utilized when the cross-sectional dimensions are very small in comparison to the beam's axis length [89].

Beam elements are the most popular type. These elements can be oriented in any 3D space and must be assigned a cross section [90]. Orientation is determined by defining an orientation vector.

These elements can withstand axial extension, bending, and torsion. Truss elements may be used if only axial solicitation is present [89].

The simplicity of these elements enables rapid computation and facilitates any necessary model modifications [91].

Software assumes that the beam section (the intersection of the beam with a plane perpendicular to the beam axis) cannot deform in its own plane, except for a constant change in cross-section area introduced by an axial strain. [89].

Beams elements may have 2 or 3 nodes and up to 6 degrees of freedom. Examples of the 2 types of beam element are shown in figure 4.3

Figure 4.3: Beam elements with 2 and 3 nodes [89]

There are also beams with 2 integration points, quadratic, or 3 integration points, cubic.

For outputs, the software is able to compute the strain and stress components, the axial and shear forces and moments [89].

2D planar elements

These elements are applicable for analyzing thin structures. When one dimension (thickness) is substantially smaller than the other two. For Abaqus software these are shell elements [89].

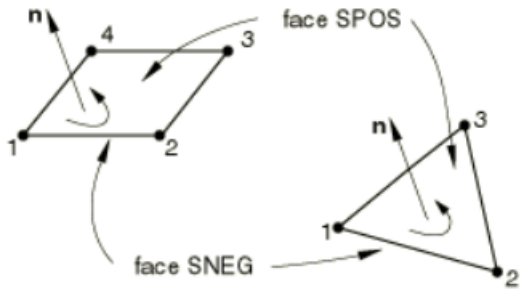

Figure 4.4: Triangular and Quadratic elements and its normal vector [89]

In this instance, the thickness is defined by the cross section. The elements have displacement and rotation degrees of freedom that are not out of plane [89]. Therefore, it does not permit rotation about the surface normal [90].

They can be either triangular or quadratic elements. Both options and their normal vectors are represented in figure 4.4.

Shell continuum elements

These elements closely resemble the 2D planar shell elements, but they exist in all three dimensions. It is crucial that these shells are oriented correctly, as the material's behavior in the thickness direction is very different from the in-plane direction.

Figure 4.5 describes the possibility of representing a specific element with either planar shell or continuum shell elements.

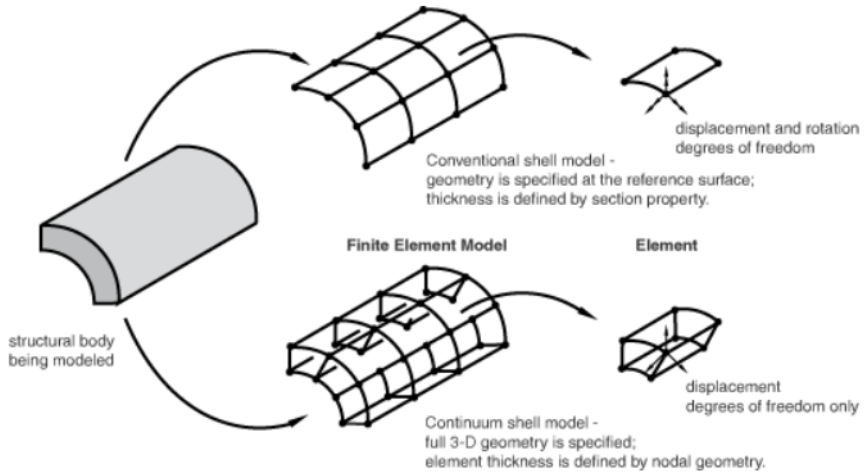

Figure 4.5: A part meshed with planar shell elements and continuum shell elements [89]

These elements also follow the triangular and quadratic approach however with double the number of nodes. The stacking direction, or thickness, is defined by the the nodal connectivity [89]. The elements are shown in figure 4.6.

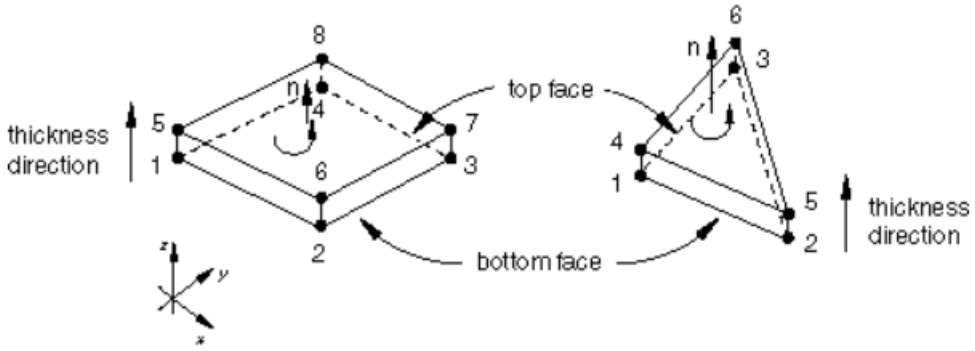

Figure 4.6: Types of continuum shell elements and its normal direction [89]

Abaqus adds the number of integration points per layer for each layer to determine the total number of section points for a composite section [89].

Typically, the required outputs consist of stress and strain behavior. These values are provided in the selected referential if a local orientation is specified. If no local coordinates are specified, the values are instead provided in the *xyz* domain [89].

Two methods can be used to validate the results via convergence and improve the accuracy of the results.

Reduce the size of the elements, thereby increasing the total number of elements on the mesh, or increase the number of nodes for each element. Figure 4.7 depicts an example of nodal number increase in 2D planar elements.

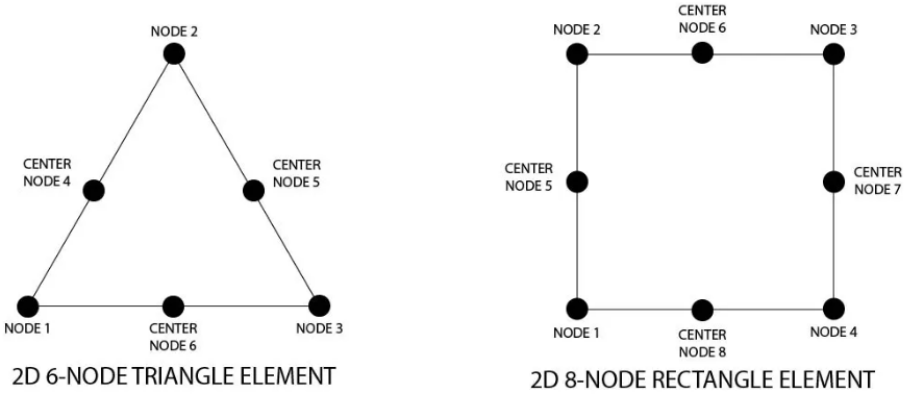

Figure 4.7: 2D shell elements with extra nodes [92]

4.3.3 Material Definition

Material definition is a crucial component of FEM analysis. In Abaqus, the material properties must first be added to the material library.

Here, you can choose between orthotropic and isotropic materials.

After that, a section is defined and assigned a material.

The sections are then assigned to the corresponding components of the landing gear or attachments.

The defined materials are:

- Material 1 - Orthotropic material with material properties equal to the equivalent laminate properties obtained via the laminate theories;
- Material 2 - Isotropic aluminum material used for the axle connection to the wheel and for the attachment components to the fuselage.

Moreover, the different laminae materials can be defined to validate the equations for equivalent composite material.

Chapter 5

Analytical Analysis

5.1 Extinguishing method

For this application, the CO_2 snow cannon was chosen because it is a simple, albeit promising, method that can have an impact on fighting forest fires and preparing and acting on the aftermath.

This method eliminates the need for firefighting balls on the drone and replaces them with two pressure vessels, one containing carbon dioxide and the other containing water and air, as well as a mixing nozzle.

For solenoid commands, the command to release the firefighting balls no longer exists, and a new command must be added to regulate the release of extinguishing mixture.

Now required are the design or selection of the nozzle and the sizing of the vessels.

5.1.1 Design of the Nozzle

The initial strategy for the design of the nozzle was to take into account the pressures of admission on the nozzle as specified by the responsible engineer.

The initial proposal is displayed schematically in the figure 5.1. Initial pressures for CO_2 and H_2O were 13 bar and 7 bar, respectively. In order to reduce the temperature and combine the gas with the fluid at 7 bar, CO_2 will be passed through a convergent tube. This tube is also depicted on the same diagram, with the entrance identified as position 0 and the exit as position e.

The properties in position 0 are given,

$$p_0 = 1300000 \tag{5.1}$$

Pa

$$T_0 = 20\ C = 293.15 \tag{5.2}$$

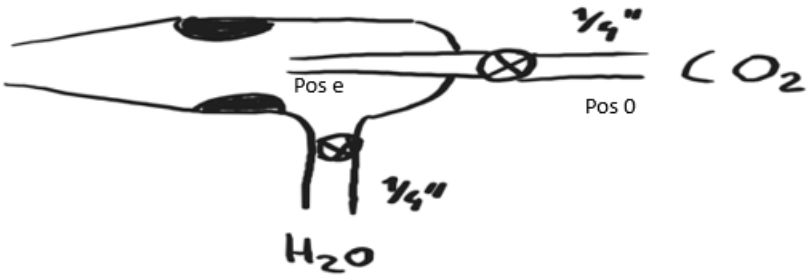

Figure 5.1: Schematic representation of the nozzle

K

$$\begin{aligned} k &= 1.289 \\ R &= 188.09 \\ \rho_0 &= 23.757 \end{aligned} \tag{5.3}$$

kg/m^3

(5.4)

Where p is the pressure, T the temperature, k is the specific heat at constant pressure divided by the constant heat at constant volume, R the constant for gases and ρ the density. All referred to the position in subscript.

For this initial properties, the critical pressure, p^*, must be obtained for Mach number = 1.

$$\begin{aligned} p^* &= p_0 * \left(\frac{2}{k+1}\right)^{\frac{k}{k-1}} \\ p^* &= 712040.6 \text{ Pa} \end{aligned} \tag{5.5}$$

Since $p^* < p_e$, until the gas reaches the end of the convergent tube, its Mach number will never be higher than 1. After this, a small expansion must occur so that the gas can reach the 7 bar and mix with H_2O coming from the other vessel.

At the end of the of the convergent, the properties are:

$$p_e = 712040.6 \text{ Pa}$$

$$T_e = \frac{p^*}{p_0} * \frac{\rho_0}{\rho_e} * T_0 \tag{5.6}$$

$$T_e = 256.14 \text{ K}$$

$$\rho_e = \left(\frac{p^*}{p_0}\right)^{\frac{1}{k}} * \rho_0 \tag{5.7}$$

$$\rho_e = 14.780 \text{ kg/m}^3$$

$$V_e = \sqrt{\frac{2k}{k+1}\frac{p_0}{\rho_0}} \tag{5.8}$$

$$V_e = 249.20 \text{ m/s}$$

Where V is the fluid speed.

And the mass flow is given by,

$$\dot{m} = V_e A_e \rho_e \tag{5.9}$$

$$\dot{m} = 0.0292 \text{ kg/s}$$

Where A is the area of the section.

Considering position b, after the small expansion upstream the convergent tube, the properties will suffer a small change,

$$p_b = 700000 \text{ Pa}$$

$$\rho_b = 14.585 \text{ kg/m}^3$$

$$T_b = 255.16 \text{ K}$$

For the H_2O that will be mixed with the CO_2 of point b, has its fluid properties,

$$p = 700000 \text{ Pa}$$

$$T = 298.15 \text{ K}$$

$$\rho = 1000 \text{ kg/m}^3$$

The Gas to Liquid Ratio (GLR) is defined as 2 since the development of the mixture is still in its early stages, and this ratio is situated in an insensitive zone in figure 5.2. Therefore,

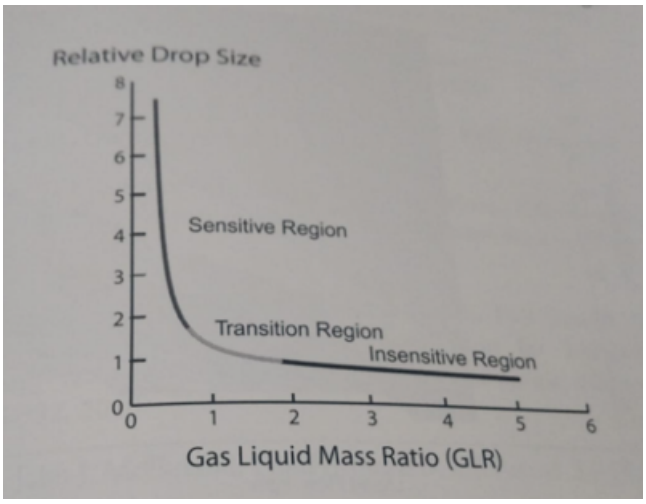

Figure 5.2: Relation between GLR and Relative size of drops. Representation of sensitive and insensitive to alterations zones [93]

$$\dot{m} = 0.0146 \text{ kg/s}$$
$$V = 0.4604 \text{ m/s}$$

The mixture will be analysed as an homogeneous fluid with mass ratio, m = 0.5. Total mass flow rate is $\dot{m} = 0.0437 kg/s$.

Since the density of H_2O is much higher than the density of CO_2, the mixture's density is given by,

$$\rho = \rho_{CO_2} * (1+m) \tag{5.10}$$
$$\rho = 21.88 \text{ kg/m}^3$$

To obtain R and k for the mixture, two different approaches can be taken.

Assuming no heat transfer between the fluids inside the mixture,

$$R = R_{C0_2}/(1+m) \tag{5.11}$$
$$k = k_{CO_2} \tag{5.12}$$

However this would be more appropriate for mixture where the velocity of the different phases are similar. This is not verified for this situation.

On the other hand, it can be assumed that there is a constant thermal equilibrium between both phases. Here R is calculated in a same way however, k is given by,

$$k = \frac{cp_{[}CO_2] + m * cp_{[}H_2O]}{cv_{[}CO_2] + m * cv_{[}H_2O]} \tag{5.13}$$

$$k = 1.075 \tag{5.14}$$

The temperature of the mixture will be 255.16 K, and it must be lowered further by passing the pseudo gas through a convergent-divergent.

The majority of the tube's characteristics are unknown. Only the properties at the entrance and those in the critical section where will have a Mach number of 1. By selecting a Mach number for the exit of this tube in accordance with iteration methods, various dimensions and pseudo gas properties are defined. An iteration is example can be found in Annex 2.

Since it leads to the exterior, the convergent tube is the final segment of the nozzle with an exit pressure of 1 atm. Also represented in the same Annex 2 are the fluid values at the exit of this final tube.

In addition, a choice must be made based on the temperature and velocity at the nozzle's exit, as well as its manufacturability.

However, after further consideration, the demand and expense of producing a customized nozzle outweigh the need to modify initial conditions in order to apply a commercially available nozzle.

Therefore, multiple suppliers were contacted in order to choose the nozzle that most effectively applies to the proposed technology.

The equations used for these approximations were obtained from the references, which can be consulted for additional information, [94] and [95].

5.1.2 Sizing of the Pressure Vessel

From BETE Spray Nozzles catalogue, the selected one was the XAD050.

The selected nozzle has internal mix and its spray shapes an hollow cone, that was referred by the manufactures as optimal for the required use. This spray can act with a reach of 4 m and at this range the mixture hits the fire with width of attack of 30 cm.

With this, it is possible to determine the area covered by the spray, using the dimensions from figure 5.3 by,

$$L_C = 2L_{dis} tan(\phi/2) \tag{5.15}$$

And,

$$A_C = \pi \left(\frac{L_C}{2}\right)^2 \tag{5.16}$$

Where the variables are defined in figure 5.3.

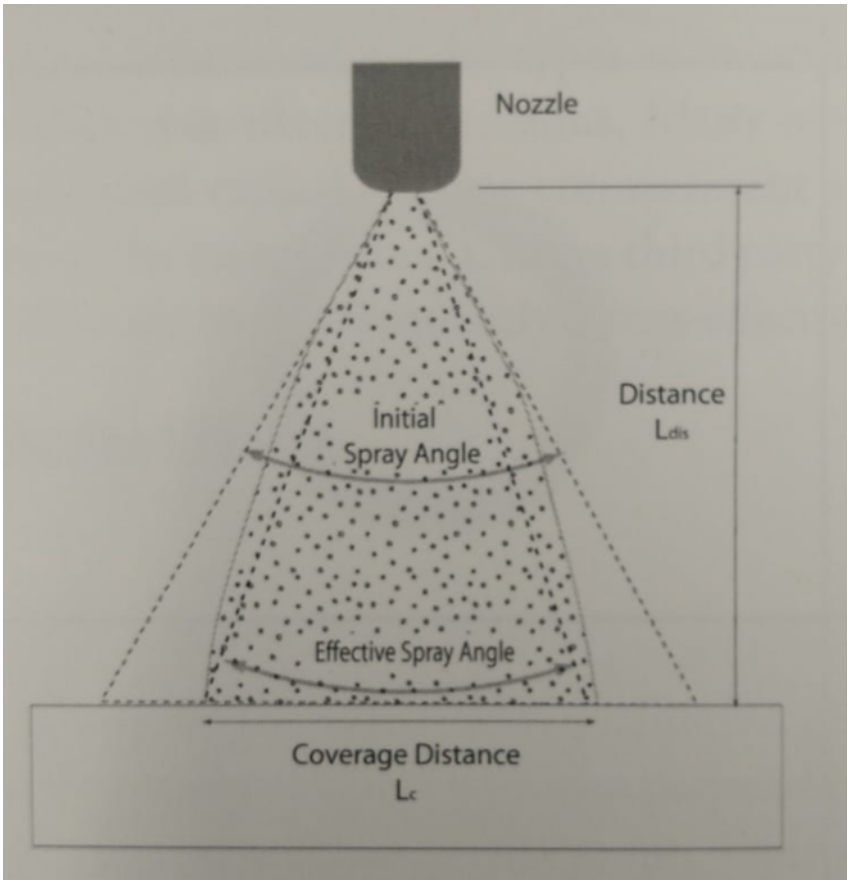

Figure 5.3: Dimensions for the calculations of area covered by a spray

The working pressures are 4 bar for both components while the flow rate is at 4.4 l/h of CO_2. The liquid to mass ratio will be the same as mentioned for nozzle design. The flow rate of H_2O will be of 2.2 l/h.

With the spray characteristics obtained, the pressure vessels can be designed by choosing a certain area of fire that can be tackled by the drone. After research and some discussion with the Póvoa de Varzim's fire department, an area that was believed to be acceptable was around 20 square meters.

Assuming that the drone will move over the fire, using its electrical capabilities, at 0.1 m/s approaching the area to a square of 4.5x4.5 m it logically understandable by figure 5.4 that the time during which the drone must be pouring the mixture onto the fire is of 675 s or 0.1875 h.

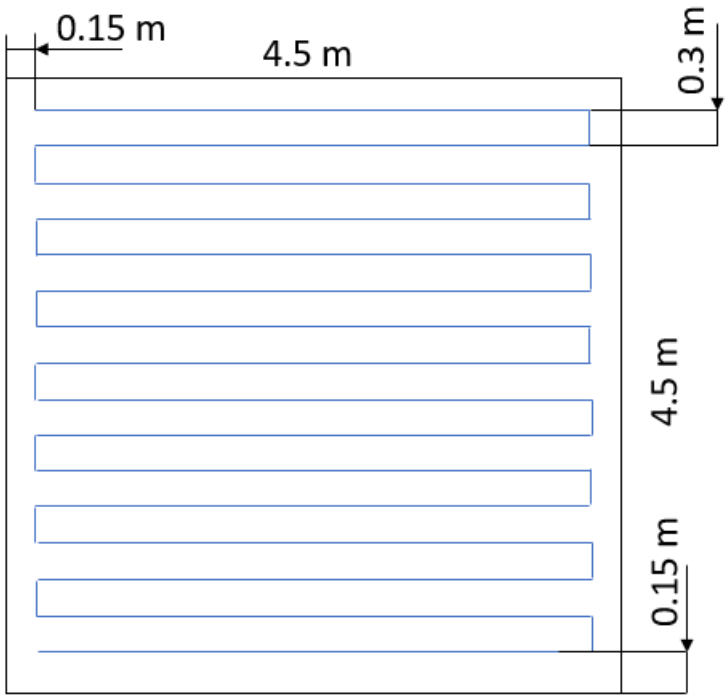

Figure 5.4: Representation of the path the drone must follow to tackle a 4.5x4.5 m fire

With the given flow rates, the volume of each component is

- $CO_2 \rightarrow 0.825$ l
- $H_2O \rightarrow 0.4125$ l

For a reservoir composed of a cylinder with spherical covers, its volume is given by

$$V = \pi r^2 L + \frac{4}{3}\pi r^3 \tag{5.17}$$

And, if $L = 3r$

$$V = \frac{13}{3}\,\pi\,r^3 \tag{5.18}$$

In order to occupy a smaller volume and create the pressure differential in order to force the fluid to flow towards the nozzle, the pressure inside the reservoir should be increased.

To be noted that, to assure the correct functioning of the mechanism, valves must be inserted in the fluid lines upstream the pressure vessels. For the CO_2 line a shut-off valve and a flow regulator valve must be inserted. For the H_2O case, only the shut-off valve is required. Pressure regulator valves were equated but its weight was deemed impractical for drone applications.

After contacting suppliers, valves by Festo were the ones selected for the CO_2 supplying line and for H_2O the selected supplier was Valsteam.

The combined weight of all the valves is roughly 1.1 kg, and they result in a 1 bar pressure drop each. Since data from the suppliers is still awaited, this value for pressure drop will be taken as provided.

The valves data sheet is annexed in the end.

Therefore, the pressure on the vessels will be 6 and 5 bar on the CO_2 and H_2O vessels, respectively, so that both reach the nozzle with the pressure referred by the supplier, 4 bar.

CO_2 Vessel

For the higher pressure the new volume, V', is calculated using the ideal gas law. Noting that, for a temperature of 25ºC, R_{CO_2} = 188.9 J/kg·K and M_{CO_2} = 44.01 kg/kmol.

$$\begin{aligned} p &= 4 \text{ bar} \\ p\,V &= \frac{m}{M}\,R\,T \\ 400000 \cdot 0.000825 &= \frac{m}{44.01} \cdot 188.9 \cdot 298.15 \\ m_{CO_2} &= 0.258 \text{ kg} \end{aligned} \tag{5.19}$$

For the new pressure,

$$\begin{aligned} p' &= 6 \text{ bar} \\ p'\,V' &= \frac{m}{M}\,R\,T \\ 600000 \cdot V' &= \frac{0.258}{44.01} \cdot 188.9 \cdot 298.15 \\ V'_{CO_2} &= 5.5 * 10^{-4}\,m^3 = 0.55\,\text{l} \end{aligned} \tag{5.20}$$

(Note: The CO_2 properties are given by Coelho, P. [96])

Replacing in equation 5.18,

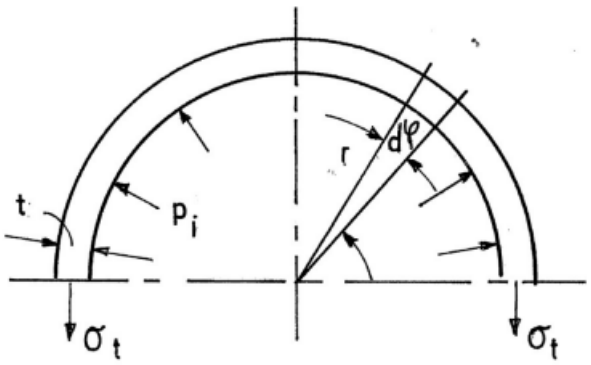

Figure 5.5: Stresses on the section of a thin wall cylinder with thickness t, internal radius r and internal pressure p_i [97]

$$r_{CO_2} = 3.43 \text{ cm}$$

The following step is obtaining the required thickness to support the stresses involved inside the reservoir. For a thin wall cylinder, in figure 5.5, $t/r \ll 0.1$ and stresses are given by:

Circumferential Stress

$$\sigma_t = \frac{p_i\, r}{t} \tag{5.21}$$

Axial Stress

$$\sigma_l = \frac{p_i\, r}{2t} \tag{5.22}$$

Radial Stress

- Inside wall

$$\sigma_r = p_i \tag{5.23}$$

- Outside wall

$$\sigma_r = 0 \tag{5.24}$$

Using Tresca's criteria the expression to obtain minimum value for thickness at the cylinder is very similar to the one given by code ASME for Boiler and Pressure Vessel. The code has that [98],

$$t_{min} = \frac{p_i r}{\sigma_{ced}/SF - 0.6p_i} \tag{5.25}$$

For the spherical covers, according to Marques, the minimum thickness is given by [99],

$$t_{min} = \frac{p_i r}{2\sigma_{ced}E/SF - 0.2p_i} \tag{5.26}$$

Where E is the welding efficiency and here it will be equal to 1.

After comparing prices and densities of common used examples, Aluminum 5454 H12 was the selected. Its properties, given by CES Edupack, are summarized in table 5.1:

Table 5.1: Aluminum 5454 H12 properties [74]

	SI Units	Imperial Units
Yield Strength	195e6	28282.4
Poisson's Ratio	0.33	0.33
Density	2690	5.219 (slug/ft3)

So, for the CO_2 pressure vessel, with a SF of 4, thickness will be,

- Cylinder $\rightarrow$ 0.425 mm
- Spherical cover $\rightarrow$ 0.211 mm

Special case on the conjunction cylinder-semisphere

On the conjunction between cylindrical shell and the spherical cover there is discontinuity stress. These forces are represented in figure 5.6. The equation for compatibility at point a is given by:

$$\begin{aligned} &\text{deflection on cylinder due to } p + H_O + M_0 = \\ &= \text{deflection on the spherical cover due to p } + H_O + M_0 \end{aligned} \tag{5.27}$$

And

$$\begin{aligned} &\text{rotation on cylinder due to } p + H_O + M_0 = \\ &= \text{rotation on the spherical cover due to } p + H_O + M_0 \end{aligned} \tag{5.28}$$

Note: the radius on the spherical cover to the thickness will be increased so that the parts match on the outside. r' = 3.69 cm.

H. Jawad, provides equations that allow to calculate the stresses involved in this interaction. For these, the properties are converted to imperial units. It gives constants to solve the equations,

$$\beta = \sqrt[4]{\frac{3(1-v^2)}{r^2 * t_{cyl}^2}} \tag{5.29}$$

$$\beta = 8.277$$

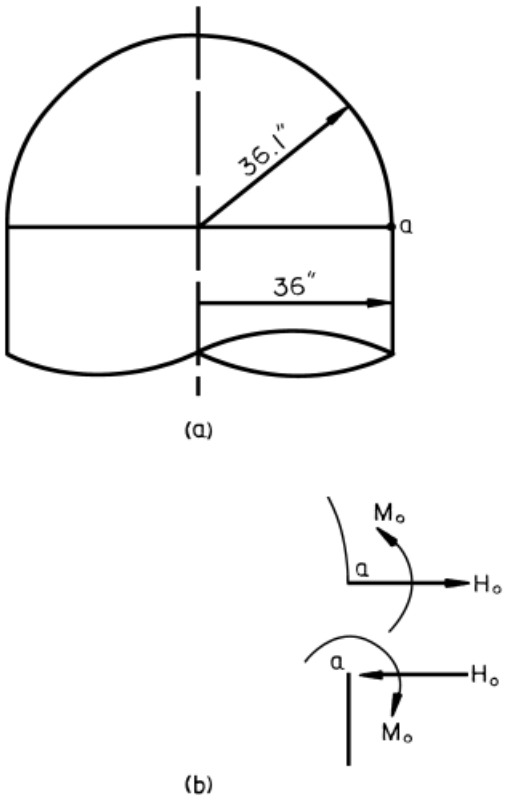

Figure 5.6: Behaviour on the junction between cylinder and spherical cover

$$D = \frac{E * t_{cyl}^3}{12(1-v^2)} \tag{5.30}$$
$$D = 4.265e^{-7}\, E$$

$$\lambda = \sqrt[4]{\left(\frac{r'}{t_{sph}}\right)^2 3(1-v^2)} \tag{5.31}$$
$$\lambda = 17.0073$$

Using equations 5.1.2 and 5.1.2, it is possible to calculate the moment and stress on the junction

$$2.573H_O + 16.87M_O = 1 \tag{5.32}$$
$$H_O + 36.42M_O = 0 \tag{5.33}$$

So,

$$H_O = 0.474\ lb/inch = 8.465\ \text{kg/m}$$

$$M_O = -0.0130\ inch-lbs/inch = -0.0579\ \text{Nm/m}$$

The negative value for the momentum means that it has the contrary direction than the predicted in figure 5.6 b).

H. Jawad also gives equations for the hoop and membrane stress on the cylindrical and spherical shells, so that,

Cylindrical shell

$$\text{longitudinal bending stress} = \frac{6M_O}{t^2} = 1.923\ \text{MPa}$$

$$\text{longitudinal membrane stress} = \frac{pr}{t} = 51.8\ \text{MPa}$$

$$\text{total longitudinal stress} = 27.823\ \text{MPa}$$

$$\text{hoop bending stress} = 0.3 * 1.923 = 0.577\text{MPa}$$

$$\text{deflection at point a} = w = 8.64\text{mm} \qquad \text{Via eq 5.1.2}$$

$$\text{hoop membrane force} = \frac{Etw}{r} = 19515.9\ N/m$$

Since the membrane force is applied through the thickness,

$$\text{hoop membrane stress} = 45.92\ \text{MPa}$$

$$\text{total hoop stess} = 46.497\ \text{MPa}$$

Spherical cover shell

$$\text{longitudinal stress} = \frac{pr'}{2t} + \frac{6M_O}{t^2} = 60.27\ \text{MPa}$$

$$\text{hoop stress} = \left(\frac{pr'}{2} + H_O\lambda - \frac{2M_O\lambda^2}{r'}\right)/t = 48.84\ \text{MPa}$$

This shows that the discontinuity stresses create an area on the vessel where the stress solicitations are larger than the for the rest of the vessel. For additional reading, one must consult [100], which contains all of the theory and equations used.

These might require the use of a stiffening ring in order to control the stress on the conjunctions between cylinder and spherical covers and maintain the SF used. However, because of its smaller dimensions, its mass will not be accounted for in the total mass added by the extinguishing method.

To obtain the total mass of the vessel, it will be assumed, for calculation purposes, that the thickness of the vessel will abruptly change on the connection between the different shapes composing the reservoir,

$$\begin{aligned} m_{vessel_{CO_2}} &= V_{vessel_{CO_2}} * \rho_{Al} \\ m_{vessel_{CO_2}} &= \left[(\pi(r+t_{cyl})^2 - \pi r^2) * 3r + \frac{4}{3}\pi((r'+t_{sph})^3 - r'^3) \right] * \rho_{Al} \\ m_{vessel_{CO_2}} &= 0.038\text{kg} \end{aligned} \tag{5.34}$$

On a full vessel,

$$m_{CO_2\ +\ vessel} = 0.296\text{kg} \approx 0.3\ \text{kg} \tag{5.35}$$

H_2O **Vessel**

The method for the water vessel is quite similar to the prior one. However, it must be considered that the water is an incompressible fluid. Therefore, in order to pressurize the tank, air,a compressible fluid, must also be stored with the water. A acceptable proportion is 30 % of air and 70 % of water in volume. Recalling, V_{H_20} = 0.4125 l, the volume of air in the vessel will be 0.1768 l, at 4 bar.

For the same method to increase pressure, now to 5 bar since only 1 valve is used. Only the air can be compressed so the volume of water will remain the same, as well as the mass,

$$m_{H_2O} = 0.4125\ \text{kg}$$

Respecting the equation for ideal gases, equation 5.1.2, and for T = 25ªC,

$$\begin{aligned} R_{Ar} &= 287\ \text{J/kg}\cdot\text{K} \\ M_{Ar} &= 28.96\ \text{kg/kmol} \end{aligned}$$

(Note: The H_2O properties are given by Coelho, P. [96])

So,

$$m_{air} = 0.0239 \text{ kg}$$
$$V'_{air} = 0.141 \text{ l}$$

The total volume will be of 0.554 l and will occupy a vessel with the same cylindrical shape as the CO_2 one.

$r_{V_{H_2O}}$ will be obtained replacing on equation 5.18,

$$r = 3.44 \text{ cm}$$

Regarding the thickness, according to the same equations 5.25 and 5.26, and With a SF of 4,

- Cylinder $\rightarrow$ 0.355 mm
- Sphere $\rightarrow$ 0.177 mm

The same strategy will be used. So there will be the use of stiffeners on the connection between cylinder shaped reservoir and its spherical covers.

And the total mass on the vessel (m_{tot}) will be equal to

$$m_{tot} = 0.4364 \text{ kg} \tag{5.36}$$

The mass of the vessel's material is given by the same equation as 5.34,

$$m_{vessel_{H_2O}} = 0.0282 \text{ kg} \tag{5.37}$$

On a full vessel,

$$m_{fluid\ +\ vessel} = 0.4646 \text{ kg} \approx 0.5\ 0.5 \tag{5.38}$$

So, the total mass added to the drone by the introduction of this method will comprehend the mass of both vessels filled with the required fluids and the valves. The other components will be negligible in comparison.

$$m_{fluid\ +\ vessel} + m_{CO_2\ +\ vessel} + m_{valves} = 1.861 \text{ kg} \tag{5.39}$$

This represents a massive reduction on the total mass of the drone when compared with the 2.8 kg of extinguishing balls solution. Allowing for a reduction on the total mass of the drone of almost 1 kg ($m = 11.682kg$), while improving the efficiency on an area of up to 20 m^2.

5.1.3 Center of Gravity Correction

As section 3.2 refers, the positioning and variation of the aircraft's CG will directly impact the positioning of the landing gear.

The alteration to the method used by the drone for extinguishing fires, by altering the total mass, will have an impact on the CG.

For the calculation of the new CG, coordinates x will be referring to each component's CG on an axis with origin on the front tip of the drone and positive towards the tail. The initial assumptions and sets of components used on the first drone design will be maintained with certain changes:

- For main battery and control, the longitudinal position is set at the tip of the drone (x=0). However, this is physically impossible. The battery has 205 mm of length and assuming its positioned 150 mm from the tip, x = 250 mm;
- The set guimball and radiometric thermal camera are not accounted for in the calculations. Their combined weight is 0.4734 kg and it is positioned near the tip of the drone (x = 150 mm);
- On review of the weights, it was discovered that sets 1 and 2 had wrong values for their mass. An electric motor has 546 g and a set of 2 propellers 87.88 g;
- From the carbon fiber used on the drone, only the tail was considered. Annex 5 form the previous work, mentions 1 kg of material. Therefore the missing 0.685 kg will be accounted for and positioned (via approximations according to the dimensions on design) at x = 700 mm.

The sets of components used for CG calculation were:

- 1 - set 1 (front electric motor + variable speed drive + 2 propellers)
- 2 - set 2 (back electric motor + variable speed drive + 2 propellers)
- 3 - main battery + drive
- 4 - servomotors on the tail
- 5 - tail's mass approximation
- 6 - internal combustion engine
- 7 - combustion motor's propellers

- 8 - fuel + tank + secondary battery
- 9 - extinguishing material
- 10 - guimball + thermal camera
- 11 - wing + fuselage material

On table 5.2, the mass of each set and its CG longitudinal position regarding the already defined axis is presented.

Table 5.2: Each set of drone's components and their total mass and respective longitudinal position

set	**m (kg)**	**x (m)**
1	0.63388	0.139
2	0.63388	1.165
3	3.6888	0.25
4	0.165	2.0011
5	0.315	2.0011
6	0.1	1.149
7	1.21	1.05
8	1.5118	0.74
9	1.861	0.6155*
10	0.4734	0.15
11	0.685	0.7

*The positioning of the extinguishing CO_2 cannon will be made so that its on the same axis as the drone's CG on full fuel tank. This is a condition already set in the original design [1], and it is created so that the rapid discharging of the tanks, and, consequent alteration on weight, does not have an impact on drone performance.

Note: The total mass of the components is still short of the new total mass of the drone by almost 0.5 kg. However this will be assigned to several small parts that were omitted and for lack of information will no be accounted for.

The position of the CG will be affected by the amount of fluid on the fuel tank, CO_2 vessel and H_2O vessel.

The extreme options will be for full fuel, full extinguisher (1); full fuel, empty extinguisher (2); empty fuel, full extinguisher (3); empty fuel, empty extinguisher (4).

For positioning the extinguisher vessels, first the CG is calculated for the drone without set 9.

$$CG = \frac{\sum_{i=1}^{8} m_i x_i + \sum_{i=10}^{11} m_i x_i}{\sum_{i=1}^{8} m_i + \sum_{i=10}^{11} m_i} \tag{5.40}$$

$$CG = 0.6155 \text{ m}$$

Since this will be equal to the longitudinal position of set 9, $CG^1 = CG^2 = 0.6155$ m.

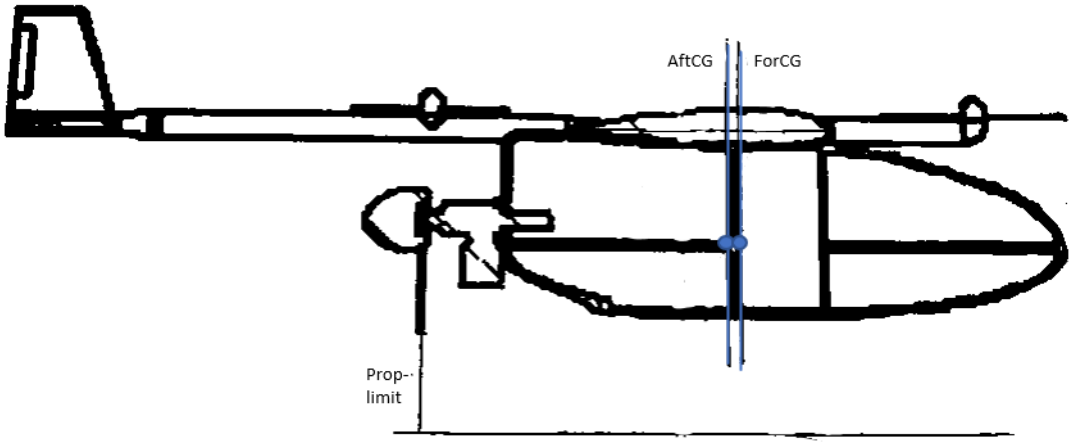

Figure 5.7: Step 1 for graphical positioning of the MLG

From annex 5, the mass of fuel on a full tank is 1.2798 kg [1]. So, for configuration 3,

$$CG = 0.5995 \text{ m}$$

And having that total mass of extinguisher pseudogas is 0.726 kg, CG on configuration 4 is,

$$CG = 0.5984 \text{ m}$$

So the aft and forward most CGs have been obtained,

$$aftCG = 0.6155m \rightarrow m = 11.761 \text{ kg}$$

$$forCG = 0.5984m \rightarrow m = 9.790 \text{ kg}$$

Note: The mass is already accounting for the fractions of total mass dismissed for CG calculations.

5.2 Landing Gear Geometric Requirements

5.2.1 Positioning

The steps for graphical positioning of the main landing gear are explained in section 3.2.1. With a side view of the drone from the technical drawings [1], these steps were performed, and represented with figures 5.7, 5.8 and 5.9.

This graphical method results in an approximate position for the main landing gear at $x = 0.71$ m from the tip of the drone.

For the nose gear, the requirements of static load distribution are used from equations 3.1 and 3.2, summed up in table 5.3.

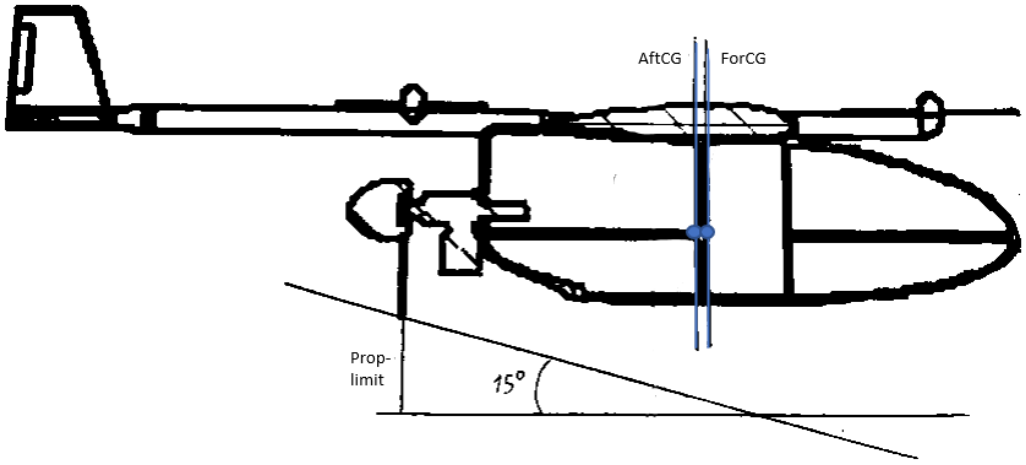

Figure 5.8: Step 2 for graphical positioning of the MLG

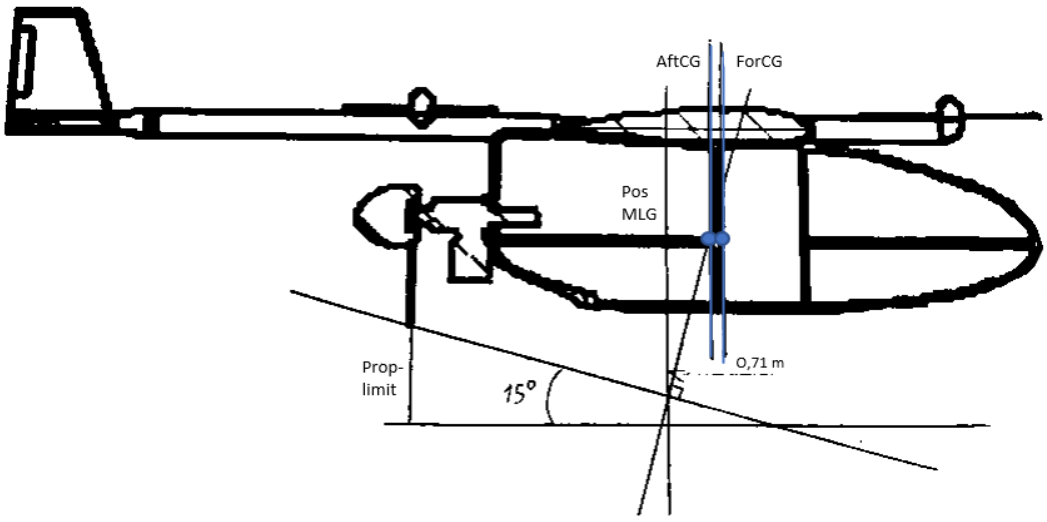

Figure 5.9: Step 3 for graphical positioning of the MLG

Table 5.3: Variables to obtain longitudinal coordinates for the nose gear; coordinates in meters

x_{MLG}	CG	B_M	B	x_{NLG}
0.71	0.5984	0.1116	0.559	< 0.152
0.71	0.6155	0.0945	0.945	> -0.235

From the table, the negative value for minimum x_NLG implies that, for this requirement, the nose gear can be placed on the nose of the drone. However, in order to position it on lowest part of the fuselage (use less material, create less drag) a closer value to the maximum allowed will be used,

$$x_{NLG} = 0.10 \text{ m}$$

5.2.2 Landing Gear Height

It will be measured from the ground to the fuselage where the gear will be attached.

From the technical drawing its understandable that the tip of the propeller is closer to the ground than the fuselage's bottom. However, values are not given on this thesis.

The vertical position of the CG is also graphically positioned very close to the root of the propeller.

It is known that the propeller must clear the ground for at least 0.2 m and a SF of 1.1 will be used to account for the difference between tip of the prop and fuselage.

Height of the landing gear will be given by,

$$H_{LG} = 0.2 * 1.1 = 0.220 \text{ m}$$

The takeoff rotation ground clearance requirement must be met. In order to compensate for the extra rotation the drone will perform after lifting from the ground, α_{TO} = 15° and AB is obtained via the analysis of the technical drawings. From equations 3.4,

$$\alpha_C = 27.7^\circ$$

Respecting the condition imposed by equation 3.3.

Moreover, this great difference suggests that the empirical prop limit of 0.2 m is to be applied to aircrafts with the propeller further away from the CG. The prop limit will now be reduced to the suggested by the graphical method, 0.1778 mm [38]. Then,

$$\alpha_C = 25^\circ$$

$$H_{LG} = 0.1778 * 1.1 \approx 0.2 \text{ m}$$

5.2.3 Wheel Base

The wheel base has been obtained by the graphical method allied to the determination of cargo distribution. Therefore,

$$B = 0.61 \text{ m}$$

$$B_{M_{ForCG}} = 0.112 \text{ m}$$

$$B_{M_{AftCG}} = 0.094 \text{ m}$$

$$B_{N_{ForCG}} = 0.498 \text{ m}$$

$$B_{N_{AftCG}} = 0.516 \text{ m}$$

5.2.4 Wheel Track

The limits for wheel track length are given by the requirements explained in section 3.2.1.3.

The height of the landing gear measured on the CG is given by the defined height plus the length of the propeller, 0.2885 m [1].

$$H_{CG} = 0.4885 \text{ m}$$

For ground lateral control requirements, the centrifugal force at an extreme turn is calculated. The speed is set to 2.00 meters per second, and the radius is calculated so that the drone can turn on a dime.

The majority of the components of ground lateral stability are unobtainable, but if the previous requirement is secured, the wheel track length will also conform to this one.

The structural integrity requires the second moment of inertia. However, neither the type nor dimensions of the 4-digit airfoil used are specified; only the wing span and wing area are provided. A worst-case scenario is used to calculate the wheel track's structural integrity's maximum allowable limit. Maximum wheel track is still determined by a maximum deflection of half the height of the landing gear (0.1 m), the Young Modulus of the carbon fiber perpendicular to the fibers (8 GPa), and wing dimensions of 0.25x0.03 m, which is a very conservative approach.

Following equation 3.17,

$$T \leq 220 \text{ m}$$

Which means that for this case, structural integrity will not be a problem.

Finally, the three remaining criteria will be used and iteration will be made following the MATLAB code in Annex 1, first code. The final value for the wheel track is,

$$T = 0.5315 \text{ m}$$

And,

$$\phi_{OT} = 32.17^{\circ}$$

The geometric characteristics of the landing gear follow presented in table 5.4

Table 5.4: Landing gear geometric characteristics

Landing Gear	
Height	0.20 m
Height_{CG}	0.4885 m
Base	0.61 m
Track (T)	0.5315 m
x_{NLG}	0.10 m
x_{MLG}	0.71 m

5.3 Landing Gear Functional Requirements

For the proper functioning of the landing gear, energy absorption requirements, introduced in section 3.2.2.1 must be complied and the loads created in several situations and drone configurations must be supported.

For reference, the total weight of the landing gear must be limited. In compliance with Roloff, the maximum value was set at 5% of the maximum takeoff weight [101].

5.3.1 Static Loads

For the static situation, the loads on main and nose landing gear will only depend on the weight and the position of the CG. So the values will be calculated for the two extreme configurations of CG, aft and forward. The loads are presented in table 5.5, with F_{NLG} the reaction on the nose gear and F_{MLG} the one on each of the main gears.

Table 5.5: Static Loads on Nose and Main Landing Gear

	Aft CG	For CG
UAV Weight (kg)	11.76	9.79
F_{MLG} (N)	48.75	39.24
F_{NLG} (N)	17.87	17.57

However it was identified that the maximum static load on the nose gear happens when the fuel tank is empty and the extinguishers are on full capacity. Here,

$$F_{NLG} = 18.61 \text{ N}$$

5.3.2 Tire and Wheel Selection

After researching different suppliers and comparing options and prices, it was found that Ultimate Jets offer 3D printed UAV tires at lower cost than any other supplier.

These tires are made from TPU polymers and offer an hardness option perfect for high temperatures while allowing use on rough or abrasive runways. This is a major advantage on this project since it considers the high temperatures present on firefighting and permits for landing of the UAV in a wider range of runways.

These tires offer customization so, if there is the need for higher load bearing capacity, the tire can be altered. However, the properties assumed for design will be the regular ones.

The wheels are also offered by the same supplier. Made from Al 6061 and CNC machined.

The chosen tires are R45-90 for the main gear and R45-70 for the nose gear. The first number being the inside diameter and the latter the outside one. The wheels will, logically, have 45 mm of outside rim and a 4mm diameter of axle.

Tire, wheel and assembly are shown in figure 5.10.

Figure 5.10: Ultimate Jets' Tire, Wheel and Tire-Wheel assembly on axle

However, after contacting the suppliers, no response was obtained about tire properties. So, even tough it is known that the tire will be responsible for absorbing some of the energy on impact this amount will not be calculated. Therefore, for the following assumptions, it is considered that the stress on touchdown is applied directly on the landing gear leg. This consideration is possible since it will be a safer approach to the problem, the design of the landing gear leg will have a higher safety factor.

To obtain the stress-deflection relation on the tire, it would require further tests by applying a certain pressure on it and analysing its total deflection.

5.3.3 Material Selection and Elastic Properties

For further calculations on different loads and landing gear behavior, the elastic properties of the material must be obtained.

Using the classic laminate theory, discussed in section 3.4.6, different stacking sequences may be analyzed in order to obtain the correspondent equivalent laminate bending and membrane properties.

Using the second MATLAB code of Annex 1, several configurations were analysed.

For the main directions of the laminate, direction 1 was defined as the tangent along the curve of the landing gear, both on the main and nose gears. Direction 2 was defined differently for each gear. On the main gear, it is oriented parallel to the forward movement of the drone with the same direction and on the nose, it is oriented perpendicularly to the movement. Direction 3, perpendicular to the other two, defines the stacking orientation on each landing gear segment.

The orientation of each layer is defined relative to direction 1.

When comparing the results for each layer the aim was on having similar Young Modulus in both direction 1 and 2 since direction 1 would have to be decreased to allow for deflection on landing and direction 2 would have to be increased in order to sustain drag forces. Knowing that in direction 3 only the matrix will have an impact on the behaviour of the material resulting on a low Young Modulus.

The laminae used are prepreg carbon and S-glass fiber and their properties are summarized in table 5.6.

Table 5.6: Properties of the used prepreg laminae [74]

	Carbon Fiber + Epoxy	S-glass + Epoxy
E_1 (GPa)	129	40
E_2 (GPa)	8.5	12.7
v_{12}	0.33	0.27
v_{21}	0.021	0.07
G_{12} (GPa)	4	4.7
ρ (kg/m^3)	1560	1840
$thickness(mm)$	152	226

Every laminate analysed is symmetric both on orientation and on types of fiber. Following the proposed laminate composite by A. R. Bunsell [77], the glass fibers are be placed on the outside and the carbon fiber on the inner part of the laminates.

5.3.3.1 Main Gear

For the main gear, 7 different laminate sequences were analysed with 28. 32, 36 or 40 plies. Here, the thickness of the laminate must be minimized since this dimension will be perpendicular to movement, creating drag.

Firstly, the laminates were loaded for a static configuration. Considering a first basic design of an elliptical leg, the stresses and displacements generated on the different laminate were analysed for a maximum cross section. The value was obtained for the maximum weight of the main landing gear set at 75% of the total landing gear weight (which by itself was set at 4% of the takeoff weight instead of the 5% defined previously to allow for further design flexibility).

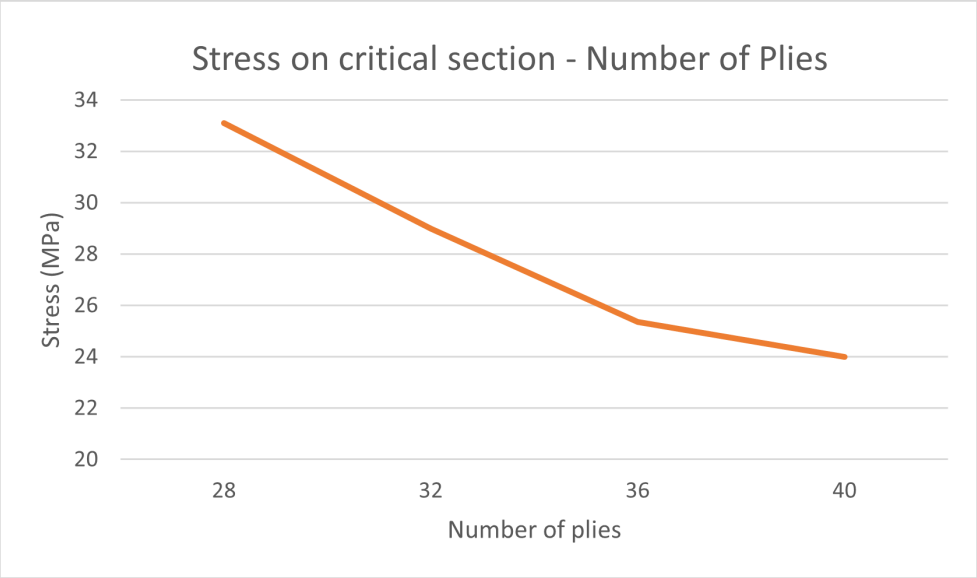

Figure 5.11: Stress on recessed elliptical beam per number of plies on the laminate

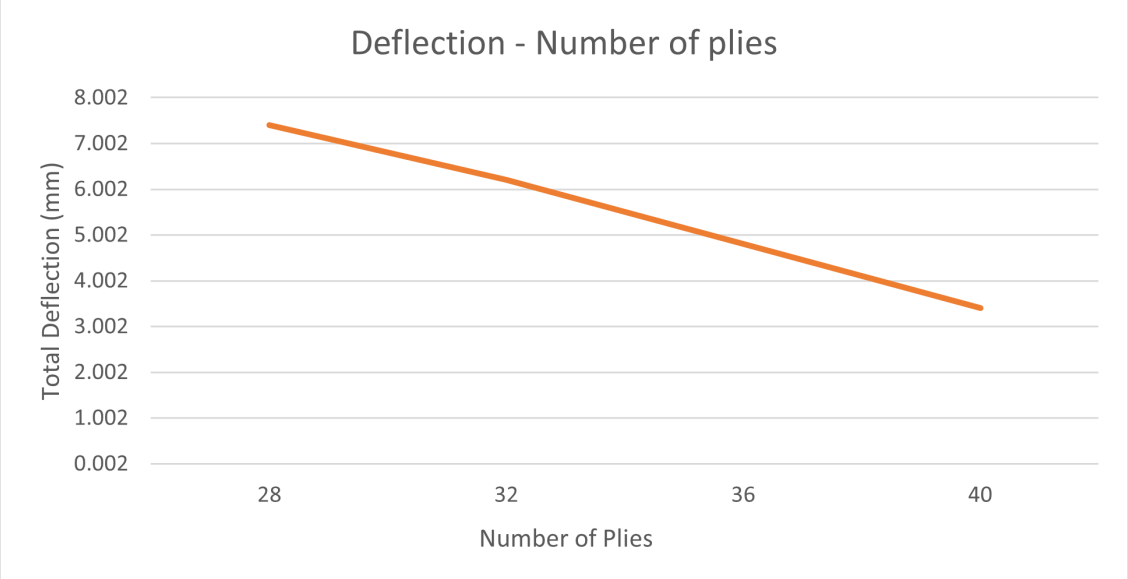

Figure 5.12: Maximum deflection on the beam per number of plies on the laminate

Figures 5.11 and 5.12 graphically represent the variation of maximum stress and displacement on the beam per number of laminae on the laminate.

From the graphic on figure 5.11 it is a fact that the increase in laminate thickness creates a significant decrease in maximum stress on the structure. Stress on the laminates with 28 and 32 plies is, as expected much higher than the one obtained for thicker laminates. This may become an issue for higher order solicitations as in tail down landing configurations.

However, it must be noted that, according to equation 3.62, from NATO-STANAG legislation [57], a decrease in deflection of the landing gear is associated with an higher load to be used for

analysis on landing situations.

The difference in deflection between using a 36 or a 40 ply laminate is not compensated by the small decrease in stress. Moreover, less laminae is associated with lower drag. Therefore, the selected laminate was a 36 ply.

Table 5.7 and graphs on figures 5.13, 5.14 compare the two 36 ply proposed laminates without the introduction of fairings. Deflection was obtained for static condition, and the reaction force was obtained via the first energy absorption approximation.

Table 5.7: Bending mechanical properties for the two 36 ply laminates

	E1 (GPa)	E2 (GPa)	v12	G12 (GPa)
k5	28.815	22.581	0.2662	9.636
k6	27.150	26.297	0.2817	9.272

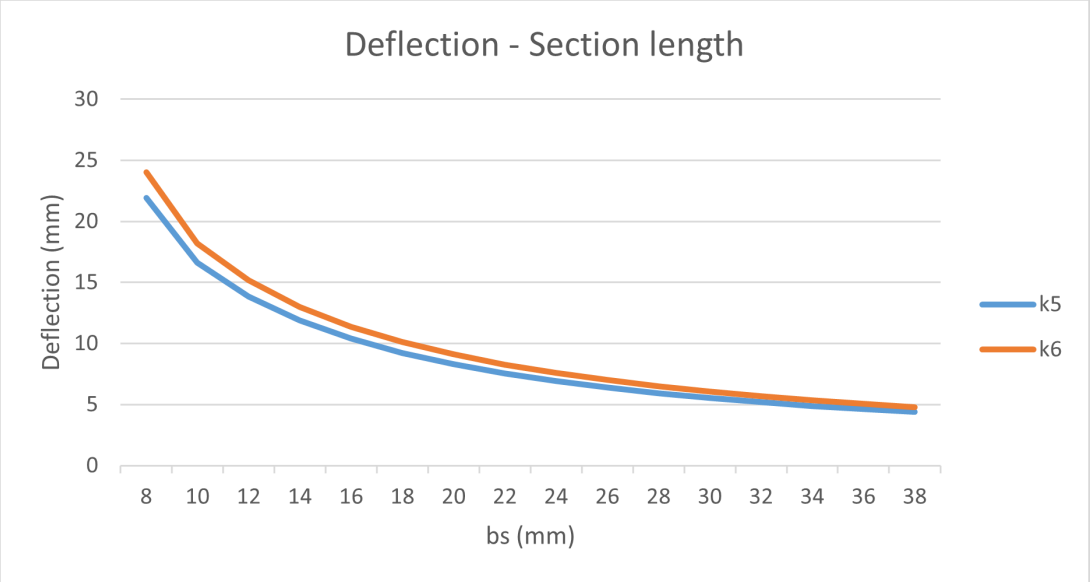

Figure 5.13: Deflection on the MLG per length of its cross section for static load, static condition

As it can be seen there are not a lot of relevant differences between both options. However, k6 has a higher Young Modulus on direction 2 which may be beneficial in order to reduce the deflection caused by drag forces.

The critical section on the landing gear will be situated on the outer layers. Here lies the main difference between these laminates, k5 has an outer lamina oriented at 45° and k6 at 90°.

According to D. Gay, 90° plies hmust sustain lower total stress compared to 45° ones for the same solicitation of the laminate. Most importantly, considering that shear strength is much lower than tensile or compressive strength in any direction, it is very advantageous that on a ply oriented 90° from the main solicitation the shear stress is reduced [72].

Likewise, and following the recommendations from section 3.4.5, laminate k6 will be selected and its configurations is as follows:

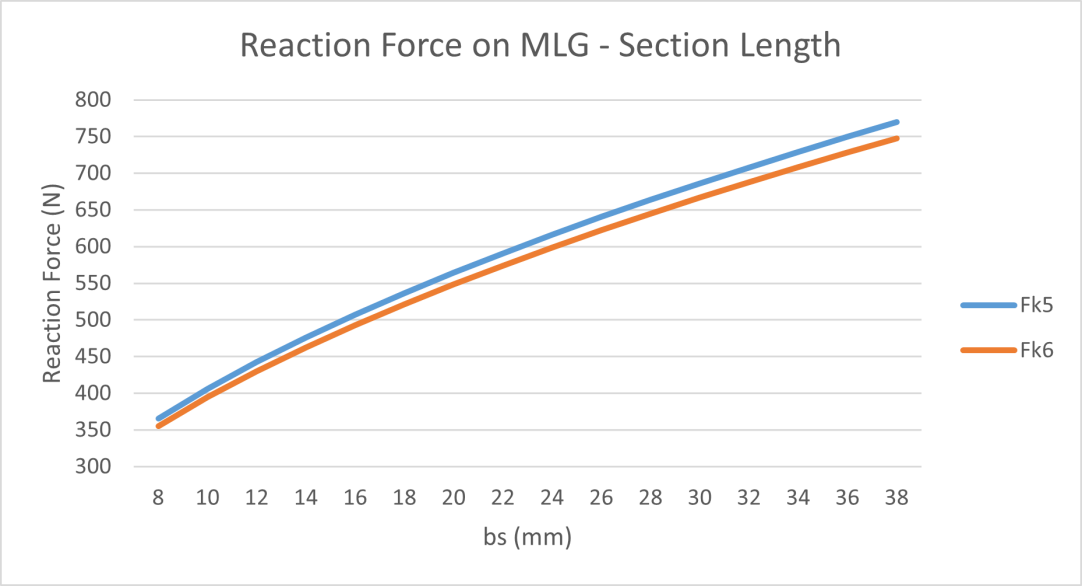

Figure 5.14: Reaction force acting on the landing gear to simulate landing conditions per length of its cross section

$$k6 = [90, +45, -45, 0_2, 90, -45, +45, 0_2, 90, -45, +45, 0, -45, 0, 45, 0]_S$$

5.3.3.2 Nose Gear

The loads acting on the nose landing gear are significantly lower than those analyzed for the main landing gear. Stacking sequences of lower laminae may therefore be utilized.

Here, and going back to figures 5.11 and 5.12, the possibilities accounted for nose gear design were of 28 and 32 laminae.

Regarding the main gear analysis, the cross section's dimensions must be specified. Now,the dimension parallel to movement, and therefore most responsible for drag, will be the width of the leg and not the thickness of the laminate. In order to permit a reduction in this dimension, a thicker laminate will be used, specifically 32 laminae for the nose gear configuration.

On this group, two stacking sequences were considered, k3 and k4,

Comparison between both options follows in table 5.8 and graphically in figures 5.15 and 5.16, for the reaction force assuming a level landing (worst case scenario for NLG) and CG in a medium configuration as previously identified. According to the drone's technical drawings, the longitudinal distance from the wheel to the fuselage attachment is 0.1 m, which is the minimum distance to a low point of the fuselage (after the nose curve). This value may be altered since stress increases with it, but so does deflection, which, according to the defined relationships for MLG, reduces the force reaction that will be used for landing studies.

Table 5.8: Bending mechanical properties for the two 32 ply laminates

	E1 (GPa)	E2 (GPa)	v12	G12 (GPa)
k3	28.420	25.321	0.253	8.942
k4	27.682	19.964	0.299	10.678

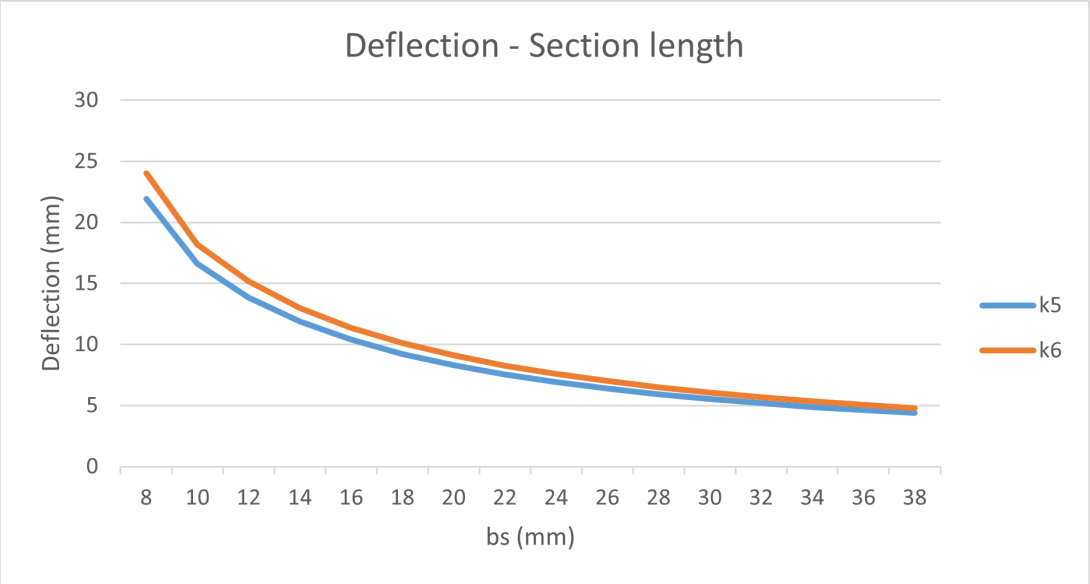

Figure 5.15: Deflection on the NLG per width of its cross section for static load, static condition

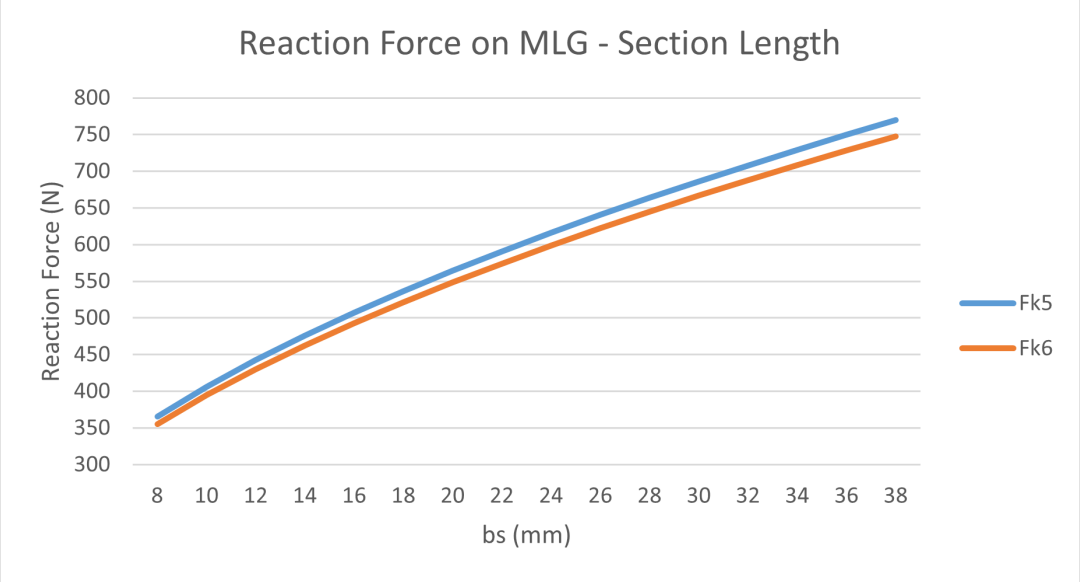

Figure 5.16: Reaction force acting on the NLG to simulate landing conditions per width of its cross section

Based on the analysis of the retrieved data, the nose landing gear behavior for stacking sequences k3 or k4 is very similar. Only E2 has a significant variance, but since side loads are

minimal, it does not have a significant effect. Consequently, using the same logic as for MLG, the stacking sequence k3 is chosen for this structure. It is configured as follows:

$$k3 = [90, 45, -45, 0_2, -45, 45, 90, 0_2, 90, 0, -45, 0, 45, 0]_S$$

5.3.4 Ground Loads

5.3.4.1 Main Gear

In order to define the proper ground loads that must be studied for the main landing gear, a second dimension for its cross section must be defined.

Knowing that the thickness of the laminate selected is 6.804 mm.

$$a_s = 6.804 \text{ mm}$$

The maximum value for b_s is 38 mm taking onto consideration the weight limit defined earlier in section 5.3.3.1.

An increase in b_s will result in a lower stress on the structure for a same solicitation. However, it also results in a decrease in deflection, which, as it was explained, is directly related with an increase in the force used for landing calculations.

An analysis on the resulting force (figure 5.14) and stress (figure 5.17) will be made for the varying b_s assuming, for now, that the landing gear only has vertical deflection by using the relation explained in section 3.2.2 and the stresses on critical section obtained via the approximation to an elliptical beam in equation 3.128.

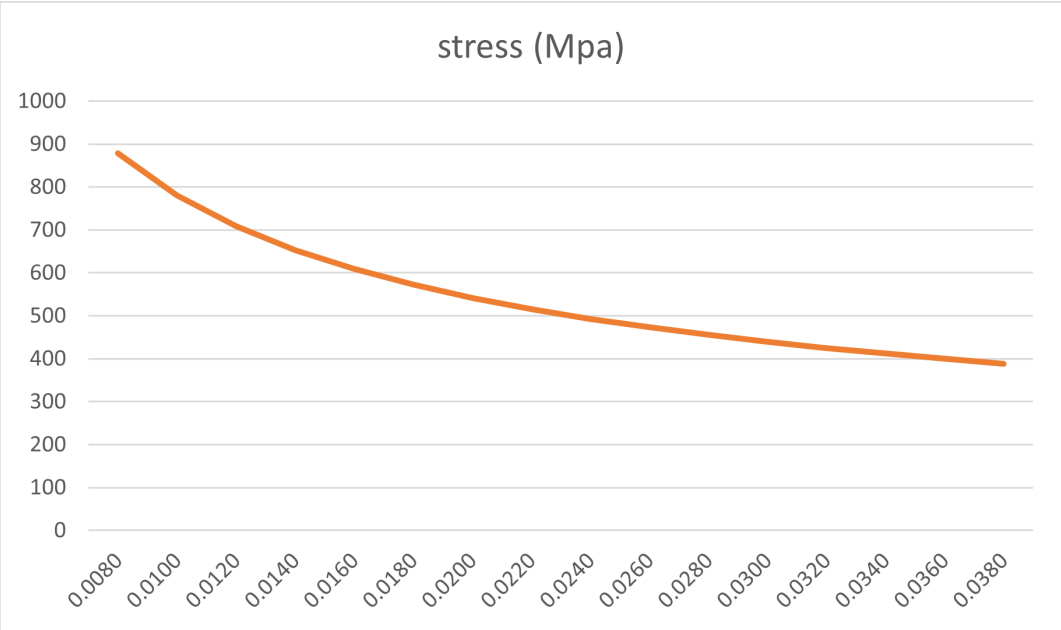

Figure 5.17: Stress created on the beam's critical section per length of its cross section

Here it can be seen that until the maximum length of cross section that keeps the total mass inside the defined limits, the increase in this dimension results in a significant decrease in resulting stress. On further optimization, this value may be altered to achieve mass and drag reduction, therefore,as a first approach to this matter, the maximum allowed,

$$b_s = 38 \text{ mm}$$

For the approximation of the main gear to a beam from figure 3.16. L, being the distance from the point of application of the force to the attachment with the fuselage (considering the beginning of attachment at the extreme point of the fuselage), it will be given by,

$$L = \frac{T}{2} - \frac{L_{fus}}{2} = 0.15075\, m \tag{5.41}$$

Replacing on equations 3.22 and 3.23,

$$I = 9.957 * 10^{-9} \text{ m}^4$$

$$k_{leg} = 23672.7 \text{ N/m}$$

Since tires are not considered,

$$k_{MLG} = 2 * k_{leg} = 47345.4 \text{ N/m}$$

Descent velocity is given by equation 3.63, for a wing lift area equal to 1.8 m^2 [1],

$$V_d = 1.426 \text{m/s}$$

However, CS-VLA 473 states that this value must be comprehended between 2.31 and 3.05 m/s. Therefore, descent velocity is,

$$V_d = 2.31\, m/s$$

For the load factor on the wheels, the drop height must be obtained.
Using equation on section 3.2.5,

$$h = 0.106 \text{ m}$$

However, the minimum value is set at 0.229 m, so this value will be considered.
The kinetic energy is given by equation 3.18,

$$E_k = 31.38 \text{ J}$$

And the potential energy, considering the absorption by the wing lift from equation 3.25,

$$E_p = 38.46d \text{ J}$$

For the selected cross section and laminate, assuming that only vertical deflection takes place the equivalent wheel factor is,

$$n_j = 12.947$$

And the reaction force on each main wheel on a tail down landing,

$$F = 746.91 \text{ N}$$

However, an iteration must be made to also account for the horizontal displacement. Using the third MATLAB code from Annex 1, table 5.9 provides the final wheel factor and equivalent force:

Table 5.9: Iterations to obtain the wheel factor to be used on main landing gear and the equivalent reaction force on one wheel

37.23 (V)	12.947	746.903	71.14	47.668
54.18	9.104	525.220	50.30	7.723
52.24	**9.418**	**543.314**	51.75	0.951

And a first design for the elliptical leg of the main landing gear is represented in figure 5.18.

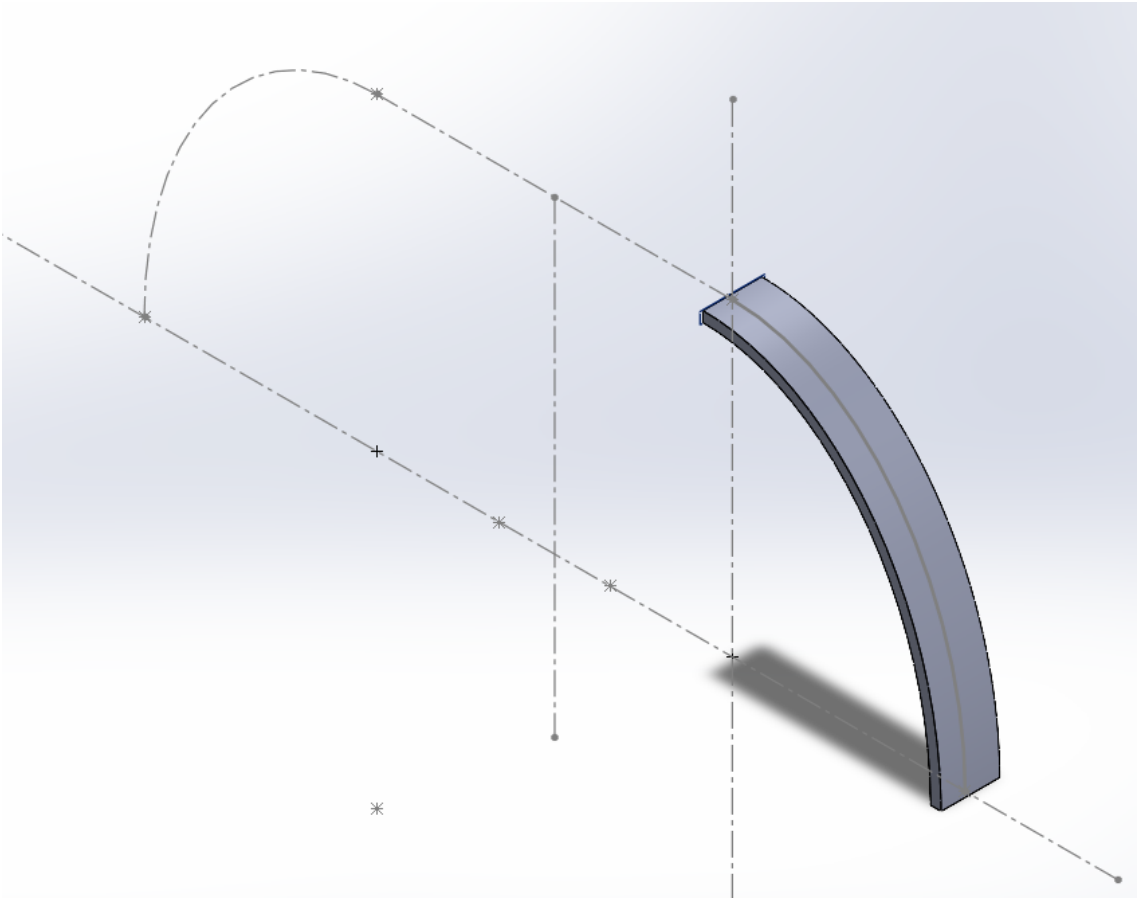

Figure 5.18: First design of main landing gear leg

5.3.5 Nose Gear

For nose gear, unlike on the main gear design, the distance from the wheel to attachment point must also be defined besides the definition of the width of cross section.

Anyway for the stacking sequence selected, width a_s is,

$$a_s = 6.048 \text{ mm}$$

To define a value for b_s, the reaction force analysis from figure 5.16 and a stress analysis in figure 5.19 are used and for these the minimum value for distance from the wheel to attachment point is used, $b = 0.1$ m.

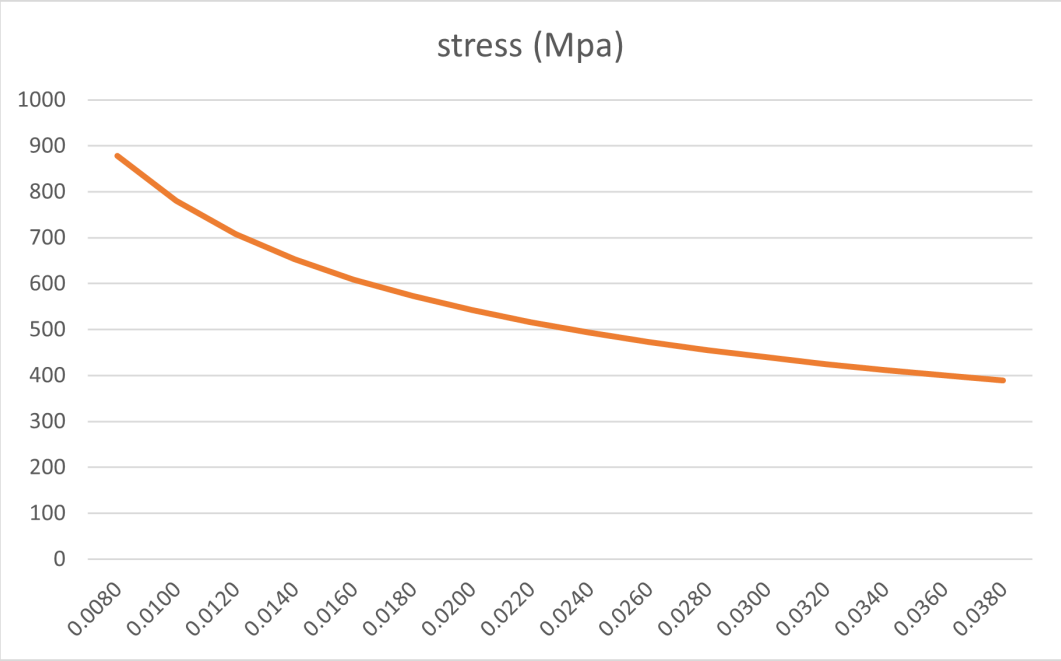

Figure 5.19: Stress created on the beam's critical section per width of its cross section for a distance to attachment of 0.10 m

From the data analysed, stress decreases continuously with an increase in cross section, as it happened for MLG. However, for this design the aim is on having a lower width of cross section. So section width will be for the start of convergence of stress values,

$$b_s = 38 \text{ mm}$$

Fixing this value, a study for distance to attachment must be made. Setting a maximum value via the weight constraint, 0.16 m. The stress analysis results follow in figure 5.20.

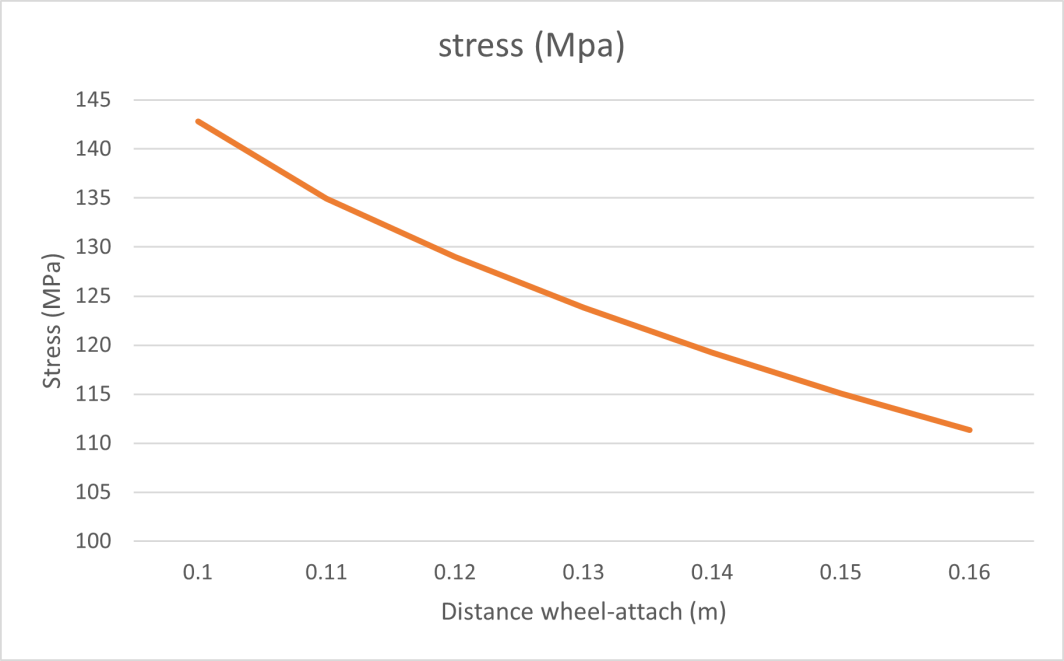

Figure 5.20: Stress created on the beam's critical section per distance wheel to attachment for cross section 6.084x38 mm

The data shows that stress decreases with an increase in the referred distance. Therefore, the maximum of 0.16 m will be adopted with the aim on reducing the cross section's width in detailed design.

Applying the straight beam approximation, where now only the percentage of mass acting on the nose gear is considered, an iteration is shown on table 5.10, to obtain the wheel factor and vertical force to be used on level landing with inclined reactions.

Table 5.10: Iterations to obtain the wheel factor to be used on nose landing gear and the equivalent reaction force the wheel

Deflection (mm)	Wheel Factor	Reaction Force (N)	Calculated Deflec. (mm)	Rel. Error (%)
27.40 (V)	17.353	322.93	47.80	42.678
37.60	12.830	238.69	35.30	6.520
36.50	**13.210**	**245.83**	36.40	0.137

And a first design of the nose gear on figure 5.21.

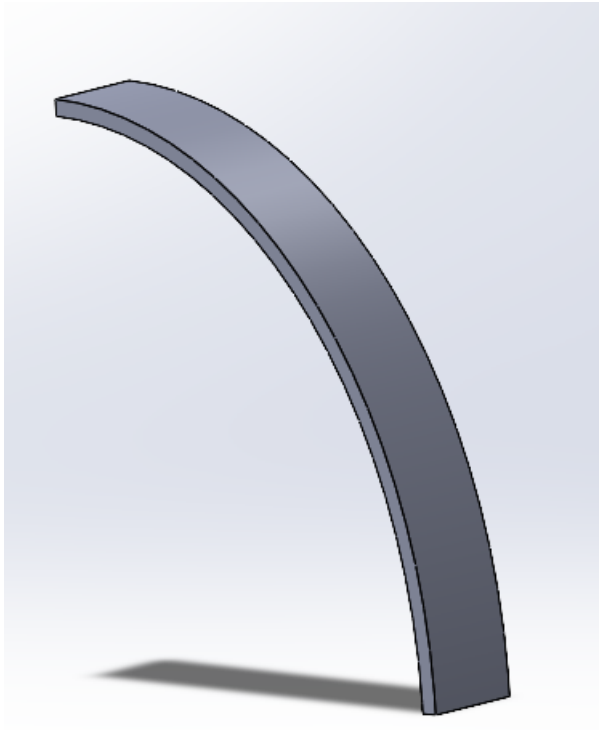

Figure 5.21: First design of nose landing gear leg

The values obtained for ground loads are summarized in table 5.11.

Table 5.11: Loads on Nose and Main Landing Gears (N)

Loading Condition	Nose Landing Gear			Main Landing Gears		
	x	y	z	x	y	z
Level Landing (Inclined Reactions)	-61.29	0	245.83	-233.67	0	468.60
Level Landing (Nose wheel off)	0	0	0	-294.75	0	554.48
Tail Down Landing	0	0	0	0	0	554.48
Side Load (Inboard)	0	0	0	0	-54.93	77.30
Side Load (Outboard)	0	0	0	0	36.25	77.30
Braked Roll	0	0	0	-59.32	0	77.30
Supplementary (Aft Loads)	-33.50	0	41.87	0	0	0
Supplementary (Side Loads)	0	29.22	41.87	0	0	0
Supplementary (Forward Loads)	16.75	0	59.55	0	0	0

Furthermore, the structure must withstand the maximum operational loads multiplied by the safety factors.

According to UL2.3 [57], the SF for PSE structures is 1.5 and must be further multiplied by the factor related to composite structures, section 3.2.3.3, 1.5.

The total SF applied must be 2.25.

Chapter 6

FEM Analysis and Detailed Design

With the obtained analytical results, FEM analysis must be performed to validate the previously used functions and proceed with the detailed design.

6.1 FEM validation of MATLAB functions

In order to validate the functions used to calculate the deflections and stresses involved in the elliptical leg simplification of the landing gear, various models will be compared to the analytical results: a 2D planar model, a 3D shell model, and a solid model made of an orthotropic material with the bending properties obtained for the equivalent laminate. In addition, a 3D shell model comprised of the exact stacking will be used as a comparison to determine the validity of the equivalent properties code.

6.1.1 Main Gear

For static loading (F = 48.75 N), the analytical results are shown in table 6.1:

Table 6.1: Caption

Deflection [d] (mm)	d_V (mm)	d_H (mm)	stress (MPa)
4.6435	2.1967	4.0910	25.3524

The first, simplistic, model consists of a 2D planar beam. The finite elements used were of beam type, more specifically B21, 2-node beam in a plane.

Force was applied on one end while the other one was defined as embedded, as in figure 6.1.

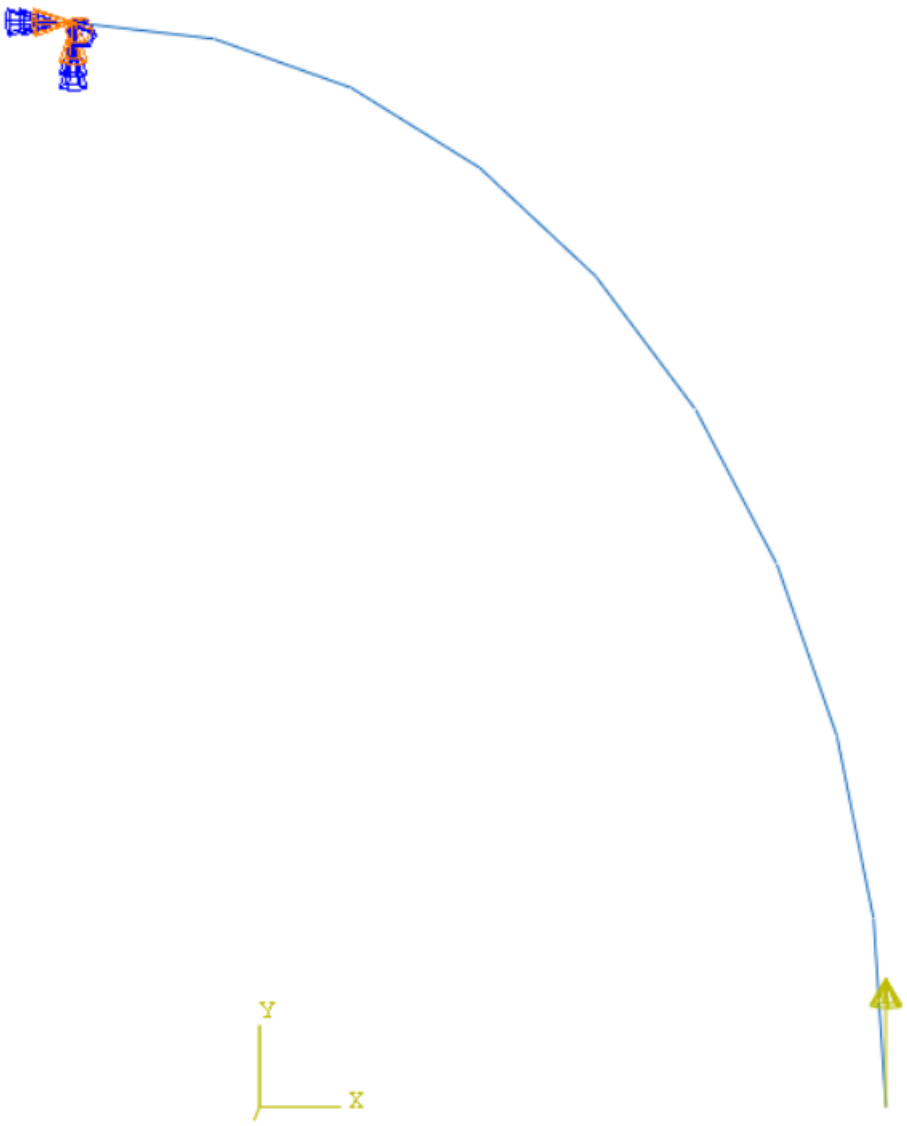

Figure 6.1: Loading conditions for static situation on beam model of MLG

And the resultant stresses and displacements are shown in figure 6.2 and 6.3.

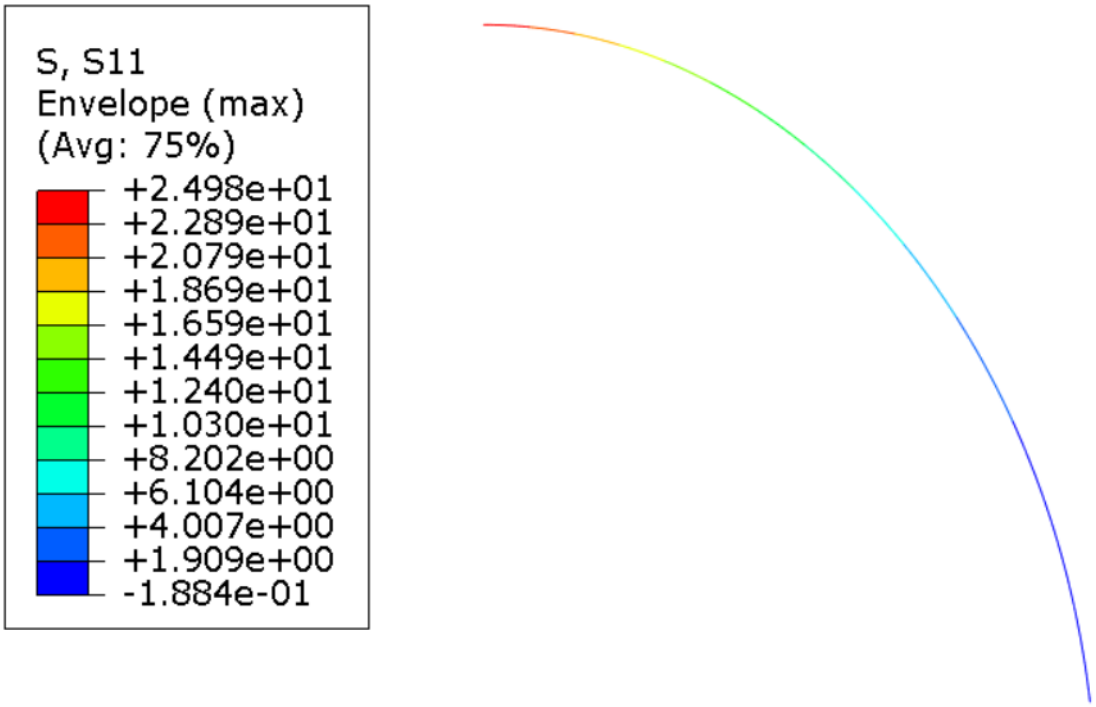

Figure 6.2: Stress on main direction (MPa) on the beam model of MLG

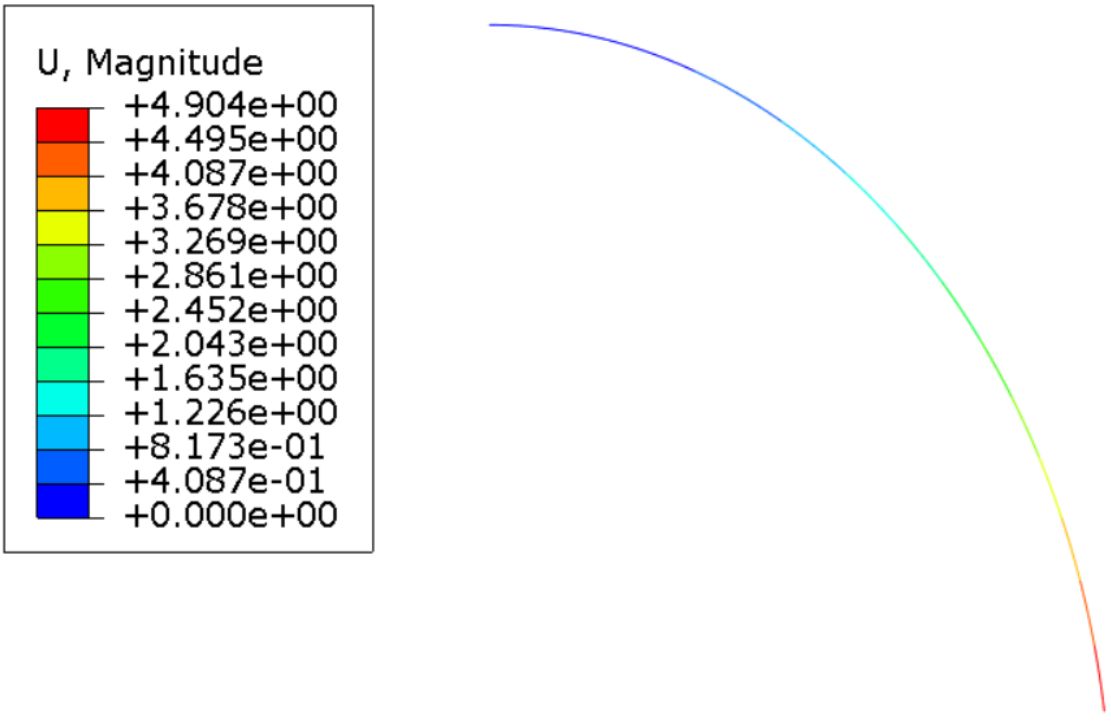

Figure 6.3: Total deflection (mm) on the beam model of MLG

For the 3D shell model, the loading conditions were modeled mostly in a same way, figure 6.4. However, the used element is now an hex mesh with 4-node elements of a thin shell, S4R.

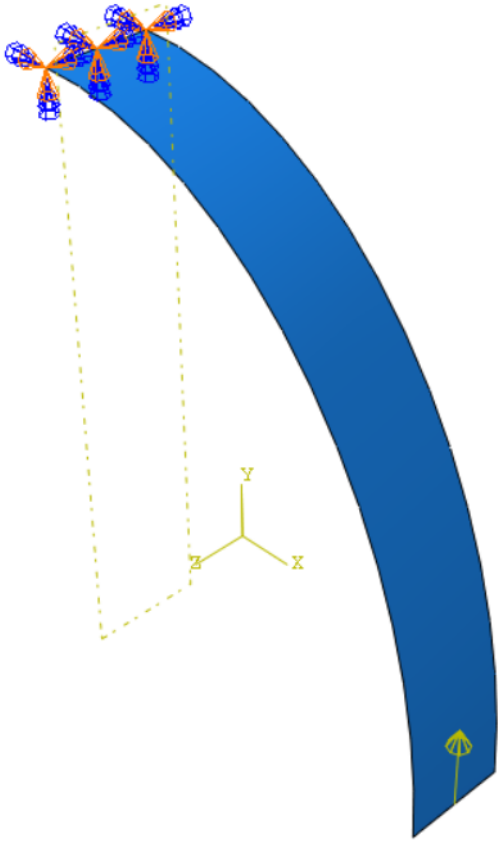

Figure 6.4: Loading conditions for static situation on 3D shell model of MLG

With static loading, the response from the model is shown in figures 6.5 and 6.6.

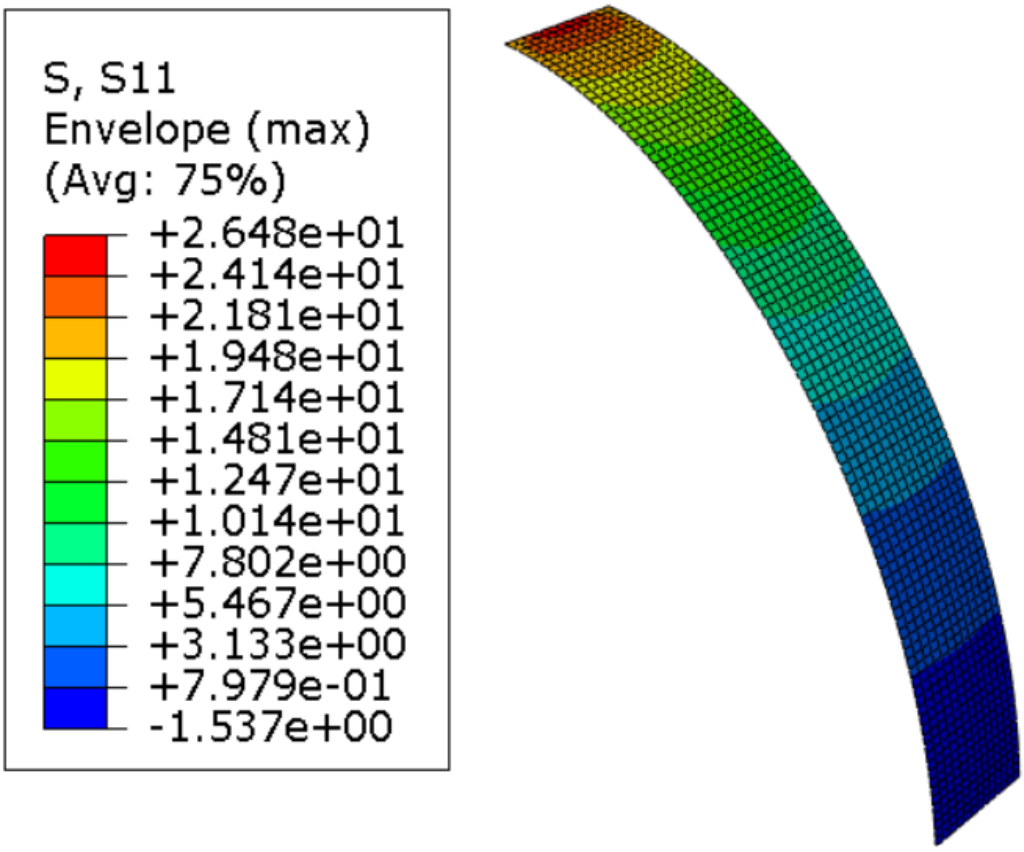

Figure 6.5: Stress on main direction (MPa) on the 3D shell model of MLG

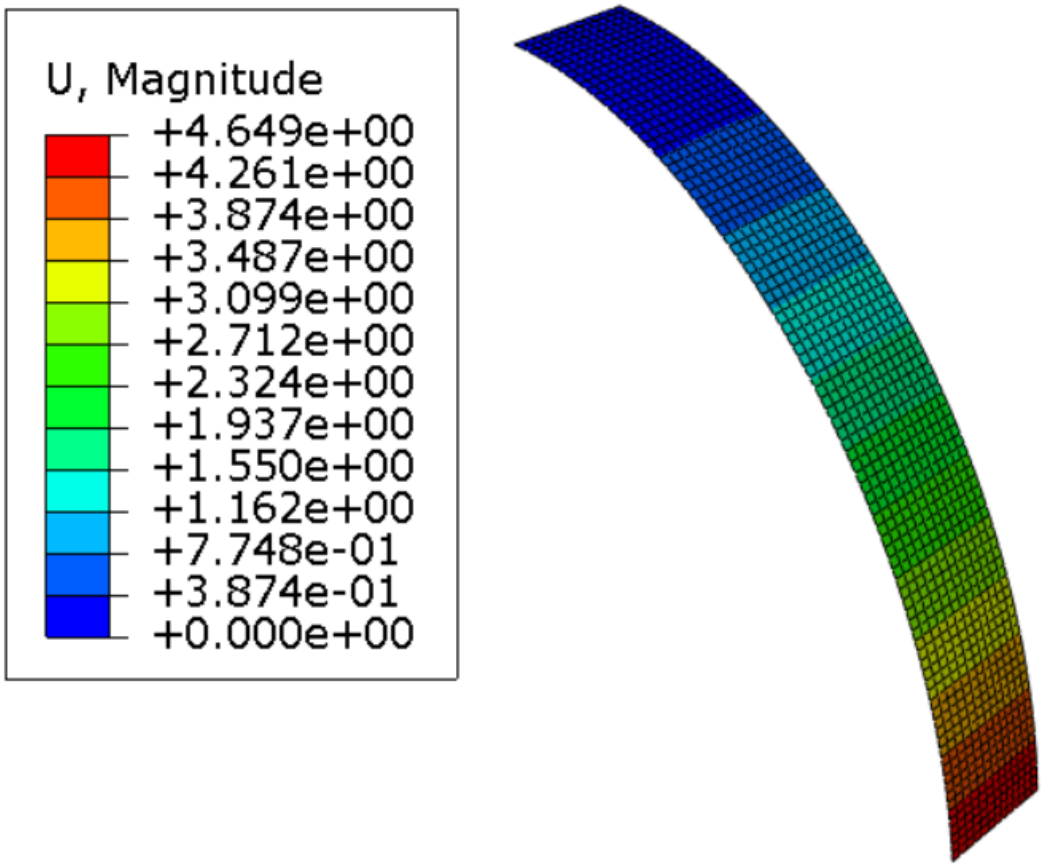

Figure 6.6: Total deflection (mm) on the 3D shell model of MLG

Finally for the solid model, the loading is defined as follows in figure 6.7. For this model, 3D elements were used. On this instance, an 8-node linear brick with reduced integration, C3D8R.

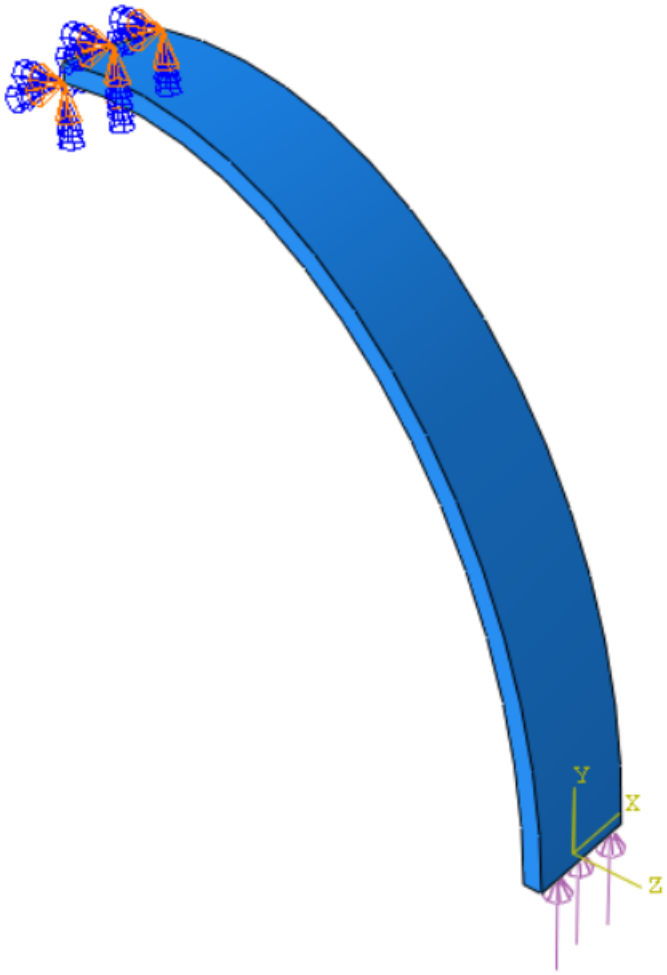

Figure 6.7: Loading conditions for static situation on solid model of MLG

And the response for this model figures 6.8 and 6.9,

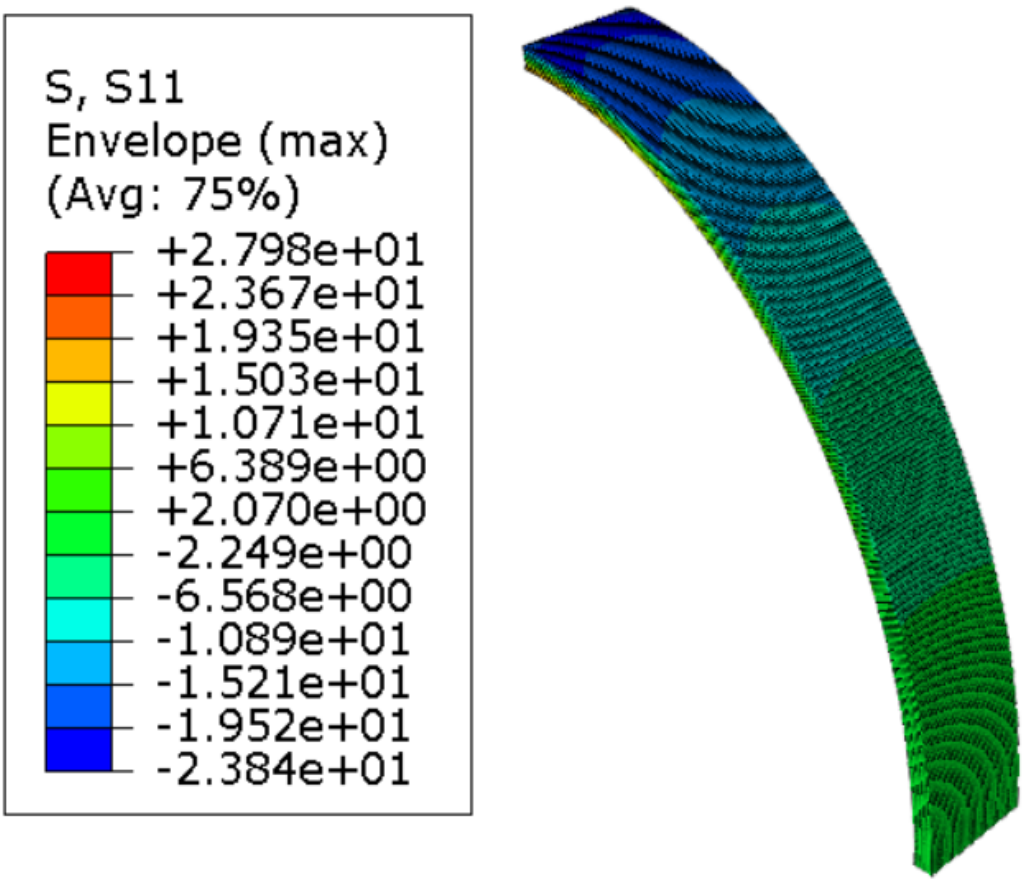

Figure 6.8: Stress on main direction (MPa) on the solid model of MLG

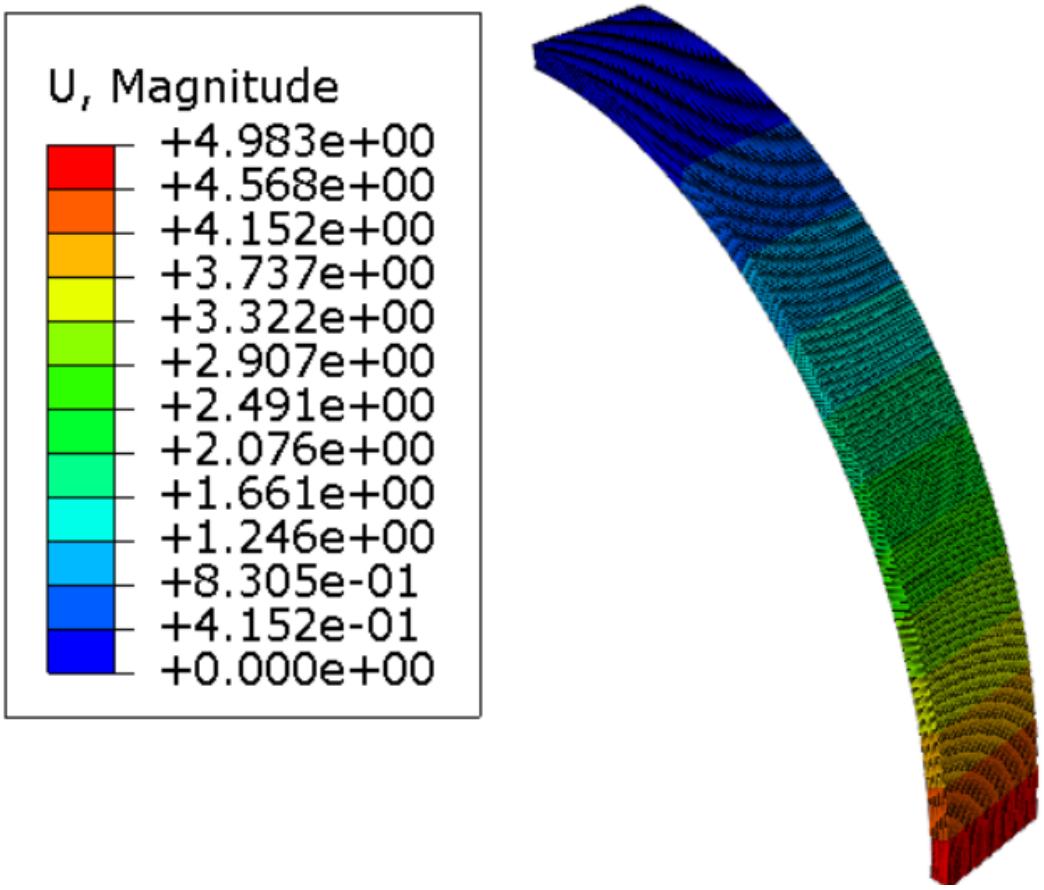

Figure 6.9: Total deflection (mm) on the solid model of MLG

An error analysis on the several models used is summarized in table 6.2.

Table 6.2: Relative error for the different models used

	Deflection (mm)	Rel. Error	Stress (MPa)	Rel. Error
Analytical	4.644		25.3524	
2D Planar	4.904	5.61%	24.98	1.47%
3D Shell	4.649	0.12%	26.48	4.45%
3D Solid	4.983	7.31%	27.98	10.36%

Following the results obtained 3D shell model presents itself as a proper solution for modelling the landing gear. Moreover, it is acceptable since one of the dimensions (thickness of the laminate) is much lower than the rest. Changes to the project and computing speed are also better for this solution when compared to a full solid model. Therefore, further analysis will be performed on 3D shell models.

As it was mentioned in section 4.3, convergence analysis is of major importance to assure that the results obtained are close to the real values. Elements of bigger size, further from convergence, may result in analysis mistakes and errors on the design.

A convergence analysis was performed on the shell model for tail down landing configuration (F = 543.314 N), which, for reference, using MATLAB coding from Annex 1, resulted in a deflection of 51.75 mm.

The convergence results are summarized in table 6.3.

Table 6.3: Convergence analysis for early design

El Size	Number Elements	Deflection (mm)	Stres (MPa)
50	12	53.56	238.1
40	14	53.73	243.8
30	18	53.94	251.5
20	28	54.14	261.3
15	54	54.01	270.2
10	112	54.03	286.9
5	440	54.03	301.9
3	1196	54.03	307.7
1	10526	54.03	310.7

According to the results presented on table 6.3, it is possible to verify that values for deflection start to converge to actual exact same values at element size 10. Although not converging to the analytical result but this will be justified by the approaches assumed for prior calculations.

Stress results only start to converge for element size 5. However, stress will be subjected to a different approach, explained later.

Anyway, even the values for very high element sizes are not very far from the convergence values. This is due to the simplicity of this first design and later on detailed design, a further convergence study must be performed.

For the same applied force, the validation for the mechanical properties of the equivalent laminate can be analysed. Using an element size of 3 the values for deflection and stress are compared to the resultant values assigning to the same beam, a section made of the different layers of the composite.

This is done via the composite layup function in Abaqus that cannot be used in more complex designs due to computing speed and capabilities.

The laminate is defined as represented in figure 6.10.

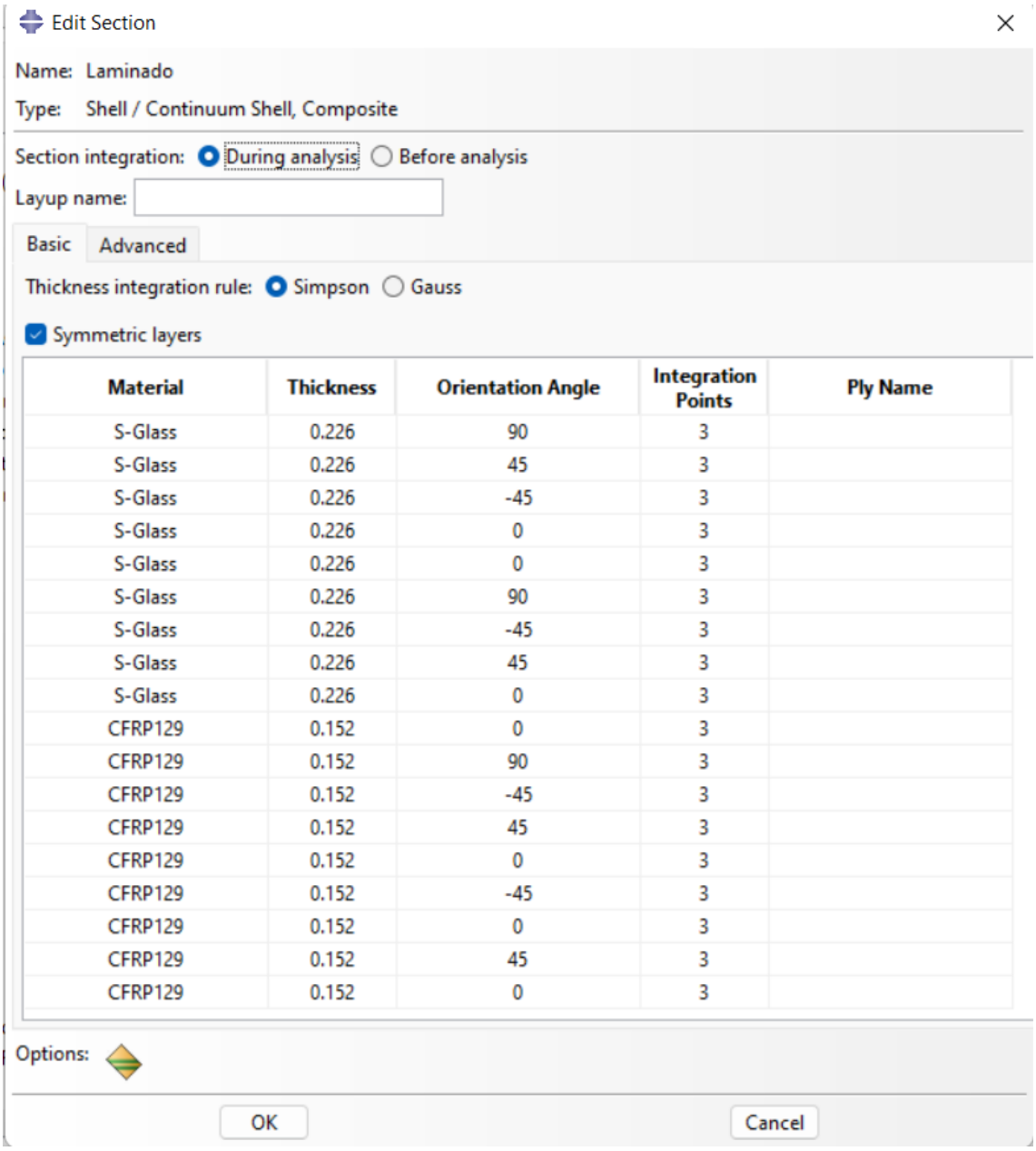

Figure 6.10: Definition of the laminate sequence on Abaqus

The deflection results (in mm) and stresses in principal directions (MPa) are compared with the ones obtained for equivalent laminate in table 6.4

Table 6.4: Displacement and stress comparison for equivalent laminate and actual laminate layup configurations

	d (Tot)	d_V	d_H	σ_1	σ_2	σ_{12}
Equivalent	54.03	25.20	47.79	307.7	75.7	32.46
Laminate	54.04	25.22	47.79	132.3	95.93	18.79

Based on the obtained results, it can be concluded that the displacements are accurately represented by modeling the laminate as an orthotropic equivalent material with the previously calculated bending properties. However, there is a significant error in the stress resultants in the different directions.

Since this is primarily a bending type of scenario, the approximation works well for displacement calculations. However, a possible explanation is that to accurately predict the stresses on a structure using an equivalent laminate, membrane properties must also be taken into account during material definition.

Since the analysis's stress results are unreliable, the Tsai-Hill criteria for failure verification cannot be applied. Following consultation with an expert in composite structures, the unit circle simplification of the omni strain envelope criteria will be used in the detailed design.

Only strain analysis is required for this, and since it is directly related to displacements, the values for equivalent bending properties will be confirmed. In any case, the envelope results for both methods are shown in table 6.5.

Table 6.5: Strain comparison for equivalent laminate and actual laminate layup configurations

	ε_1	ε_2	ε_{12}
Equivalent	1.059 %	0.252 %	0.259 %
Laminate	1.027%	0.266 %	0.400 %

6.1.2 Nose Gear

For nose gear the results will be presented in a less detailed manner.

Static loading as its maximum for a force of F = 18.70 N. The error analysis for the 3 possible representations is presented in table 6.6.

Table 6.6: Relative error for the different models used

	Deflection (mm)	Error	Stress (MPa)	Error
Analytical	2.8414		13.0467	
2D Planar	2.883	1.46%	12.88	1.28%
3D Shell	2.855	0.48%	13.16	0.87%
3D Solid	2.91	2.41%	13.41	2.78%

Shell models maintain the optimal relationship with analytically obtained results.

The remaining conclusions were extremely similar to those obtained for MLG. The convergence analysis yielded an element size of six for the beginning of convergence on results.

6.2 Detailed Design

Finally, the design of the two components constituting the landing gear will be specified in detail. The attachment of the primary components to the fuselage and tire-wheel assembly is crucial.

6.2.1 Main Gear

The tire selected for the primary gear will have an outer diameter of 90 mm. Therefore, at a distance of 45 mm from the ground, a 4 mm diameter through hole is required to couple the wheel's axis. In addition, the MLG leg will be slightly shortened to reduce the likelihood of the composite leg making contact with the ground during landing and to improve weight reduction. To facilitate this connection and prevent interference between the tire and leg, the segment closest to the wheel attachment will be straight. In order to prevent the formation of stress concentration factors, the beginning of the elliptical segment of the leg is tangent to this straight segment. The modifications made to this section are depicted in figure 6.11.

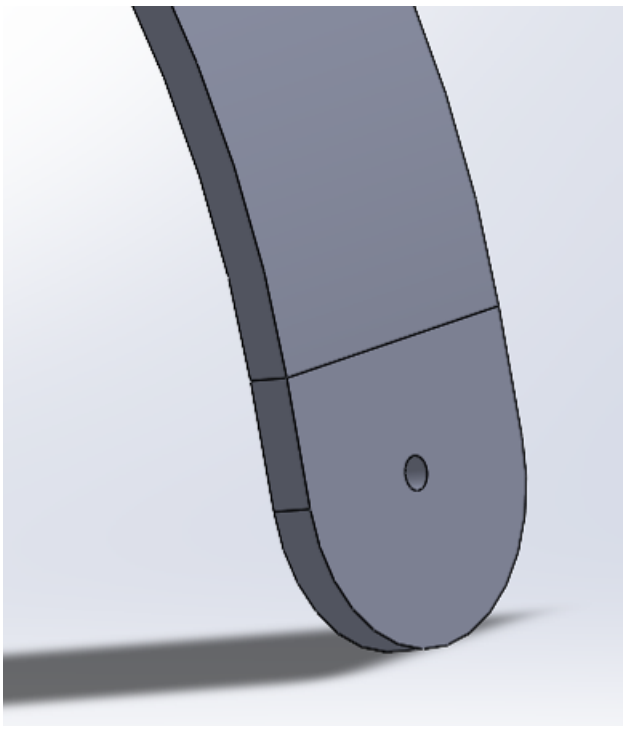

Figure 6.11: Segment of the MLG for wheel attachment

For the attachment to the fuselage, a straight segment connecting both legs of the MLG with a width comparable to the fuselage will be incorporated (230 mm). To avoid stress concentration factors, this section will be tangent to the elliptical legs.

Here, four through holes will be used for connecting bolts to the drone. Bolting is advantageous in a practical sense because it allows for simple drone assembly and disassembly and facilitates transport. The location and dimensions of the holes must conform to the specifications presented in figure 6.12.

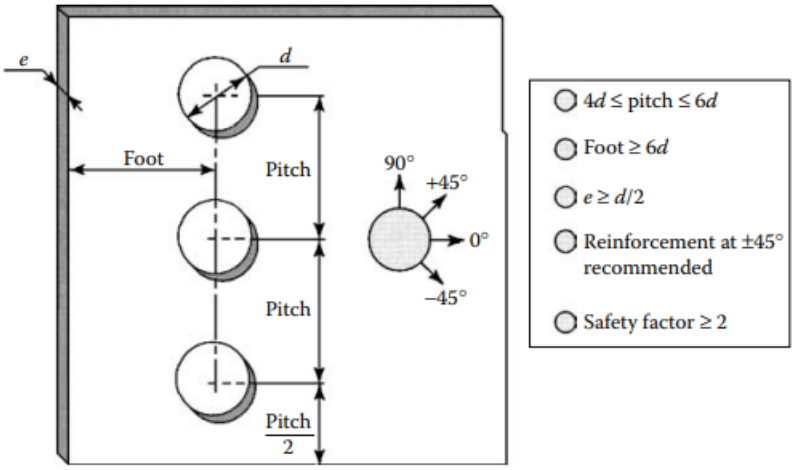

Figure 6.12: Recommended dimensions for holes in bolted joints for composite materials [72]

Following the thickness constraint, the maximum diameter of the holes will be 12 mm. However, the pitch constraint is more stringent. Given that the length of the landing gear cross section is 38 mm and that two holes must be drilled through it, the pitch dimension will be 19 mm. The diameter of the holes will therefore be 4 mm. The foot is defined by the transition between the elliptical and straight sections.

The placement of the holes is shown in figure 6.13.

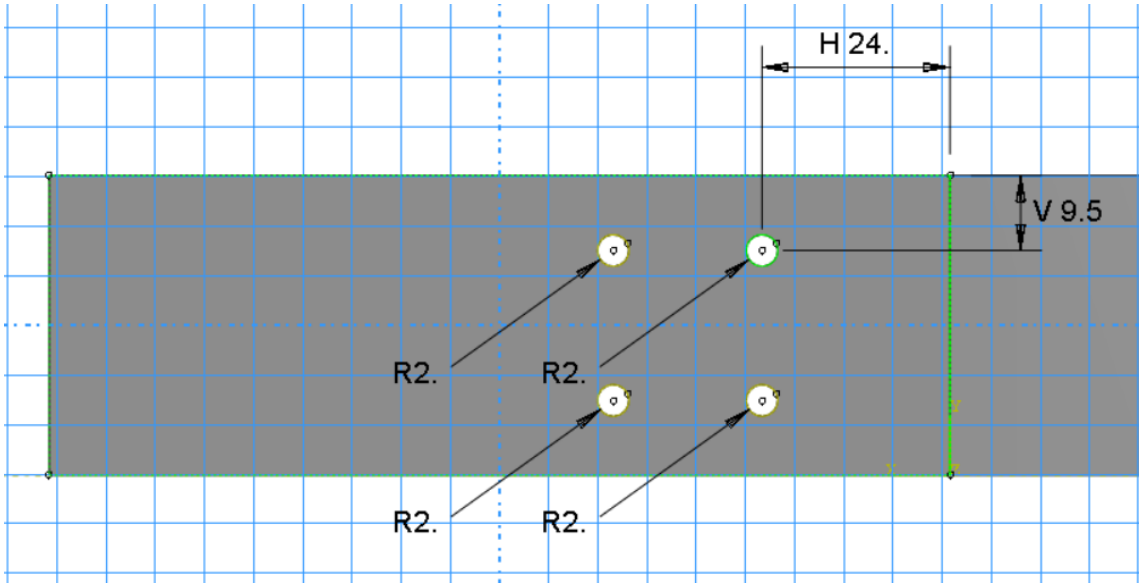

Figure 6.13: Positioning of the holes for bolted connection to the fuselage (half of the MLG)

The complete detailed design for the MLG is shown in figure 6.14.

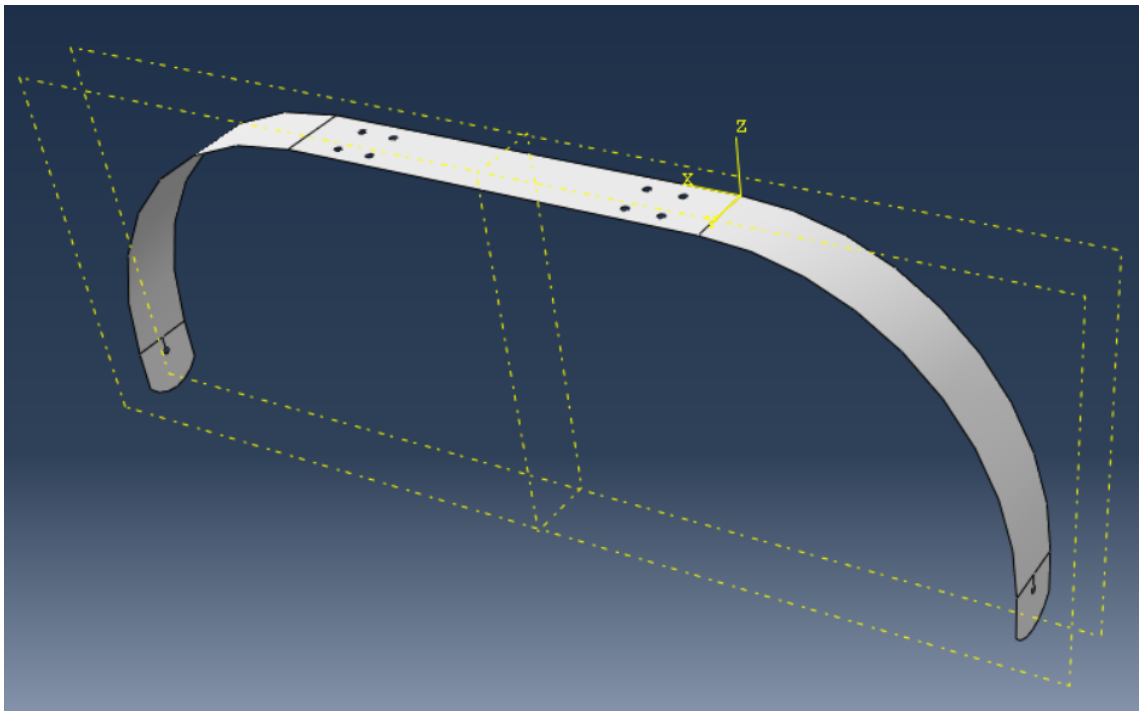

Figure 6.14: Detailed Design for the MLG

To simulate landing conditions, the worst possible scenario, a level landing with the nose wheel just off the ground, will be used. It introduces an unaccounted-for drag force in tail down landing.

For the simulation, only half of the model is examined, and a symmetric boundary condition is applied. On the bolted connections, the contact area will be increased by using ISO 7089 washers. The diameter of the washers for an M4 bolt is 9 mm, [102] and this component will be fixed in the software.

The applied loads will be concentrated on one end of a 12 mm beam that will simulate the axis of the wheel and the tire forces. On the opposite end, the beam is connected to the attachment hole for the wheel-tire assembly. Al 6061 is selected, the same material used for the wheel. For the simulation of this relationship, a coupling constraint was utilized.

Boundary conditions and loading applications are shown in figure 6.15.

After a convergence analysis, element size 1 was selected.

The results for the detailed analysis are shown in figures 6.16, 6.17 and 6.18.

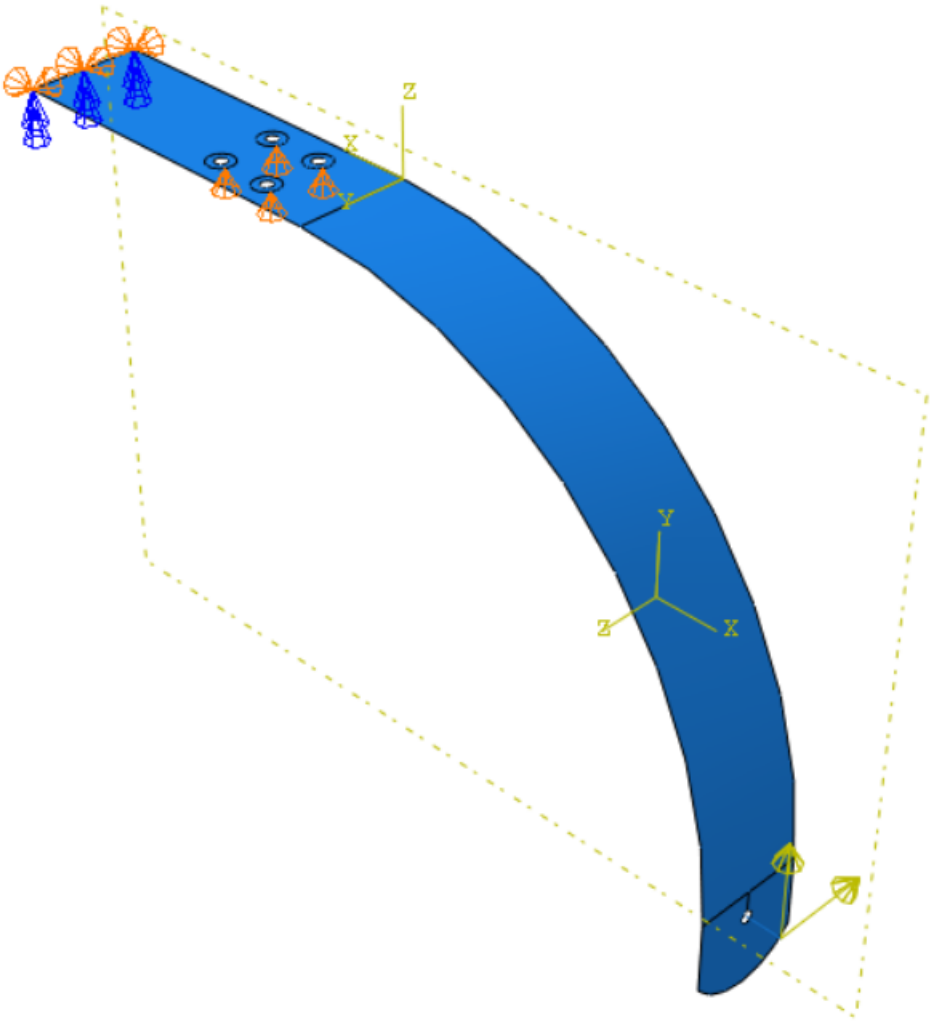

Figure 6.15: Boundary conditions and loading for the analysis of the main gear on detailed design

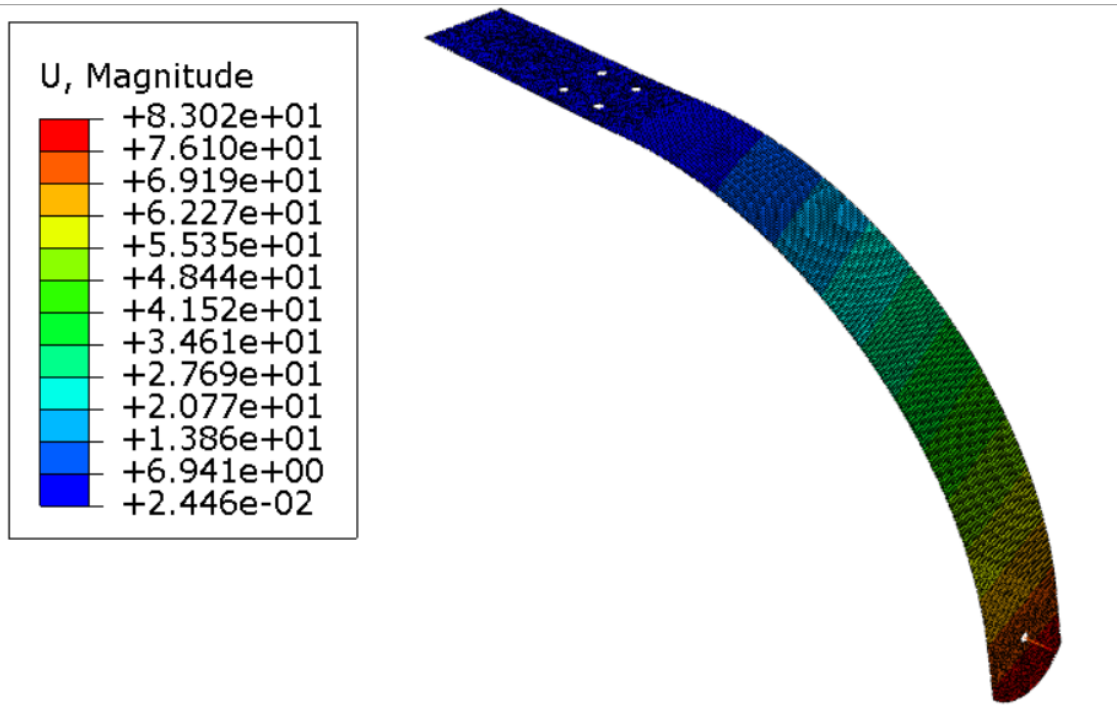

Figure 6.16: Total displacements on the MLG

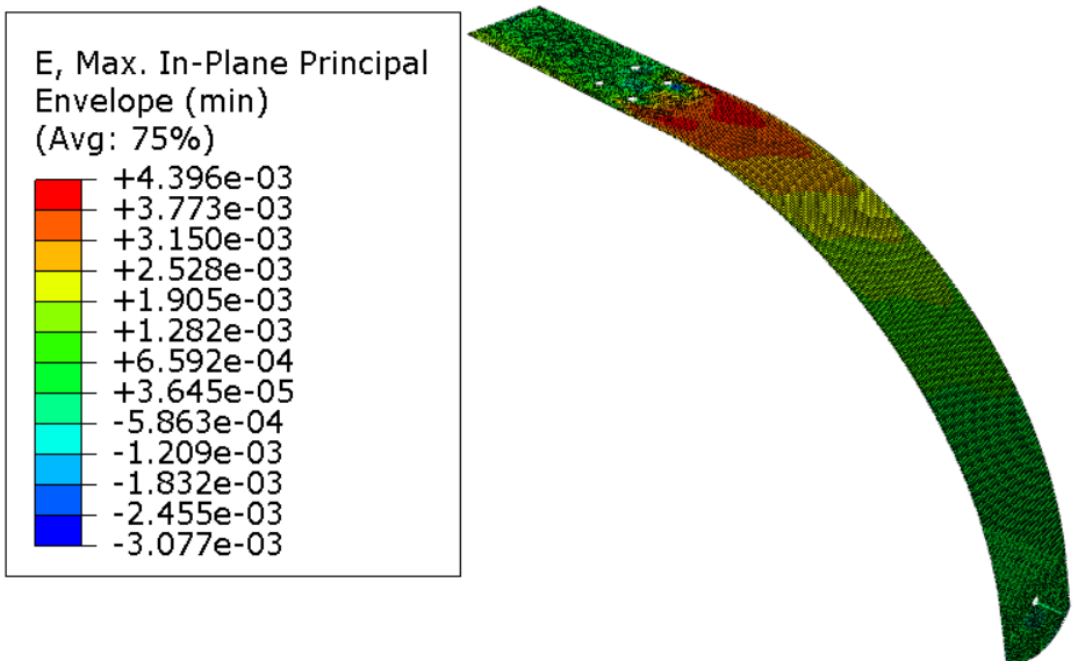

Figure 6.17: Compressive strains on the MLG

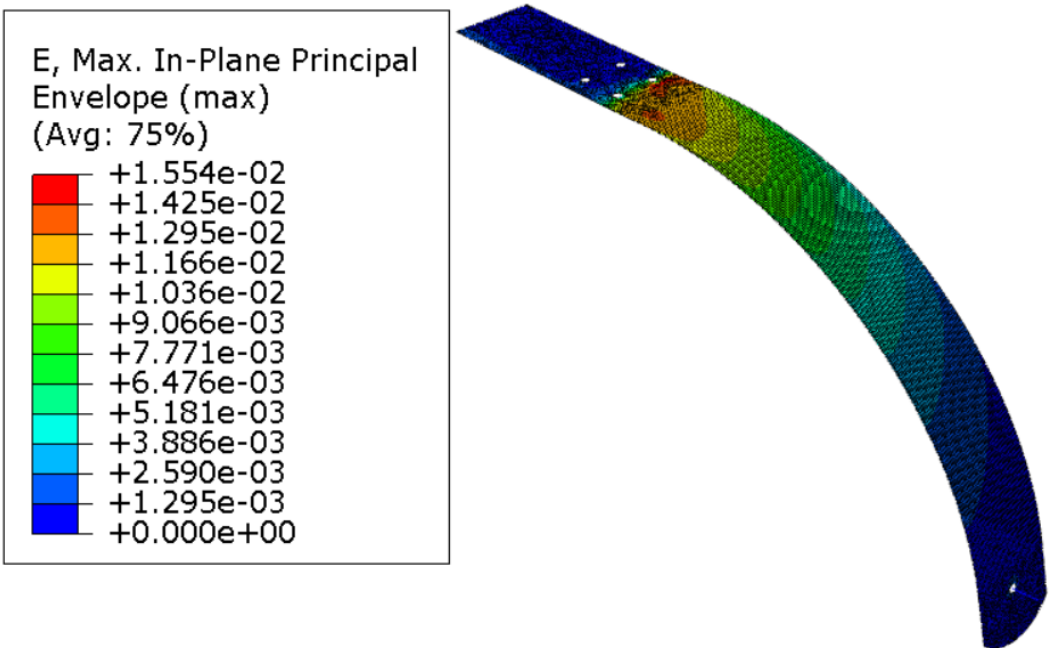

Figure 6.18: Tensile strains on the MLG

Failure Analysis

Maximum strain values in the two main directions on the whole envelope were obtained below:

$$\varepsilon_1 = 1.552 * 10^{-2}$$
$$\varepsilon_2 = 4.396 * 10^{-3}$$

In tension and,

$$\varepsilon_1 = -1.717 * 10^{-2}$$
$$\varepsilon_2 = -3.713 * 10^{-3}$$

On compression.

The properties for the fibers used on this laminate were obtained via CES Edupack [74].

For Carbon fiber + Epoxy,

$$\begin{aligned} X^T &= 1740 \text{ MPa} \\ X^C &= 1410 \text{ MPa} \\ E^T &= 129000 \text{ MPa} \\ E^C &= 123000 \text{ MPa} \end{aligned} \tag{6.1}$$

And for S-Glass Fiber + Epoxy,

$$\begin{aligned} X^T &= 1700 \text{ MPa} \\ X^C &= 1160 \text{ MPa} \\ E^T &= 47600 \text{ MPa} \\ E^C &= 47300 \text{ MPa} \end{aligned} \tag{6.2}$$

Failure will be analysed in the laminae more prone to fail, both for being the outer layer and the least resistant, S-Glass.

For the main tensile strains, the maximum strain calculated for the criteria is:

$$\varepsilon_X = \frac{X^T}{E^T} = 3.57 * 10^{-2}$$

To obtain the safety factor, k is equal to 1 and the maximum strain divided by a unknown variable SF.

$$1 = \sqrt{\left(\frac{\varepsilon_1}{\varepsilon_X/SF}\right)^2 + \left(\frac{\varepsilon_2}{\varepsilon_X/SF}\right)^2} \tag{6.3}$$

$$SF = 2.20 \tag{6.4}$$

For the main strains in compression, the maximum strain is,

$$\varepsilon'_X = \frac{X^C}{E^C} = 2.45 * 10^{-2}$$

And SF given by,

$$1 = \sqrt{\left(\frac{\varepsilon_1}{\varepsilon'_X/SF}\right)^2 + \left(\frac{\varepsilon_2}{\varepsilon'_X/SF}\right)^2} \tag{6.5}$$

$$SF = 1.395 \tag{6.6}$$

The obtained value for strains in compression is significantly lower than the SF recommended by regulation. Therefore, additional measures are required to increase the safety factor.

As depicted in figure 6.19, the maximum compressive strain follows the main direction of the MLG and is obtained near the bolted connection holes. Holes in composite structures are typically undesirable and may cause structural issues. To possibly increase the SF, it is necessary to examine the possibility of connecting the landing to the fuselage using structural adhesives. Additionally, an increase in attachment zone area can reduce the total strain of the structure.

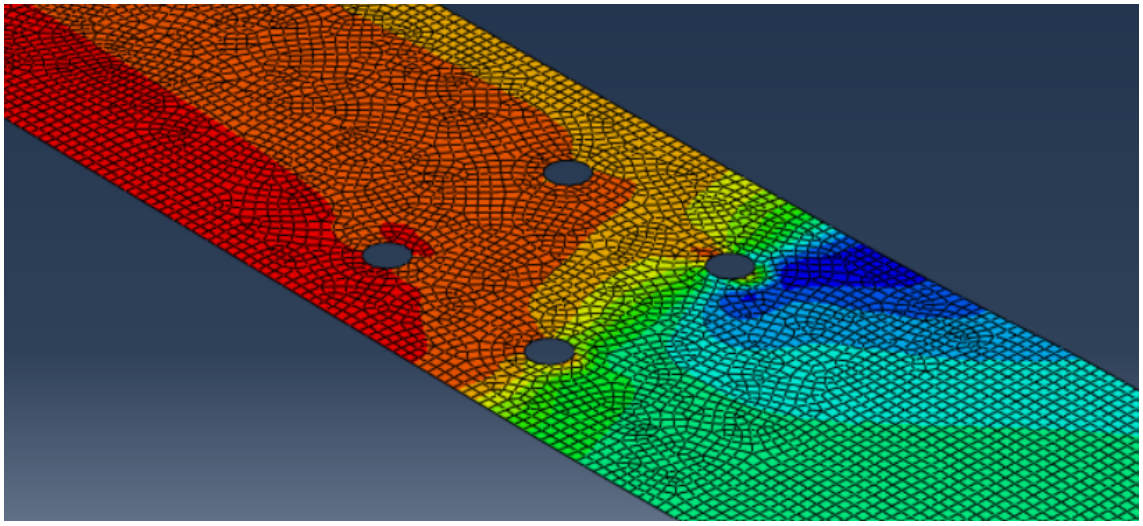

Figure 6.19: Area for the maximum compressive strain on the MLG

It can also be seen in figure 6.16, relative to the values previously used to calculate wheel factor, the maximum deflection of the MLG increased. Taking into account this distinct behavior, a new iteration is required to determine the new wheel factor. After calculation, the wheel factor is 8.023, and the worst-case landing forces are 462.83 N vertically and 249.97 N for drag.

Now, the maximum compressive strains are:

$$\varepsilon_1 = 1.355 * 10^{-2}$$
$$\varepsilon_2 = 2.902 * 10^{-3}$$

The SF is now increased to 1.77, an improvement of 26.9%. Still lower than the SF defined via legislation.

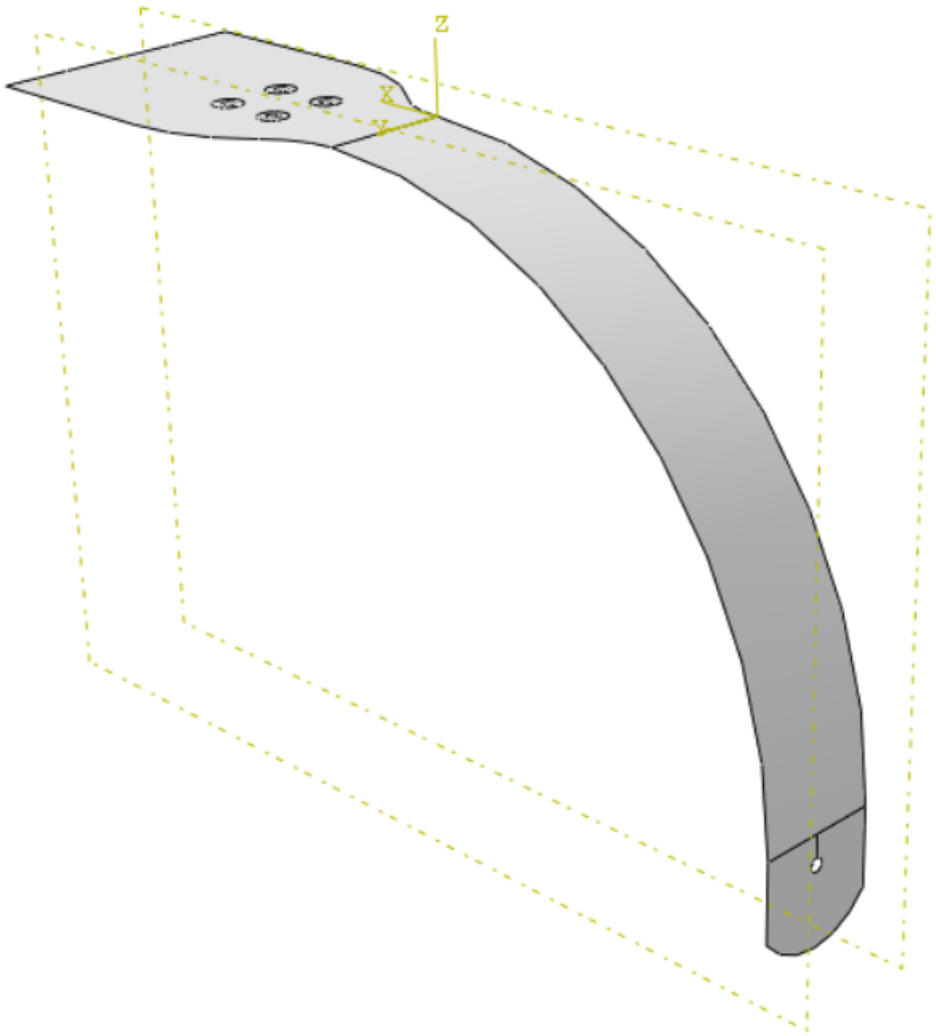

Figure 6.20: Detailed design for the MLG with an increase in section for the attachment with fuselage

Therefore, a further measure will be analysed, the increase in cross section length on the area around the holes.

For this analysis half of the new geometry for detailed design is represented in figure 6.20.

The necessary iterations to obtain the new wheel factor and analysis of convergence were carried out. 7.43 is the new wheel factor. The maximum compression strains are:

$$\varepsilon_1 = 1.129 * 10^{-2}$$
$$\varepsilon_2 = 2.966 * 10^{-3}$$

Giving a SF = 2.10, an increase of 18.6%.

One final method will be employed in an effort to attain the legal safety factor. Since the

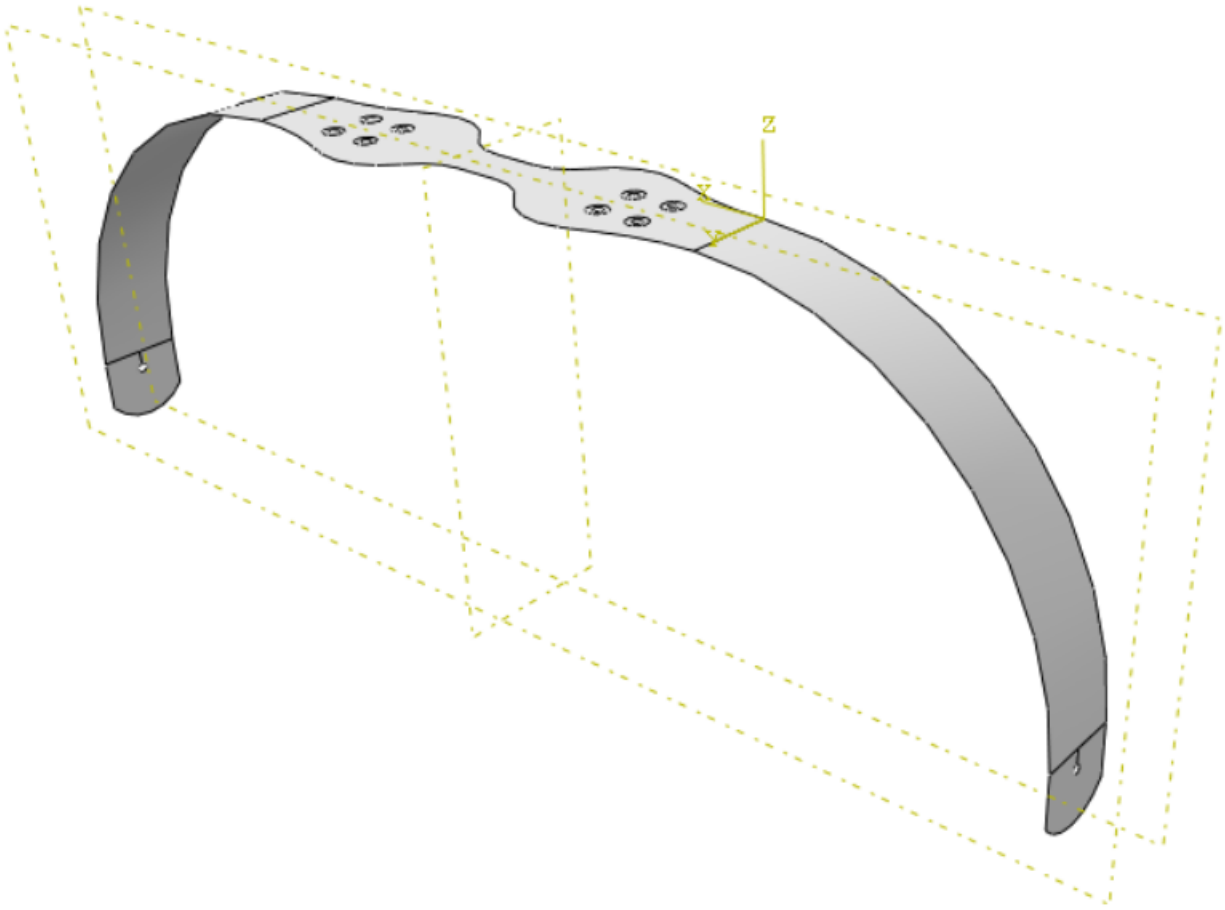

Figure 6.21: Final design for the MLG

greatest strain values are found on the curvature used to lengthen the cross section, this transition will be diminished.

After numerous alterations to the dimensions and analyses, the SF did not increase significantly.

Then the value of 2.10 for SF will be accepted despite being lower than the one proposed. However, since this is a conservative failure criterion, the risk is minimized. In addition, this simulation assumes that no tires are used and that the forces act directly on the axle, a very conservative assumption.

Analysing the area next to the symmetry plan, it can be concluded that there the strains are very low. It allows for a reduction of section on this area, that, in theory, will not affect the behaviour of the rest of the structure and will provide a reduction in total weight.

In reducing significantly this area, there was no change in maximum deflection of the strut, so not affecting the wheel factor. The SF was also maintained since the critical strains were maintained.

The final design for the MLG is defined in figure 6.21.

6.2.2 Nose Gear

The selected tire for the nose gear has an outside diameter of 70 mm. However, this tire-wheel assembly will not be attached directly via the axle. It necessitates the incorporation of a fork component that serves as the link between the axle and composite leaf spring. All extra parts are made of Aluminum 6061.

This fork is constructed to support both ends of the wheel axle and connect to the landing gear leg via two M4 bolts. The illustration 6.22 depicts the fork part's shell design:

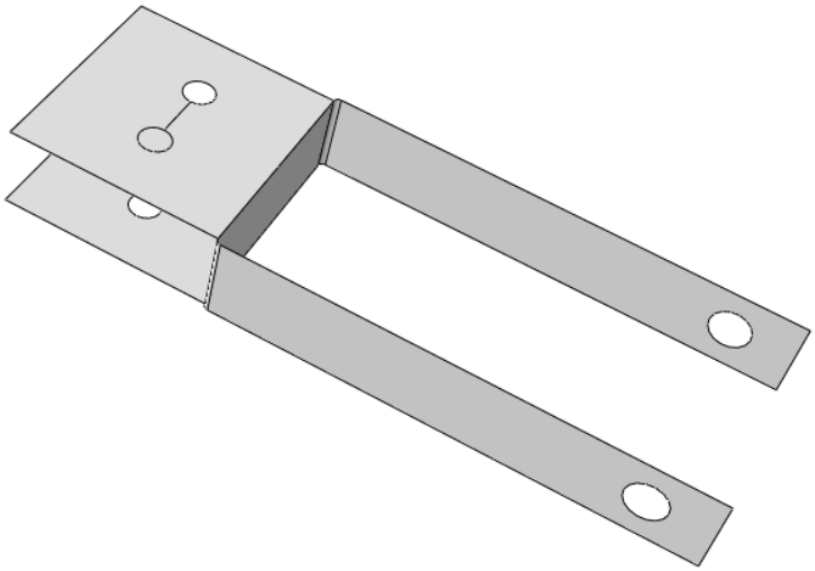

Figure 6.22: Shell representation of the fork part

Following figure 6.23, all simulation components are connected as shown. The fork is connected to the composite leg via fastener properties for the two holes and referring to all three crossed faces with all degrees of freedom dependent. A coupling connection from the center of the beam to both of the fork's holes determines the connection to the wheel axle.

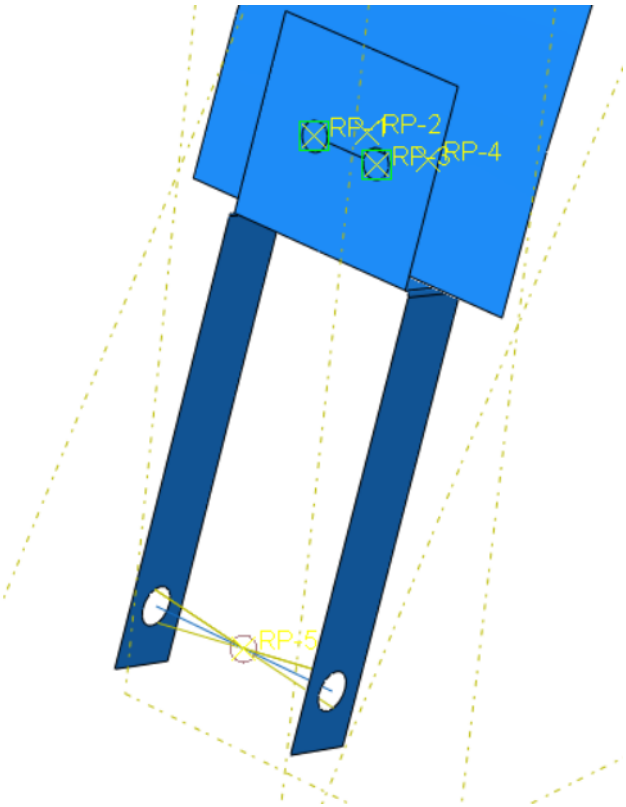

Figure 6.23: Assembly and connections with the fork part for the NLG

On an area equal to the washers, which have a 9 mm diameter for M4 bolts, the only boundary conditions defined were for the bolted attachment to the fuselage. Here, the structure is fixed. The loads are applied to the middle of the beam (wheel axle) in order to simulate tire loads. Figure 6.24 illustrates boundary conditions and load application.

After convergence analysis, element size 2 was selected. And the results for the detailed analysis are shown in figures 6.25, 6.26 and 6.27.

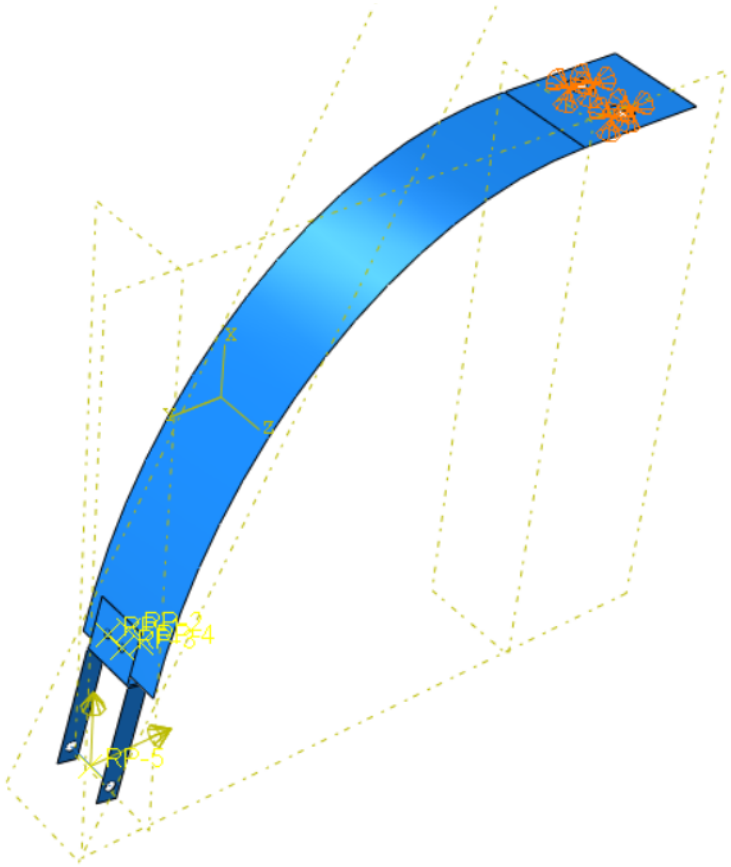

Figure 6.24: Loading on the NLG's detailed design

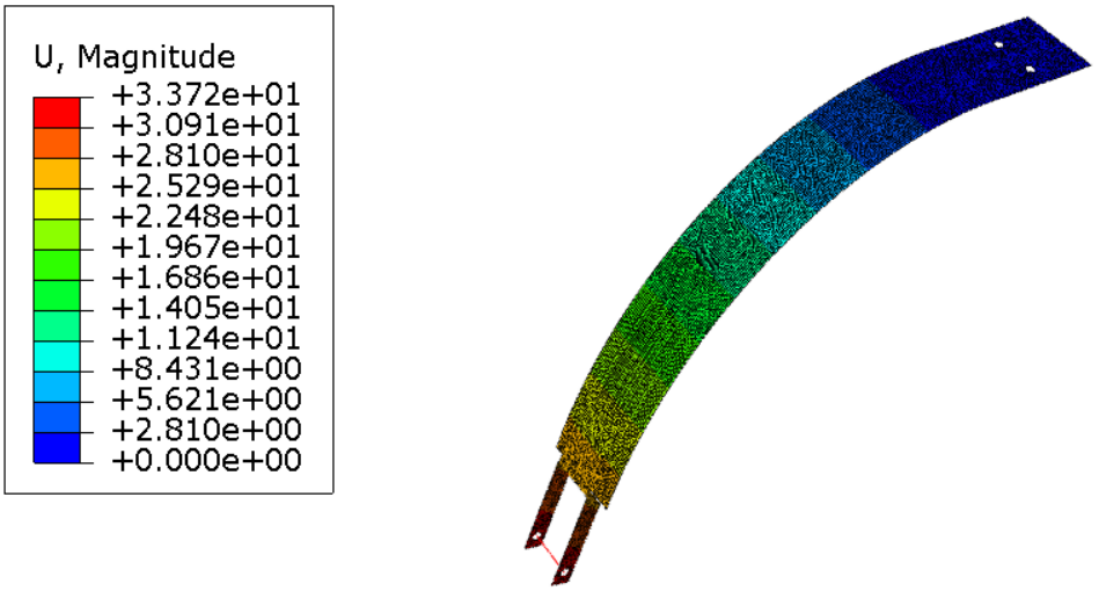

Figure 6.25: Total displacements on the NLG

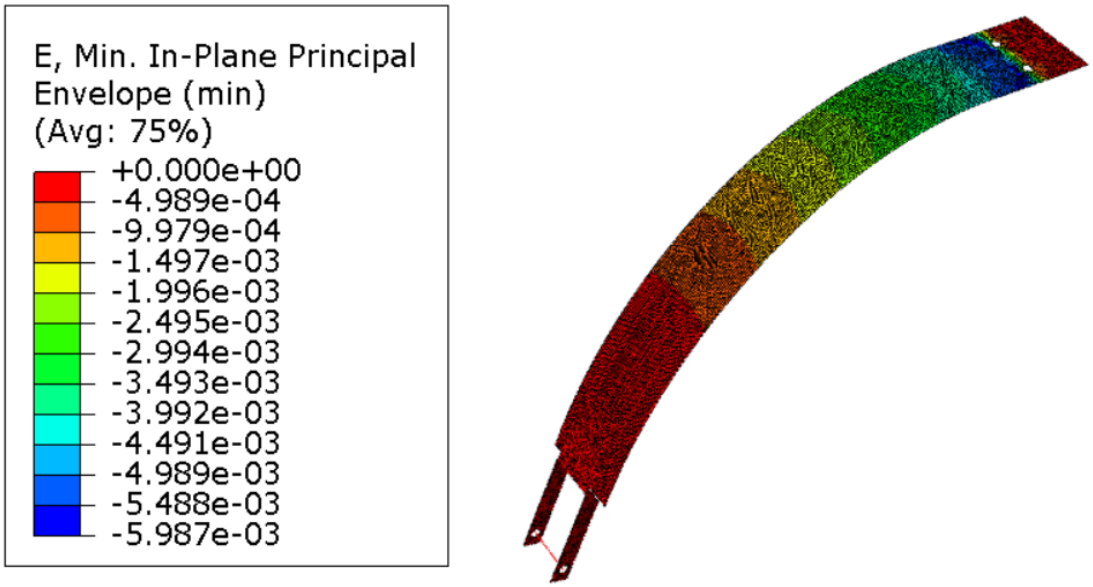

Figure 6.26: Compressive strains on the NLG

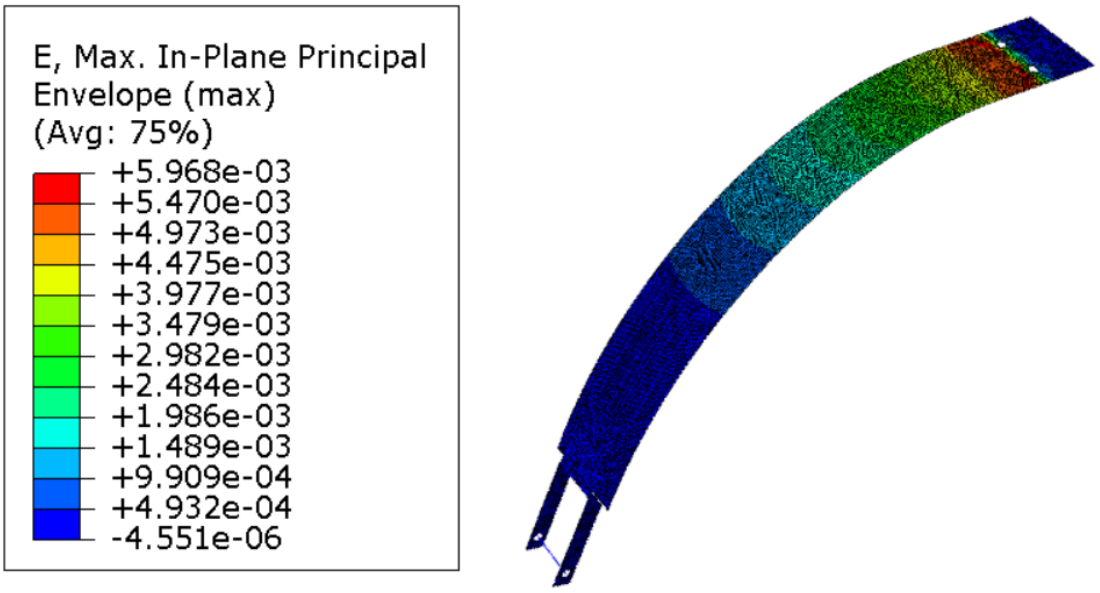

Figure 6.27: Tensile strains on the NLG

Using the failure criteria for tensile and compressive strain for just the leaf strut:

$$1 = \sqrt{\left(\frac{\varepsilon_1}{\varepsilon_X/SF}\right)^2 + \left(\frac{\varepsilon_2}{\varepsilon_X/SF}\right)^2} \tag{6.7}$$

$$SF = 3.49 \tag{6.8}$$

$$1 = \sqrt{\left(\frac{\varepsilon_1}{\varepsilon'_X/SF}\right)^2 + \left(\frac{\varepsilon_2}{\varepsilon'_X/SF}\right)^2} \tag{6.9}$$

$$SF = 2.34 \tag{6.10}$$

For analysis of the aluminum parts, von mises criteria is used and the maximum stress can be directly taken from FEM model in figure 6.28.

Since the tensile strength of the material is 300 MPa, the associated SF is 4.24.

This high level of safety factor values allows for design optimization. Beginning with changing the design of the leaf strut leg from a quarter ellipse to a straight part tangent to an elliptical area, then reducing the cross section's width while maintaining a safety factor above the required 2.25.

The optimization process follows summarized in table 6.7. Note that, displacement is always analysed in order to maintain an adequate wheel factor for all FEM analysis.

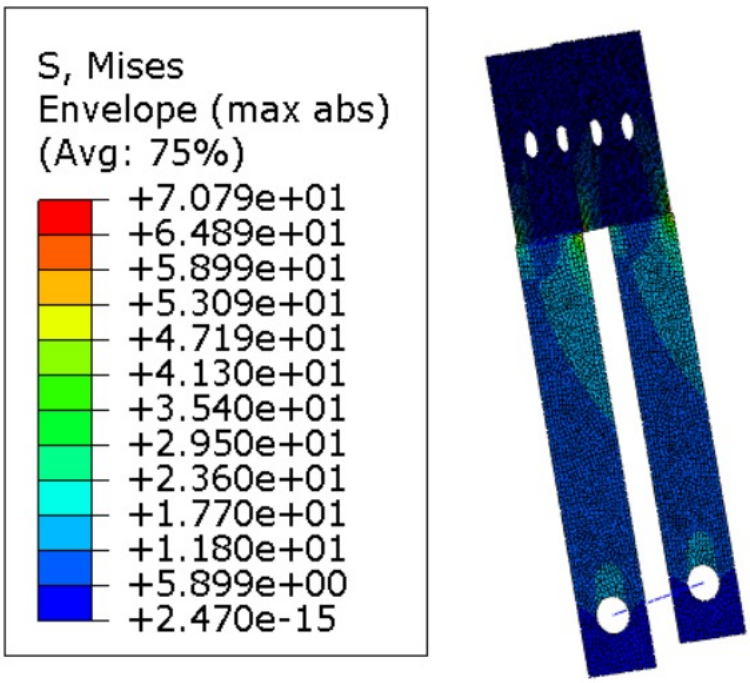

Figure 6.28: Stress analysis on aluminum parts

Table 6.7: NLG leaf strut optimization

Optimization Step	Safety Factor	Change (%)
First Detailed Design	2.34	
Change in Leg Format	3.93	+ 67.9 %
Width reduction to 34 mm	3.85	-2%
Width reduction to 30 mm	3.62	- 6%
Width reduction to 22 mm	3.24	- 10.5%

Note: For width lower than 32 mm, the bolts used are M3 and relative washers have 7 mm diameter. For width lower than 24 mm, bolts are M2 and washers have 8 mm diameter.

Due to the geometry of the fork, the minimum width possible is 22 mm. The modification to the shape of the leaf struts was highly effective in boosting the SF of the structure. With a final SF of 3.24, the final design will adopt a width of 22 mm. Iterative models determined the wheel factor to be 13.56, the landing loads to be 252.42 N vertically and the drag component to be 62.93 N.

The final optimized design of the NLG is shown in figure 6.29.

Finally, total weight must be analysed in order to check for compliance with maximum weight constraints.

Via MATLAB code for the equivalent properties of the laminate (Annex 1, code 2), the density of each composite material selected can be obtained via the densities of each type of prepreg and

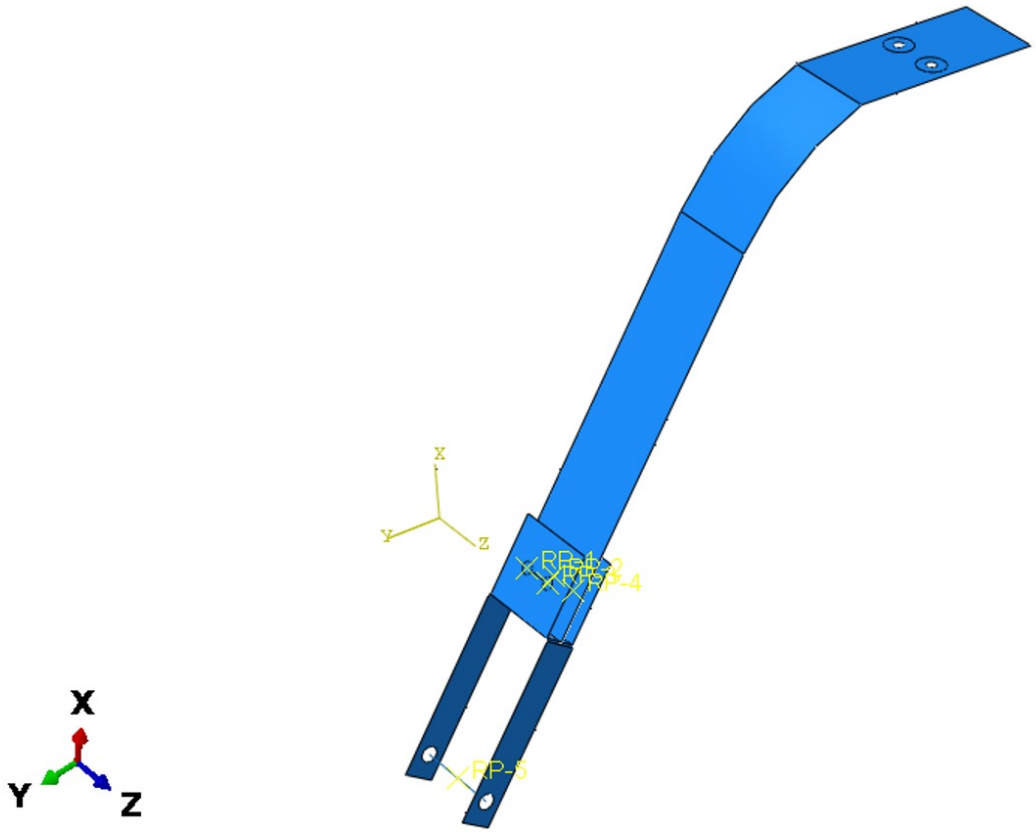

Figure 6.29: Optimized detailed design of NLG

the volume percentage of carbon fiber given by the code. Since the number of carbon and S-glass plies are the same, the density will also be equal for both composites.

Therefore, density for the laminae composites is,

$$\rho = PVC * \rho_{CFRP} + (1 - PVC) * \rho_{GFRP} = 1727,4kg/m3$$

Via the FEM software capabilities, the total mass of the parts is easily obtained:

$$m_{NLG} = 51.52g$$

$$m_{MLG} = 356.78g$$

$$m_{Tot} = 408.30g$$

It is a value way below the 5% of total weight of the drone defined as maximum for the landing gear (588.05 g) which represents compliance with the restriction while still having leverage to account for bolts used for attachment and the tire wheel assembly.

Chapter 7

Conclusions

This master's thesis focused primarily on two areas of modification to a previously designed drone. One section was devoted to the integration of a novel forest firefighting technology and the design of the necessary components, while the other section, the primary one, was devoted to the development of a tricycle landing gear.

One had to be chosen from the few presented alternatives for the extinguishing method.

The CO_2 snow cannon proved to be an effective alternative to conventional firefighting techniques. For its application, the possibility of designing a custom-made nozzle was considered; however, the design was abandoned after it was determined that its manufacturability would be challenging and its price would not be proportional to its benefits.

The selection of a nozzle and the sizing of the pressure vessels for a given area of fire demonstrated that, by not relying solely on water, this technology provides a large area of fire that can be extinguished per volume of extinguisher occupied in the fuselage. Even after accounting for all the valves required for proper operation, the weight was advantageous because it provided a reduction compared with the solution previously defined for the development of the drone.

The initial landing gear design analysis was analytic. The material was selected by focusing on theoretical models for curved beams and theories of equivalent laminates.

Different stacking sequences were analyzed for both segments, and theoretical models were used to predict the behavior of the struts. To reduce calculation time, MATLAB code was developed and later validated using FEM.

Evidently, FEM analysis revealed that deflections could be accurately predicted by the bending properties of the equivalent laminate, whereas stress analysis revealed significant differences when compared to lamina-by-lamina stacking.

One possible explanation for these results is that FEM software must also take membrane properties into account for accurate stress analysis. Alternatively, it can be explained by the stress distribution per laminae that exists in a composite stacking but does not exist when the material is simplified to a single lamina with equivalent properties.

Regardless, these results limit the application of stress-based failure criteria. This prompted the search for alternative standards, which resulted in the adoption of a strain-based, unit-circle

criterion.

The final detailed design for both components of the landing gear, as well as their attachment to the fuselage and wheel-tire assembly, were defined via optimization.

The primary objectives were met as it was demonstrated that the designed structure could withstand the loads specified by law, the weight fell within the maximum criteria established, and resistance to high temperatures was achieved (by selection of the ablative, not actual design of the layer).

7.1 Future Works

The designs of the landing gear and components for the extinguishing method are not finalized until the production and testing of their prototypes. It is an important aspect of future work to verify or refute the results of this project.

Additional testing is required to determine the exact efficacy of the extinguishing method against small and large-scale fires. If the results are positive, there will be a recommendation to implement this technology in larger firefighting vehicles because it can significantly enhance disaster response capabilities.

The landing gear requires significant additional testing. For heat resistance, the outer layer material was chosen; however, an in-field analysis of temperatures is necessary to design the ablative layer effectively. This outer layer is also a recommendation to be implemented throughout the drone.

Moreover, vibration analysis of the two segments is also a significant factor, as this phenomenon can have catastrophic effects on the structure if improperly designed. Due to time constraints, it could not have been incorporated into the current project.

Finally, the introduction of adhesive materials for attachment to the fuselage should be investigated so that holes are not necessary, thereby reducing the stress concentration caused by them.

In addition, fatigue was not a topic of study in the present work, so a proper study to comprehend the landing gear life-cycle may be of interest.

Bibliography

[1] Lúcia Sofia Batalha de Moura. Master's thesis - drone de combate aos incêndios florestais. *Faculdade de Engenharia da Universidade do Porto*, 2019.

[2] António Matos Guerra, José Augusto Coelho, and Ruben Elvas Leitão. Fenomenologia da combustão e extintores. *Manual de Formação Inicial do Bombeiro*, 7, 2003.

[3] Carlos Ferreira de Castro, Gouveia Serra, José Parola, José Reis, Luciano Lourenço, and Sérgio Correia. Combate a incêndios florestais. *Escola Nacional de Bombeiros*, 13, 2003.

[4] Technology and Tools. Fire extinguishing ball | extinguisher bomb. https://www.youtube.com/watch?v=L_0sawCkIk4, 2018. [Online; accessed 30-April-2022].

[5] Elidefire - fire extinguishing ball. https://www.elidefire.com/. Accessed: 2022/04/30.

[6] Time watch two students extinguish fire using sound. https://time.com/3760361/students-extinguish-fire-with-sound/. Accessed: 2022/04/30.

[7] Dell Technologies sound waves to fight wildfires: How does it work? https://www.dell.com/en-us/perspectives/fighting-fire-with-bass-using-sound-waves-to-drown-flames/. Accessed: 2022/04/30.

[8] Lockheed Martin sikorsky firehawk aircraft. https://www.lockheedmartin.com/en-us/products/sikorsky-firehawk.html. Accessed: 2022/04/30.

[9] Aeroin portugal compra helicópteros americanos para substituir modelo russo. https://aeroin.net/portugal-compra-helicopteros-americanos-para-substituir-modelo-russo/. Accessed: 2022/09/04.

[10] Canadair the unparalleled aerial firefighting aircraft. https://aerialfirefighter.vikingair.com/. Accessed: 2022/04/30.

[11] Diario de Notícias força aérea diz que aeronaves canadair estiveram inoperacionais 17 dias desde julho. https://www.dn.pt/sociedade/forca-aerea-diz-que-aeronaves-canadair-estiveram-inoperacionais-17-dias-des
html. Accessed: 2022/09/04.

[12] Radio Renascença novos canadair só chegam em 2024. "até lá temos de viver com o que temos", avisa costa. https://rr.sapo.pt/noticia/pais/2022/08/12/novos-canadair-so-chegam-em-2024-ate-la-temos-de-viver-com-o-que-temos-avi
295660/. Accessed: 2022/09/04.

[13] Insider ehang has developed a firefighting autonomous flying vehicle for high-rise fires in dense cities — see how it works. https://www.businessinsider.com/ehang-developed-firefighting-autonomous-aerial-vehicle-for-high-rise-fires-2020 Accessed: 2022/04/30.

[14] Insider a latvian company is developing drones that can put out fires. https://www.businessinsider.in/a-latvian-company-is-developing-drones-that-can-put-out-fires/articleshow/63600390.cms. Accessed: 2022/04/30.

[15] BoldMethod 4 types of landing gear strut. https://www.boldmethod.com/learn-to-fly/systems/how-the-4-types-of-landing-gear-struts-work/. Accessed: 2022-05-15.

[16] SESAR Joint Undertaking. European drones outlook study. *OJ*, November 2016.

[17] Penn State CEMS classification of the unmanned aerial systems. https://www.e-education.psu.edu/geog892/node/5. Accessed: 2022/08/30.

[18] FNAC drones: A nova marcação de classe europeia. https://www.fnac.pt/Drones-a-nova-marcacao-de-classe-europeia/cp2359/w-4. Accessed: 2022/08/30.

[19] AUAV drone tyoes: Multi-rotor vs fixed-wing vs ssingle rotor vs hybrid vtol. https://www.auav.com.au/articles/drone-types/. Accessed: 2022/08/30.

[20] CW nasa all-electric experimental aircraft to begin ground testing. https://www.compositesworld.com/articles/nasa-all-electric-experimental-aircraft-to-begin-ground-testing. Accessed: 2022/04/30.

[21] JEC Composites. A "one shot" aircraft to revolutionize the light aviation sector. *JEC Composites Magazine*, 2018.

[22] The Engineer. Autoflight air taxi completes transition test flight. *The Engineer*, 2022.

[23] Tronair types of landing gear equipment and tools. https://www.tronair.com/resources/types-of-landing-gear-equipment-and-aircraft-servicing-tools. Accessed: 2022-04-30.

[24] Academic conventional landing gear. https://en-academic.com/dic.nsf/enwiki/525308#cite_note-GroundUp-1. Accessed: 2022-04-30.

[25] GroundSchool takeoff considerations. http://web.archive.org/web/20080719131723/http://www.auf.asn.au/groundschool/umodule11.html#handy. Accessed: 2022-04-30.

[26] Aircraft Wiki tricycle landing gear. https://aircraft.fandom.com/wiki/Tricycle_landing_gear. Accessed: 2022-04-30.

[27] Sourav Sinha, Siddharth Raj Gupta, Siddharth Prasad, Ronit Bansal, and Ritesh Maurya. Designing of an aircraft based on preliminary mission requirement. *Indian Institute of Technology Kanpur*, 2017.

[28] Aircraft landing gear layouts. http://www.aerospaceweb.org/question/design/q0200.shtml. Accessed: 2022-04-30.

[29] Academic Dictionaries and Encyclopedias ground loop (aviation). https://en-academic.com/dic.nsf/enwiki/470937. Accessed: 2022/08/31.

[30] Why bother with retractable landing gear. https://www.planeandpilotmag.com/article/why-bother-with-retractable-gear/. Accessed: 2022-05-15.

[31] Flight Mechanics fixed vs retractable landing gear. https://www.flight-mechanic.com/landing-gear-types-fixed-and-retractable-landing-gear-part-one/. Accessed: 2022-05-15.

[32] Pasquale M Sforza. *Commercial airplane design principles*. Elsevier, 2014.

[33] 2017 suzuki gsx-r1000 and gsx-r1000r previews. https://www.motorcycle.com/manufacturer/suzuki/2017-suzuki-gsx-r1000-and-gsx-r1000r-previews.html/attachment/100416-2017-suzuki-gsx-r1000-no-fairing. Accessed: 2022/06/30.

[34] The Pilot's Manual Editorial Team. *The Pilot's Manual: Ground School*. ASA, 2020.

[35] Aeronautics Guide landing gear types. https://www.aircraftsystemstech.com/p/landinggear-types-aircraft-landing-gear.html. Accessed: 2022-05-15.

[36] Documentary Base. ury And The Flames - German Aircraft Of WW1 - Full Documentary. https://www.youtube.com/watch?v=Ju1HLf1x0L4, 2020. [Online; accessed 15-May-2022].

[37] Collins Dictionary. helicopter. https://www.collinsdictionary.com/pt/dictionary/english/helicopter. [Online; accessed 21-August-2022].

[38] Snorri Gudmundsson. *General aviation aircraft design: Applied Methods and Procedures*. Butterworth-Heinemann, 2013.

[39] Aeronautics Guide landing gear shock strut. https://www.aircraftsystemstech.com/p/there-are-many-different-designsof.html. Accessed: 2022-05-15.

[40] Adrian P Mouritz. *Introduction to aerospace materials*. Elsevier, 2012.

[41] A Rashidi and AS Milani. Finite element analysis of a composite landing gear and effect of runway material. In *Canadian Society for Mechanical Engineering International Congress, June*, pages 26–29, 2016.

[42] Kaushik Kumar, Divya Zindani, and J Paulo Davim. *Sustainable engineering products and manufacturing technologies*. Academic Press, 2019.

[43] Jeff Sloan. 2019 paris air show. *CompositesWorld*, August 2019.

[44] Ashley Graber. Developing of thermoplastic composites for use in commercial aircraft. *Aerospace & Defense Technology*, October 2021.

[45] Zübeyir CEYLAN. Design of landing gear for hürkuş. *Academia*, 2017.

[46] G Vasanth, R Deepack, S Murali, and S Magesh. Comprehensive analysis on mechanical behavior of airworthy raw materials for aircraft landing gear system. In *AIP Conference Proceedings*, page 020096. AIP Publishing LLC, 2020.

[47] Tuan H Tran. *Master's Thesis - Landing-Gear Impact Response: A Non-linear Finite Element Approach*. University of North Florida, 2019.

[48] J Pauliny. Master's thesis - landing gear design for single-engine four-seat aircraft. *Brno University of Technology, Faculty of Mechanical Engineering: Brno, Czechia*, 2014.

[49] Dorothea C Walden. Applications of composites in commercial airplanes. *Structural Composites: Design and Processing Technologies*, pages 77–82, 1990.

[50] Amit Goyal. Light aircraft main landing gear design and development. *MS Ramaiah, School of Advanced Studies, INDIA*, 2002.

[51] PK Mallick. Thermoset matrix composites for lightweight automotive structures. In *Materials, Design and Manufacturing for Lightweight Vehicles*, pages 229–263. Elsevier, 2021.

[52] Albertino Arteiro. Polímeros e compósitos de matriz polimérica - matérias-primas e processos de fabrico para materiais compósitos de matriz polimérica. University Lecture, 2019.

[53] freemanmfg. Vacuum Bagging a Carbon Fiber/Composite Part - Complete Video. https://www.youtube.com/watch?v=_ik6e8ttEf0, 2021. [Online; accessed 21-August-2022].

[54] FIBREGLAST what are prepregs? https://www.fibreglast.com/product/about-prepregs/Learning_Center. Accessed: 2022/08/29.

[55] Castro Composites preimpregnados. https://www.castrocompositesshop.com/pt/8-preimpregnados. Accessed: 2022/08/29.

[56] Formlabs how to manufacture carbon fiber parts. https://formlabs.com/blog/composite-materials-carbon-fiber-layup/. Accessed: 2022/08/29.

[57] Legislation NATO stanag 4703 - light unmanned aircraft systems airworthiness requirements, 2014.

[58] NATO standards for unmanned aerial vehicles. https://www.nato.int/cps/en/natolive/news_7819.htm. Accessed: 2022-05-15.

[59] Mohammad H Sadraey. *Aircraft design: A systems engineering approach*. John Wiley & Sons, 2012.

[60] Rikard Benton Heslehurst. Undercarriage lateral tip-over criteria: a parametric study. *Journal of aircraft*, 48(6):1825–1828, 2011.

[61] Norman S Currey. *Aircraft landing gear design: principles and practices*. Aiaa, 1988.

[62] Z. Husain, M.Z. Abdullah, and Tze Chuen YAP. Two-dimensional analysis of tandem/staggered airfoils using computational fluid dynamics. *International Journal of Mechanical Engineering Education*, 33:195–207, 07 2005.

[63] NASA thrust to weight ratio. https://www.grc.nasa.gov/www/k-12/airplane/fwrat.html. Accessed: 2022/07/20.

[64] RisingUp Aviation federal aviation regulations. https://www.risingup.com/fars/info/part23-485-FAR.shtml, 1993.

[65] Braked Roll Conditions loads and dynamics harmonization. https://www.faa.gov/regulations_policies/rulemaking/committees/documents/media/TAEladhT12-6101994.pdf, 1994.

[66] CS-VLA easy access rules for very light aeroplanes. https://www.easa.europa.eu/en/downloads/66873/en. Accessed: 2022/07/20.

[67] Carlos Fernandes. Orgãos de máquinas ii - curved beams. University Lecture, 2021.

[68] Hariharan Iyer. *The effects of shear deformation in rectangular and wide flange sections*. PhD thesis, Virginia Tech, 2005.

[69] Daniel Poelaert, Joachim Schniewind, and Frank Janssens. Surface area and curvature of the general ellipsoid. *arXiv preprint arXiv:1104.5145*, 2011.

[70] S Timoshenko. Strength of materials-part 1 elementary theory and problems . new york city, 1940.

[71] Pilkey WD. Peterson's stress concentration factors. *Hoboken: Wiley*, page 524, 1997.

[72] Daniel Gay and Suong V. Hoa. *Composite Materials: Design and applications*. CRC Press, Taylor and Francis Group, 2007.

[73] William F. Smith and Javad Hashemi. *Fundamentos de Engenharia e Ciência dos Materiais*. AMGH Editora Ltda., 2012.

[74] Ansys. Granta edupack - 2021 r1. https://www.ansys.com/products/materials/granta-edupack. Accessed: 07-09/2022.

[75] José Miguel Casaca Faria Silva. Master's thesis - development of a nose landing gear of an unmanned aircraft (rpas). *Faculdade de Engenharia da Universidade do Porto*, 2017.

[76] TWI - Global thermoset vs thermoplastic (what is the difference?). https://www.twi-global.com/technical-knowledge/faqs/thermoset-vs-thermoplastic#WhatistheDifferencebetweenThermosetandThermoplastic. Accessed: 2022/07/15.

[77] AR Bunsell and B Harris. Hybrid carbon and glass fibre composites. *Composites*, 5(4):157–164, 1974.

[78] Ionut Ciobanu, Liviu Drăgus, Laura Tigleanu, Cătălin Frunza, Dan Bălăuta, and Serban Olaru. Manufacturing of a landing gear using composite materials for an aerial target. In *Journal of Physics: Conference Series*, volume 1297. IOP Publishing, 2019.

[79] Daniel Rodrigues. Compósitos ablativos para veículos de reentrada atmosférica. *Faculdade de Engenharia da Universidade do Porto*, 2016.

[80] L Torre, JM Kenny, and AM Maffezzoli. Degradation behaviour of a composite material for thermal protection systems part i–experimental characterization. *Journal of Materials Science*, 33(12):3137–3143, 1998.

[81] Robin AS Beck. Ablative thermal protection system fundamentals. In *International Planetary Probe Workshop*, 2013.

[82] José Meseguer, Isabel Pérez-Grande, and Angel Sanz-Andrés. *Spacecraft thermal control*. Elsevier, 2012.

[83] Cork Composites. Reinventing panels & composites, multilayer, core & decking materials. https://amorimcorkcomposites.com/media/6312/brochura-pc_en_digital.pdf.

[84] Robert M Jones. *Mechanics of composite materials*. CRC press, 2018.

[85] Junuthula Narasimha Reddy. *Mechanics of laminated composite plates and shells: theory and analysis*. CRC press, 2003.

[86] Albertino Arteiro. Aircraft structural materials and joints - advanced composites. failure modes and failure criteria. University Lecture, 2022.

[87] Albertino Arteiro. Polímeros e compósitos de matriz polimérica - modos de rotura de compósitos de matriz polimérica reforçados por fibras contínuas. University Lecture, 2019.

[88] Richard Gordon Budynas, J Keith Nisbett, et al. *Shigley's mechanical engineering design*, volume 9. McGraw-hill New York, 2011.

[89] Abaqus guide book. http://130.149.89.49:2080/v6.10ef/books/usb/default.htm?startat=pt06.html. Accessed: 2022/09/15.

[90] FEA-CAE ENGINEERING fea element types. http://fea-cae-engineering.com/fea-cae-engineering/element_types.htm. Accessed: 2022/09/15.

[91] EnterFEA what are the types of elements used in fea? https://enterfea.com/what-are-the-types-of-elements-used-in-fea/. Accessed: 2022/09/15.

[92] ASR Engineering fea mesh elements & nodes guide | intro to fea. https://asrengineering.com/2019/09/23/fea-mesh-elements-nodes-guide-intro-to-fea/. Accessed: 2022/09/15.

[93] Scott Jenkins. Practical spray technology: Fundamentals and practice. *Chemical Engineering*, 119(9):9–10, 2012.

[94] Graham B Wallis. *One-dimensional two-phase flow*. Courier Dover Publications, 2020.

[95] Patrick H Oosthuizen and William E Carscallen. *Compressible fluid flow*, volume 179. McGraw-Hill New York, 1997.

[96] Paulo Coelho. *Tabelas de Termodinâmica*. Lidel, 2017.

[97] Carlos Fernandes. Orgãos de máquinas ii - tensões em peças cilíndricas. University Lecture, 2019.

[98] ASME boiler and pressure vessel certification. https://www.asme.org/certification-accreditation/boiler-and-pressure-vessel-certification. Accessed: 2022/09/06.

[99] P. J. S. Lourenço Marques. Dimensionamento/projecto de reservatórios sob pressão (rsp) segundo a norma asme. *Universidade de Aveiro - Departamento de Engenharia Mecânica, Portugal*, 2007.

[100] Maan Jawad. *Theory and design of plate and shell structures*. Springer Science & Business Media, 2012.

[101] Gerd Roloff. Airbus aircraft of the landing gear, evolution of a system. `https://web.archive.org/web/20081122135510/http://www.fzt.haw-hamburg.de/pers/Scholz/dglr/hh/text_2002_04_11_Fahrwerk.pdf`. Accessed: 2022/09/07.

[102] Simões Morais. Desenho técnico básico 3. *Porto Editora*, 2006.

ANNEX 1 - MATLAB CODES

Wheel Track calculation

```
function [T] = WheelTrack(H, xMLG, xNLG, m, V, CG, T)
err = 1 ;
itt = 0 ;
T_ = T;
B = xMLG - xNLG ;
Bm = xMLG - CG ;
while err > 0.02 && itt < 100
T = (T_ + T) /2 ;
phi1 = 0.4363 ;
T1 = 2*H*tan(phi1) ;
aux1 = atan(T/(2*B)) ;
aux2 = atan(2*Bm/T) ;
aux3 = pi/2 - aux1 - aux2 ;
aux4 = aux3 + aux1 ;
y = T/(2*sin(aux4)) ;
x = sin(aux3) * y ;
phi2 = atan(x/H) ;
T2 = tan(phi2)*2*H;
h = T/2 ;
R = sqrt(B^2+h^2) ;
Fc = m*V^2/R ;
phi3 = atan (Fc/(m*9.81)) ;
T3 = tan(phi3)*2*H ;
T_ = max ([T1,T3]) ;
if T_ > T
err = 1 ;
else
err = T-T_;
end
itt = itt+1 ;
end
end
```

Equivalent Properties of the Laminate

```
function [PropB, PropM, T, PVC] = EquivProps(k, PropC, PropG)
N = numel (k)/2;
mid = N/2;
Qc = [PropC(1)/(1-PropC(3)*PropC(4)), PropC(3)*PropC(2)/(1-PropC(3)*PropC(4)), 0; PropC(3)
*PropC(2)/(1-PropC(3)*PropC(4)), PropC(2)/(1-PropC(3)*PropC(4)), 0; 0, 0, PropC(5)];
Qg = [PropG(1)/(1-PropG(3)*PropG(4)), PropG(3)*PropG(2)/(1-PropG(3)*PropG(4)), 0; PropG(3)
* PropG(2)/(1-PropG(3)*PropG(4)), PropG(2)/(1-PropG(3)*PropG(4)), 0; 0, 0, PropG(5)];
for i = 1 : N
```

```
k(i) = deg2rad(k(i));
q=k(i);
T(i*3-2:i*3,1:3) = [cos(q)^2, sin(q)^2, 2*cos(q)*sin(q);
sin(q)^2, cos(q)^2, -2*cos(q)*sin(q); -cos(q)*sin(q), cos(q)*sin(q), cos(q)^2 - sin(q)^2] ;
end
for i = 1 : mid
Trans = T(i*3-2:i*3,1:3);
P = inv(Trans);
Y = inv(Trans.');
Q(i*3-2:i*3,1:3) = P*Qg*Y;
t(i) = 0.226;
end
for i = mid+1 : N
Trans = T(i*3-2:i*3,1:3);
P = inv(Trans);
Y = inv(Trans.');
Q(i*3-2:i*3,1:3) = P*Qc*Y;
t(i) = 0.152;
end
T = sum(t);
PVC = sum(t(mid+1:N))/T;
A = Q(1:3,1:3) * t(1);
D = Q(1:3,1:3) * (T^3 - (T - t(1))^3);
for i = 2 : N
A = A + Q(i*3-2:i*3,1:3) .* t(i);
D = D + Q(i*3-2:i*3,1:3) .* ((T-sum(t(1:i-1)))^3-(T-sum(t(1:i)))^3);
end
T=T*2;
A = A * 2;
D = D * 2 / 3;
E1B = 12 * (D(1,1)* D(2,2) - D(1,2)^2)/(D(2,2)*T^3);
E2B = 12 * (D(1,1)* D(2,2) - D(1,2)^2)/(D(1,1)*T^3);
v21B = D(1,2)/D(2,2);
v12B = D(1,2)/D(1,1);
G12B = 12 * D(3,3)/(T^3);
E1M = (A(1,1)* A(2,2) - A(1,2)^2)/(A(2,2)*T);
E2M = (A(1,1)* A(2,2) - A(1,2)^2)/(A(1,1)*T);
v12M = A(1,2)/A(2,2);
v21M = A(1,2)/A(1,1);
G12M = A(3,3)/T;
PropB = [E1B, E2B, v12B, v21B, G12B];
PropM = [E1M, E2M, v12M, v21M, G12M];
```

Stress and deflections on the leaf strut

```
function [D] = Displacement(EB1, as, H, b, F)
a=H;
e=sqrt((a/b)^2-1);
```

```
D=zeros (30, 4);
for i = 1 : 30
bs=0.006 + 0.002*i;
I=as^3*bs/12;
syms x
expr = (1 - cos(x))^2*sqrt(1+e^2*cos(x)^2);
f=pi/2;
Fint = int(expr,x,[0 f]);
dispV = F*b^3/(EB1*I) * vpa(Fint);
syms x
expr = sin(x)*(1-cos(x))*sqrt(1+e^2*cos(x)^2);
Fint = int(expr,x,[0 f]);
dispH = F*a*b^2/(EB1*I) * vpa(Fint);
disp = sqrt((dispV^2 + dispH^2));
r1 = a - as/2;
r2 = a + as/2;
r = a;
e = r - as/log(r2/r1);
M = F * b;
stress = M * ((as / 2)-e) / (as * bs * e * (r-as/2));
stress = stress * 10^(-6);
N = i, bs, disp, stress, dispV, dispH;
for j=1:6
D(i,j) = Nj;
end
end
```

ANNEX 2 - NOZZLE ITERATION

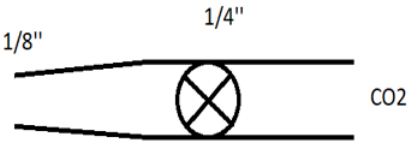

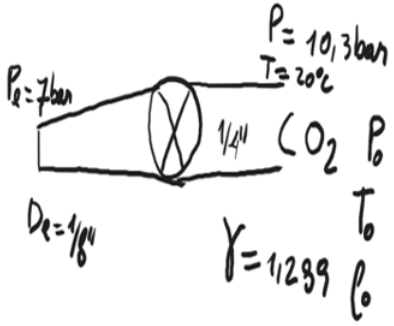

pe	700000	Pa	p0	1300000	Pa
P*	712040.5521	Pa	T0	20	ºC
p* > pe	pe = p*	Ma>1	k	1.289	
Ve	249.1990387	m/s	R	188.09	J/(kgK)
r	0.0015875	m	ro 0	23.57695678	kg/m3
A	7.9173E-06	m2			
ṁ	0.029160074	kg/S	0.02916		

By the end of the converging nozzle, the Mach number will never be greater than 1, outlet pressure equal to the critical pressure. There should be a small expansion after the nozzle to reach the pressure of 7 bar

Assuming isentropic

					b	after expansion outside the convergent		assuming the expansion isentropic
ro e	14.77967623	kg/m3			ro b	14.5854169	kg/m3	
T e	256.1380516	K	-17.0119	ªC	T b	255.1605246	K	
a e	249.1990387	Proving Mach number = 1 at the exit of tho nozzle						

At pressure 7bar, CO2 joins the H20, flow is assumed homogeneous

H20

p	700000	Pa			
T	20	ºC			
caudal volumetrico de H20 = 1/100 caudal volumétrico CO2					
m	0.014580037	kg/s	1/2 m CO2		
ro	1000	kg/m3			
r	0.003175	m			
A	3.16692E-05	m2			
V	0.460385139	m/s			

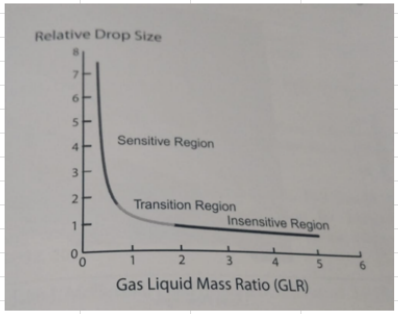

Should be in the area that does not suffer from alterations - insensitive reguon
In this case, if the real ratio is 2, 3, 4, 5, ... there will be no major changes in the final results
For practical effects, the value is assumed to be 2 or now

m	0.50	mass ratio			
ar			density H20 >>> density ar		
T	255.1605246	K			
R	188.09	J/(kgK)	mistura		
ro	14.5854169	kg/m3	ro	21.87812535	kg/m3
V	249.1990387	m/s	R	125.3933333	J/(kgK)
k	1.289		k	1.289	
			zero heat transfer inside the mixture		
			it assumess equal speed for both phases		
			it is not appliable to the situation		

m	0.04374011		
cp J2O	4.18	cv agua	4.15
cp CO2	0.846	cv CO2	0.657
R	125.393333		
k	1.07467057		
having therma	equilibrium		

Pseudogas will go through a convergent -divergnent in order to decrese its temperature

k	1.074670571				A*	1.07817E-05	1.663992412	1.79407E-05	m2		Ae	1.81082E-05
ro 0	21.87812535				r*			0.002389708	m		ro e	12.10664932
p0	700000	Pa			p*	413035.2553	Pa				pe	370614.6601
T0	255.1605246	-17.9895			T*	245.9769066	K				Ve	199.5168958
V 0	124.8297119				V*	182.0631572				arbitrar	Me	1.1
a0	185.4307031	185.431			ro *	13.39116435					Te	244.131705
Assuming v0 as the sum of both phases												
M 0	0.673187934											
A 0	1.60159E-05											
	Ae	1.9E-05	1.9E-05	2.05425E-05	2.20421E-05	2.39497E-05	2.63295E-05	2.9266E-05	3.28684E-05	3.72756E-05		
	ro e	10.8501	9.64148	8.49676535	7.427948725	6.443161556	5.546984788	4.740876927	4.02367058	3.392096858		
	pe	329442	290174	253320.3839	219243.0267	188167.026	160193.4476	135317.5259	113448.4411	94429.39894		
	Ve	216.766	233.797	250.5959052	267.1513561	283.4522513	299.4887313	315.252012	330.7343756	345.9291535		
	Me	1.2	1.3	1.4	1.5	1.6	1.7	1.8	1.9	2		
	Te	242.142	240.016	237.761792	235.386984	232.9003024	230.3102813	227.6255039	224.8545436	222.0059087		
Followed by a convergen where the outside pressure is 1 atm												
pb	101325	Pa										
p*	218681.3154	194387	171217	149471.7849	129364.4278	111028.0223	94522.20214	79844.15553	66940.29405	55718.10128		
Ve	178.0850319	177.358	176.578	175.7463682	174.8664722	173.9403552	172.9704795	171.9593467	170.9094829	169.823424		